

# Mathematical Modeling of the Twin Roll Casting Process for Magnesium Alloy AZ31

by

Amir Hadadzadeh

A thesis  
presented to the University of Waterloo  
in fulfillment of the  
thesis requirement for the degree of  
Doctor of Philosophy  
in  
Mechanical Engineering

Waterloo, Ontario, Canada, 2013

©Amir Hadadzadeh 2013

## **AUTHOR'S DECLARATION**

I hereby declare that I am the sole author of this thesis. This is a true copy of the thesis, including any required final revisions, as accepted by my examiners.

I understand that my thesis may be made electronically available to the public.

Amir Hadadzadeh

## **Abstract**

Although Twin Roll Casting (TRC) process has been used for almost 60 years in the aluminum industry, TRC of magnesium is relatively new. In TRC, molten metal is fed onto water-cooled rolls, where it solidifies and is then rolled. Solidification of the molten metal starts at the point of first metal-roll contact and is completed before the kissing point (point of least roll separation) of the two rolls. The unique thermo-physical properties inherent to magnesium and its alloys, such as lower specific heat and latent heat of fusion and larger freezing ranges (in comparison with aluminum and steel) make it challenging for TRC of this alloy. Therefore, a comprehensive understanding of the process and the interaction between the casting conditions and strip final quality is imperative to guarantee high quality twin roll cast strip production. A powerful tool to achieve such knowledge is to develop a mathematical model of the process.

In this thesis, a 2D mathematical model for TRC of AZ31 magnesium alloy has been developed and validated based on the TRC facility located at the Natural Resources Canada Government Materials Laboratory (CanmetMATERIALS) in Hamilton, ON, Canada. The validation was performed by comparing the predicted exit strip temperature and secondary dendrite arm spacing (SDAS) through the strip thickness with those measured and obtained by experiments. The model was developed in two stages, first a thermal-fluid model was developed followed by validation and then a thermal-fluid-stress model was developed. This is the first time a comprehensive thermal-fluid-stress model has been developed to simulate the TRC process for magnesium alloys. The work has led to new knowledge about the TRC process and its effects on magnesium strip quality including the following:

- 1) Using ALSIM and ANSYS<sup>®</sup> CFX<sup>®</sup> commercial packages a 2D mathematical model of thermal-fluid-stress behavior of the magnesium sheet during TRC was successfully developed and validated.

- 2) An average value of  $11 \text{ kW/m}^2\text{°C}$  for the Heat Transfer Coefficient (*HTC*) was found to best represent the heat transfer between the roll and the strip during TRC casting of AZ31 using the CanmetMATERIALS facility.
- 3) Modeling results showed that increasing casting speed, casting thicker strips and applying higher *HTCs* led to less uniform microstructure through thickness in terms of SDAS.
- 4) Simulations showed the importance of casting parameters such as casting speed and set-back distance on the thermal history and stress development in the sheet during TRC; higher casting speeds led to deeper sumps and higher exit temperatures as well as lower overall rolling loads and lower total strains experienced during TRC.
- 5) The effect of roll diameter on the thermal history and stress development in the strip was also studied and indicated how larger roll diameters increased the surface normal stress and rolling loads but had little effect on the mushy zone thickness.
- 6) The correlation between the mechanisms of center-line and inverse segregation formation and thermo-mechanical behavior of the strip was performed. The modeling results suggested that increasing the set-back distance decreases the risk of both defects. Moreover, increasing the roll diameter reduces the propensity to inverse segregation but has a minor effect for center-line segregation formation.

## Acknowledgements

First of all I am grateful of God who cares and supports every time and everywhere.

I would like to express my best and deepest appreciation to my supervisor Professor Mary A. Wells. With her insightful ideas, encouragements and supports I could start and afford a new career in my academic life. Whenever I felt despondent of my research she made me confident with her warm encouragements. She taught me the key for success not even in research, also in life is patience. Without her supports, I could never accomplish this research.

I should thank my dear friend Dr. Amir Baserinia because of his helps in understanding and developing the CFD model.

This research was financially supported by the NSERC strategic network-MagNET. I would like to thank them for their support. Parts of the experimental procedure have been done at the Natural Resources Canada Government Materials Laboratory (CanmetMATERIALS) located in Hamilton, ON, Canada. Dr. M. S. Kozdras and his team Dr. A. Javaid, Mr. G. Birsan and Mr. P. Newcombe conducted some trials for us. I would like to appreciate all their supports.

My deepest gratitude goes to my father, mother and sisters for all their help and love provided me in my life. Finally, I would like to appreciate and thank my lovely wife, Sepideh. As my best friend she always supports me in my life. She patiently endures all of the difficulties in our life and encourages me not to give up. She is who brought the pure love to my life. I love you Sepideh, now and forever.

## **Dedication**

*To My Lovely and Beautiful SEPIDEH*

*And*

*Little ARIANA*

## Table of Contents

<b>AUTHOR'S DECLARATION.....</b>	<b>ii</b>
<b>Abstract.....</b>	<b>iii</b>
<b>Acknowledgements .....</b>	<b>v</b>
<b>Dedication .....</b>	<b>vi</b>
<b>Table of Contents .....</b>	<b>vii</b>
<b>List of Figures.....</b>	<b>xi</b>
<b>List of Tables .....</b>	<b>xviii</b>
<b>Chapter 1 Introduction.....</b>	<b>1</b>
1.1 Need for Lightweight Materials in the Transportation Sector .....	1
1.2 Challenges in Producing Magnesium Sheet.....	6
<b>Chapter 2 Twin Roll Casting (TRC) of Magnesium Alloys .....</b>	<b>8</b>
2.1 Magnesium Alloy Sheet Production .....	8
2.2 Twin Roll Casting Process .....	9
2.3 Use of TRC for Aluminum Alloys and Steel .....	12
2.4 Magnesium Twin Roll Casting .....	12
2.4.1 Microstructure of Twin Roll Cast Magnesium Strips .....	13
2.4.2 Microstructural Defects in Twin Roll Cast Magnesium Sheets .....	15
2.5 Mathematical Modeling of the Twin Roll Casting Process .....	19

2.5.1 Fluid Models .....	19
2.5.2 Thermal-Fluid and Thermal-Fluid-Stress Models .....	20
2.6 Summary .....	35
<b>Chapter 3 Scope and Objectives .....</b>	<b>36</b>
<b>Chapter 4 Experimental Measurements .....</b>	<b>38</b>
4.1 TRC Procedure at CanmetMATERIALS.....	38
4.1.1 Casting Conditions .....	41
4.2 Microstructure Analysis .....	42
<b>Chapter 5 Mathematical Model Development .....</b>	<b>45</b>
5.1 Thermal-Fluid Model (ANSYS® CFX®) .....	45
5.1.1 Geometry and Computational Domain.....	45
5.1.2 Mathematical Model.....	46
5.1.2.1 Governing Equations .....	47
5.1.2.2 Boundary Conditions .....	49
5.2 Thermal-Fluid-Stress Model (ALSIM) .....	52
5.2.1 Mathematical Model.....	52
5.2.2 Solution Domain and Boundary Conditions.....	54
5.2.3 Mesh Size Sensitivity Analysis .....	56
5.3 Material Properties .....	57

5.4 Model Validation.....	61
<b>Chapter 6 Microstructure Analysis Results .....</b>	<b>65</b>
<b>Chapter 7 Thermal-Fluid Model Application .....</b>	<b>74</b>
7.1 Biot Number Analysis .....	74
7.2 Effect of Casting Conditions on Thermal-Fluid History of the Strip.....	76
7.2.1 Exit Strip Temperature and Temperature Gradient through Thickness .....	78
7.2.2 Sump Depth and Mushy Zone Thickness.....	82
7.2.3 Microstructure Uniformity .....	86
7.3 Summary .....	94
<b>Chapter 8 Thermal-Fluid-Stress Model Application .....</b>	<b>96</b>
8.1 Effect of Casting Conditions on Thermal-Fluid-Stress History of the Strip.....	96
8.1.1 Thermal History of the Cast Strip.....	97
8.1.2 Surface Stress Development.....	100
8.1.3 Roll Separating Force .....	108
8.1.4 Effective Strain at the Center-line .....	110
8.2 Effect of Roll Diameter (Scale-Up Modeling).....	114
8.2.1 Strip Thermal History .....	115
8.2.2 Surface Normal Stress .....	119
8.2.3 Effective Strain at the Center-Line .....	121

8.2.4 Roll Separating Force .....	122
8.3 Defect Formation.....	125
8.3.1 Center-Line Segregation.....	125
8.3.2 Inverse Segregation .....	132
8.3.3 A Comparison to Literature.....	140
8.4 Summary .....	144
<b>Chapter 9 Summary, Conclusions and Future Work.....</b>	<b>146</b>
9.1 Summary and Conclusions.....	146
9.2 Future Work .....	149
<b>References.....</b>	<b>151</b>
<b>Appendix A Equivalent Specific Heat Calculation .....</b>	<b>163</b>

## List of Figures

Figure 1-1- Fuel consumption affected by vehicle weight [6].....	2
Figure 1-2- Estimated average required fleet-wide fuel economy under proposed CAFE Standards [3].....	2
Figure 1-3- The world production of primary magnesium metal, data reproduced from [10, 11]. .....	3
Figure 1-4- Magnesium consumption by application for: a) 1997 and b) 2009 [7, 8]. .....	4
Figure 1-5- Magnesium alloys usage breakdown by sector in 2005 [12].....	5
Figure 1-6- Car weight distribution [4].....	7
Figure 2-1- DC casting vs. TRC for sheet production [19]. .....	9
Figure 2-2-Simple schematic of twin roll casting process (horizontal position). .....	10
Figure 2-3- Relationship between roll material, use of lubricant and maximum roll speed at which AA5182 aluminum alloy strip can be cast; (A) steel roll coated with lubricant (B) steel roll (C) copper roll, graph reproduced from [27].....	11
Figure 2-4-Successful manufacturing condition for AZ31B (O: successful conditions, Δ: unsuccessful conditions) [45]. .....	13
Figure 2-5- Typical microstructure of a twin roll cast AZ31 magnesium strip through thickness [67].....	14
Figure 2-6- Optical images of a) center-line segregation and b) inverse segregation observed for AZ31 magnesium alloy [69]. .....	15
Figure 2-7- Schematic representation of squeezing path for the solute-rich liquid toward the strip surface to from the inverse segregation. ....	17
Figure 2-8- Side dam showing thermocouple positions (shown by •) to capture temperature during casting [79]. .....	21
Figure 2-9- Solidified shell and predicted isotherms in the liquid region [79].....	21
Figure 2-10- Three methods of <i>HTC</i> definition reproduced from Bradbury [82]. .....	23
Figure 2-11- Experimental points versus modeled lines for separating force [28].....	24

Figure 2-12- Nusselt number variation along the roll surface for different exit thicknesses [86].....	26
Figure 2-13- Modeling and measurement results comparison for different a) pouring temperatures and b) casting speed [98, 101].....	28
Figure 2-14- Mechanism used to specify variation in heat flux [41].....	30
Figure 2-15- Equipped rolls with thermocouples used for steel TRC to evaluate <i>HTC</i> [41].	30
Figure 2-16- (a) Temperature-time data recorded by TCs, (b) corresponding heat flux calculated by inverse method, (c) heat flux variation during the contact time [41]. .....	31
Figure 2-17- Effect of casting speed on the <i>HTC</i> in the roll bite [41].....	32
Figure 2-18- <i>HTCs</i> of (a) different peak values and (b) different peak positions [106].....	33
Figure 2-19- Comparison of predicted versus measured surface temperature of the twin roll cast strip after exiting roll bite, l shows the distance to the exit region [112]. .....	34
Figure 4-1- Twin roll caster at CanmetMATERIALS used for magnesium alloys [19]. .....	39
Figure 4-2- TRC layout for magnesium alloys at CanmetMATERIALS [19]. .....	40
Figure 4-3- Recorded data during AZ31 TRC for trial #1 at CanmetMATERIALS.....	42
Figure 4-4- Schematic representation of sample selection for microstructural study. ....	43
Figure 4-5- Sample SDAS measurement procedure, the red lines show the primary dendrite arms and the black lines represent the distance between the secondary arms.....	44
Figure 5-1- Schematic of the twin roll casting process; region 1 is the liquid metal, region 2 is the mushy zone and region 3 is the solid strip, $\ell_1$ , $\ell_2$ and $\ell_3$ are set-back distance, sump depth and mushy zone thickness, respectively. Note: The perspective of the TRC is not to scale and the nozzle size and position are magnified with respect to the rolls .....	46
Figure 5-2- Boundary regions on the solution domain of the twin roll casting process, ANSYS <sup>®</sup> CFX <sup>®</sup> software.....	51
Figure 5-3- Solution domain used for thermal-fluid-stress model and the boundary regions.	54
Figure 5-4- Solution domain and finite element mesh at t=0s.....	56
Figure 5-5- Mesh sensitivity analysis for a) strip exit temperature, b) roll separating force and c) computational time. .....	57

Figure 5-6- Non-equilibrium fraction solid (Scheil cooling condition) for AZ31 magnesium alloy, graph reproduced from Reference [122].....	58
Figure 5-7- Temperature dependent a) elastic modulus and b) thermal expansion coefficient of AZ31 magnesium alloy [124].....	60
Figure 5-8- Stress-strain curves for AZ31 magnesium alloy for different temperatures and strain rates of a) $0.0001\text{s}^{-1}$ , b) $0.001\text{s}^{-1}$ , c) $0.01\text{s}^{-1}$ and d) $0.1\text{s}^{-1}$ [121]. .....	60
Figure 5-9- Comparison of predicted and measured temperature for the conditions shown in Table 4-1, using an $HTC=11\text{kW/m}^2\text{°C}$ . The two dotted lines show $\pm 10\%$ form the correct value.....	62
Figure 5-10- Predicted (solid lines) and measured (symbol) SDAS ( $\lambda$ ) through the strip thickness for a) trial #3 all data, b) trial #3 averaged data, c) trial #4 all data and d) trial #4 averaged data. The dotted lines show $\pm 20\%$ from the model predictions. ....	64
Figure 6-1- As-cast AZ31 twin roll cast strip surface quality a) the whole width and b) strip side, small black arrows show the cracks. ....	65
Figure 6-2- Optical image of the superficial cracks at the edge of the cast strip.....	66
Figure 6-3- As-cast microstructure of twin roll cast AZ31 through thickness for trial #3....	67
Figure 6-4- Optical image of microstructure of the strip above the center-line, the black arrows show the columnar dendrites growth direction, the red circle on lower legends shows where the sample has been chosen.....	67
Figure 6-5- Optical image of the center-line segregation a) continuous and b) non-continuous segregates.....	69
Figure 6-6- Optical image of the center-line segregation, the microstructure of the segregate is absolutely different with the surrounding area.....	70
Figure 6-7- SEM image of the center-line segregation and the region of EDS analysis (points 1 and 2 are inside the center-line segregate and point 3 is inside the bulk material).....	70
Figure 6-8- Optical microstructure of the inverse segregation on the bottom surface of the strip. ....	72
Figure 6-9- Inter-granular cracks in the inverse segregate region. ....	72

Figure 6-10- SEM image of the inverse segregation and the region of EDS analysis (point 1 is inside the inverse segregate and point 2 is inside the bulk material). ....	73
Figure 7-1- Variation of the Biot number along the roll bite during TRC showing the effect of heat transfer coefficient and strip exit thickness.....	76
Figure 7-2- Model-predicted effect of casting speed and final thickness on the surface temperature of the exit strip using an $HTC=11\text{kW/m}^2\text{C}$ .....	79
Figure 7-3- Model-predicted effect of casting speed and heat transfer coefficient on the surface temperature of the exit strip for an exit strip thickness of a) 4mm, b) 5mm and c)6mm. ....	81
Figure 7-4- Model-predicted temperature difference between strip surface and center for different casting speeds, exit strip thicknesses and $HTCs$ . ....	82
Figure 7-5- Model-predicted liquid sump depth for a final strip thickness of a) 4mm, b) 5mm and c) 6mm. ....	84
Figure 7-6- Model-predicted mushy zone thickness for $HTC=11\text{kW/m}^2\text{C}$ and different exit strip thickness.....	85
Figure 7-7- Effect of casting speed on the model-predicted cooling rate during solidification for the AZ31 twin roll cast strip at the surface and center-line for final thickness of a) 4mm, b) 5mm and c) 6mm ( $HTC=11\text{kW/m}^2\text{C}$ ).....	88
Figure 7-8- Model-predicted effect of $HTC$ on the solidification cooling rate at a) center-line and b) strip surface for final thickness of 6mm. ....	89
Figure 7-9- Model-predicted effect of casting speed on the secondary dendrite arm spacing through normalized thickness (0 = top and 1 = bottom) for an $HTC=11\text{kW/m}^2\text{C}$ and final thickness of a) 4mm, b) 5mm and c) 6mm. ....	91
Figure 7-10- Model-predicted SDAS through thickness for final thickness of 6mm and $HTC$ of a) $13\text{kW/m}^2\text{C}$ and b) $15\text{kW/m}^2\text{C}$ .....	92
Figure 7-11- Model-predicted effect of casting speed and final thickness on the microstructure uniformity through thickness for AZ31 twin roll cast strip casting with $HTC=11\text{kW/m}^2\text{C}$ .....	93

Figure 7-12- Model-predicted effect of casting speed and heat transfer coefficient on the microstructure uniformity through the thickness of 4mm AZ31 twin roll cast strip.....	94
Figure 8-1- Model-predicted effect of casting speed on the temperature profile at the strip center-line for a $SB=32.5\text{mm}$ .....	98
Figure 8-2- Model-predicted effect of casting speed and set-back distance on the exit temperature of the strip at the center-line position. ....	98
Figure 8-3- Model-predicted surface shear stress development for $SB=32.5\text{mm}$ and $v=1.0\text{m/min}$ .....	101
Figure 8-4- Model-predicted strip surface stress development (upper graph) and the corresponding liquid-solid profile (lower graph) for $SB=32.5\text{mm}$ and $v=1.0\text{m/min}$ .....	102
Figure 8-5- Model-predicted effect of casting speed on the surface normal stress for set-back distance of a) 32.5mm (12to6), b) 37.5mm (14to6), c) 41.8mm (16to6), d) 37.5mm (12to4) and e) 41.8mm (12to2).....	103
Figure 8-6- Model-predicted effect of casting speed on the amount of solidified material in the roll bite for $SB=32.5\text{mm}$ and casting speed of a) 1.0m/min, b) 2.0m/min and c) 3.0m/min. ....	104
Figure 8-7- Model-predicted effect of set-back distance on (a) the surface normal stress and (b) position at which stress begins to develop at $v=2.0\text{m/min}$ .....	105
Figure 8-8- Model-predicted sump depth for a set-back distance of a) 32.5mm, b) 37.5mm and c) 41.8mm for final thickness of 6mm and $v=2.0\text{m/min}$ .....	106
Figure 8-9- Model-predicted surface shear stress affected by casting speed for set-back distance of a) 32.5mm (12to6), b) 37.5mm (14to6), c) 41.8mm (16to6), d) 37.5mm (12to4) and e) 41.8mm (12to2).....	107
Figure 8-10- Model-predicted effect of casting speed on the roll separating force for different set-back distances.....	109
Figure 8-11- Model-predicted effective strain at the center-line (upper graph) in conjunction with the liquid-solid profile (lower graph) for $SB=32.5\text{mm}$ and $v=1.0\text{m/min}$ .....	111

Figure 8-12- Model-predicted effect of casting speed on the effective strain at the center-line for set-back distance of a) 32.5mm (12to6), b) 37.5mm (14to6), c) 41.8mm (16to6), d) 37.5mm (12to4) and e) 41.8mm (12to2).....	112
Figure 8-13- Effect of set-back distance on the effective strain development at the center-line for $v=2.0\text{m/min}$ . .....	113
Figure 8-14- Effect of casting speed and roll diameter on the model-predicted temperature at the center-line, the symbols show the modeling results and the lines show the linear correlation.....	116
Figure 8-15- Contour map showing the effect of casting speed and roll diameter during TRC on strip center-line exit temperature. ....	117
Figure 8-16- Model-predicted effect of casting speed and roll diameter on the mushy zone thickness at the center-line.....	118
Figure 8-17- Model-predicted effect of roll diameter on the average solidification cooling rate.....	119
Figure 8-18- Model-predicted effect of roll diameter on the surface normal stress at $v=2.0\text{m/min}$ . ....	120
Figure 8-19- Model-predicted amount of solidified material in the roll bite for a roll diameter of a) 355mm, b) 600mm and c) 1150mm at $v=2.0\text{m/min}$ . ....	121
Figure 8-20- Model-predicted effect of roll diameter on the effective strain at the center-line for $v=2.0\text{m/min}$ . ....	122
Figure 8-21- Model-predicted roll separating force per unit width of the strip for different casting speeds and roll diameters.....	123
Figure 8-22- Model-predicted relationship between maximum effective strain at the center-line ( $\varepsilon_{eff - max}$ ) and roll separating force for different roll diameters. ....	125
Figure 8-23- Model-predicted solidification profile contour map for $SB=32.5\text{mm}$ and $v=3.0\text{m/min}$ . ....	126
Figure 8-24- Model-predicted solid fraction at the center-line for $SB=32.5\text{mm}$ . ....	128
Figure 8-25- Model-predicted solute distribution at the center-line for $SB=32.5\text{mm}$ . ....	129

Figure 8-26- Model-predicted mushy zone thickness for different set-back distances and casting speeds.....	131
Figure 8-27- Model-predicted effect of scaling up on the mushy zone thickness.....	131
Figure 8-28- Model-predicted effect of casting speed on the a) solidified shell profile and b) corresponding shell thickness for $SB=32.5\text{mm}$ .....	133
Figure 8-29- Model-predicted yy-stress (compressive stress) development at the center-line (lower graph) in conjunction with the corresponding solidification contour map (upper graph) for $SB=32.5\text{mm}$ and $v=1.0\text{m/min}$ .....	136
Figure 8-30- Model-predicted effect of casting speed on the yy-peak stress in the mushy zone for $SB=32.5\text{mm}$ .....	137
Figure 8-31- Model-predicted propensity of cast strip to inverse segregation affected by casting speed for $SB=32.5\text{mm}$ . .....	137
Figure 8-32- Model-predicted effect of set-back distance on the inverse segregation propensity for $v=2.5\text{m/min}$ . .....	138
Figure 8-33- Model-predicted effect of caster scale up on the inverse segregation propensity. ....	139
Figure 8-34- Defect map for AA3105 aluminum alloy TRC (B: inverse segregation, Seg: center-line segregation, DF: defect free) [33].....	140
Figure 8-35- Propensity of modeled data points in the current study to defect formation for an entry height=12mm (IS: inverse segregation, CS: center-line segregation, DF: defect free). ....	141
Figure 8-36- Model-predicted contour map of strip final thickness-specific load- a) casting speed and b) <i>Stress/Thickness</i> for an entry height=12mm.....	143
Figure A-1- Typical enthalpy-temperature relationship of an alloy. ....	163
Figure A-2- Equivalent specific heat of AZ31 magnesium alloy includes the effect of latent heat of fusion.....	167

## List of Tables

Table 1-1- Some examples of automotive components production by magnesium [9] .....	5
Table 1-2- Examples of the use of magnesium in the automotive industry [4, 5, 9, 13].....	6
Table 1-3-Cost comparison (in USD/kg) to produce both DC cast and sheet products (from DC cast ingots) for both aluminum and magnesium alloys (2005-2008 data) [14, 15].....	7
Table 2-1 <sup>*</sup> -Cost comparison (in USD/kg) for AZ31 sheet production by conventional and TRC processes [15].....	8
Table 2-2 <sup>*</sup> - Typical thermo-physical properties of aluminum alloys and magnesium alloys [14, 44, 77].....	18
Table 4-1- Casting conditions for each trial .....	41
Table 5-1- Thermo-physical properties of AZ31 magnesium alloy .....	59
Table 5-2- AZ31 magnesium alloy Young's modulus [124] .....	59
Table 5-3- Parameters represented in Equation (5-18) for AZ31 magnesium alloy [121]....	59
Table 6-1- The chemical composition analysis corresponding to Figure 6-7.....	71
Table 6-2- The chemical composition analysis corresponding to Figure 6-10.....	73
Table 7-1- Casting conditions employed in the current study for the thermal-fluid model ...	77
Table 8-1- Casting conditions employed for thermal-fluid-stress model .....	97
Table 8-2- The relation between casting speed ( $v$ ) and exit temperature at the CL ( $TCL$ ) ....	99
Table 8-3- Separating force ( $SF$ )-casting speed ( $v$ ) relationship .....	110
Table 8-4- The % reduction experienced by the solidified material for each set-up at $v=2.0\text{m/min}$ .....	114
Table 8-5- Casting conditions used for effect of roll diameter study .....	115
Table 8-6- Exit temperature at the CL ( $TCL$ )-casting speed ( $v$ ) relationship .....	117
Table 8-7- Separating force ( $SF$ ) per unit width of the strip -casting speed ( $v$ ) relationship	123
Table 8-8- Maximum effective strain at the CL ( $\varepsilon_{eff - max}$ ) - separating force ( $SF$ ) relationship.....	124

# **Chapter 1**

## **Introduction**

### **1.1 Need for Lightweight Materials in the Transportation Sector**

Currently twenty-five percent of greenhouse gas (GHG) emissions in Canada is attributed to the release of carbon dioxide into the atmosphere which is created via the transportation sector by both light-duty and heavy-duty vehicles [1]. The long term goal for the Canadian government is to reduce total GHG emissions 45-65 percent by 2050 [2]. To achieve this goal, one alternative in the transportation sector is to use lightweight materials to produce cars. In particular, the North American automotive industry has set a target of substituting heavier parts fabricated by steel and/or aluminum alloys with lighter ones. There is a direct correlation between vehicle fuel consumption and hence GHG emissions and vehicle weight as shown in Figure 1-1. Also, the Corporate Average Fuel Economy (CAFÉ) standards have been aggressively set over the near term (reaching 56MPG by 2025) to force auto makes to improve fuel efficiency [3]. In order to meet the CAFÉ standards the automotive industry will have to use new lightweight materials as part of the solution.

One material which is attractive to light weight cars is magnesium with a much lower density than steel ( $\sim 1.7\text{g/cm}^3$  versus  $\sim 7.8\text{g/cm}^3$ ) or aluminum ( $\sim 1.7\text{g/cm}^3$  versus  $\sim 2.7\text{g/cm}^3$ ). Other attractive features for the use of magnesium in automotive applications includes: its high specific strength ( $\sigma/\rho$ ) and stiffness ( $E/\rho$ ), absorption of vibration and good weldability and machinability [4, 5]. One target of the North American automotive industry is to reduce weight by increasing the current 5kg magnesium used in each automobile to 160kg per vehicle by 2020 [2].

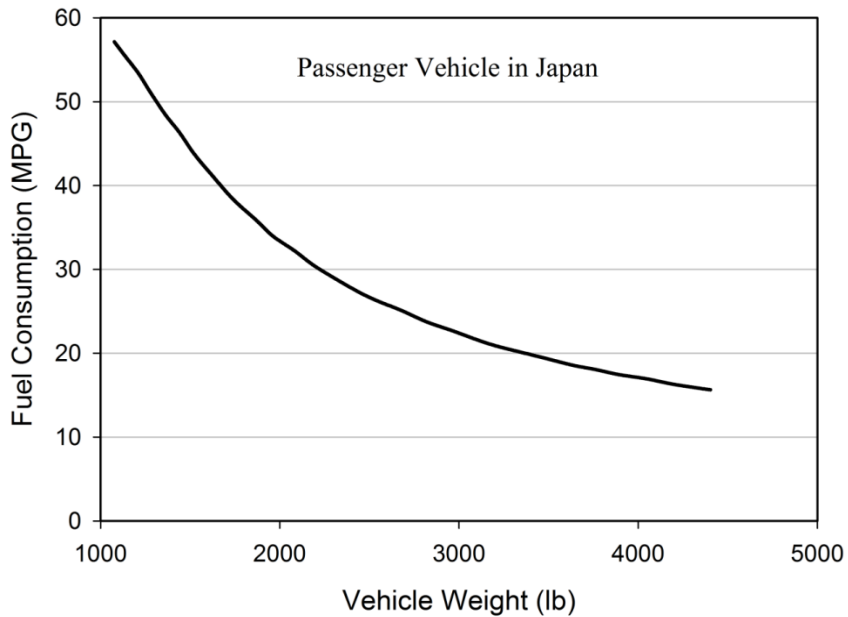


Figure 1-1- Fuel consumption affected by vehicle weight [6].

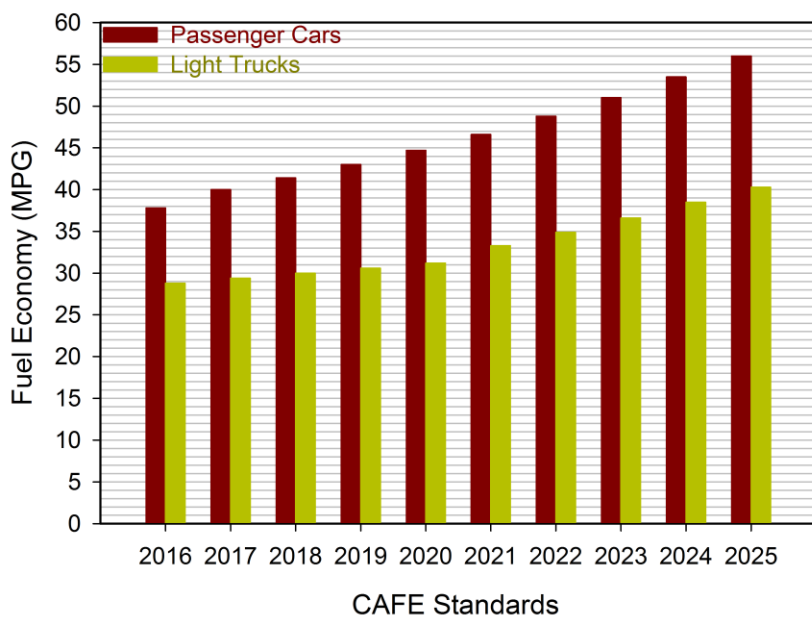


Figure 1-2- Estimated average required fleet-wide fuel economy under proposed CAFE Standards [3].

Figure 1-3 shows the rapid rise in the production of primary magnesium over the past 80 years, as interest and knowledge in this material has grown. The jump of magnesium production from ~400ktonnes in 2000 to ~800ktonnes in 2010 shows the importance of magnesium in the 21<sup>st</sup> century. Figure 1-4 shows magnesium consumption by sector in 1997 and then again in 2009 [7, 8]. Reduction of the magnesium application in aluminum alloying from 44.4% in 1997 to 27.8% in 2009 and increase of the magnesium consumption in die casting from 27.6% in 1997 to 40.8% in 2009 shows that interest in the direct application of magnesium in the industry has grown significantly. This promising trend in magnesium production and consumption by application draws a bright perspective for magnesium usage in car industry. Figure 1-5 illustrates the magnesium alloys usage by commercial sector in 2005. As shown, 72% of the magnesium produced was used for the automotive industry. Table 1-1 shows the impact of magnesium usage on the vehicle weight reduction for a typical car [9] and in Table 1-2 examples of current magnesium alloys applications in the automotive industry are shown.

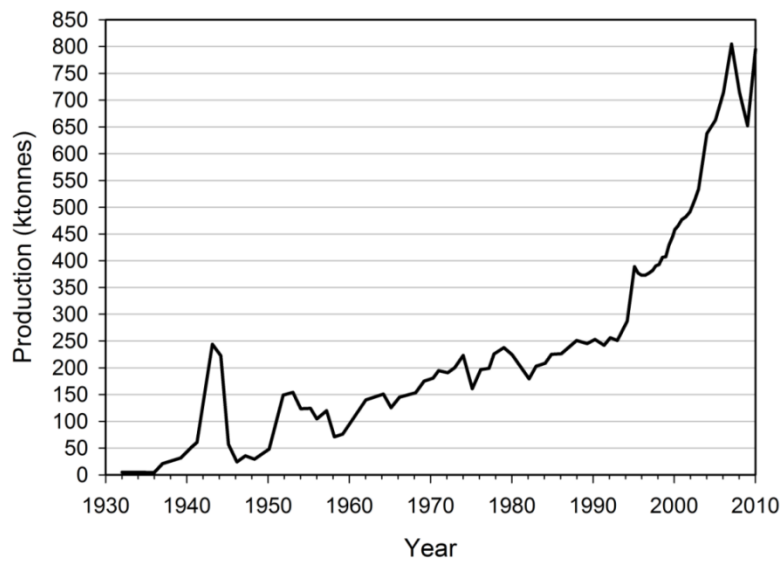


Figure 1-3- The world production of primary magnesium metal, data reproduced from [10, 11].

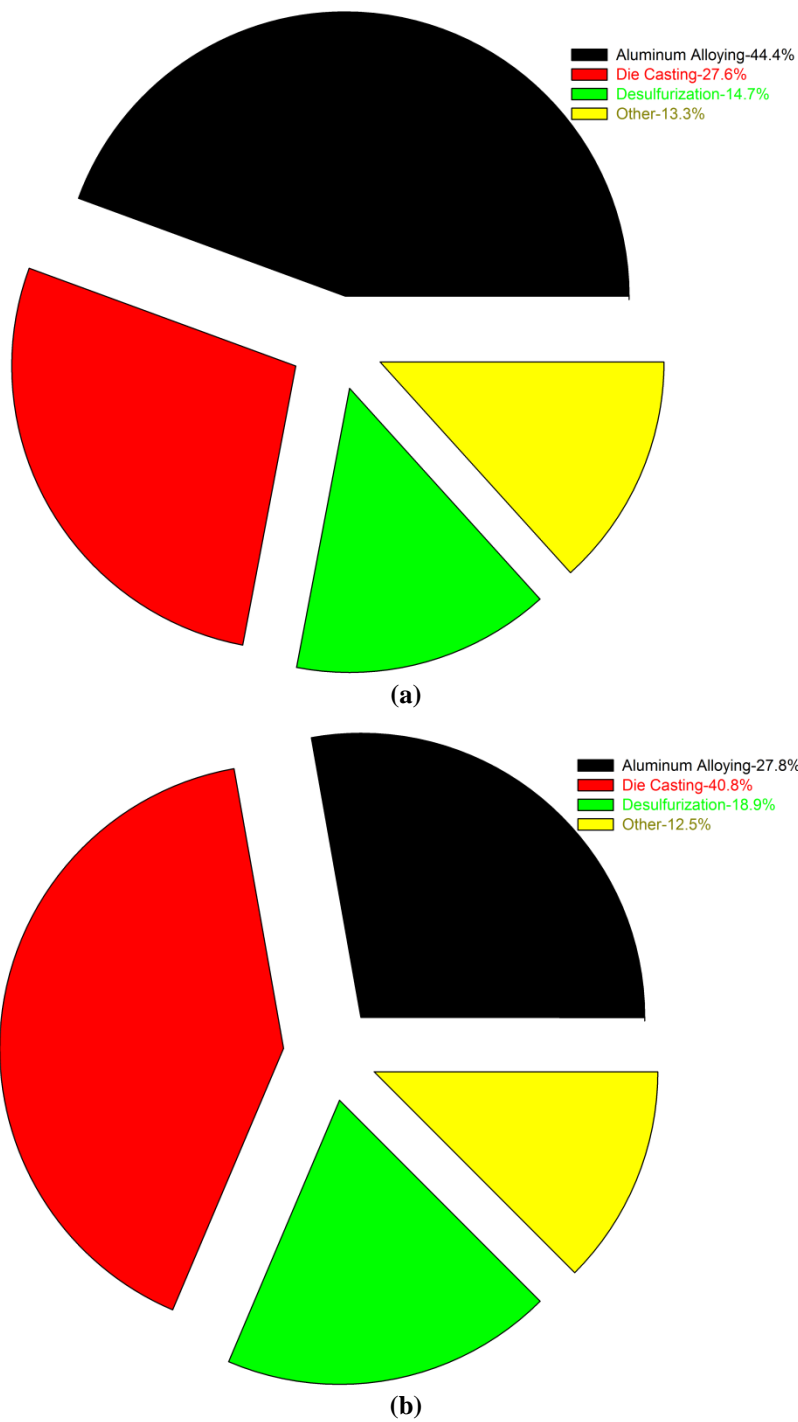


Figure 1-4- Magnesium consumption by application for: a) 1997 and b) 2009 [7, 8].

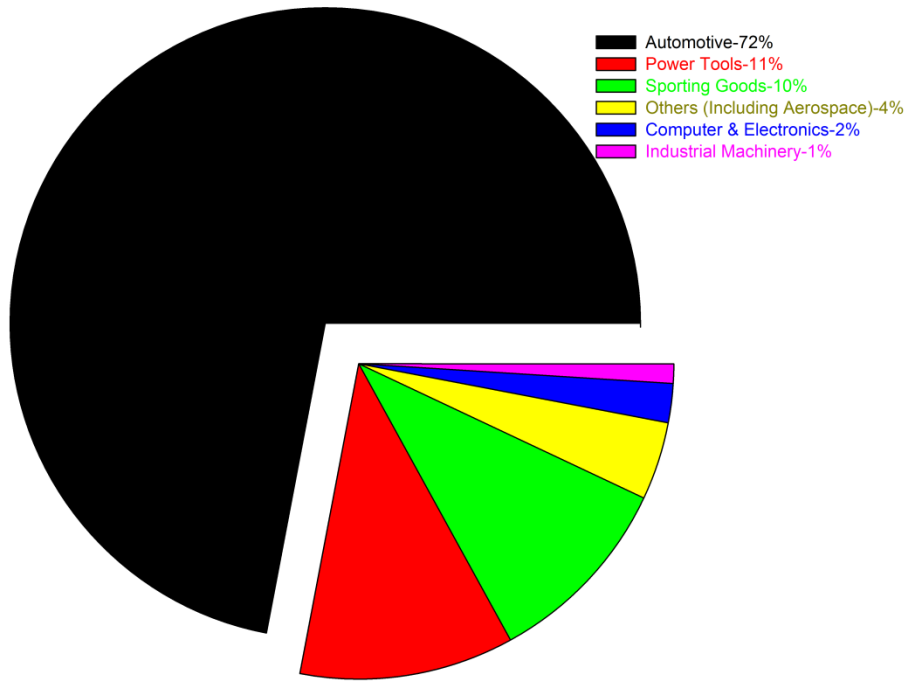


Figure 1-5- Magnesium alloys usage breakdown by sector in 2005 [12].

Table 1-1- Some examples of automotive components production by magnesium [9]

Component	Current Material	Current Weight (kg)	Weight in case of magnesium usage (kg)	Weight Reduction (%)
Engine	Steel/Aluminum	60/22	15	22 to 70
Transfer Case	Steel	15.6	11.4	28
Door Inner	Aluminum	8.2	5.4	33
Steering Wheel Core	Steel	1.4	0.9	33
Steering Column	Steel	2.3	1.4	40
Car Seat Frame	Steel	5	1.8	64
Instrument Panel	Steel	5	1.8	64

Table 1-2- Examples of the use of magnesium in the automotive industry [4, 5, 9, 13]

Company	Part	Model
Ford	Clutch housing, steering column	Ranger
GM	Valve cover, air cleaner, clutch housing	Corvette
Porsche	Miscellaneous components (45kg)	911
Mercedes-Benz	Fuel tank cover	SLK
Volkswagen	Gearbox housing	VW Passat
Toyota	Steering wheels	Lexus, Celica, Carina, Corolla
Opel	Roof	G90
BMW	Engine block, air intake system	3 Series

From a strategic perspective, Canada is interested in developing a stronger knowledge base about magnesium alloys. Hence in 2007, an NSERC strategic network was established across Canada entitled: “Development of Wrought Magnesium Materials for the Transportation Sector - MagNET” [2].

## 1.2 Challenges in Producing Magnesium Sheet

There is great potential for magnesium application in the automotive industry in the form of sheet components; almost 26% of a car weight is distributed on the body as shown in Figure 1-6. On the other hand, a limiting factor in terms of manufacturing wrought or sheet magnesium is its Hexagonal Close Packed (HCP) crystal structure which limits its formability and ability to undergo large levels of deformation. Hence, conventional processing to produce sheet/strip is much more costly for magnesium alloys as the deformation steps must be done in small increments with annealing stages in between. Table 1-3 shows a cost comparison between the raw material versus the production of sheet for both magnesium and aluminum. A large barrier to the widespread use of magnesium in automotive applications is the cost of the magnesium sheet relative to aluminum and steel. In order to reduce the cost of producing magnesium sheet, an alternative more cost effective process is required to produce magnesium sheet. One such process is Twin Roll Casting (TRC) which incorporates both casting and some hot deformation stages in one step.

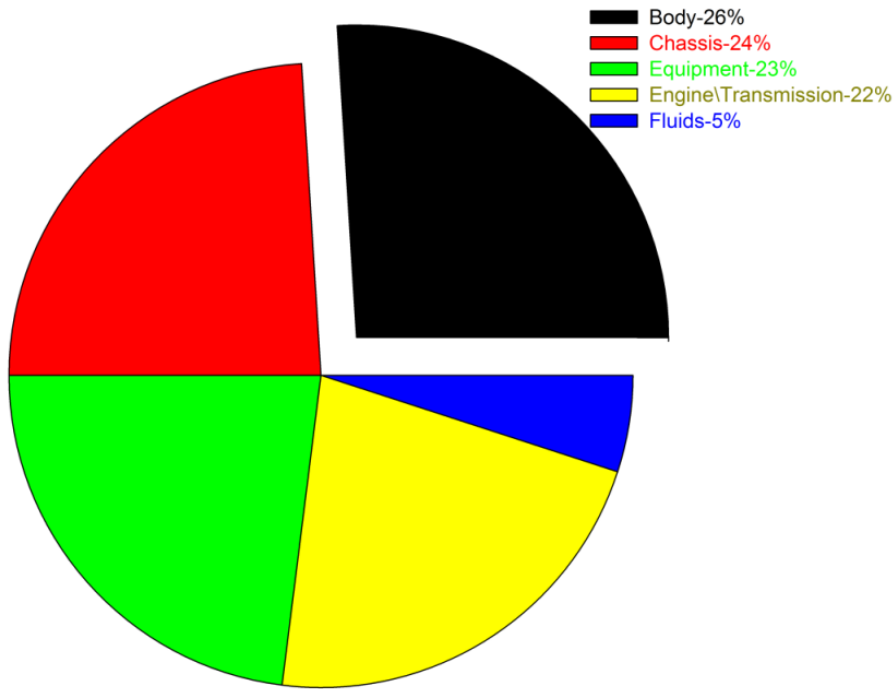


Figure 1-6- Car weight distribution [4].

Table 1-3-Cost comparison (in USD/kg) to produce both DC cast and sheet products (from DC cast ingots) for both aluminum and magnesium alloys (2005-2008 data) [14, 15]

Product	Al	Mg
<b>DC Cast Ingot</b>	2.2-2.8	~3
<b>Sheet</b>	4-5	~10

## Chapter 2

### Twin Roll Casting (TRC) of Magnesium Alloys

#### **2.1 Magnesium Alloy Sheet Production**

Conventionally, magnesium sheet alloys are fabricated via the Direct Chill (DC) casting process followed by homogenization, hot and cold rolling and final heat treatment. DC cast magnesium slabs are typically 0.3m×1m (in cross section) ×2m (in length). The final magnesium sheet thickness after hot rolling is typically 5-6mm and after cold rolling 1-3mm. A disadvantage to this route is the need to perform many annealing heat treatments between deformation passes (at ~340°C) and to limit deformation reduction to a maximum of 5-20% [16].

An alternative process to fabricate magnesium alloys sheets, which can considerably reduce the costs by eliminating intermediate steps (i.e. homogenization, hot rolling and most of the finishing stages) and decrease energy consumption, is the near-net-shape manufacturing process; Twin Roll Casting (TRC) [17]. Relative to the conventional sheet production process, the cost to produce TRC sheet is significantly lower (\$4.34/kg versus \$9.92/kg, as shown in Table 2-1). The final as-cast thickness is much lower (2-12 mm) [18] versus conventional DC cast material with a starting thickness of 300mm. Figure 2-1 shows a schematic comparison between DC casting and TRC process used for sheet fabrication.

Table 2-1\*-Cost comparison (in USD/kg) for AZ31 sheet production by conventional and TRC processes [15]

Manufacturing Process	Costs
Conventional	9.92
Twin Roll Casting	4.34

\* 10,000 tpy of 1.5mm thick×1m wide AZ31 sheet

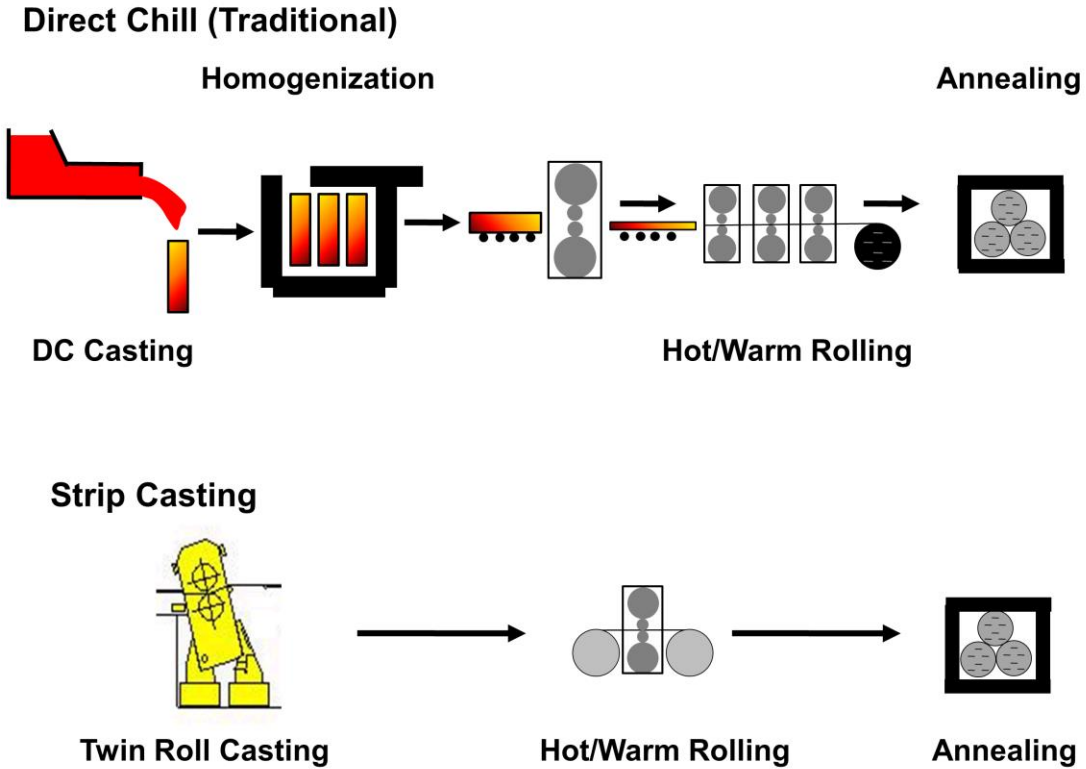


Figure 2-1- DC casting vs. TRC for sheet production [19].

## 2.2 Twin Roll Casting Process

The first concepts of the Twin Roll Casting process were introduced by Sir Henry Bessemer in the mid-19<sup>th</sup> century [20]. The set-up introduced by him was a vertical caster. Figure 2-2 shows a simple schematic of the process in the horizontal orientation; the facility consist two counter-rotating rolls (similar to cold or hot rolling process) and a feeding system known as nozzle or tip. The nozzle is connected to a head box which contains molten metal with a level of height above the nozzle entry level. This height difference acts as driving force to feed the molten metal into the roll bite region. The molten metal is provided from the furnace by a pumping system and transfer tube. For active metal casting such as magnesium, a cover gas

(shielding gas) is used to protect the molten metal from oxidation ( $\text{SF}_6$  or  $\text{SF}_6$  and  $\text{CO}_2$  mixture [21- 23]). Once the melt is fed into the space between two rolls, the roll surfaces act as a mold for the molten metal to transfer the heat and the solidification starts at the very beginning of the contact region between the melt-roll surfaces. Continuing the process, more heat is extracted from the material and solidification continues to reach the solidus temperature and then lower values. The cooling rates achieved during this process are in the range of  $100\text{-}1000^\circ\text{C/s}$  [18]. Following by the solidification process, the fully solid material is exposed to the hot rolling while the material is pulled inside the roll bite region by the rotating rolls. Hence, the TRC process incorporates casting and hot rolling in one process.

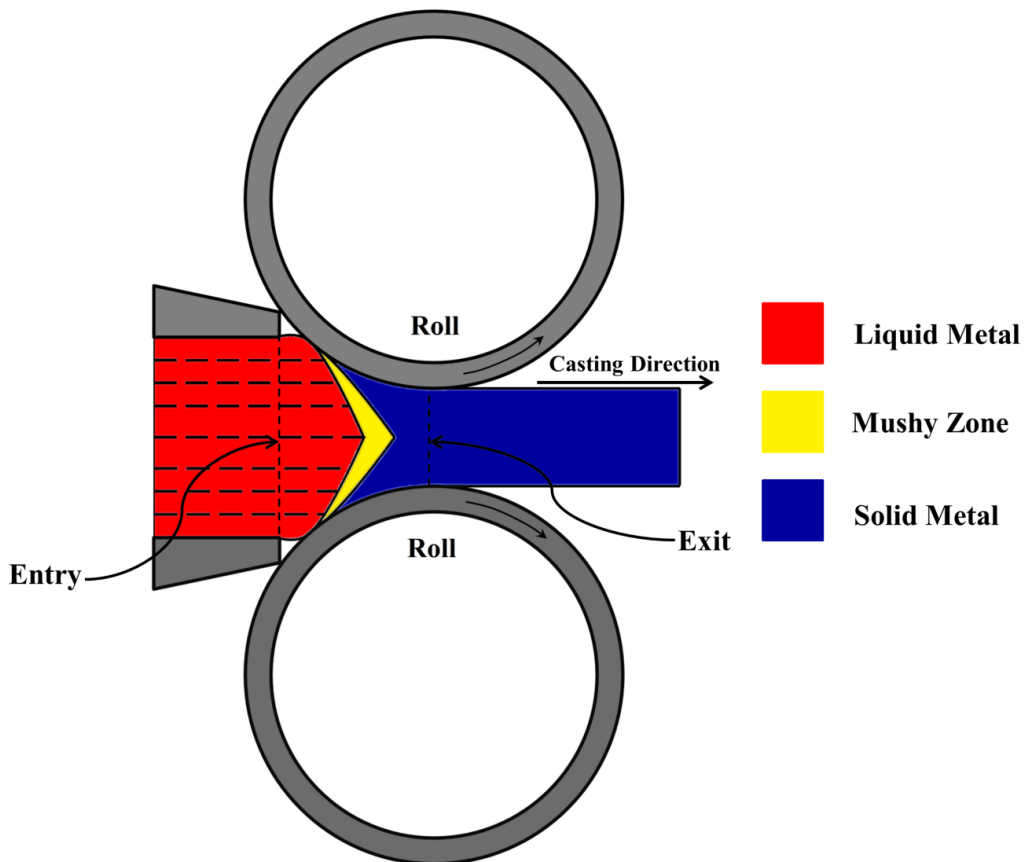


Figure 2-2-Simple schematic of twin roll casting process (horizontal position).

The rolls are water cooled from the inside to improve the heat transfer during the process and the speed they rotate at determines the process speed (casting speed). The roll material used can vary and historically both copper and steel rolls have been successfully used for TRC. The roll material can have a significant effect on the heat flux experienced by the solidifying strip with typically copper rolls able to extract more heat than steel rolls due to its higher thermal conductivity. In some cases a lubricant is sprayed on the surface of the rolls to prevent sticking of the strip to the roll [24]. The lubricant also acts as a thermal barrier and hence lowers the heat transfer coefficient and solidification rate [25]. Both the roll material and the existence of the lubricant affect the process speed, as illustrated in Figure 2-3 for AA5182 aluminum alloy. The roll diameter used in the earliest TRC machines was about 600 mm [26]; today roll diameters of 1200mm are more common. The TRC process can be classified into Vertical TRC (VTRC) and Horizontal TRC (HTRC) with respect to the orientation of the strip as it is being cast and rolled.

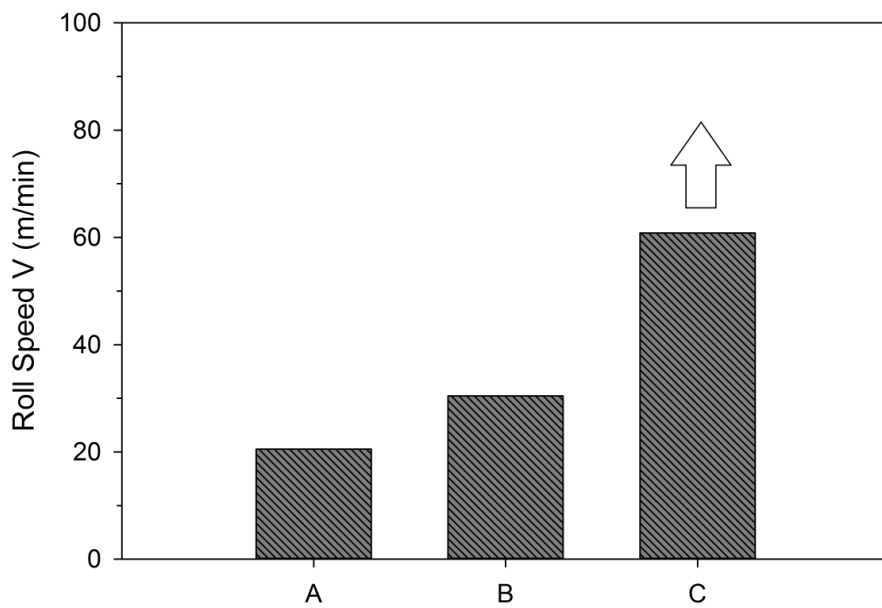


Figure 2-3- Relationship between roll material, use of lubricant and maximum roll speed at which AA5182 aluminum alloy strip can be cast; (A) steel roll coated with lubricant (B) steel roll (C) copper roll, graph reproduced from [27].

## **2.3 Use of TRC for Aluminum Alloys and Steel**

The TRC process has been used in the aluminum industry for almost 60 years [28] in both vertical and horizontal positions. Early casters were able to produce 5-7mm thickness strips with less than 1m/min casting speed. Process speeds were increased by varying roll material and size and today TRC machines can reach speeds up to 60m/min to fabricate a wide range of aluminum alloys [24, 25, 27-40]. In addition to aluminum, the TRC process is also used to produce both carbon and stainless steels with speeds up to 150m/min [20, 41, 42]. In comparison, TRC of magnesium alloys is in its infancy and there is still much work and knowledge needed to be able to effectively twin roll cast magnesium alloys.

## **2.4 Magnesium Twin Roll Casting**

Serious consideration in using the TRC process to produce magnesium strips was initiated around 2000 [16]; however, the very first efforts in this field were made in the early 1980s which were postponed for a while due to economic reasons [43]. The development focused on modifying the TRC process used in the aluminum industry for magnesium.

The research group working under supervision of Professor Toshio Haga in the “*Osaka Institute of Technology*” (Japan) and Professor Hisaki Watari in the “*Gunma University*” (Japan) in various works [44-53] assessed the feasibility of the TRC process for magnesium alloys and studied the effect of casting parameters on the strip properties. In their studies they employed casters with rolls fabricated from pure copper and copper alloys with diameters of 300mm and widths of 150mm. AZ31, AZ61, AZ91, AM60 and also high aluminum content AZ111 and AZ112 magnesium alloys were cast successfully using this technology. Casting speeds ranged up to 180m/min to produce strips with thicknesses varying between 2-5mm. Based on the observations achieved in this research work, process maps for TRC of magnesium alloys were initiated; an example is shown in Figure 2-4. During the past decade, more research by other research groups on the TRC process has been

done for the magnesium alloys such as AZ31 [18, 21-23, 54-60], AZ21 [61], AZ41 [62, 63], AZ91 [64, 65] and AM31 [66].

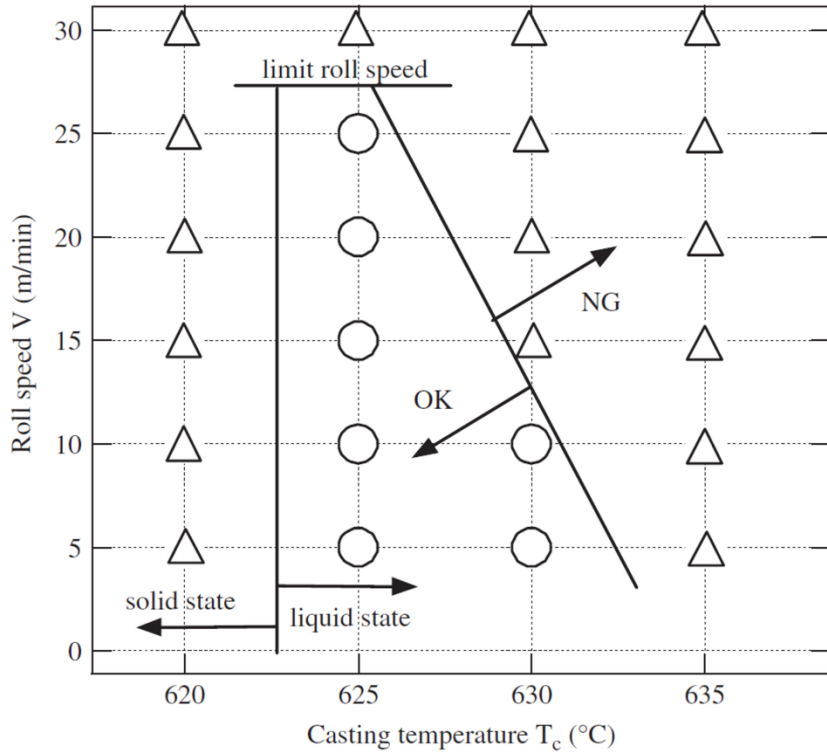


Figure 2-4-Successful manufacturing condition for AZ31B (O: successful conditions, Δ: unsuccessful conditions) [45].

#### 2.4.1 Microstructure of Twin Roll Cast Magnesium Strips

The typical microstructure of a twin roll cast magnesium alloy consists of different regions through the thickness since the cooling rate varies from the strip surface toward the centerline, as shown in Figure 2-5. At the strip surface, where direct contact between the molten material and roll surface occurs, the cast material experiences the highest cooling rate during the process. Initially, a thin layer of a rapid cooled microstructure is formed on the surface of the strip which is known as the chill zone. Following the chill zone, a columnar dendritic

zone develops in the direction of heat removal. Due to the rotation of the rolls these columnar grains incline from the surface to the center of the strip. By growing the columnar zone toward the center of the strip, the solute is rejected to the remaining liquid metal and also the impurities move to the central zone. Due to different cooling conditions and the presence of the solute rich liquid material and impurities an equiaxed zone is formed at the strip center [64, 67].

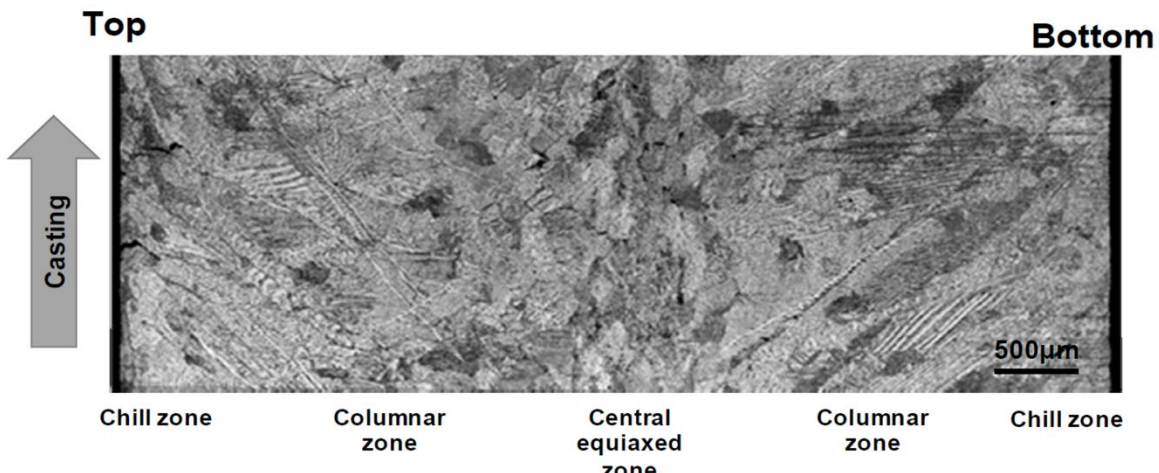


Figure 2-5- Typical microstructure of a twin roll cast AZ31 magnesium strip through thickness [67].

Since the solidification cooling rates during TRC are orders of magnitude higher than DC casting (100-1000°C/s for the former and 1-50°C/s for the latter), the as-cast microstructure obtained in TRC is much finer. Studies on magnesium alloy AZ31 show that a finer grain size and better morphology and distribution of the  $\gamma$ -phase ( $Mg_{17}Al_{12}$ ) is achieved when the casting process changes from DC casting to TRC [18, 54-56]. The same behavior for secondary dendrite arm spacing has been observed, where 5-6.5 $\mu m$  Secondary Dendrite Arm Spacing (SDAS) are achieved after TRC, compared to 34 $\mu m$  SDAS after DC casting [23, 58]. The improvement of microstructure leads to better mechanical properties of twin roll cast magnesium alloys.

## 2.4.2 Microstructural Defects in Twin Roll Cast Magnesium Sheets

Although the TRC process has shown the potential of producing strips with finer microstructure and more even distribution of second phase, the unique conditions of the process can sometimes lead to the formation of defects in the cast strip. The defects are generally categorized into micro and macro-defects [68]. Two micro-defects that are very common for magnesium twin roll cast strips include center-line segregation and inverse (surface) segregation [14, 64, 69] as shown in Figure 2-6.

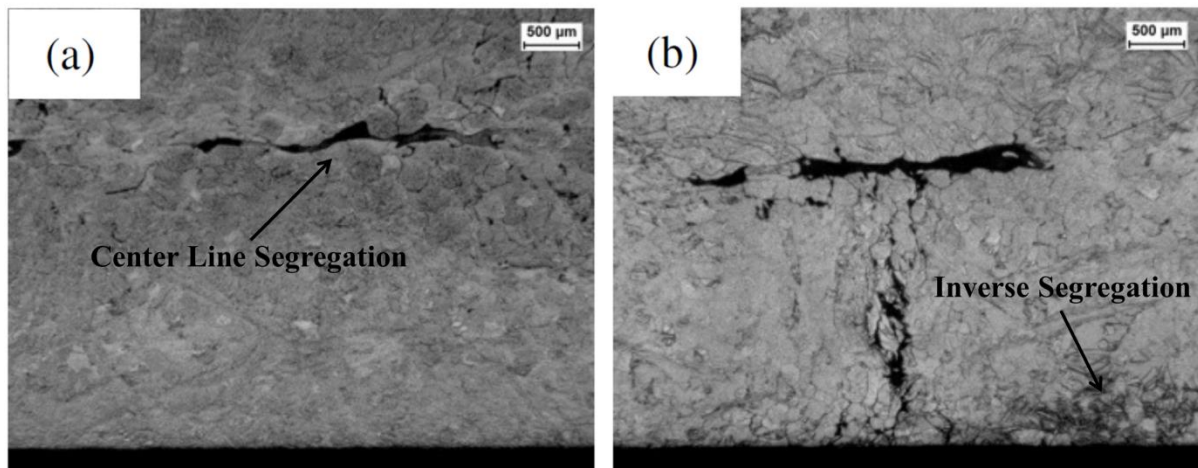


Figure 2-6- Optical images of a) center-line segregation and b) inverse segregation observed for AZ31 magnesium alloy [69].

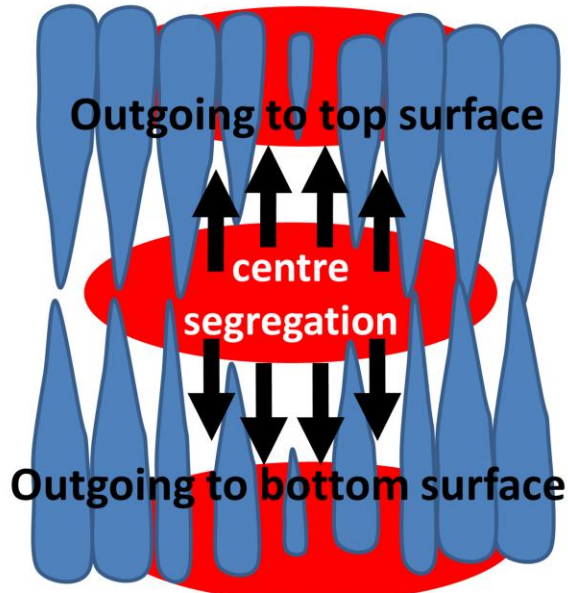
To date two major research groups have conducted studies on center-line and inverse segregations formation for aluminum alloys TRC; the research group working under supervision of Professor John D. Hunt at the “*Oxford University*” (UK) [28, 33, 68, 70-75] and the research group working in Norway at “*SINTEF*” and “*Hydro Aluminium*” [76].

The studies done by Prof. Hunt Group on the aluminum TRC shows that center-line segregates contain low melting point materials which generally have an equiaxed microstructure [33]. These segregates are elongated in the casting direction and form at the

central region of the cast strip. The reason center-line segregation occurs is because as solidification proceeds from the surface, solute from the solidification front is rejected into neighboring liquid and eventually freezes last at the center-line creating a variation in composition through the thickness of the solidified strip. Casting parameters which increase the sump depth along the centerline reduce the time available for uniform diffusion of the solute and a large amount of solute-rich liquid remains in the liquid sump.

Another common defect during TRC of both magnesium and aluminum is “inverse segregation” or “Surface Bleeding” [33, 72]. In the solidified strip, inverse segregation manifests itself as pockets of isolated solute rich regions at the surface of the strip. This can lead to discoloration and a variation in strip surface properties. In some cases the inverse segregates at the surface are connected to the center-line segregates. This type of morphology has been observed for AA5052 aluminum alloy by Norwegian research group [76] and AZ31 magnesium alloy by Kim *et al.* [69]. All of the studies show that once the casting speed exceeds a critical value, inverse segregation can occur in the cast strip. One theory to explain inverse segregation during TRC relates squeezing of the solute rich liquid at the center of the strip up through the inter-dendritic region towards the surface of the strip, as shown schematically in Figure 2-7. Hence this defect relates both the solidification process as well as stress the material experiences close to the center during solidification.

## Inverse segregation on top surface



## Inverse segregation on bottom surface

Figure 2-7- Schematic representation of squeezing path for the solute-rich liquid toward the strip surface to from the inverse segregation.

The Norwegian Group believes that inverse segregation is caused by a low pressure zone (in terms of hydrostatic stress) occurs on the strip surface during TRC process. This phenomenon is the driving force for solute rich liquid flow from the center-line toward the strip surface.

Another proposed mechanism for inverse segregation by Professor Hunt's group [28, 33, 68, 70-74] involves the formation of a “buckle” on the strip surface due to the relevant motion between the roll and strip surface. Based on this mechanism, during plastic deformation of the solidified shell on the roll surface, the deformed material moves back to the roll entry and to compensate for this backward slip (since the material is moving toward the exit region) a buckle appeared occurs on the surface.

Despite being able to manufacture magnesium alloy sheets by the TRC process on a laboratory scale, some of the material properties inherent to the magnesium alloys, as shown in Table 2-2 in comparison with aluminum, make it challenging. The specific heat capacity and latent heat of fusion of Mg are lower than steels and aluminum (i.e. Mg heat capacity: 1.4 kJ/kg°C at T<sub>m</sub> / Al heat capacity: ~2 kJ/kg°C at T<sub>m</sub>, Mg latent heat of fusion: 340 kJ/kg, Al latent heat of fusion: 390 kJ/kg), which can result in solidification during melt delivery and blocking of the nozzle tip [14]. Magnesium alloys also typically have a larger solidification range than Al alloys (50-130°C for Mg alloys, 10-20°C for Al alloys). This large solidification range creates difficulties in producing defect-free sheets [16, 44]. In fact, the short contact time between the molten pool and the cooling rolls in conjunction with the large solidification range can sometimes lead to incomplete alloy solidification before it exits the roll bite. Moreover, magnesium alloys are very active with oxygen in the molten state and tend to burn in the air; hence, special requirements in dealing with the molten metal are necessary to achieve a high quality product.

Table 2-2<sup>\*</sup> - Typical thermo-physical properties of aluminum alloys and magnesium alloys [14, 44, 77]

Material	Specific Heat Capacity (kJ/kg°C)	Latent Heat of Fusion (kJ/kg)	Solidification Range (°C)	Thermal Conductivity (W/m°C)	Density (kg/m <sup>3</sup> )	Thermal Diffusivity (m <sup>2</sup> /s)
Aluminum Alloys	~2	390	10-20	222	2700	4.11×10 <sup>-5</sup>
Magnesium Alloys	1.4	340	50-130	120	1780	4.81×10 <sup>-5</sup>

\* Except solidification range, other properties are attributed to AA1100 aluminum alloy and AZ31 magnesium alloy.

Producing magnesium strips with a controlled microstructure and free of both macro and micro-defects is challenging during magnesium TRC. Formation of various defects in the cast strips besides the non-uniform microstructure is a common issue in the TRC of magnesium. The close interaction between the TRC process parameters and the conditions that promote defect formation and microstructure evolution is complex and there is a need to understand the TRC process comprehensively and quantitatively.

## **2.5 Mathematical Modeling of the Twin Roll Casting Process**

The need for a quantitative understanding of the process and conditions that lead to high quality sheet production means that it is imperative to develop a knowledge-based process model of the TRC process for magnesium alloys. During the past few years, various models of the TRC process have been developed by considering transport phenomena coupled with solidification effects. In very limited cases, mechanical deformation was also taken into account in the model (for aluminum and steel TRC). A critical aspect of the model is the correct determination of the boundary conditions. The governing equations and boundary conditions once selected are solved using various numerical solution methods. To date, very few attempts have been made to model the TRC process for magnesium alloys however there has been other work done for other alloy systems.

Models developed for the TRC process can be categorized into three main categories:

- 1- Models which include just fluid flow (fluid models),
- 2- Models which include fluid flow and heat transfer (thermal-fluid models), and
- 3- Models which include fluid flow, heat transfer and plastic deformation (thermal-fluid-stress models).

### **2.5.1 Fluid Models**

In 1992, Lee [78] modeled only the flow field during steel TRC and ignored solidification and heat transfer. The aim of the investigation was to analyze the flow field and study the sensitivity of the process to inlet velocity and entry and exit thickness. Although, ignoring solidification prevents the prediction of the melt sump, mushy zone and solid region, the behavior of fluid flow could be still predicted and analyzed in the vicinity of the nozzle region. The author believed the presence of the solidified shell on the roll surface does not affect the flow field significantly which means ignoring solidification is a reasonable assumption; however neither the evidence of this assumption's reliability nor any verification

was presented. The results show that the inlet velocity has a significant effect on the flow field; however, ignoring heat transfer causes the lack of knowledge on the interactions between flow field and thermal history. This work is considered as a very simple modeling to study just flow field at the vicinity of the entry region. Nevertheless, the authors suggested an extension to their work as coupling a thermal model to get more accurate results.

### **2.5.2 Thermal-Fluid and Thermal-Fluid-Stress Models**

As one of the first attempts in 1989, Saitoh *et al.* [79] modeled the TRC process for Sn-15Pb alloy by considering fluid flow and heat transfer. Since the heat transfer coefficient (*HTC*) at the roll/strip interface was unknown, the researchers used a constant temperature (which is not provided in literature) on the roll surface. On the other hand, it is believed by the researcher that the solidified shell thickness is proportional to the second root of the contact time, which can then be correlated to the roll rotation speed. Hence the thickness of the solidified shell can be predicted by knowing the casting speed. Here two boundary conditions are defined; solidus temperature at solidification front (interface of the solidified shell and liquid region) and constant temperature on the roll surface. By these conditions, code predicts temperature distribution in solid and liquid regions with "known predefined shapes". Using this approach the interfacial heat transfer is applied indirectly. The model predictions were validated by running a series of experiments to measure the temperature in the roll bite. This was achieved by placing a thin plate equipped by thermocouples in the side dam position, as shown in Figure 2-8. The temperature data were then used to figure out solidus and liquidus profile and solidification front during casting and compared to model results. The process was assumed to be 2D (through the thickness and along the length at the mid-thickness and edge locations). Temperature (TC) data were used for both edge and mid-plane positions. Figure 2-9 shows the predicted and measured results. As shown in Figure 2-9, the presumed solidified shell (solidus temperature profile) is in good agreement with the measured (experimental) data, but there is a significant variant for the predicted and measured liquidus

temperature profiles. So, applying more accurate boundary condition at the strip/roll interface ( $HTC$ ) seems to be necessary to get more accurate results.

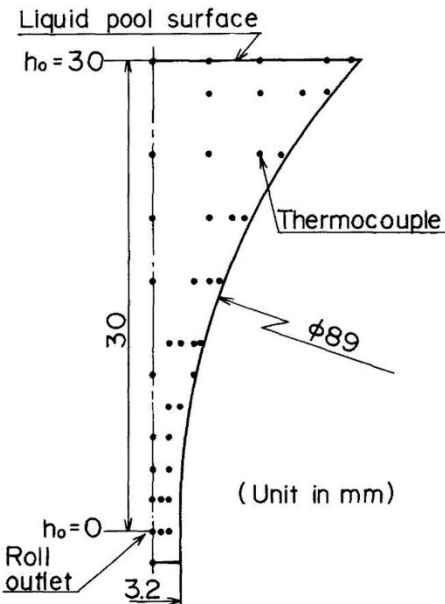


Figure 2-8- Side dam showing thermocouple positions (shown by •) to capture temperature during casting [79].

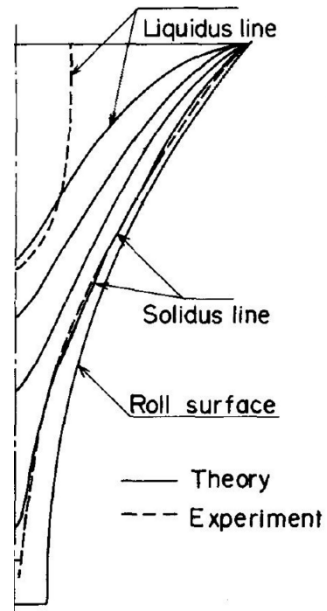


Figure 2-9- Solidified shell and predicted isotherms in the liquid region [79].

Building on the work done by Saitoh *et al.* [79], S. M. Hwang *et al.* [80] used the experimental data for a Sn-15Pb and found that a constant  $HTC=25\text{kW/m}^2\text{°C}$  in the roll bite provided a good match between the measurements and the predictions. Once the model was verified, it was then modified for TRC of stainless steel (with different geometry) and the  $HTC$  was varied between 15, 17.5 and  $20\text{kW/m}^2\text{°C}$  to study the effect of casting conditions and  $HTC$  boundary conditions on the results.

O'Malley *et al.* [81] employed a 2D coupled fluid flow and heat transfer model for a vertical caster used for aluminum TRC. This model was then coupled to a 1D deformation model. Two important unknown boundary conditions were studied in this work to determine the optimum values for both the  $HTC$  and friction coefficient ( $\mu$ ). A 3000 series alloy was cast using a pilot scale caster to measure some parameters and compare them to predictions to verify the model. Strip exit temperature, strip exit speed and roll torque were chosen as check points to determine the  $HTC$  and  $\mu$ . By employing different values of  $HTC$  and  $\mu$  and comparing the numerical and experimental results, best values were determined as  $73.6\text{kW/m}^2\text{°C}$  throughout the roll bite and 0.18 for  $HTC$  and  $\mu$ , respectively.

Bradbury *et al.* [70, 82] and Yun *et al.* [28] coupled fluid flow, heat transfer and plastic deformation for Al-4%Cu, Al-8%Cu, Al-16%Cu and Al-24%Cu TRC. Three methods were used to apply the  $HTC$  over the arc of contact in this research, as shown in Figure 2-10;

- I. Method I; Constant  $HTC=30\text{kW/m}^2\text{°C}$  (evaluated by comparing to the strip exit temperature through experiment).
- II. Method II; Step function: in this method, the  $HTC$  distribution was adopted as a step function in which the step position and shape was determined based on the solid fraction at the center-line. It seems the solid fraction had been predicted using the constant  $HTC$  (Method I). By comparing to the experimental results, low and high values of this step function were evaluated as 22.5 and  $60\text{kW/m}^2\text{°C}$ , respectively.

- III. Method III;  $HTC$  is a function of contact pressure: the pressure along the contact region was calculated (in Method I) and normalized to be between 0 and 1. Then,  $HTC$  was defined as Equations (2-1) to (2-3):

$$HTC = h_{min} + P_{nor}(h_{max} - h_{min}) \quad (2-1)$$

$$HTC = h_{max} \text{ if } HTC > h_{max} \quad (2-2)$$

$$HTC = h_{min} \text{ if } HTC < h_{min} \quad (2-3)$$

where  $P_{nor}$  is the normalized contact pressure.  $h_{min}$  and  $h_{max}$  were determined to be 22 and 60kW/m<sup>2</sup>°C, respectively through comparison the modeling and experimental results.

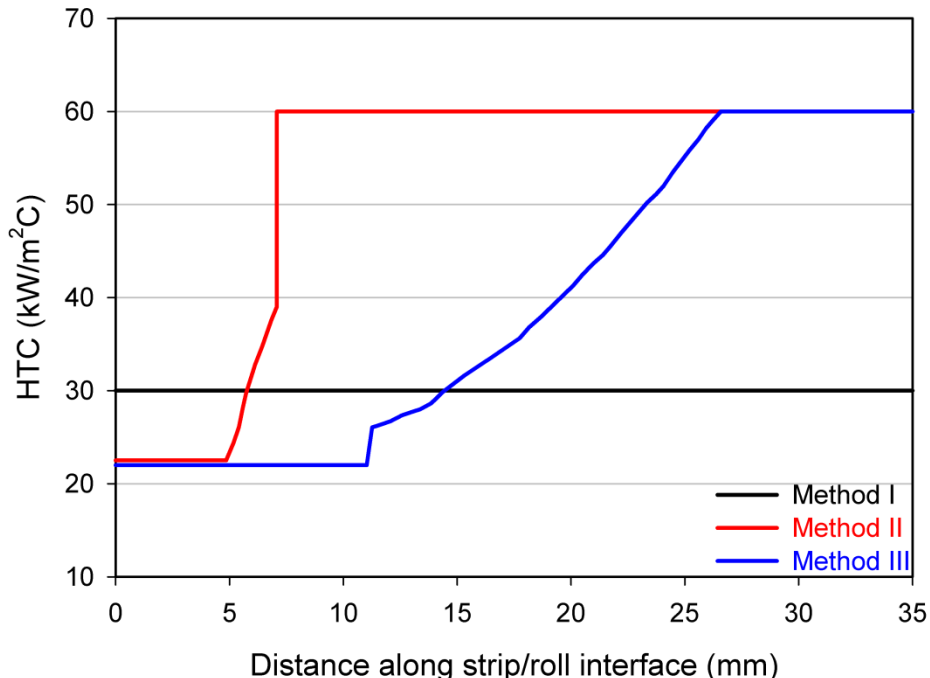


Figure 2-10- Three methods of  $HTC$  definition reproduced from Bradbury [82].

In addition to comparing to the experimental results (specifically exit strip temperature and roll surface temperature) to determine low and high values for the *HTC* using Methods II and III, it was presumed that the area under the heat flux curve along the arc of contact must remain constant for each method. All three conditions led to very good agreement between modeled and experimental results (errors of  $\pm 10\%$ ) and no significant advantage was observed in using one method over the other two; however, the authors eventually employed Method III in their work. This decision was made based on further comparison to experimental data gained through casting of thin strips, which showed better agreement. For the mechanical part of the simulation, the sticking condition at the strip/roll interface was assumed to model the friction. For validation, the modeled roll separating force was compared to the experimental results, as shown in Figure 2-11.

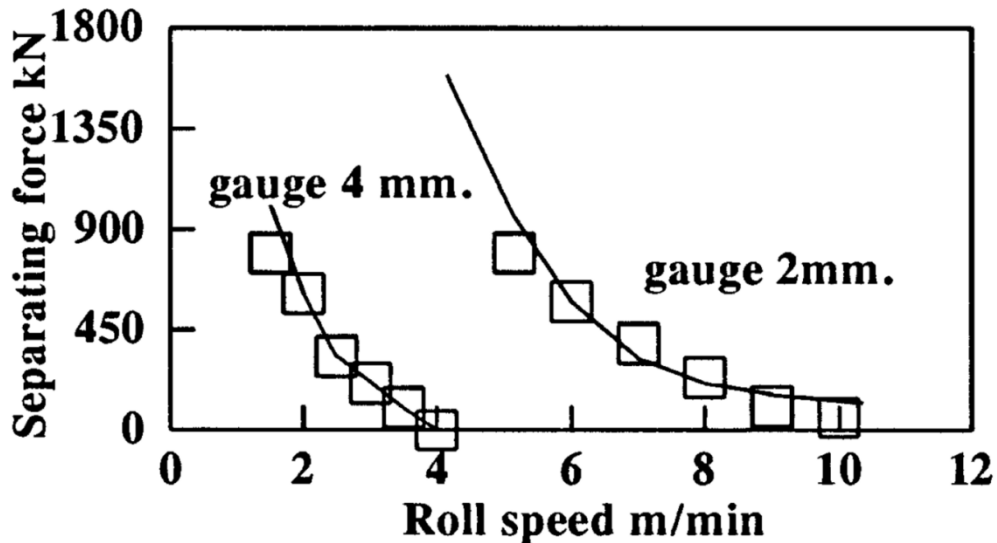


Figure 2-11- Experimental points versus modeled lines for separating force [28].

Chang *et al.* [83, 84] coupled heat transfer and fluid flow to model stainless steel TRC. First, they validated the formulation of fluid flow and heat transfer separately by modeling two simple fluid flow and heat transfer problems, respectively (validation was done

indirectly). Then the modeling was focused on TRC. The challenging problem introduced by the authors is the procedure of determining the interface position between solid and liquid region. For simplicity the solidification range was ignored by assuming a melting point, similar to pure metals. Using this assumption the effect of mushy zone on the fluid flow is neglected. Moreover, the heat transfer coefficient (*HTC*) between roll and strip was assumed to have a value between  $6.7\text{-}67\text{ kW/m}^2\text{°C}$ . Modeling results show the flow field has 2D behavior and affects the thermal history significantly.

J. D. Hwang *et al.* [85] modeled the transient state of the pouring (early) stage to get knowledge on the melt pool development and solidified shell for steel TRC. Effects of latent heat of fusion and solidification temperature interval were considered, and *HTC* was taken as  $23.1\text{ kW/m}^2\text{°C}$ . To validate the model, a side dam was made of kaowool material. During casting, the kaowool was eroded and the resulting profile provided some details on the spatial temperature distribution and fluid flow patterns. This benchmark was compared to the temperature contour predicted from the model.

Kim *et al.* [86] investigated the effect of two different shaped nozzles on the flow field and thermal history during the vertical TRC process. In order to handle the boundary condition at the roll interface, it was assumed that the roll surface temperature remained at the steel liquidus temperature ( $1454\text{°C}$  in this case). This assumption allows just superheat removal in terms of heat transfer from the roll surface. After obtaining the temperature distribution in the liquid zone (melt sump) by modeling, a Nusselt number analysis was performed along the roll surface, where the dimensionless Nusselt number is calculated using Equation (2-4):

$$Nu = \frac{hs}{K} \quad (2-4)$$

where  $h$  is averaged heat transfer coefficient (in  $\text{W/m}^2\text{°C}$ ),  $K$  is the thermal conductivity of the fluid (in  $\text{W/m°C}$ ) and  $s$  is the distance along the roll surface (in m). The Nusselt number,

the ratio of convective to conductive heat transfer across (normal to) a boundary, is also calculated by Equation (2-5):

$$Nu = \frac{s}{(T_{in} - T_r)} \frac{\partial T}{\partial n} |_{roll} \quad (2-5)$$

where  $T$  is temperature (in °C) and subscripts  $in$  and  $r$  refer to inlet of nozzle and roll surface, respectively. Subscript  $n$  shows the normal direction to the roll surface. By equating the right hand sides of Equations (2-4) and (2-5), the effective heat transfer coefficient was estimated as  $20\text{ kW/m}^2\text{°C}$ . Figure 2-12 illustrates the results; the trend of the *HTC* seems to be similar to the Nusselt number variation along the arc of contact. Moreover, these investigators concluded a submerged nozzle causes more stabilize melt pool (in terms of smaller velocity vectors at free surface; upper part of the sump) in compare with a non-submerged one; therefore, it's preferable to apply such nozzles.

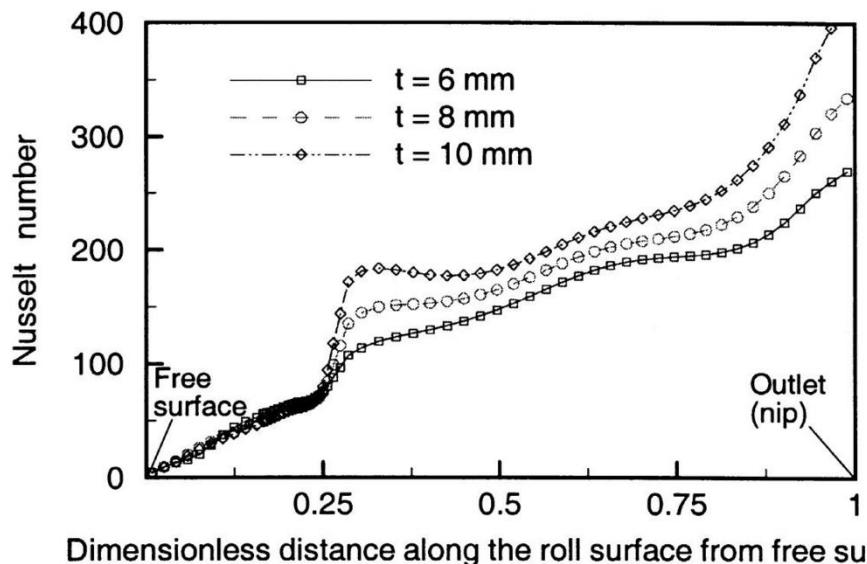


Figure 2-12- Nusselt number variation along the roll surface for different exit thicknesses [86].

Sahai *et al.* [87] and Saxena *et al.* [88] coupled fluid flow and heat transfer to simulate a horizontal TRC process for Al-4.5%Cu and Al-1.1%Mg. Their work indicated that the most important parameter in the TRC process is the sump depth; minimizing the sump depth causes the least segregation. In their modeling study, inlet velocity and pouring temperature were considered against various values of *HTC* ranging from 1-15kW/m<sup>2</sup>°C. As expected, higher *HTC* at the roll interface, lower inlet velocity and lower pouring temperature lead to smaller sump and lower segregation and minimized the temperature gradient at the exit for the set-up studied.

Cruchaga *et al.* [89] analyzed thermal history experienced by a steel strip under different casting parameters, while *HTC* was assumed to be constant at 4-6kW/m<sup>2</sup>°C. Validation was performed by comparing the results from this study to modeling results presented in the literature (done by Chang *et al.* [83]).

Wang *et al.* [90-93], J. Zhang *et al.* [94] and Fang *et al.* [95] designed an optimum nozzle shape for a vertical type twin roll caster using a physical model. It was concluded that an optimum nozzle is one which causes less fluctuation at the free surface of the melt pool. In the next step, they modeled the process by coupling fluid flow and heat transfer for both steel and stainless steel twin roll casting to predict the effect of *HTC*, roll gap, casting speed, roll diameter and superheat on the strip's thermal history. The *HTC* was assumed constant, 3-5kW/m<sup>2</sup>°C for steel and 8kW/m<sup>2</sup>°C for stainless steel type 304. For stainless steel twin roll casting, the strip exit temperature for one casting condition was measured to use as a benchmark for validation. The measured value varied between 1345-1370°C while the predicted value was 1358°C. Once the model was validated using this benchmark the rest of the models were postulated as reasonable ones. Based on these works, Zhang *et al.* [96] later modeled the stress field developed during TRC of 304 stainless steel. They studied the effect of casting speed, strip thickness, casting temperature and roll diameter on the mean stress developed on the strip surface and through the thickness.

X. Zhang *et al.* [97-100] and Miao *et al.* [101-103] coupled fluid flow and heat transfer to model TRC process for stainless steel. To apply the *HTC* the contact region was divided into four regions and for each region an appropriate *HTC* was defined, with values ranging between 3-18kW/m<sup>2</sup>°C which changed with casting speed. The strip exit temperature was used to verify the model as shown in Figure 2-13 for a range of pouring temperatures and casting speeds.

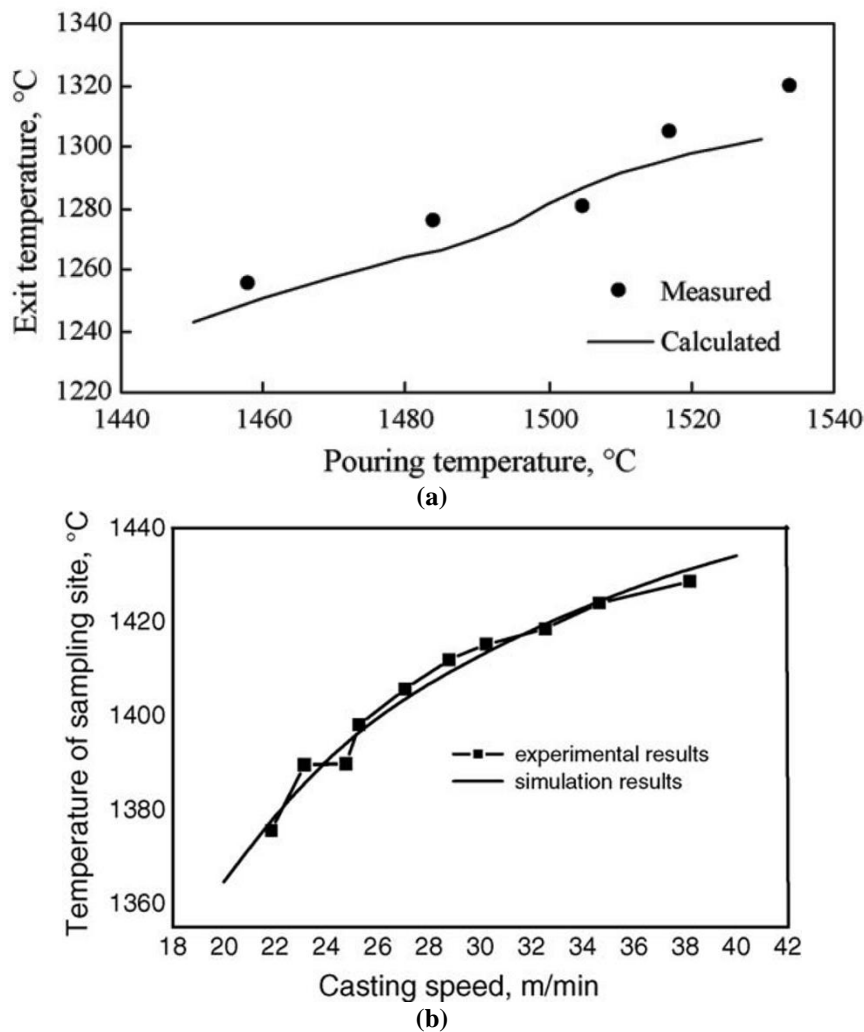


Figure 2-13- Modeling and measurement results comparison for different a) pouring temperatures and b) casting speed [98, 101].

Guthrie *et al.* [41, 104] and Tavares *et al.* [105] modeled the TRC process for low carbon steel by coupling fluid flow and heat transfer to determine the optimum feeding system. Currently, they are the only investigators who applied the most realistic *HTC* boundary conditions which varied spatially as a function of rolling force. Figure 2-14 shows schematically the mechanism they proposed which leads to variation in interfacial heat flux and *HTC* for a vertical caster. Briefly speaking, solidification starts at the first contact point of metal/roll surface due to heat transfer from metal to the roll and a thin air film forms between the solidified shell and roll surface. The presence of this thin film causes two modes of heat transfer: conduction at points where metal/roll surface contact does exist and convection and somewhat radiation in regions which air trapped between shell and roll. Low heat flux is the result of this phenomenon; region 1 in Figure 2-14. Roll expansion can then occur due to temperature elevation and also the pressure on the solidified shell rises because of the increase in metallostatic pressure (melt pool level increases). These phenomena cause the air film to be eliminated and more contact area provided for strip/roll surface which then causes higher heat flux; region 2 in Figure 2-14. After the peak value, the solidified shell starts to shrink and less contact area provided for heat transfer which causes less heat flux, region 3. It seems the mechanism could be also explained by roll pressure which has the same shape as heat flux graph. These authors were also the first who attempt to estimate *HTC* by embedding thermocouples into the rotating roll. In order to evaluate *HTC*, instrumented rolls with thermocouples were used for TRC (illustrated schematically in Figure 2-15) and temperature-time data implemented in an inverse heat transfer code to estimate the interfacial heat flux and consequently *HTC*, as depicted in Figure 2-16. They also studied the relation between *HTC* and casting speed. As shown in Figure 2-17, increasing casting speed causes *HTC* raise.

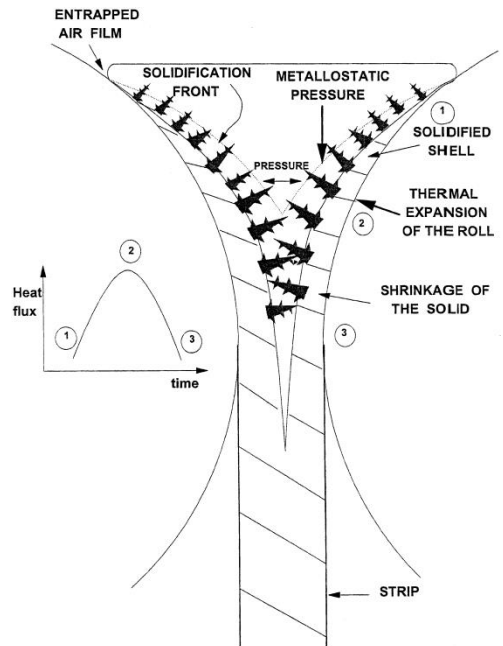


Figure 2-14- Mechanism used to specify variation in heat flux [41].

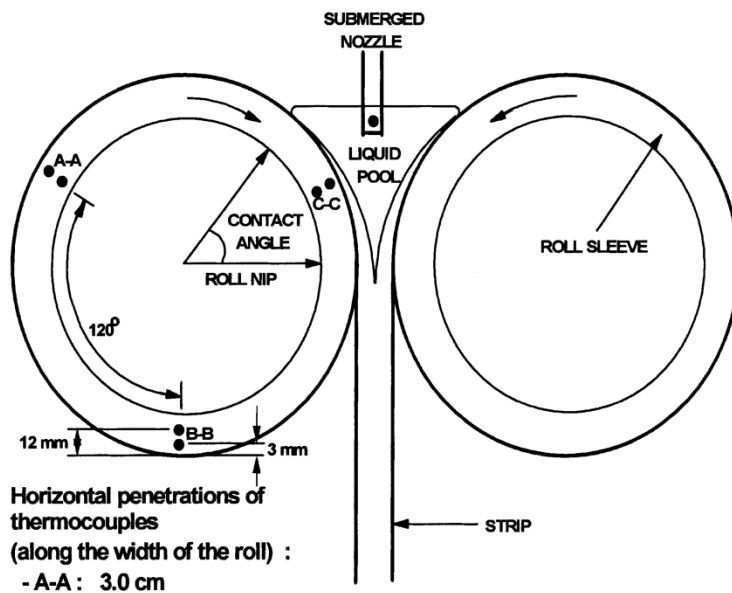


Figure 2-15- Equipped rolls with thermocouples used for steel TRC to evaluate *HTC* [41].

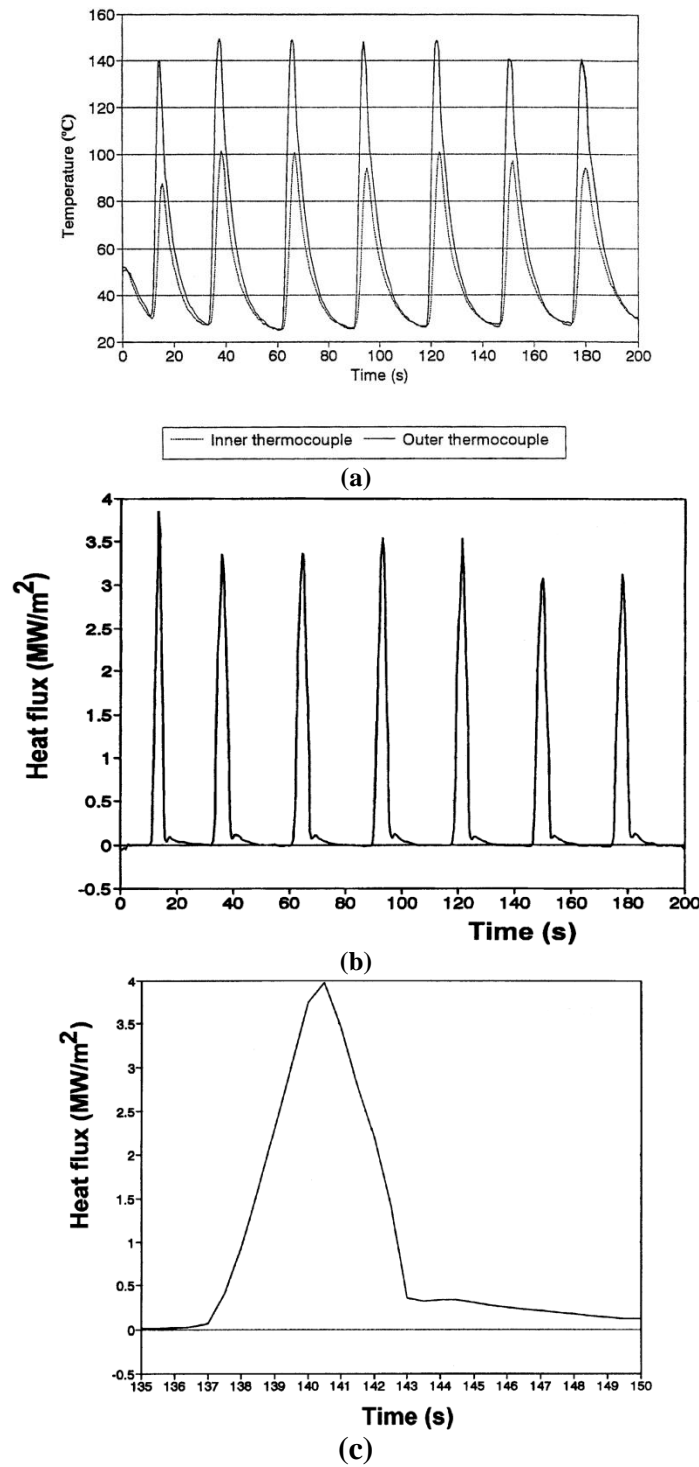


Figure 2-16- (a) Temperature-time data recorded by TCs, (b) corresponding heat flux calculated by inverse method, (c) heat flux variation during the contact time [41].

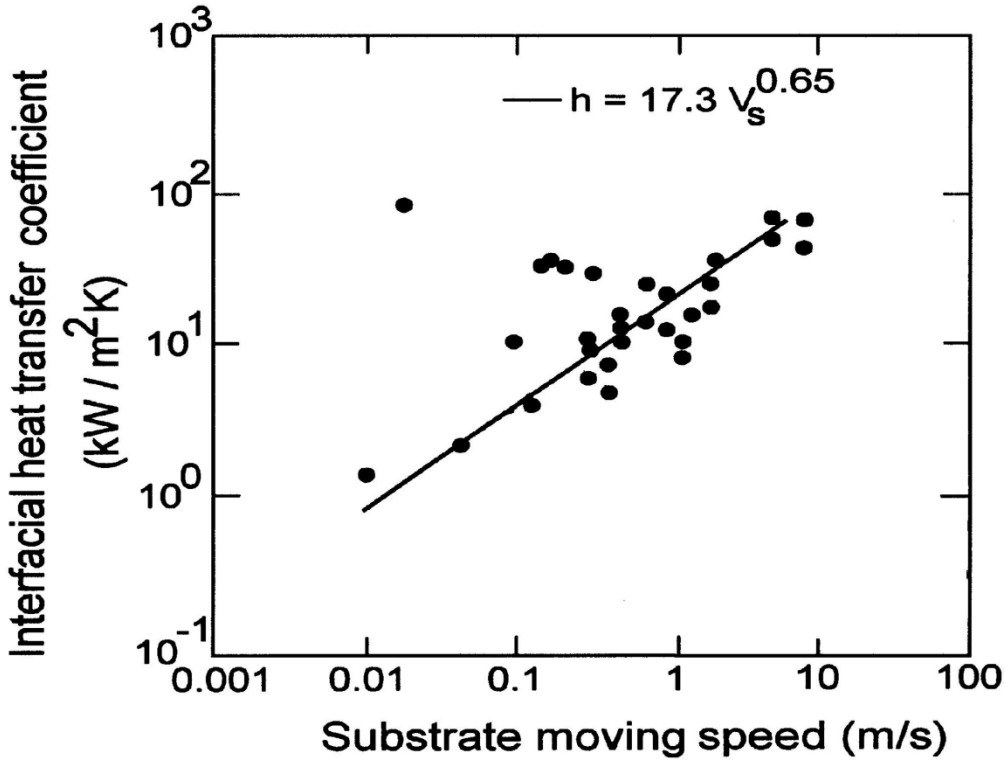


Figure 2-17- Effect of casting speed on the *HTC* in the roll bite [41].

Lixin *et al.* [106] studied the effect of *HTC* peak value and position on the solidification process for stainless steel twin roll casting using a non-constant interfacial heat transfer coefficient between the strip and the roll surface. The simulation included a simple heat transfer model with no fluid flow. Regardless of the actual *HTC* profile along the arc of contact, six different values and positions for the *HTC* were assumed; peak values of 40, 60 and 80kW/m<sup>2</sup>°C positioned at 50% of contact length and peak value of 60kW/m<sup>2</sup>°C positioned at 10, 50 and 90% of contact length, as shown in Figure 2-18. All of the conditions were designed so that the average *HTC* remains around 10kW/m<sup>2</sup>°C. The results show for a constant peak value (60kW/m<sup>2</sup>°C), different peak positions have more significant effects on the results than changing peak value for a fixed position. In other works, *HTC* was taken as 9kW/m<sup>2</sup>°C for steel TRC [107] and 10kW/m<sup>2</sup>°C for aluminum TRC [108].

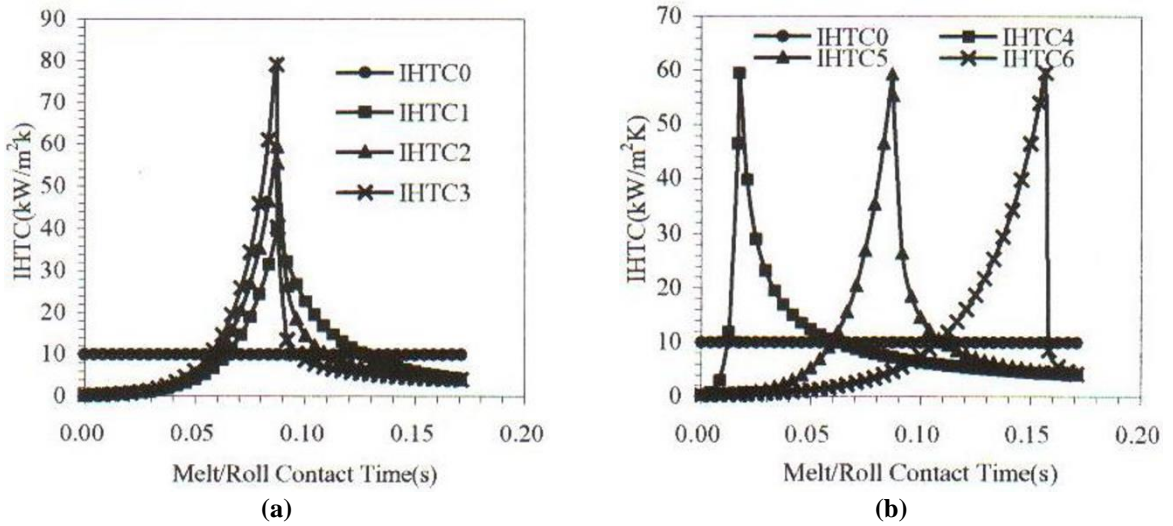


Figure 2-18- HTCs of (a) different peak values and (b) different peak positions [106].

To date, some research has been done to model magnesium TRC. Ju *et al.* [109] and Hu *et al.* [110] modeled both vertical and horizontal TRC process for AZ31 magnesium alloy by FEM. Based on the nozzle design, the flow was assumed to be turbulent (this design causes high Reynolds number). During the process the *HTC* for the horizontal process was assumed to be constant ( $10\text{kW/m}^2\text{C}$ ) and for vertical one three constant *HTC*'s were evaluated namely: 10, 15 and  $20\text{kW/m}^2\text{C}$ . For each process the effect of nozzle shape, casting speed and set-back distance were analyzed to determine the optimum casting conditions. The optimum casting conditions were determined based on the more uniform flow field and temperature distribution.

Bae *et al.* [111] employed a 2-D finite difference model for AZ91 magnesium alloy vertical TRC. Both the melt pool and roll were taken into account in the simulation. The *HTC* was chosen as  $20\text{kW/m}^2\text{C}$  before complete solidification occurred and  $8\text{kW/m}^2\text{C}$  after that. The effect of nozzle configuration and casting speed on the temperature distribution and flow field in the roll bite region was studied. The results were studied in terms of cooling rate and solidification front position.

Zeng *et al.* [112] developed a CFD model to predict the fluid flow and temperature distribution during twin roll casting of AZ31 with an asymmetric nozzle which provided different contact lengths on the upper and lower rolls. The *HTC* was assumed to be 4 and  $3.3\text{ kW/m}^2\text{ }^\circ\text{C}$  for strip exit thicknesses of 3 and 4mm, respectively. The effects of casting speed and exit thickness were studied in terms of thermal history and fluid flow and it was concluded that an asymmetric contact zone leads to an asymmetric microstructure. The exit temperature of the strip was measured for a 1m length to validate the modeling results as shown in Figure 2-19.

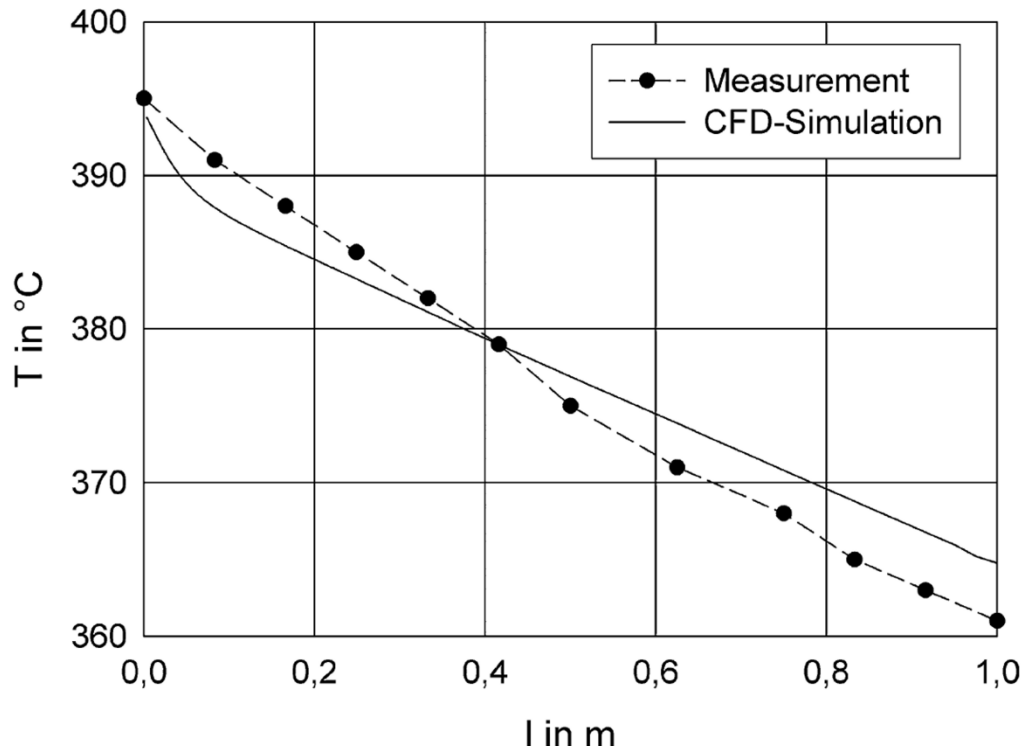


Figure 2-19- Comparison of predicted versus measured surface temperature of the twin roll cast strip after exiting roll bite, *l* shows the distance to the exit region [112].

Zhao *et al.* [113] obtained the flow field and temperature distribution of the strip for AZ31 magnesium alloy by developing an FEM model to analyze the effect of casting speed, strip exit thickness, heat transfer coefficient and pouring temperature. The strip temperature at the exit point was measured to validate the model.

## 2.6 Summary

Reviewing the literature on the TRC of magnesium and other alloys, it is obvious that very limited work has been done to develop a comprehensive mathematical model for the magnesium TRC process and the subsequent use of a validated model to understand defect formation. A particular area which has limited knowledge is the Heat Transfer Coefficient (*HTC*) at the interface between the roll and the strip and also the effect of cooling conditions on the microstructure evolution. Moreover, the mechanical behavior of the strip during the process and the effect such behavior on the strip final quality has not been studied. In particular, there is a need to correlate the casting conditions, mechanical behavior of the strip and defect formation conditions. Hence, modeling the TRC process requires comprehensive knowledge of the interactions between roll and strip (solidified shell) and the effect of them on the thermal-fluid behavior and stress-strain development in the strip during the casting.

## **Chapter 3**

### **Scope and Objectives**

A key aspect of the scientific and commercial development of sheet magnesium materials is detailed knowledge and know-how of successfully employing the Twin Roll Casting (TRC) process to produce high quality magnesium sheet. TRC consists of a complicated combination of many process parameters which will affect the final sheet product. Development of a mathematical model of the magnesium TRC process can provide a knowledge based approach to more fully understanding the TRC process for magnesium as well as provide insight on the effect of each process parameter and their inter-dependence on the final sheet product produced.

Specific objectives for this work include:

- Development and validation of a comprehensive thermal-fluid-stress mathematical model of the TRC process for magnesium during steady state casting,
- Improvement of the current knowledge on the heat transfer at the interface between the roll and the strip and how it affects the results,
- Understanding of how the solidified microstructure forms during twin roll cast AZ31 magnesium alloy strips and how it is affected by casting parameters such as casting speed and set-back distance,
- Understanding the thermo-mechanical behavior of the cast strip during the process,
- Development of knowledge around defect formation (center-line and inverse segregation) and what factors influence it, and
- Simulation of the effect of roll diameter so that scale up of lab scale TRC units to commercial sizes will be better understood in terms of strip quality.

To achieve these objectives, the first step was the development and validation of a comprehensive mathematical model of the Twin Roll Casting process for magnesium alloys based on the experimental Twin Roll Casting (TRC) facility at the Natural Resources Canada Government Materials Laboratory (CanmetMATERIALS). This model was able to predict fluid flow, heat transfer and mechanical deformation experienced by the cast material during the process. Validation was done by comparing the predicted quantities (obtained by modeling) and measured ones (obtained by experimental trials) to show the effectiveness and reliability of the model. The model was then used so that a quantitative understanding of the influence of the process parameters on the final sheet could be gained. Final sheet quality is dominated by as-cast sheet mechanical, physical and chemical (corrosion) properties and also the amount of micro and macro defects that form in the sheet. These properties depend on the cast material solidified microstructure which is directly a result of the thermal history and amount of deformation experienced by the sheet during TRC. In support of this work, CanmetMATERIALS commissioned a laboratory twin roll caster for magnesium alloys. This twin roll caster for magnesium is the only one operating in Canada and one of a handful across the world.

The uniqueness of this work lies in the fact that this is the first time a fully coupled thermal-fluid-stress model for TRC of magnesium alloys has been developed and published. In addition, detailed knowledge on the effect of TRC process parameters (including roll diameter) on the formation of the solidified microstructure and defect formation was elucidated.

## **Chapter 4**

### **Experimental Measurements**

#### **4.1 TRC Procedure at CanmetMATERIALS**

In this chapter an overview of the TRC experiment done at CanmetMATERIALS is presented. Figure 4-1 shows a picture of the TRC machine at CanmetMATERIALS, the equipment consists [19]:

- Melting furnace
- Pump and transfer tube
- Headbox
- Delivery nozzle (tip)
- Twin roll caster stand
- Pinch rolls
- Moving shear unit
- Stacking unit (or coiler), as shown in Figure 4-2.

The roll diameter of the TRC facility at CanmetMATERIALS is 355mm. The rolls are made from tool steel H13 and have the ability to speed up to 6m/min. The thickness of the cast strip could vary between 2-8mm and the width of strip ranges in 150-250mm.



Figure 4-1- Twin roll caster at CanmetMATERIALS used for magnesium alloys [19].

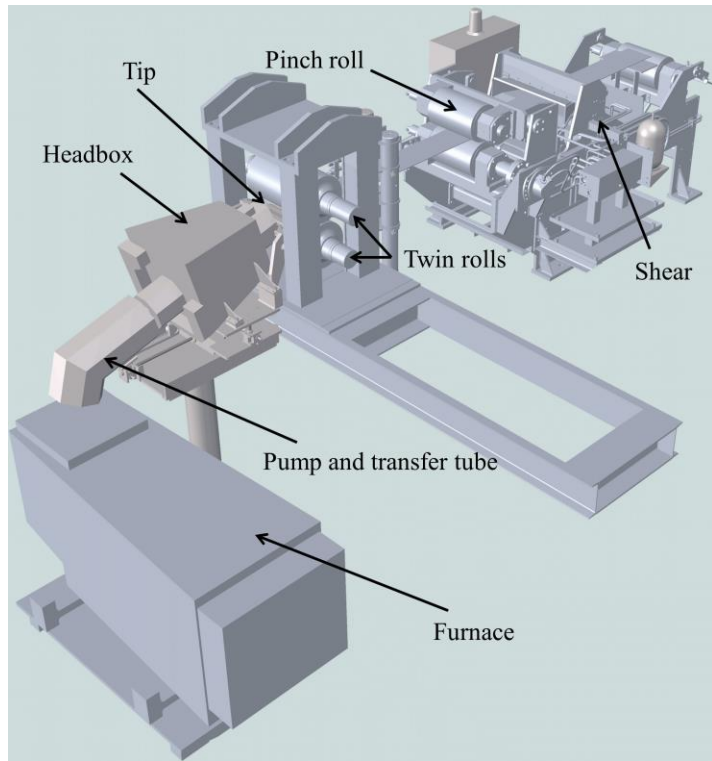


Figure 4-2- TRC layout for magnesium alloys at CanmetMATERIALS [19].

An electric resistance furnace is used to melt the commercial AZ31 magnesium alloy ingots under protective gas; mixture of SF<sub>6</sub> and N<sub>2</sub>. A melt delivery system is used to transfer the molten material to the headbox. The temperature of the molten material at the headbox is monitored to be maintained at the desire value.

In the early trials an electrical heated steel nozzle was used with the opening of 10-12mm. The technical problems in heating such a nozzle led to a change; ceramic nozzle was replaced. The opening of the ceramic nozzle varies between 6-9mm and a hot air blower system is used to heat up the nozzle prior to the experiments. The nozzle is equipped with two thermocouples on the sides to monitor the temperature to prevent solidification inside the nozzle. Occurrence of such phenomenon, known as early freezing, causes the process to stop unexpectedly.

The gap between two rolls is set to the desire strip thickness and once the temperature of the nozzle reaches an appropriate value (~700°C) the molten magnesium is fed through the nozzle to the roll bite region. Melt temperature at the furnace, melt level and temperature at the headbox, nozzle temperature, strip surface temperature at the exit point of the caster, casting speed and roll surface and coolant water temperature are acquired during the process. The cast strip are then cut and marked to sort properly.

#### **4.1.1 Casting Conditions**

Figure 4-3 shows the measured casting speed and strip exit temperature for one of the trials (#1) at CanmetMATERIALS. Referring to Figure 4-3, to determine the steady state conditions, an average is taken for each parameter. The averaged values will be then considered as casting conditions to develop the corresponding models. Table 4-1 illustrates the casting conditions conducted at CanmetMATERIALS.

Table 4-1- Casting conditions for each trial

Trial #	Pouring Temperature (°C)	Casting Speed (m/min)	Entry Thickness (mm)	Exit Thickness (mm)	Exit Temperature (°C)
<b>1</b>	740	2.82	12	5	471
<b>2</b>	712	2.10	12	5	397
<b>3</b>	700	2.50	8	5	376
<b>4</b>	677	1.70	12	6	400
<b>5</b>	670	2.10	8.5	5	290
<b>6</b>	666	1.97	8.5	5	273
<b>7</b>	680	2.50	7.8	5	307
<b>8</b>	680	3.00	8.8	5	350

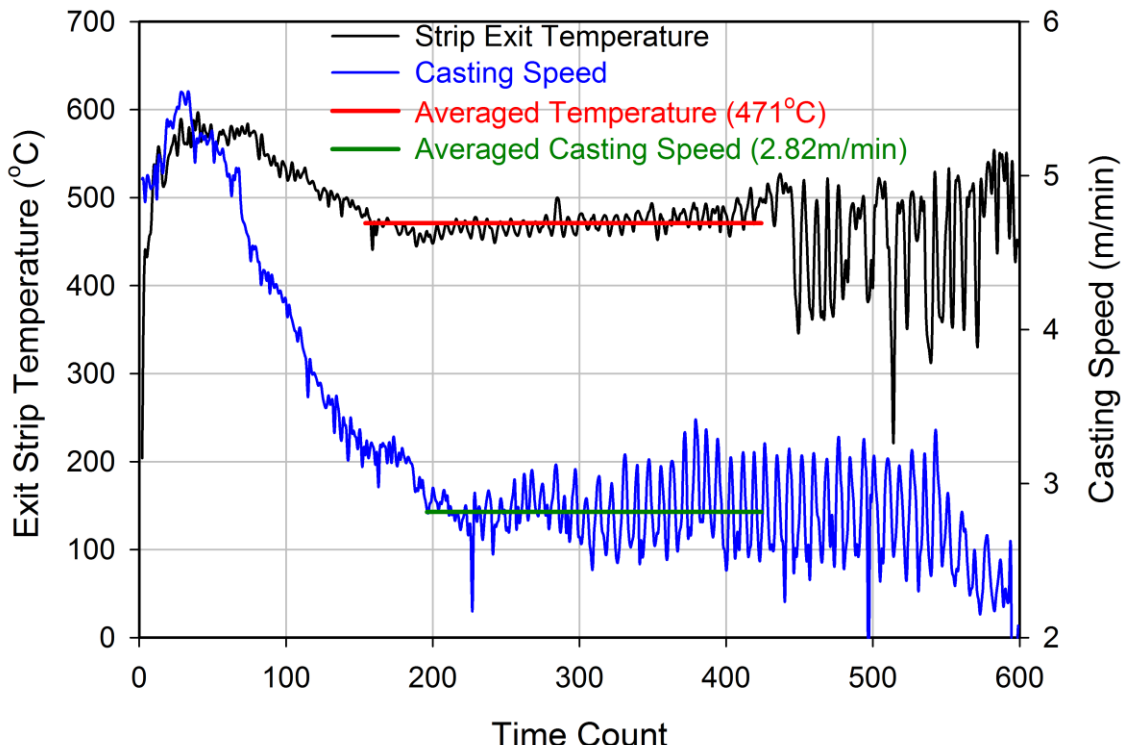


Figure 4-3- Recorded data during AZ31 TRC for trial #1 at CanmetMATERIALS.

## 4.2 Microstructure Analysis

The twin roll cast strips were analyzed in terms of microstructural evolution through thickness, defect (center-line and inverse segregation) formation and secondary dendrite arm spacing (SDAS). The samples were chosen from the center and side of the cast strip from three different locations as shown schematically in Figure 4-4 and were analyzed from side view along the whole thickness. Grinding was done with 500, 800, 1000 and 4000 grit grinding papers followed by polishing with  $3\mu\text{m}$  and  $0.04\mu\text{m}$  SiC suspensions. The etchant solution to reveal the dendritic microstructure was chosen with following compositions:

1ml Nitric Acid, 20ml Acetic Acid, 20ml Water and 60ml Ethylene Glycol.

The microstructure of the samples was studied under optical microscope with various magnifications. To measure the SDAS, the primary dendrite branches were recognized and then the secondary dendrite arms were considered as those developed from the primary arms [114-116]. The center to center distance between the neighbor arms was then measured to determine the SDAS, as shown in Figure 4-5. The procedure was repeated for all clearly visible dendrites through the thickness to determine SDAS for the whole thickness.

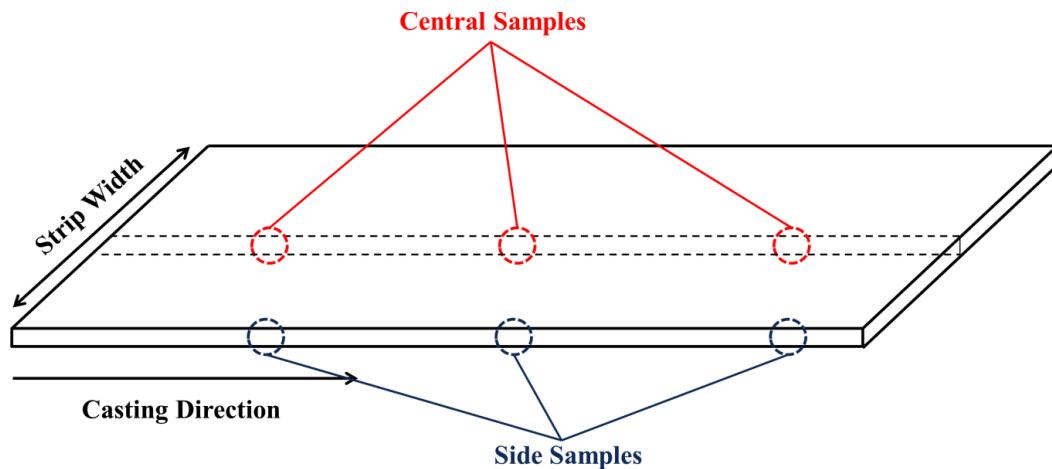


Figure 4-4- Schematic representation of sample selection for microstructural study.

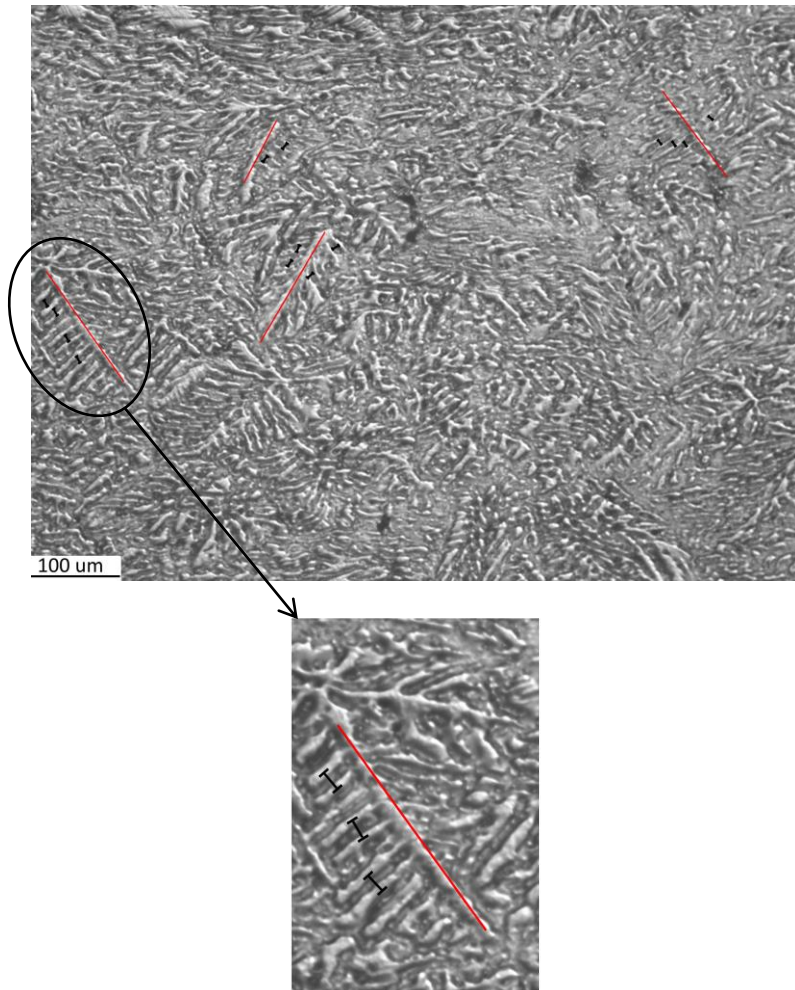


Figure 4-5- Sample SDAS measurement procedure, the red lines show the primary dendrite arms and the black lines represent the distance between the secondary arms.

Besides the optical microscopy, the scanning electron microscope (SEM) was also used to perform more detailed characterization of the microstructure and also conduct a spatial chemical analysis using EDS. This allowed studying the concentration of solute (Al, Zn and Mn) in the cast material in different regions. By performing such analysis, characterization of both center-line and inverse segregation could be analyzed.

## **Chapter 5**

### **Mathematical Model Development**

For the current research, a two-dimensional thermal-fluid-stress model for the TRC process for AZ31 magnesium alloy was developed to model the caster at CanmetMATERIALS. The model simulates what occurs in the strip at the mid-width position during steady state TRC.

The development of the fully coupled thermal-fluid-stress mathematical model was done in stages, with each stage increasing the complexity of the model. The commercial package ANSYS® CFX® and ALSIM were used to develop the mathematical model. ANSYS® CFX® was used to develop a thermal-fluid model to study the thermal history of the strip. ALSIM, a commercial FE code developed by the Institute for Energy Technology (IFE) Company in Norway is one of the few codes that can be used to couple the fluid flow, heat transfer and stress during TRC.

#### **5.1 Thermal-Fluid Model (ANSYS® CFX®)**

##### **5.1.1 Geometry and Computational Domain**

As described earlier, the TRC facility consists of two counter rotating rolls between which liquid metal is fed through a nozzle across the width of the rolls. As the liquid metal contacts the rolls it is simultaneously cooled and pulled into the roll bite. In the roll bite the strip continues to cool and is also deformed until at the exit it emerges as a solid strip. Figure 5-1 shows 2D schematic of a twin roll caster. The figure also illustrates some of the terminology used in this study when discussing results.

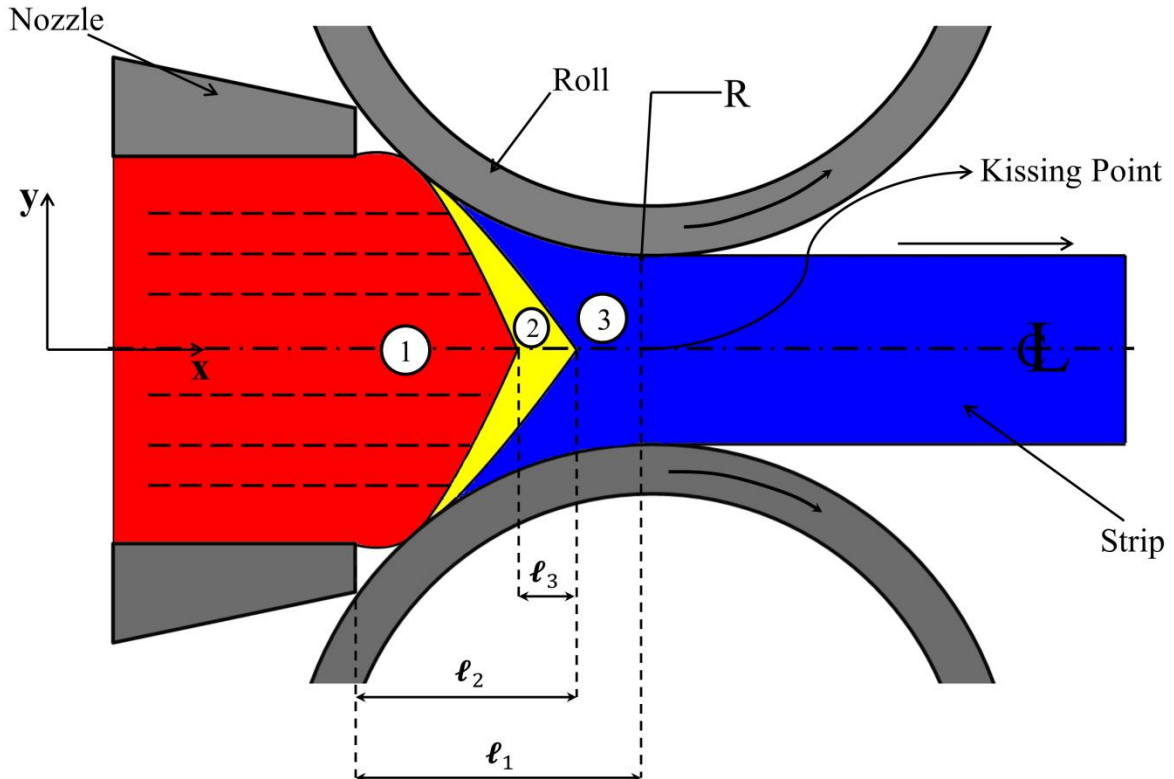


Figure 5-1- Schematic of the twin roll casting process; region 1 is the liquid metal, region 2 is the mushy zone and region 3 is the solid strip,  $\ell_1$ ,  $\ell_2$  and  $\ell_3$  are set-back distance, sump depth and mushy zone thickness, respectively. Note: The perspective of the TRC is not to scale and the nozzle size and position are magnified with respect to the rolls

### 5.1.2 Mathematical Model

Initially, a thermal-fluid analysis will be run using CFX<sup>®</sup>. The following assumptions are considered concerning to the geometry and phenomena happened during the process, for the thermal-fluid model:

- I. The process is dominated by transport phenomena and deformation in two dimensions. In the third dimension (across the width) there is no significant heat transfer or fluid flow as the simulation is done at the mid-width location,
- II. Due to symmetry only the top half of the strip and part of the top roll was modeled in the simulation,

- III. The fluid flow is laminar when exiting the nozzle tip and entering the roll bite,
- IV. The rolls are rigid and do not deform elastically.

The important physical phenomena happen during the process which are included in the thermal-fluid model are:

- I. Heat transfer and fluid flow in the melt sump (liquid metal, zone 1 in Figure 5-1),
- II. Heat transfer, fluid flow and latent heat of fusion release in the mushy zone (zone 2 in Figure 5-1),
- III. Heat transfer in the solid phase (zone 3 in Figure 5-1), and
- IV. Heat transfer from the magnesium sheet to the roll surface.

### 5.1.2.1 Governing Equations

The basis of the numerical simulation of the fluid flow and heat transfer is the conservation laws of mass, momentum and energy. Since the process is being modeled during steady state, time independent governing equations are considered, as shown in Equations (5-1) to (5-3):

- Mass conservation equation:

$$\frac{\partial}{\partial x_j} (\rho u_j) = 0 \quad (5-1)$$

- Momentum conservation equation:

$$\frac{\partial}{\partial x_j} (\rho u_i u_j) = \rho g_i + \frac{\partial}{\partial x_j} \left( \mu \frac{\partial u_i}{\partial x_j} \right) - \frac{\partial p}{\partial x_i} \quad (5-2)$$

- Energy conservation equation:

$$\frac{\partial}{\partial x_j} (\rho u_j C_p T) = \frac{\partial}{\partial x_j} \left( k \frac{\partial T}{\partial x_j} \right) \quad (5-3)$$

where the subscripts  $i$  and  $j$  show the directions,  $u$  is the velocity (in m/s),  $\rho$  is the density (in kg/m<sup>3</sup>),  $g$  the gravity vector (in m/s<sup>2</sup>),  $\mu$  dynamic viscosity (in Pa.s),  $p$  pressure (in Pa),  $C_p$  specific heat capacity (in J/kg°C),  $k$  thermal conductivity (in W/m°C) and  $T$  temperature (in °C).

To account for solidification, two important effects of this phenomenon on the fluid flow and heat transfer need to be included; the effect of a semisolid region on the fluid flow and the latent heat that is released during solidification. Since alloy solidification occurs over a temperature interval, a mushy zone (mixture of solid and liquid) is formed which will damp or inhibit fluid flow in that zone. It's assumed this mushy region acts as a porous medium and obeys Darcy's equation [104, 112]; so an additional term is added to the momentum conservation equation and Equation (5-2) is modified as shown in Equation (5-4):

$$\frac{\partial}{\partial x_j} (\rho u_i u_j) = \rho g_i + \frac{\partial}{\partial x_j} \left( \mu \frac{\partial u_i}{\partial x_j} \right) - \frac{\partial p}{\partial x_i} - C \frac{(1 - f_l)^2}{f_l^3 + \varepsilon} (u_j - u_{r,j}) \quad (5-4)$$

where  $C$  is a constant of the liquid phase between 10<sup>4</sup>-10<sup>7</sup> for AZ31 magnesium alloy [112],  $f_l$  is the fraction liquid,  $\varepsilon$  a small number to avoid division by zero when the liquid fraction approaches zero and  $u_{r,j}$  is the roll velocity component in the  $j$ -direction (in this case it is assumed to be casting velocity in the  $x$ -direction and 0 in other directions). By adding this source term, velocities in the mushy zone gradually approach the corresponding component of the actual velocity, as the fraction liquid goes to zero.

The second effect of solidification; the release of latent heat, is modeled by considering an equivalent specific heat capacity [112], as shown in Equation (5-5); which then is implemented in the energy conservation equation.

$$H = H_{ref} + \int_{T_{ref}}^T C_p dT \quad (5-5)$$

where  $H$  is the enthalpy (in J/kg),  $H_{ref}$  reference enthalpy (here the latent heat of fusion, in J/kg),  $C_p$  specific heat capacity (in J/kg°C) and  $T_{ref}$  reference temperature (here solidus in °C).  $C_p$  is calculated by Equation (5-5) and then will be substituted in the energy conservation equation.

### 5.1.2.2 Boundary Conditions

A critical aspect of the model development will be quantifying boundary conditions to describe the twin roll casting process accurately. There are six process boundary conditions as described below and depicted in Figure 5-2:

- Inlet (region 1): the boundary condition in this region consists of the casting temperature and velocity; Equations (5-6) and (5-7).

$$V_x = V_{in}, V_y = 0 \quad (5-6)$$

$$T = T_{cast} \quad (5-7)$$

where  $V_x$  and  $V_y$  are the components of velocity in  $x$  and  $y$  directions, respectively,  $V_{in}$  is the inlet velocity (in m/min) and  $T_{cast}$  is the casting temperature (in °C). The liquid velocity at the inlet is calculated from the casting speed while the mass is conserved during the process.

- Nozzle surface (region 2): this region is assumed to be adiabatic (no heat loss) and that there is a no-slip wall condition (no relative velocity between the fluid and the boundary).

$$V_x = V_y = 0 \quad (4-8)$$

$$\partial T / \partial y = 0 \quad (4-9)$$

- Roll/strip interface (region 3): In this region a no-slip rotating wall is defined. The heat transfer between the roll and the strip is defined using a heat transfer coefficient (*HTC*) as shown in Equation (5-10).

$$-k \frac{\partial T}{\partial n} = HTC(T_s - T_0) \quad (5-10)$$

where  $k$  is the thermal conductivity (in W/m°C),  $T$  temperature (in °C),  $HTC$  is the heat transfer coefficient (in W/m<sup>2</sup>°C),  $n$  is the normal direction to the strip surface,  $T_s$  is the strip surface temperature and  $T_0$  is the roll surface temperature (in °C). The roll surface temperature was assumed to be constant at 60°C based on the measurements during the experimental trials.

- Exiting strip upper surface (region 4): For the surface of the exit strip radiation is neglected in this region because of the low temperatures but a low value of  $HTC=12W/m^2°C$  [112] is used to account for heat transfer from the strip to the air. Heat transfer is governed by Equation (5-10) and the ambient temperature is 25°C. The interface is defined as free-slip wall.
- Outlet (region 5): The exit velocity is equal to the casting speed.

$$V_x = V_{cast}, V_y = 0 \quad (5-11)$$

where  $V_{cast}$  is the casting speed (in m/min).

- Center-line (CL): the center-line is considered to be a symmetry boundary with no fluid flow or heat transfer across the interface.

$$V_y = 0, \partial V_x / \partial y = 0 \quad (5-12)$$

$$\partial T / \partial y = 0 \quad (5-13)$$

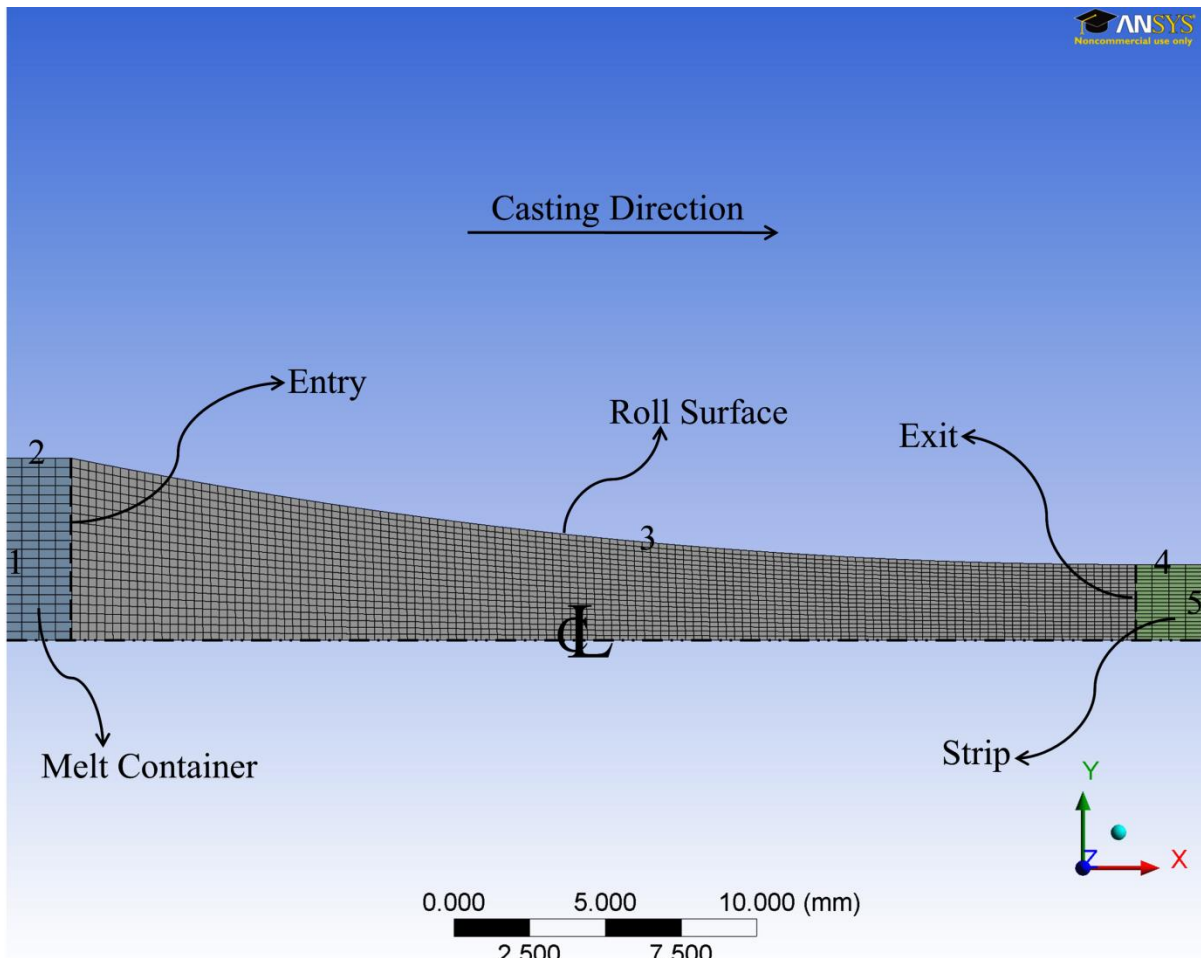


Figure 5-2- Boundary regions on the solution domain of the twin roll casting process, ANSYS® CFX® software.

The ANSYS® CFX® commercial package is used to define geometry, mesh, boundary conditions and to solve the heat transfer and fluid flow equations. The mesh used is structured quadrilateral as illustrated in Figure 5-2. The elemental size used for generating the mesh for the strip ranged from a minimum of 0.1mm (in the melt sump) to a maximum of 2mm (near inlet and outlet) in side length. These values were determined based on a mesh size sensitivity analysis [116].

## 5.2 Thermal-Fluid-Stress Model (ALSIM)

In the next stage the ALSIM software is employed to model the heat transfer, fluid flow and plastic deformation that occur during the TRC process. The assumptions are similar to those mentioned in section 5.1.2, but the physical phenomena integrated in the model are modified as:

- I. Heat transfer and fluid flow in the melt sump (liquid metal, zone 1 in Figure 5-1),
- II. Heat transfer, fluid flow and latent heat of fusion release in the mushy zone and deformation in the material once the coherency point is reached, (zone 2 in Figure 5-1),
- III. Heat transfer and plastic deformation in the solid phase (zone 3 in Figure 5-1),
- IV. Heat transfer from the magnesium sheet to the roll surface, and
- V. Heat transfer inside the roll material and from the roll's sleeve to the circulated water.

### 5.2.1 Mathematical Model

For the thermal elastic-plastic model, the material is defined as an isotropic elastic-viscoplastic material. The velocity field below the coherency temperature which is used to calculate the strain is determined by minimizing the energy functional as shown in Equation (5-14) [117].

$$\delta\pi = \int_{\Omega} \delta\boldsymbol{\varepsilon}^* \cdot \boldsymbol{\sigma} d\Omega - \int_{\Omega} \delta\mathbf{u}^* \cdot \rho\mathbf{g} d\Omega - \int_{\Gamma} \delta\mathbf{u}^* \cdot \mathbf{t} d\Gamma = 0 \quad (5-14)$$

where superscript “\*” denotes the transpose of a vector or matrix,  $\mathbf{g}$  is the gravity vector (in  $\text{m/s}^2$ ),  $\rho$  density (in  $\text{kg/m}^3$ ),  $\mathbf{t}$  the force per unit length acting on the boundary  $\Gamma$  (in  $\text{N/m}$ ),  $\delta\mathbf{u}$  and  $\delta\boldsymbol{\varepsilon}$  virtual variations of displacement  $\mathbf{u}$  and associated strain vector  $\boldsymbol{\varepsilon}$ , respectively and  $\Omega$  is the solution domain.

The total strain imposed to the material is subdivided to thermal, elastic and viscoplastic components, as shown in Equation (5-15) [118].

$$\boldsymbol{\varepsilon} = \boldsymbol{\varepsilon}_T + \boldsymbol{\varepsilon}_e + \boldsymbol{\varepsilon}_p \quad (5-15)$$

where  $\boldsymbol{\varepsilon}$  is strain and subscripts  $T$ ,  $e$  and  $p$  show thermal, elastic and viscoplastic components, respectively. Thermal strain is calculated by Equation (5-16).

$$\boldsymbol{\varepsilon}_T = - \int_T^{T_{Coh}} \beta(T) dT \cdot \mathbf{I} \quad (5-16)$$

where  $\beta$  is thermal expansion coefficient as a function of temperature,  $\mathbf{I}$  is the identity tensor and  $T_{Coh}$  is the coherency temperature, at which the solidified material could develop stress (this temperature is between liquidus and solidus temperature, so it shows the fraction solid at which the mushy material acts as a fully solid material in stress development).

Elastic strain below the coherency temperature is calculated by Hook's law as shown by Equation (5-17).

$$\boldsymbol{\sigma}_e = \mathbf{D}(T) \cdot \boldsymbol{\varepsilon}_e \quad (5-17)$$

where the material's temperature dependent elastic modulus and Poisson's ratio enters the matrix  $\mathbf{D}$  [117, 118].

The constitutive behavior of the AZ31 magnesium alloy is modeled by the extended Ludwig equation [119, 120] validated by Howes *et al.* [121] as shown in Equation (5-18).

$$\boldsymbol{\sigma} = K(T) \cdot (\dot{\boldsymbol{\varepsilon}}_P + \dot{\varepsilon}_{po})^{m(T)} (\boldsymbol{\varepsilon}_P + \varepsilon_{po})^{n(T)} \quad (5-18)$$

where  $\boldsymbol{\sigma}$  is the stress tensor (in Pa),  $\dot{\boldsymbol{\varepsilon}}_P$  the strain rate (in  $s^{-1}$ ),  $\boldsymbol{\varepsilon}_p$  the strain,  $K$  strength coefficient,  $n$  the strain hardening exponent and  $m$  the strain rate sensitivity exponent.  $\dot{\varepsilon}_{po}$  and  $\varepsilon_{po}$  are small numerical constants needed to ensure that at a plastic strain of zero, the yield stress of the material is correct.

## 5.2.2 Solution Domain and Boundary Conditions

Since the roll is also taken into the simulation for the thermal-fluid-stress model, the solution domain is slightly different with the thermal-fluid model domain as shown in Figure 5-3.

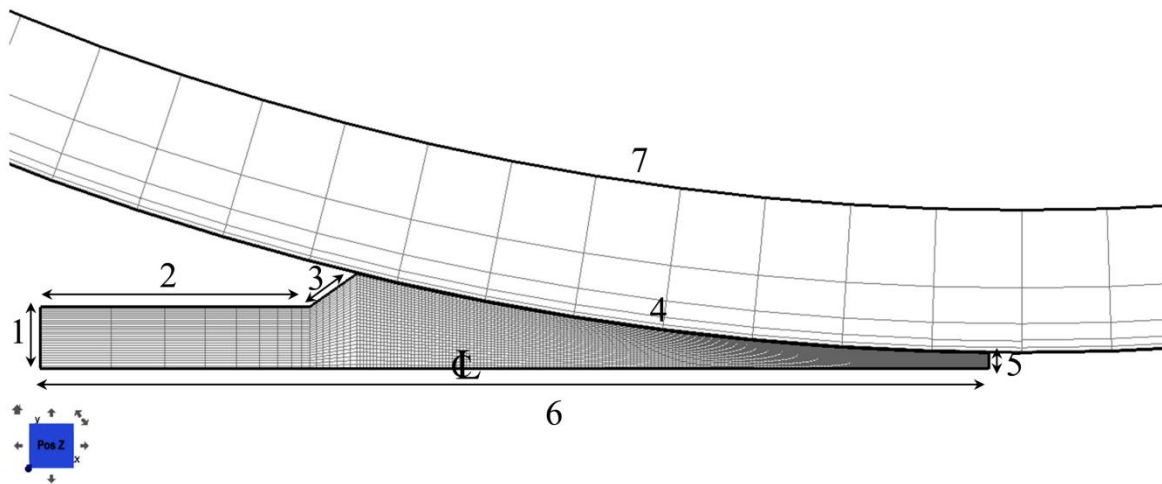


Figure 5-3- Solution domain used for thermal-fluid-stress model and the boundary regions.

The velocity and thermal boundary conditions are similar to those mentioned for the thermal-fluid model in section 5.1.2.2; there is just one more boundary condition:

- Inner roll surface/circulated water interface (region 7 referring to Figure 5-3): there is heat transfer from the roll material to the coolant water inside the roll. Similar conditions of Equation (5-10) is governing here, the water temperature is 40°C and the  $HTC=40\text{kW/m}^2\text{°C}$  is applied.

Besides thermal and fluid boundary conditions, the appropriate mechanical boundary conditions have been assigned to the model. At the free surfaces; i.e. inlet and nozzle surface (regions 1, 2 and 3), there are no constraints on the displacements. The effect of material constraint at the outlet is simulated by assigning a fixed normal pressure, while at the center-

line a fixed normal distributed stiffness plays the same role [120]. The interaction between the cast material and the roll surface at the strip/roll interface, region 4, is described using a friction law shown by Equation (5-19).

$$\tau_{crit} = \mu P \quad (5-19)$$

where  $\tau_{crit}$  is the critical shear stress (in Pa),  $P$  normal pressure (in Pa) and  $\mu$  the coefficient of friction. For the present study a coefficient of friction  $\mu=0.4$  was chosen which is typical for hot rolling.

For the finite element discretization, rectangular isoparametric elements with four nodes were chosen as depicted in Figure 5-4. Since the TRC process is a continuous casting process and a part of the domain is moving with the casting speed, appropriate coordinate system is needed to be considered. So, the solution domain for the cast material is divided to two subdomains; a fixed domain and an expanding domain, referring Figure 5-4. For the fixed domain, which consists the region inside the nozzle, an Eulerian coordinate system is defined. This coordinate system is fixed in space. The expanding domain represents the part of the domain moving inside the roll bite region as the process proceeds. So, an Arbitrary Eulerian Lagrangian (ALE) coordinate system is applied to define the expanding domain and moving grid properly. This coordinate system is moving in space, not at the same speed of the material; so, at each time step a procedure equivalent to “re-meshing” process happens. Moreover, the roll is described by a Lagrangian coordinate system as well. Once the discretized domain is defined it's imported to the commercial FEM package ALSIM in addition to the boundary conditions and material properties to couple and solve the equations to perform modeling. The process starts at t=0s with the domain shown in Figure 5-4, the domain is expanded and the process experiences the transient conditions and after a while it reaches the steady state conditions. The check point to assure the steady state conditions is rolling force; once it gets a constant value over time the process is steady.

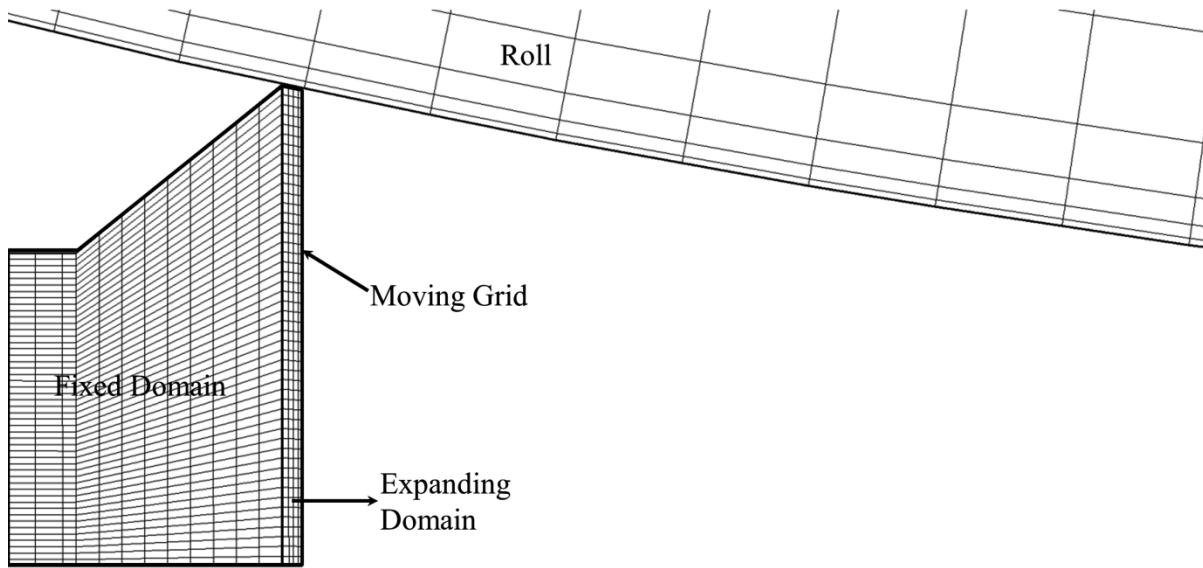


Figure 5-4- Solution domain and finite element mesh at  $t=0s$ .

### 5.2.3 Mesh Size Sensitivity Analysis

In order to ensure the optimum mesh size, an analysis was conducted for five different mesh sizes. One thermal response (exit temperature at the strip surface) and one mechanical response (roll separating force) of the strip during simulation besides the computational time were considered. The analysis showed that for mesh size smaller than 0.28mm the thermo-mechanical response of the strip didn't change. However for higher amount of reductions and bigger roll diameters the mesh size was reduced to 0.1mm. Figure 5-5 shows the results.

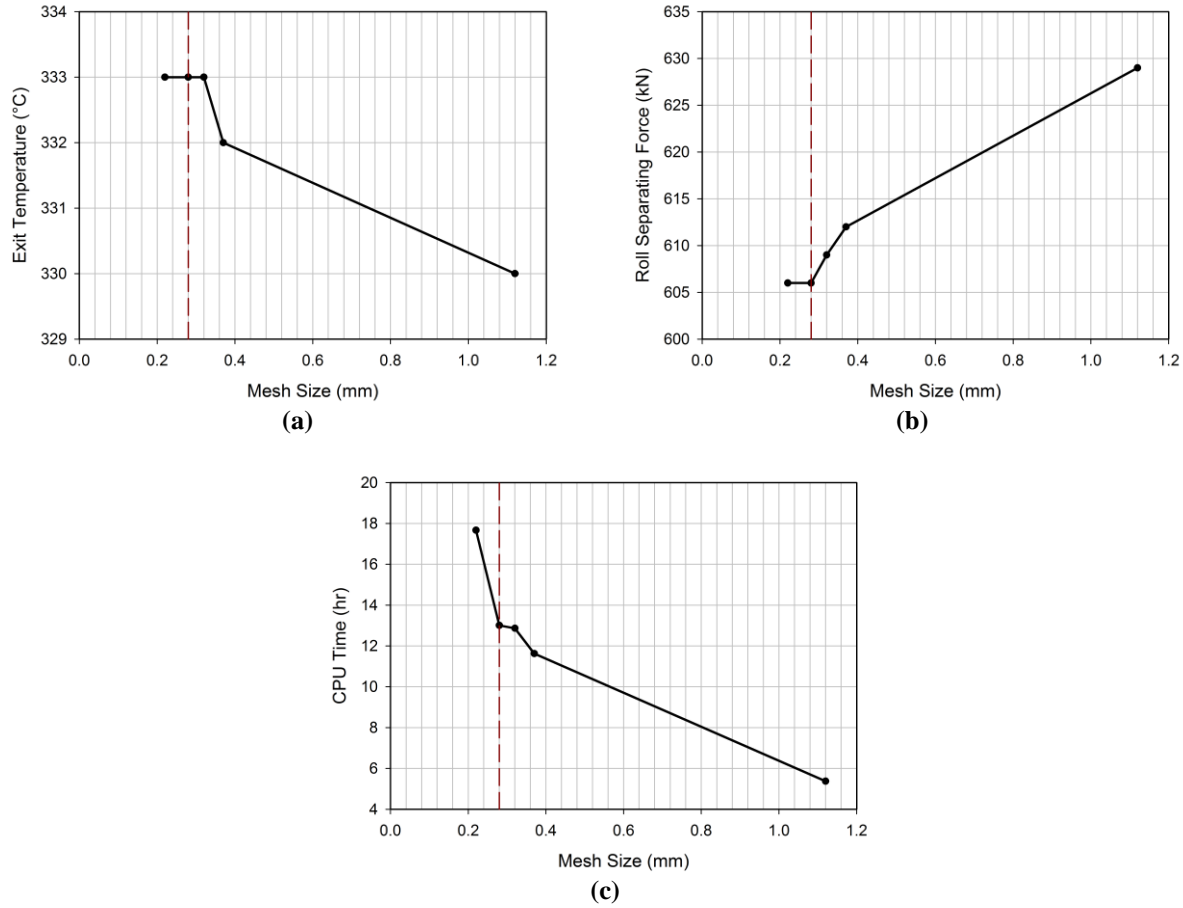


Figure 5-5- Mesh sensitivity analysis for a) strip exit temperature, b) roll separating force and c) computational time.

### 5.3 Material Properties

Thermo-physical properties of AZ31 magnesium alloy, used for the model in the current study, were available in the literature as shown in Table 5-1. In order to conduct a proper modeling of the TRC process, the non-equilibrium solidus and liquidus temperatures (Scheil cooling condition) were taken in account. So, the values reported by Hao *et al.* [122], generated by the computational thermodynamics database JMatPro, were chosen. The non-equilibrium (Scheil) fraction solid used for latent heat release calculation is shown in Figure 5-6. Table 5-2 and Figure 5-7 illustrate AZ31 Young's modulus and thermal

expansion coefficient as functions of temperature. Figure 5-8 represents the corresponding stress-strain curves for AZ31 magnesium alloy for different strain rates and temperatures.

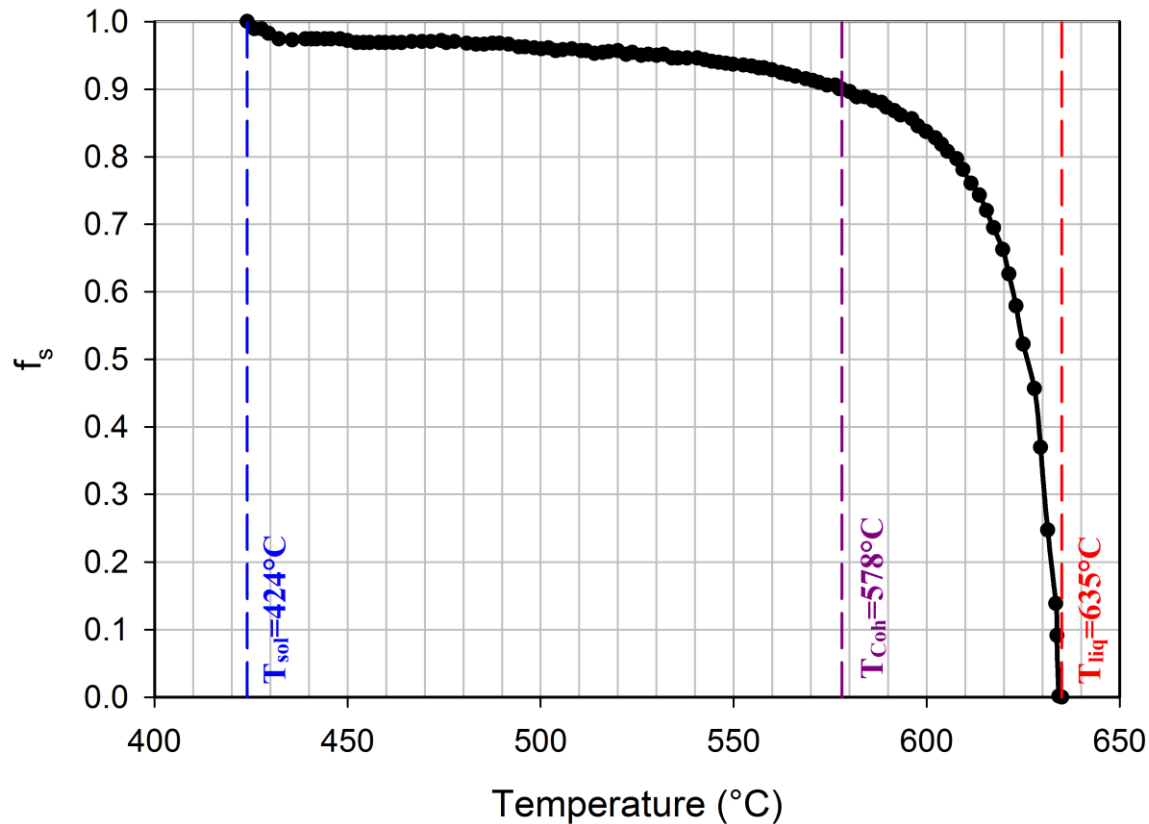


Figure 5-6- Non-equilibrium fraction solid (Scheil cooling condition) for AZ31 magnesium alloy, graph reproduced from Reference [122].

Table 5-1- Thermo-physical properties of AZ31 magnesium alloy

Property	Value/Function							
Density, $\rho$ (kg/m <sup>3</sup> ) [113]	1780							
Latent heat of fusion, $L$ (J/kg) [113]	340000							
Specific heat, $C_p$ (J/kg°C) [123]	$820 + (0.79 \times T) - ((3.6 \times 10^6) / (T - 255)^2)^*$							
Thermal conductivity, $k$ (W/m°C) [122]	50°C 83.9	100°C 87.3	200°C 97.0	250°C 101.8	424°C 118.5	630°C 60	635°C 120	680°C 240
Solidus, $T_{sol}$ (°C) [122]	424							
Liquidus, $T_{liq}$ (°C) [122]	635							
Coherency Temperature, $T_{Coh}$ (°C) [124]	578**							
Melting point of pure Mg, $T_f$ (°C) [123]	650							
Partition coefficient, $k$ [123]	0.2							

\* Temperature in Kelvin.

\*\* At a fraction solid of 0.9.

Table 5-2- AZ31 magnesium alloy Young's modulus [124]

Temperature (°C)	Young's modulus, $E$ (GPa)	Thermal expansion coefficient, $\beta$ (10 <sup>-6</sup> /C)
27	45	30.7
102	43	31.4
202	41	32.4
297	38	33.2
342	37	33.7
397	35.5	34.2
424	34.5	34.4
578	15	35.9
608	1	0
632	0	0

Table 5-3- Parameters represented in Equation (5-18) for AZ31 magnesium alloy [121]

Parameter	Temperature (°C)	Value
$K$	$T < 118$	$-0.0835T + 394.4$
	$394 > T \geq 118$	$-1.1639T + 521.76$
	$T \geq 394$	$-0.5761T + 316.62$
$n$	$T < 150$	0.38
	$T \geq 150$	$-0.0013T + 0.5769$
$m$	$T < 168$	$2.89 \times 10^{-5}T - 1.83 \times 10^{-3}$
	$T \geq 168$	$0.00042T - 0.0638$
$\dot{\varepsilon}_{P0}$	-	0.0001
$\varepsilon_{P0}$	-	0.002382

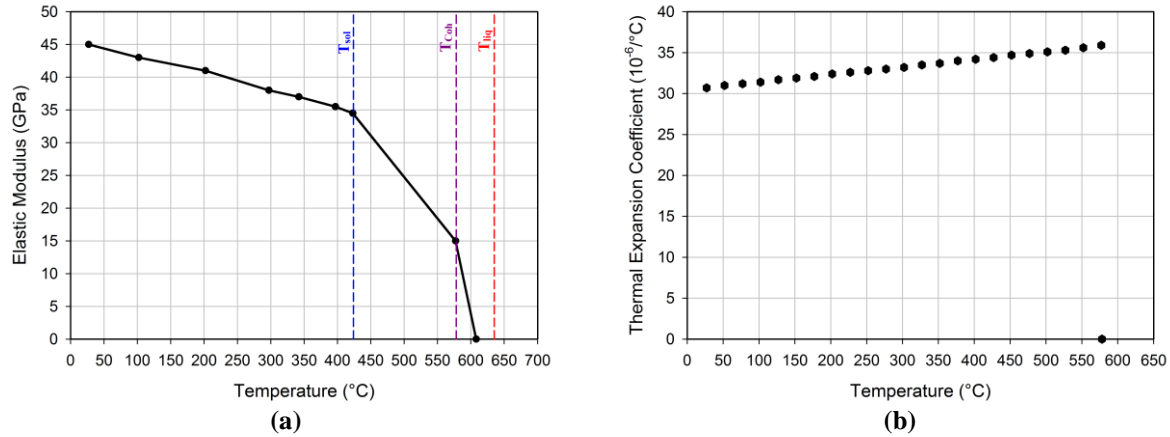


Figure 5-7- Temperature dependent a) elastic modulus and b) thermal expansion coefficient of AZ31 magnesium alloy [124].

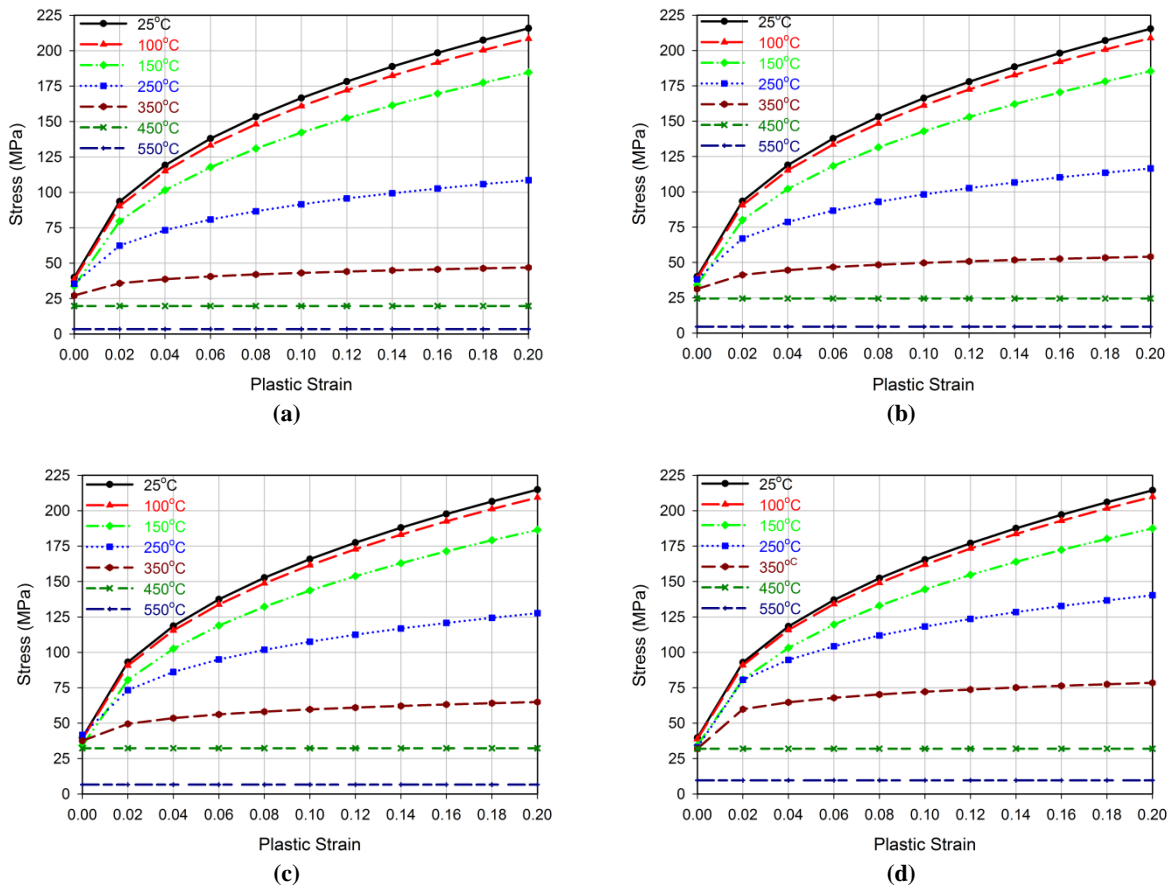


Figure 5-8- Stress-strain curves for AZ31 magnesium alloy for different temperatures and strain rates of a)  $0.0001\text{s}^{-1}$ , b)  $0.001\text{s}^{-1}$ , c) $0.01\text{s}^{-1}$  and d) $0.1\text{s}^{-1}$  [121].

## 5.4 Model Validation

Model validation is performed by comparing the predicted exit strip temperature and secondary dendrite arm spacing through the thickness with those measured at CanmetMATERIALS for strip cast using their TRC machine.

One of the most important and least well known boundary conditions for the twin roll casting process is the heat transfer coefficient (*HTC*) between the strip and roll surface. The *HTC* can be influenced by factors such as: roll texture and roughness, thermo-physical properties of the roll and strip material, pressure at the interface (roll pressure) and superheat of the molten metal entering the roll gap. As a first approximation the *HTC* during TRC was considered to be constant along the roll bite, which is an approach adopted by many other researchers [108, 110-113]. The *HTC* can then be adjusted to so that experimental measurements of the strip temperature are matched against model predicted ones [82]. In the current study, the *HTC* was fit against strip surface temperature measurements made 5cm from the exit point of the CanmetMATERIALS twin roll caster. Another method to validate the heat transfer part of the TRC model was to compare model predictions of the secondary dendrite arm spacing (SDAS) to those measured in the strip.

Figure 5-9 shows predicted temperature against measured ones for all trials using an  $HTC=11\text{kW/m}^2\text{ }^\circ\text{C}$  which indicate that the predictions are within 10% of the measurements. This procedure indicates that the optimum value for *HTC* for CanmetMATERIALS facility is  $11\text{kW/m}^2\text{ }^\circ\text{C}$ .

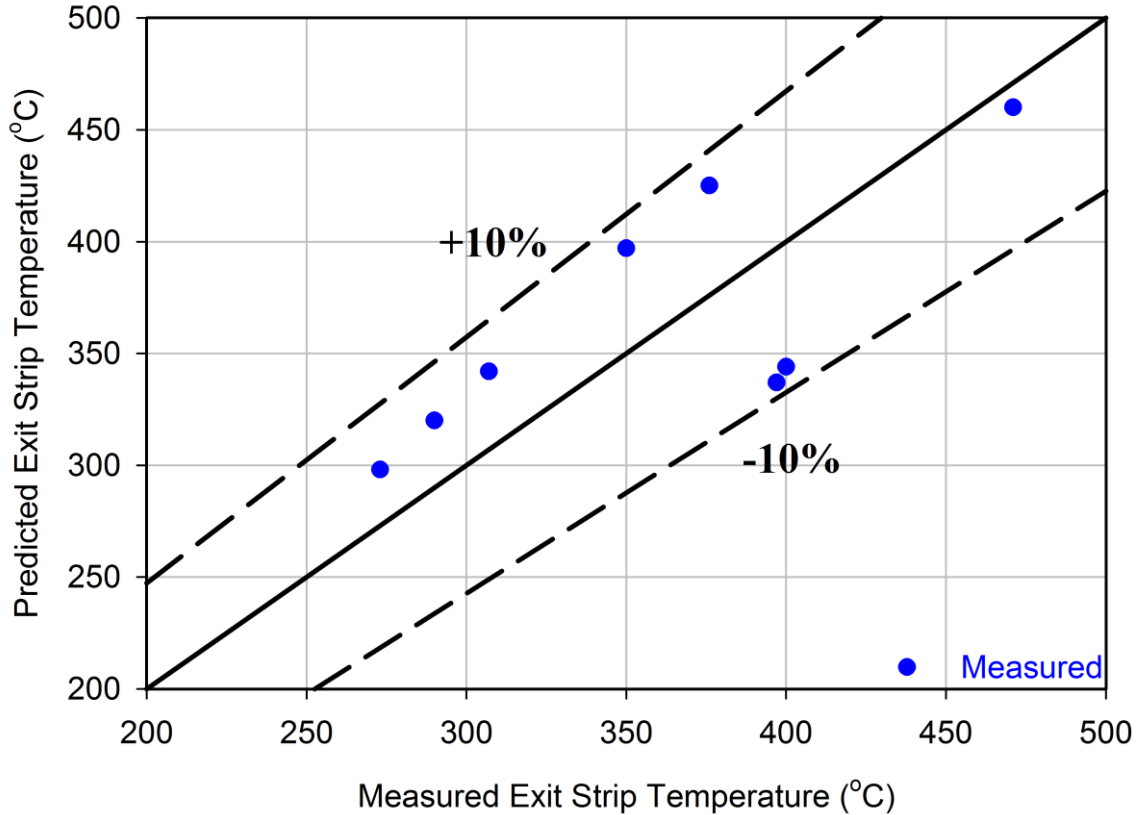


Figure 5-9- Comparison of predicted and measured temperature for the conditions shown in Table 4-1, using an  $HTC=11\text{kW/m}^2\text{°C}$ . The two dotted lines show  $\pm 10\%$  form the correct value.

The model predictions were also validated by comparing the predicted secondary dendrite arm spacing (SDAS) to those measured in the strip. Trials #3 and #4 (Table 4-1) are those used for microstructure study. By calculating the cooling rate at each position of the strip using the model predictions, the SDAS at each position is predicted. To do so, according to the work done by Allen *et al.* [125], Equation (5-20) is used to correlate SDAS and solidification cooling rate for AZ31 magnesium alloy for cooling rate ranges  $10^{-1}$  to  $10^6\text{°C/s}$ .

$$\lambda = 35.5R^{-0.31} \quad (5-20)$$

where  $\lambda$  is SDAS in  $\mu\text{m}$  and  $R$  is the averaged solidification cooling rate in  $\text{°C/s}$ .

Cooling rates used for SDAS predictions were calculated by considering an average solidification cooling rate at various positions through the thickness of the strip. Solidification time from the model at a discrete location was evaluated using Equation (5-21), which then is used to calculate the average cooling rate using Equation (5-22). Since 90% of solidification process is accomplished at the coherency temperature and the dendrites are characterized at this point, the averaged solidification cooling rate was calculated between liquidus and coherency temperature. The results were in agreement with the measurements.

$$t = \int_{x_0}^{x_1} \frac{dx}{v(x)} \quad (5-21)$$

$$R = \frac{T_{liq} - T_{Coh}}{t} \quad (5-22)$$

where  $t$  is the solidification time (in s),  $v(x)$  is the speed profile in the solidification range (in m/s) and  $x_0$  and  $x_1$  are the solidification start and end positions (corresponding to the positions of liquidus and coherency temperature in the temperature profile) (in m),  $R$  is the averaged cooling rate (in °C/s) and  $T_{liq}$  and  $T_{Coh}$  are liquidus and coherency temperature (in °C).

In Figure 5-10 the measured SDAS through thickness versus the predicted values are shown for two trials. For each trial two sets of results are presented; the first set shows the discrete individual measurements of the SDAS through the thickness and the second set shows the averaged values for SDAS at the top and bottom surfaces, center-line and quarter and three quarter positions. As observed, there is a fairly good agreement (within 20%) between the measured and predicted values. This validation procedure proved the liability and accuracy of the developed model.

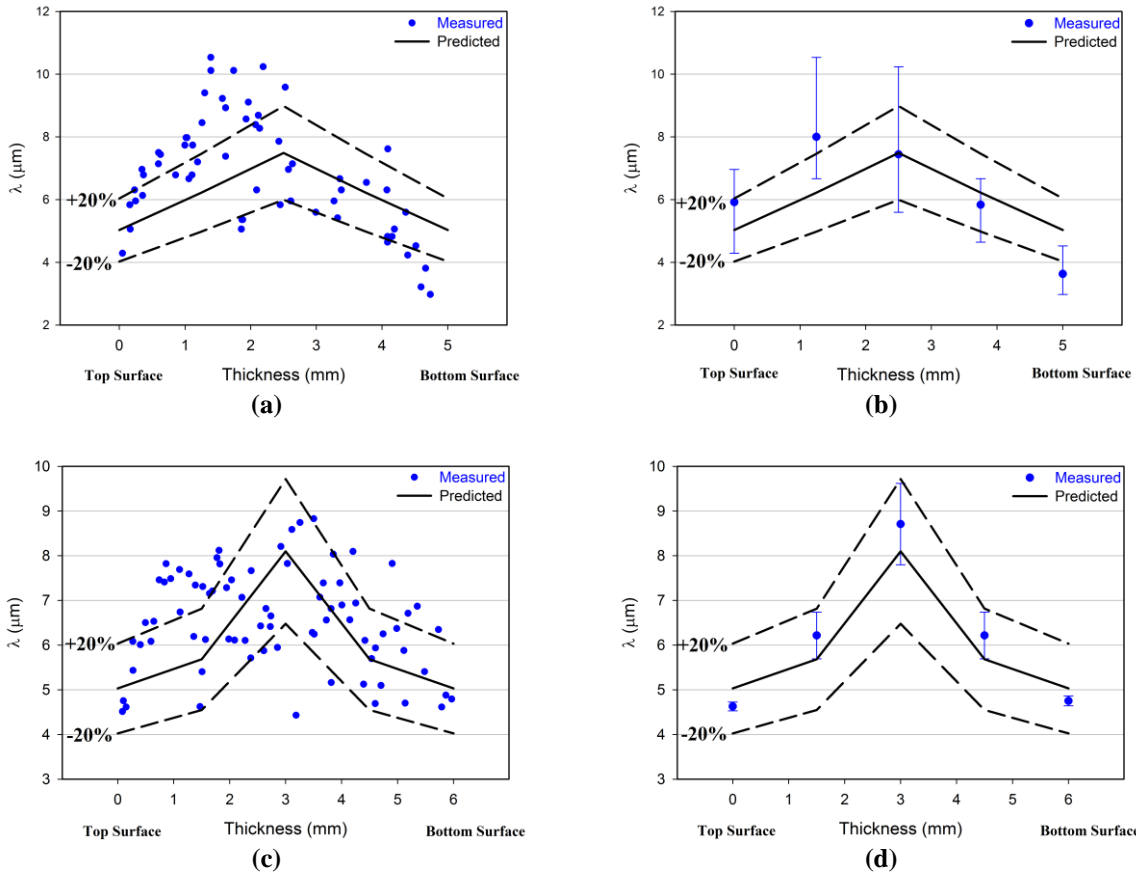


Figure 5-10- Predicted (solid lines) and measured (symbol) SDAS ( $\lambda$ ) through the strip thickness for a) trial #3 all data, b) trial #3 averaged data, c) trial #4 all data and d) trial #4 averaged data. The dotted lines show  $\pm 20\%$  from the model predictions.

## Chapter 6

### Microstructure Analysis Results

Figure 6-1 illustrates the surface quality of the twin roll cast AZ31 magnesium alloy strip for trial #3. At the middle-width of the strip some small cracks were observed on the surface. Close to the edges of the sheet but on the surface, the number of cracks and their length increases. Upon closer observation under an optical microscope it was observed that the central cracks are very shallow in depth and short in length so that grinding the samples eliminates them. On the other hand, the side cracks are deeply penetrated to the strip thickness and exist in two forms; open and close (isolated) cracks as shown in Figure 6-2.

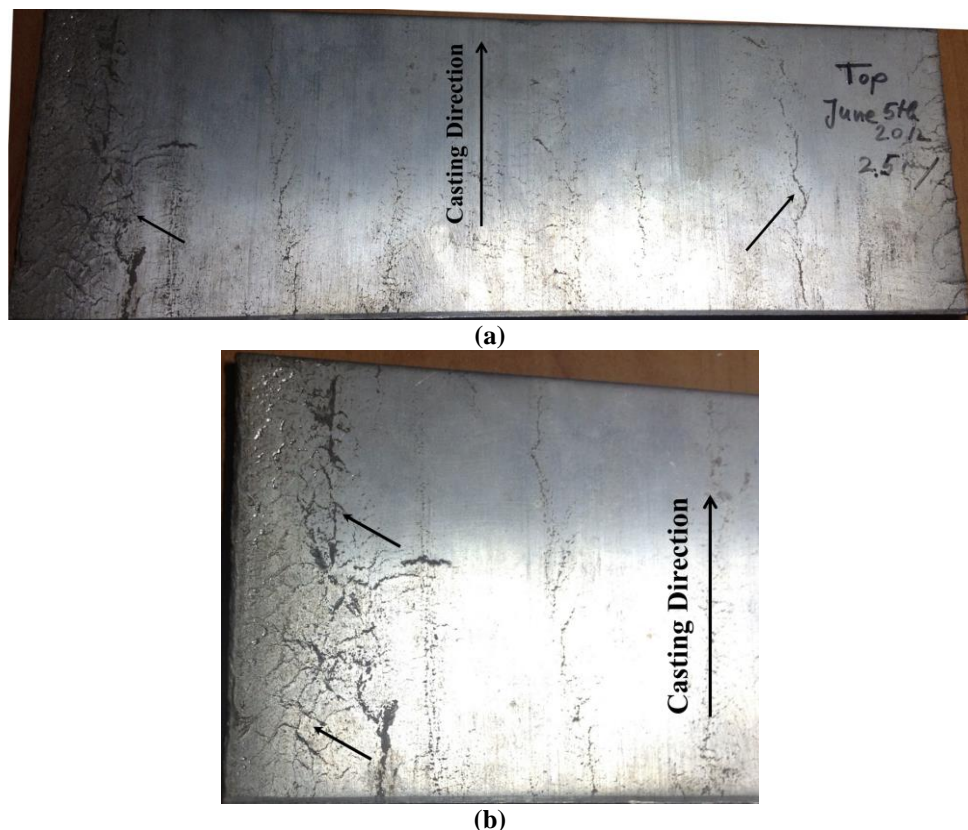


Figure 6-1- As-cast AZ31 twin roll cast strip surface quality a) the whole width and b) strip side, small black arrows show the cracks.

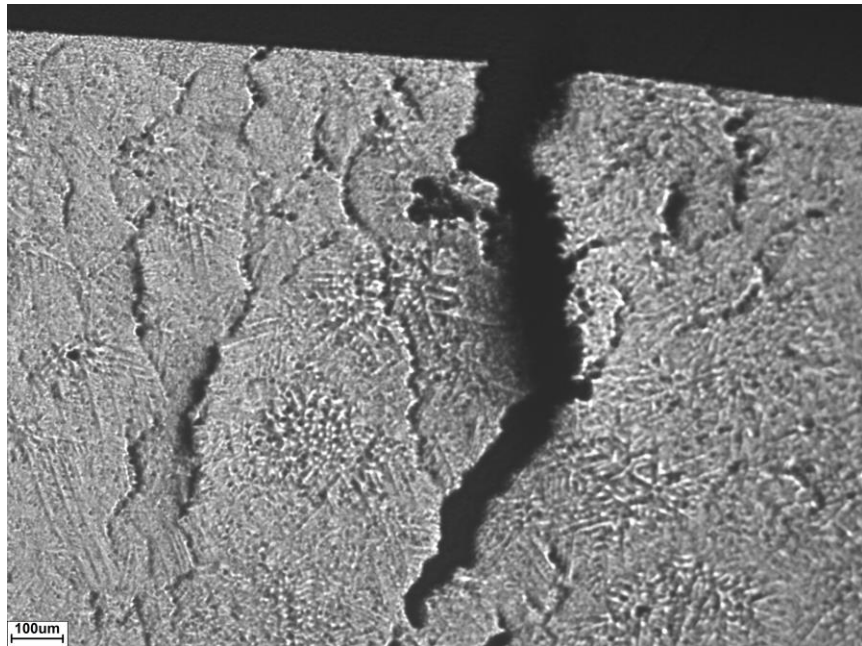


Figure 6-2- Optical image of the superficial cracks at the edge of the cast strip.

Figure 6-3 shows the as-cast microstructure of the twin roll cast AZ31 through the thickness. As expected, the microstructure near strip surface (top and bottom) comprises a chill zone due to high cooling rates achieved at the surface followed by an inclined columnar dendritic zone. At the strip surface an equiaxed zone exists.

Figure 6-4 shows more details on the microstructure of the AZ31 twin roll cast strip above the center-line of the strip. The black arrows on the microstructure illustrate the direction of the columnar dendrites growth. During TRC, the solidification of the liquid metal begins on the roll surface and proceeds toward the center-line. The heat transfer direction is perpendicular to the roll/strip interface. The rotation of the roll causes an inclination to the heat transfer path toward the exit region and consequently the dendrites grow in the direction shown by the arrows in Figure 6-4.

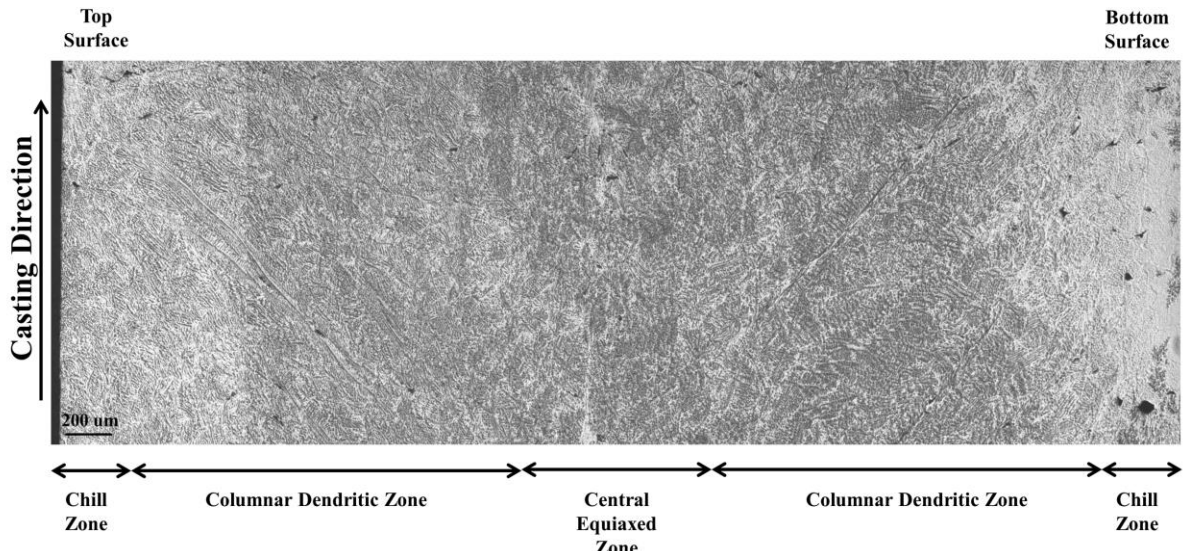


Figure 6-3- As-cast microstructure of twin roll cast AZ31 through thickness for trial #3.

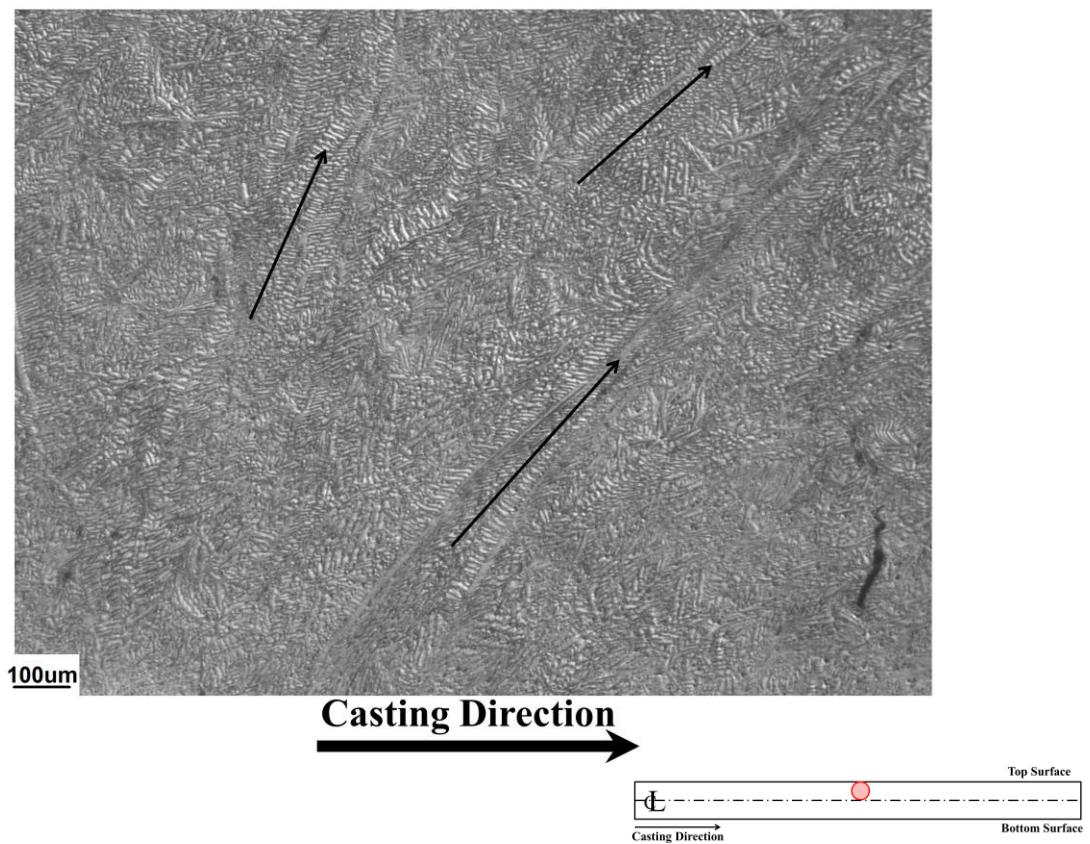
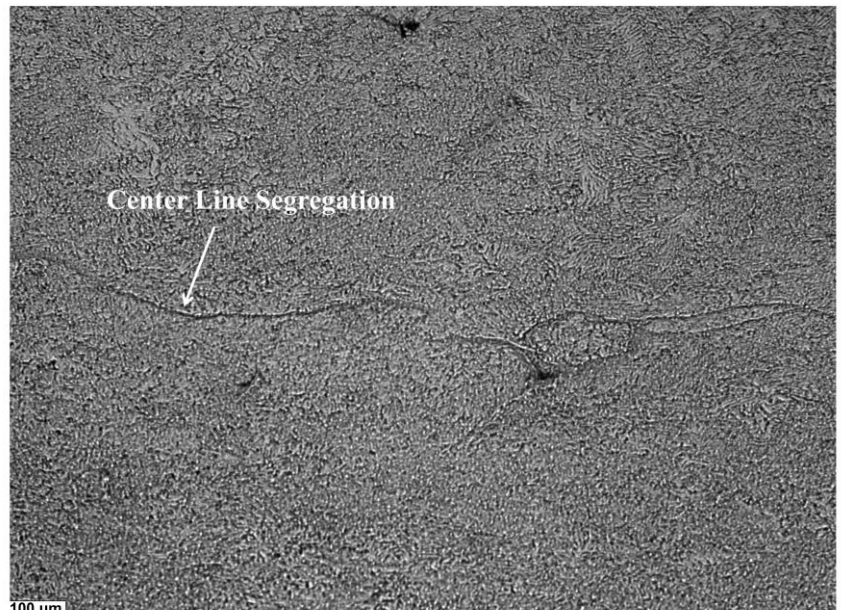


Figure 6-4- Optical image of microstructure of the strip above the center-line, the black arrows show the columnar dendrites growth direction, the red circle on lower legends shows where the sample has been chosen.

Center-line segregates are shown in Figure 6-5. Two possible morphologies have been observed for center-line segregation. Referring to Figure 6-5, both continuous and non-continuous segregates are formed at the central region of the AZ31 twin roll cast strip. A closer look to the center-line segregation reveals the microstructure of the segregated compound. As shown in Figure 6-6, regardless of continuity or discontinuity, the center-line segregates have an equiaxed microstructure while the surrounding zones have dendritic structure. It is mentioned previously that the solidification begins at the strip/roll interface and develops toward the central region by a dendritic morphology. Continuing the solidification, the solute element(s) is rejected to the remaining liquid in the mushy zone. Moreover, the possible inclusions (include magnesium oxide) also remain in the mushy zone. The unique “U” shape of the liquid sump in TRC causes the highest concentration of the solute element(s) and inclusion to be occurred at the center-line. Solute-rich remaining liquid is close to eutectic composition which tends to solidifies with equiaxed morphology. Moreover, the presence of inclusions as nucleation sites promotes equiaxed structure.

Figure 6-7 illustrates the SEM image of the center-line segregation for trial #3. The EDS analysis has been done in both defect area and the bulk material. The results are shown in Table 6-1. As observed, the amount of aluminum (as the main solute element) is 2.11 wt.% in the bulk material; while, in the center-line segregate area the amount of aluminum increases up to 4.17 wt.%. A same scenario is also observed for zinc; however, in the defect area as aluminum weight percent increases the zinc weight percent decreases.



(a)



(b)

Figure 6-5- Optical image of the center-line segregation a) continuous and b) non-continuous segregates.

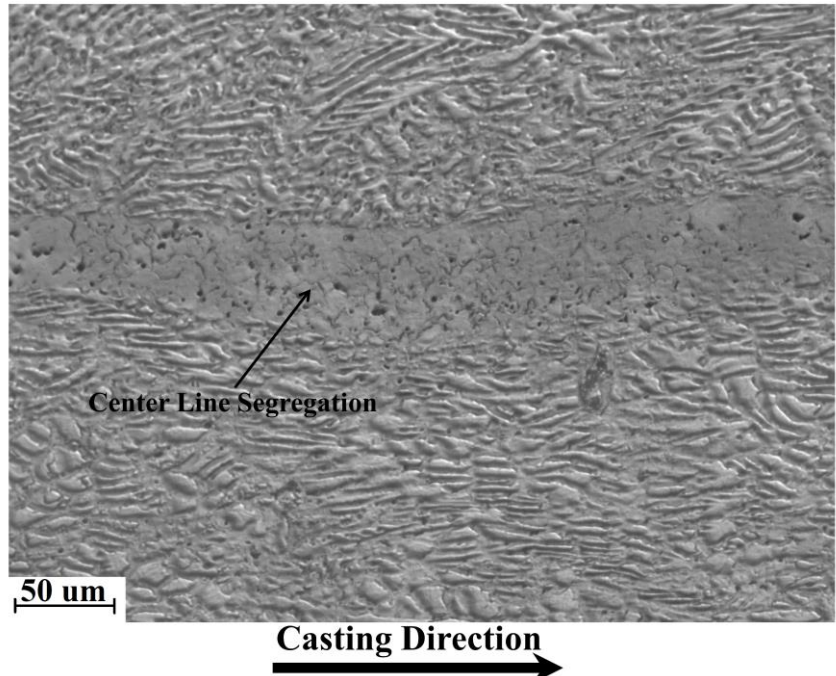


Figure 6-6- Optical image of the center-line segregation, the microstructure of the segregate is absolutely different with the surrounding area.

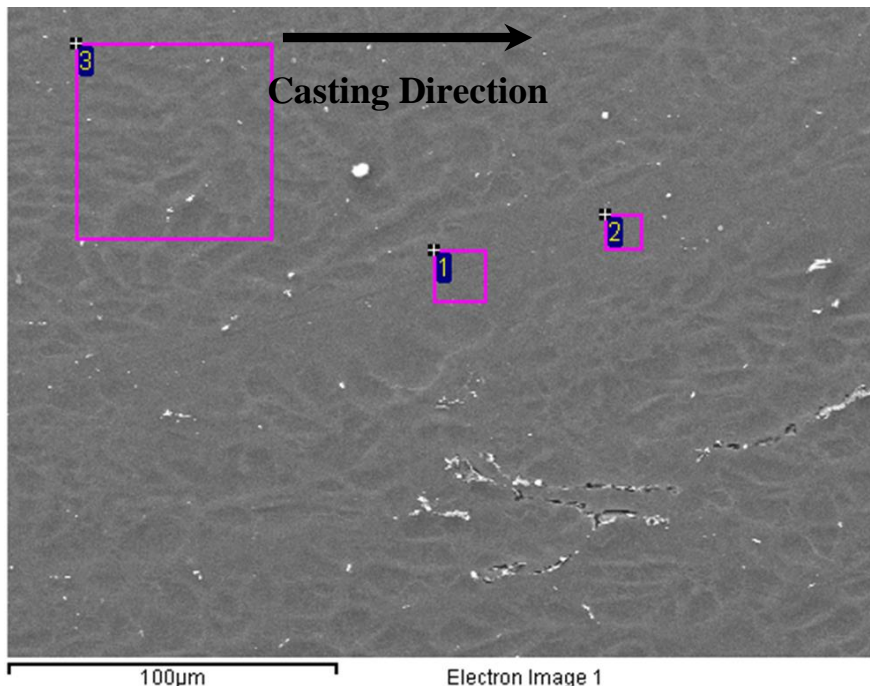


Figure 6-7- SEM image of the center-line segregation and the region of EDS analysis (points 1 and 2 are inside the center-line segregate and point 3 is inside the bulk material).

Table 6-1- The chemical composition analysis corresponding to Figure 6-7

Spectrum	In stats.	Mg	Al	Zn	Total
1	Yes	95.13	4.17	0.70	100.00
2	Yes	94.56	3.33	2.11	100.00
3	Yes	97.42	2.11	0.46	100.00

Figure 6-8 shows the optical image of an isolated inverse segregate on the bottom surface of the AZ31 twin roll cast strip. Similar to center-line segregation, this defect also appears with equiaxed morphology. However, the size of the grains is quite larger than the center-line segregates. Apparently, during squeezing stage of the liquid metal, the inclusions were trapped in the dendritic path and consequently the nucleation sites were eliminated on the surface. Therefore, larger grains formed in the inverse segregates. In Figure 6-9 the inverse segregate is shown with a higher magnification. The black arrows show the inter-granular cracks; these cracks form due to contraction occurrence at the last stage of solidification. Presence of these cracks could lead to damages and defects in the post-rolling procedures.

Figure 6-10 illustrates the SEM image of the inverse segregation and the points of EDS analysis. The results of chemical composition analysis are shown in Table 6-2. As expected, the concentration of the main solute (Al) is higher in the inverse segregate zone; 4.5 wt.%.

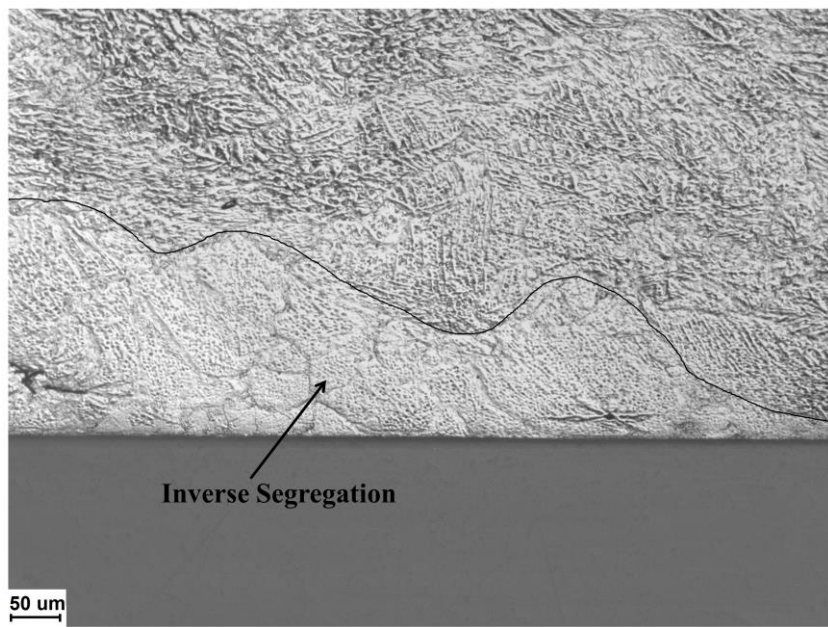


Figure 6-8- Optical microstructure of the inverse segregation on the bottom surface of the strip.

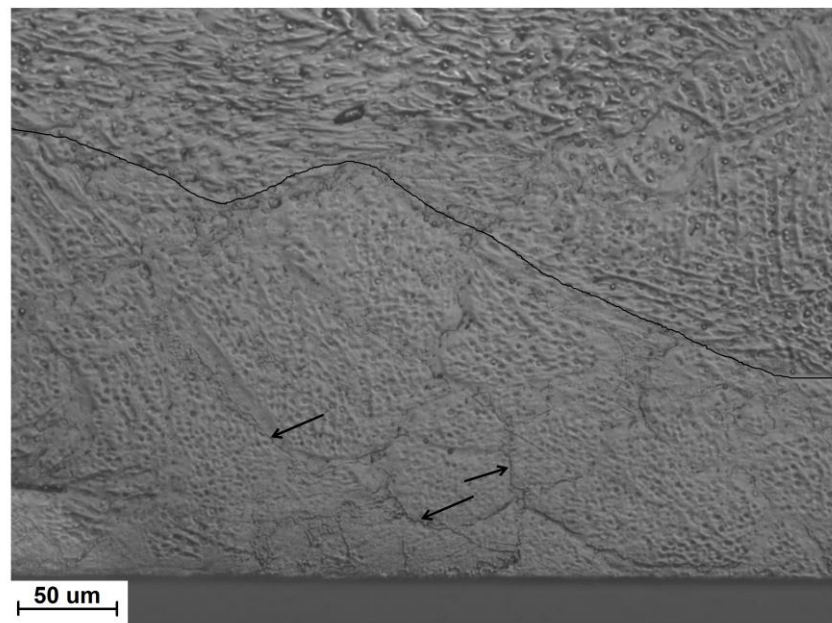


Figure 6-9- Inter-granular cracks in the inverse segregate region.

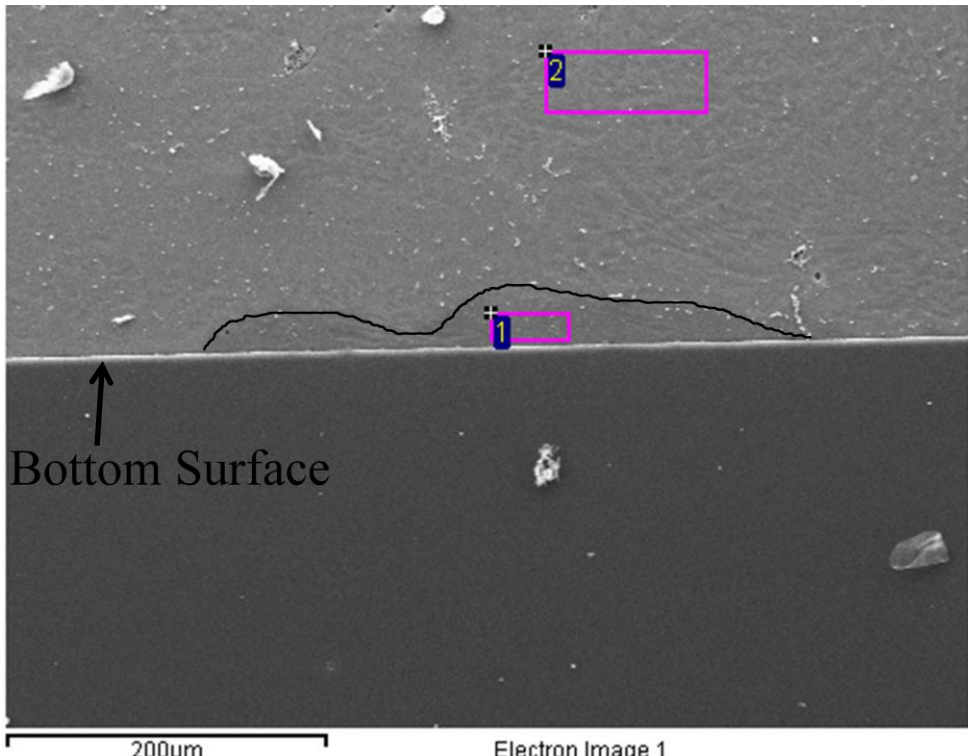


Figure 6-10- SEM image of the inverse segregation and the region of EDS analysis (point 1 is inside the inverse segregate and point 2 is inside the bulk material).

Table 6-2- The chemical composition analysis corresponding to Figure 6-10

Spectrum	In stats.	Mg	Al	Zn	Total
1	Yes	93.27	4.50	2.23	100.00
2	Yes	97.10	2.51	0.39	100.00

## Chapter 7

### Thermal-Fluid Model Application

In this chapter, the results obtained by applying the thermal-fluid model developed in ANSYS® CFX® are reviewed. Since the *HTC* along the arc of contact is the most complicated boundary condition in TRC modeling, this is a key parameter that is used throughout the analysis to assess the sensitivity of the model predictions to his value. The effect of casting parameters such as speed, set-back distance and strip thickness on the thermal and microstructure evolution in the strip is elucidated.

#### 7.1 Biot Number Analysis

In order to conduct a quantitative analysis on heat transfer and process sensitivity to the *HTC*, a Biot number analysis was performed. The Biot number is a dimensionless number applied for conduction problems include surface convection effect. This number reveals the relation between resistance to conduction within the bulk material and resistance to convection across the surface [126], as shown in Equation (7-1).

$$Bi = \frac{R_{cond}}{R_{conv}} = \frac{(L/kA)}{(1/hA)} = \frac{hL}{k} \quad (7-1)$$

where  $Bi$  is the Biot number,  $R_{cond}$  and  $R_{conv}$  represent resistance to conduction and convection, respectively,  $h$  is the heat transfer coefficient at the surface of the quenched sample (in  $\text{W}/\text{m}^2\text{°C}$ ),  $L$  the characteristic dimension of the material being cooled (in this case, the thickness of the solidifying strip in the roll) (in m) and  $k$  the thermal conductivity of the material being quenched (in  $\text{W}/\text{m°C}$ ). There are three possible situations for  $Bi$ ; if  $Bi \ll 1$ , the resistance to conduction across the bulk material is less than the resistance to convection along surface, so temperature distribution in bulk material is much more uniform than the surface. In other words, heat transfer is dominated externally. In this situation the heat

transfer coefficient on the surface (*HTC*) plays a significant role in heat transfer. For  $Bi \gg 1$ , there is a contrary condition, where the temperature distribution along the surface is much more uniform than bulk, which means heat transfer is dominated internally by thermal conductivity. For  $Bi = 1$ , where heat transfer due to conduction and heat transfer due to external convection are equal, heat transfer dominates both internally and externally.

For the analysis, the thermal conductivity was considered to be  $45\text{W/m}^{\circ}\text{C}$  for magnesium as this is representative of the thermal conductivity of magnesium in the liquid state. The *HTC* was chosen in the range of  $2\text{-}20\text{kW/m}^2\text{C}$ , the entry height was assumed to be 12mm and final thickness of 4 and 8mm were studied. Referring to Figure 7-1, it appears that for high heat transfer coefficients ( $>8\text{kW/m}^2\text{C}$ ) the process will initially be dominated internally. As the thickness of the strip changes in the roll bite and is reduces the process switches over to being dominated externally. The transition point, where internal domination switches to external domination, moves to the right hand side by increasing the exit thickness, which means thicker exit thickness causes the strip to be dominated internally in a longer period of time. For lower heat transfer rates of  $4\text{kW/m}^2\text{C}$ , throughout the roll bite the process is dominated externally along the whole roll bite region.

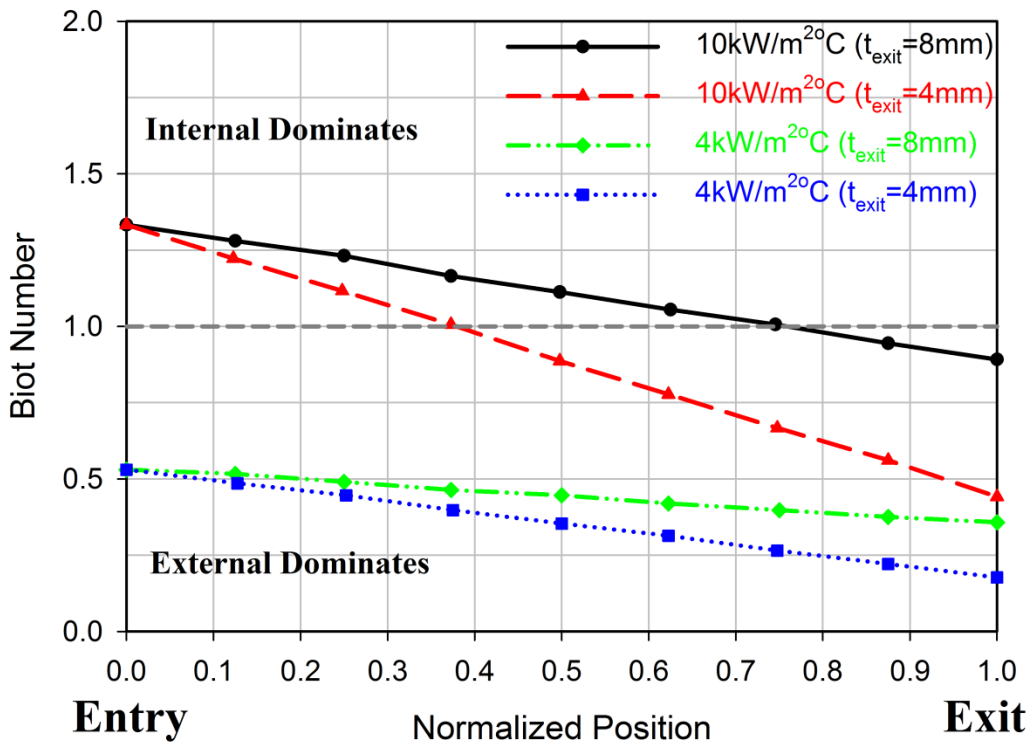


Figure 7-1- Variation of the Biot number along the roll bite during TRC showing the effect of heat transfer coefficient and strip exit thickness.

## 7.2 Effect of Casting Conditions on Thermal-Fluid History of the Strip

The casting conditions used in this part of the study to model the TRC process for AZ31 magnesium alloy are shown in Table 7-1. A total of 54 simulations were run under a range of conditions. The aim of the modeling is to assess the effect of casting speed, final thickness and heat transfer coefficient (*HTC*) at the roll/stripe interface on the thermal history and microstructure evolution of the cast stripe. The final thickness affects the set-back distance ( $\ell_1$  in Figure 5-1) which is an important parameter in controlling the twin roll casting process. Set-back (*SB*) for the TRC process is calculated using Equation (7-2).

$$SB = \ell_1 = \sqrt{R\Delta h - 0.25\Delta h^2} \quad (7-2)$$

where  $R$  is the roll radius (in mm) and  $\Delta h$  is the reduction (the difference between entry and exit thickness) (in mm).

Table 7-1- Casting conditions employed in the current study for the thermal-fluid model

Casting Temperature (°C)	Entry Height (mm)	Exit Thickness (mm)	Set-Back Distance (mm)	Heat Transfer Coefficient (kW/m <sup>2</sup> °C)	Casting Speed (m/min)*
677	12	4	37.5	11, 13 & 15	0.5, 1.0, 1.7, 2.0, 2.5 & 3.0
		5	35.1		
		6	32.5		

\* The modeling results revealed that casting speed of 0.5m/min leads to failure for all final thicknesses and heat transfer coefficients due to nozzle blocking (solidification inside the nozzle). So, for the rest of the study casting speed of 0.5m/min was excluded.

The effect of casting speed, *HTC* and exit thickness on the thermal history in the strip during TRC was studied. Thermal history was studied in terms of temperature gradient through the thickness of the strip at the exit region, sump depth at the center-line ( $\ell_2$  in Figure 5-1), mushy zone thickness ( $\ell_3$  in Figure 5-1) and averaged cooling rate at different positions in the strip. The cooling rate was then correlated to the predicted microstructure evolution in terms of the secondary dendrite arm spacing (SDAS).

The experimental trials suggested that it is not necessary to obtain a fully solid strip at the exit point of the caster; once the strip temperature reaches the coherency temperature at which the solidified material could develop stress (this temperature is between liquidus and solidus temperature, so it shows the fraction solid at which the mushy material acts as a fully solid material in stress development) and a fully coherent strip exit the caster, the process is conducted successfully. So, in the current study the criterion for an acceptable casting condition was determined based on the coherency temperature not solidus temperature. Consequently, the liquid sump depth ( $\ell_2$ ) was considered as the distance between the nozzle entry and coherency temperature position at the center-line and the mushy zone thickness

$(\ell_3)$  was calculated as the distance between liquidus and coherency temperature position at the center-line.

### 7.2.1 Exit Strip Temperature and Temperature Gradient through Thickness

As the molten material enters the roll bite and is in contact with the roll surface, the temperature at the surface of the strip drops rapidly to the liquidus temperature and solidification starts. Continuing along the arc of contact, more heat is extracted from the material as it fully solidifies and then heat is conducted from the solid strip to the roll surface. As more heat is extracted from the strip to the rolls, a lower temperature at the surface of the exit strip is obtained. The model predicted exit strip surface temperature for different casting speeds and final thicknesses is shown in Figure 7-2. As expected, increasing the casting speed causes less time for heat transfer from the strip to the roll and as a consequence the overall amount of heat extracted from the strip is reduced. Moreover, decreasing the final exit thickness of the strip provides a longer set-back distance (Equation (7-2)) and longer arc of contact which then leads to more heat transfer from the cast material to the roll. As observed in Figure 7-2, the sensitivity of the process to the final thickness in terms of exit temperature is more significant at higher casting speeds; the difference between exit temperature for final thicknesses of 4 and 6mm at 1.0m/min is 85°C and at 3.0m/min is 153°C. Similar trends were observed for  $HTC$  values of 13 and 15kW/m<sup>2</sup>°C. However, the predicted exit temperature became more sensitive to the final thickness for higher casting speeds at higher heat transfer coefficients; i.e. 50°C and 171°C difference in exit temperature for thicknesses of 4 and 6mm at 1.0m/min and 3.0m/min, respectively (for  $HTC=15$ kW/m<sup>2</sup>°C). Besides showing the heat transfer behavior of the caster, the exit strip surface temperature is a helpful parameter in controlling the dynamic recrystallization and grain growth experienced by the twin roll cast strip. At higher temperatures, dynamic recrystallization is more likely to occur if there is sufficient strain energy in the strip, followed by grain coarsening if enough heat is retained in the strip [38].

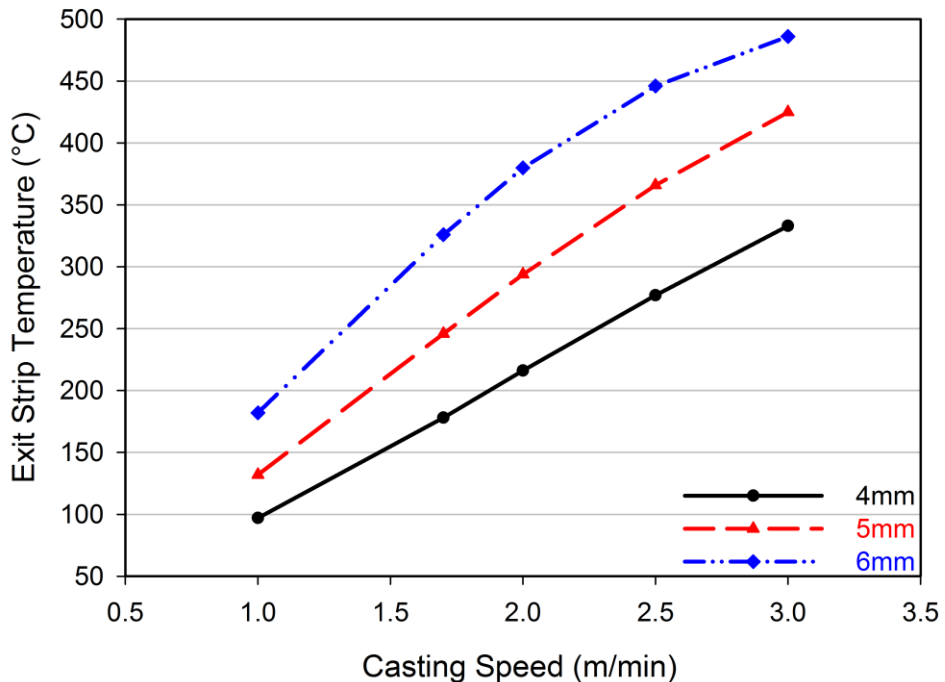
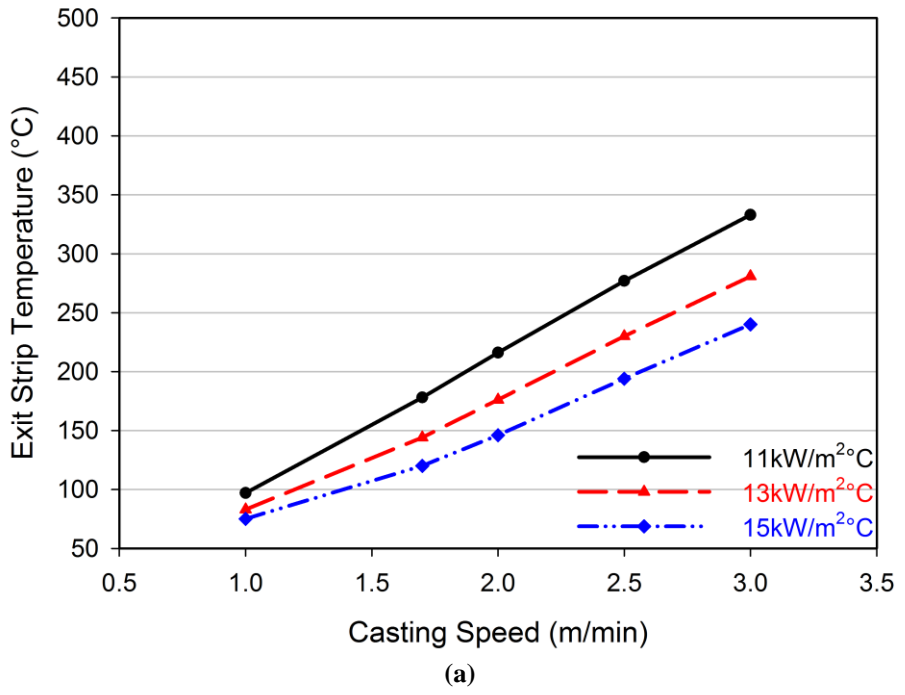
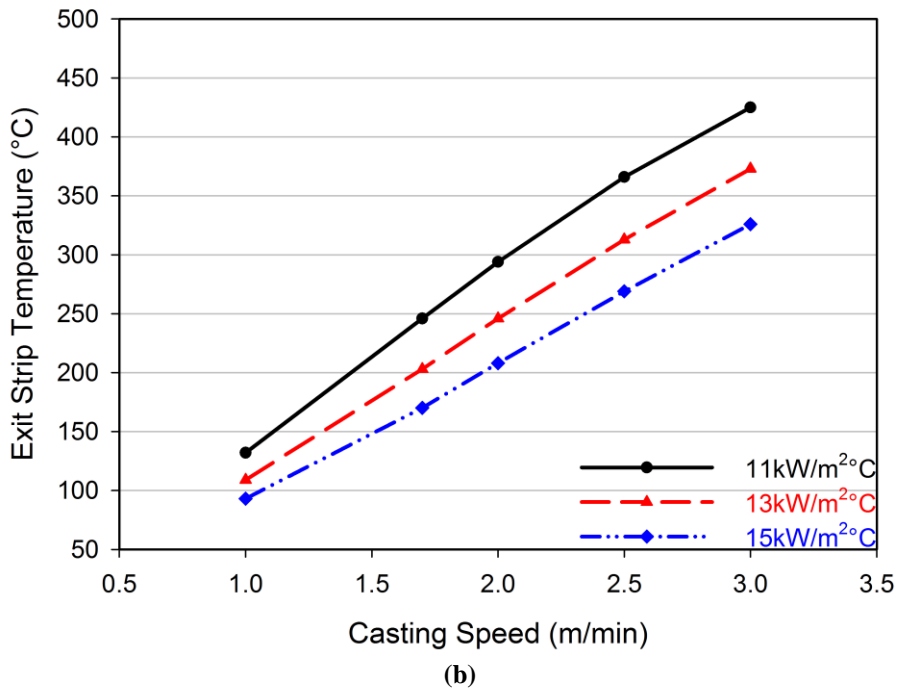


Figure 7-2- Model-predicted effect of casting speed and final thickness on the surface temperature of the exit strip using an  $HTC=11\text{kW/m}^2\text{°C}$ .

Figure 7-3 shows the influence of heat transfer coefficient on the exit strip temperature for a final strip thicknesses of 4, 5 and 6mm cast under different casting speeds. As expected, as the heat transfer coefficient is increased, the exit strip temperature is decreased for a given casting speed. Quantitative knowledge of the thermal history is imperative as the solidification structure and amount of deformation that occurs during TRC, as well as the final microstructure through the strip thickness are dependent on it.



(a)



(b)

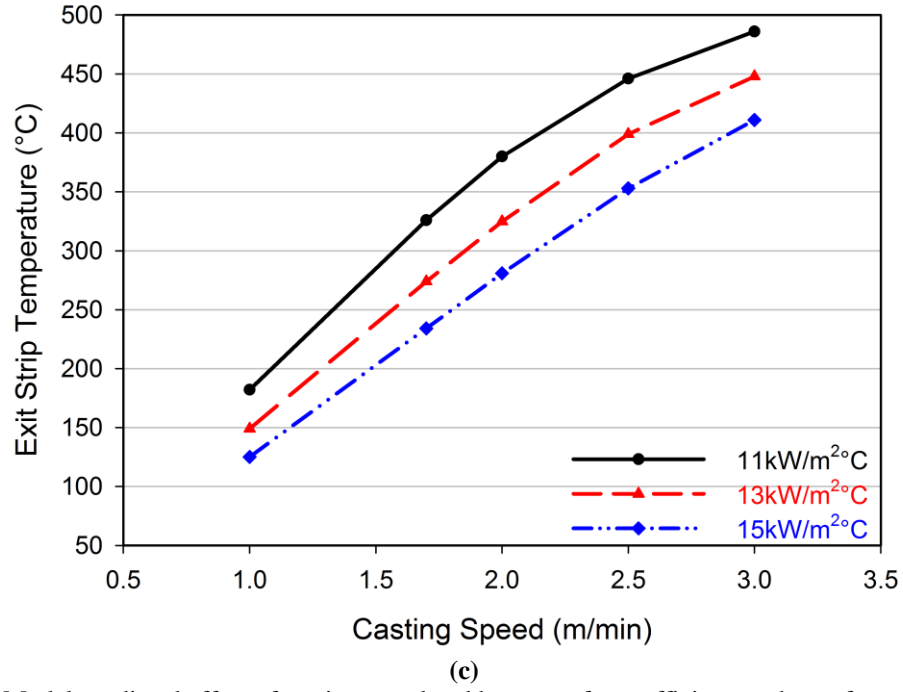


Figure 7-3- Model-predicted effect of casting speed and heat transfer coefficient on the surface temperature of the exit strip for an exit strip thickness of a) 4mm, b) 5mm and c)6mm.

In addition to the strip surface temperature at the twin roll caster exit, the temperature gradient at the exit region, i.e. the difference between strip surface and center temperature is another important parameter. Sahai *et al.* [87] and Saxena *et al.* [88] believe a higher temperature gradient (at the exit) induces higher stress through the thickness which increases the probability of crack formation in the solidified strip. As illustrated in Figure 7-4 a larger temperature gradient is predicted as the casting speed increases. Moreover, there is a stronger dependency on casting speed for thicker exit strips. As expected, thicker exit strips experience a larger temperature gradient at the twin roll caster exit for the same casting speed. In contrast with the surface exit temperature, the temperature gradient was not observed to be sensitive to the heat transfer coefficient for final thicknesses of 4 and 5 mm. For the final thickness of 6mm at casting speeds of 2.5 and 3.0m/min, the temperature gradient was predicted to be more sensitive to the heat transfer coefficient for the conditions

studied. Referring to the Biot number analysis, as strip thickness increases less uniform temperature distribution in the bulk material achieved which leads to a larger temperature gradient. It was observed that for thinner strips the external heat transfer domination reaches in a shorter distance which eventually causes more uniform temperature distribution along strip thickness.

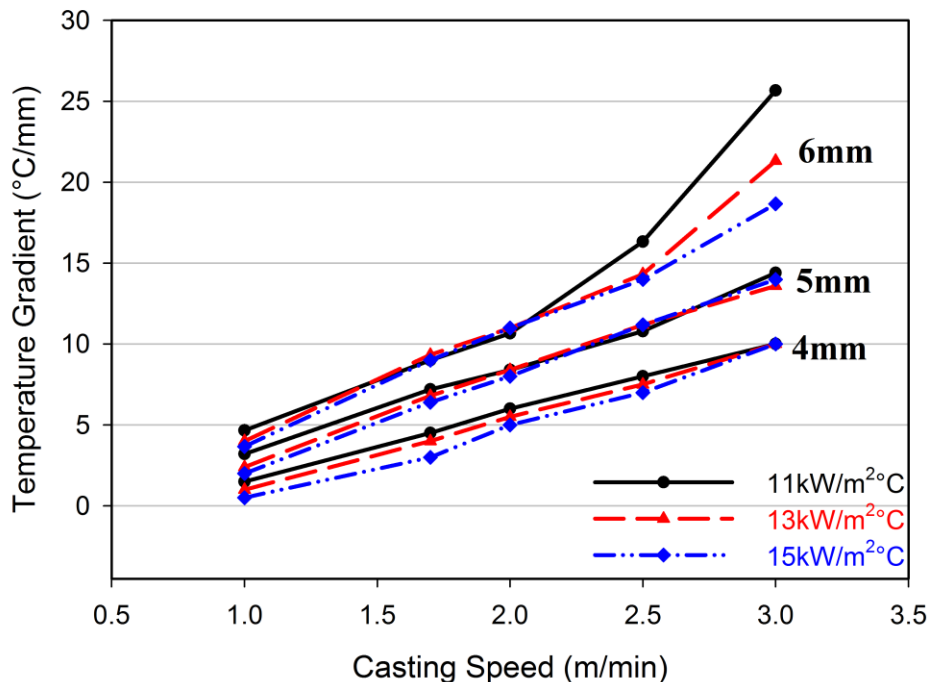
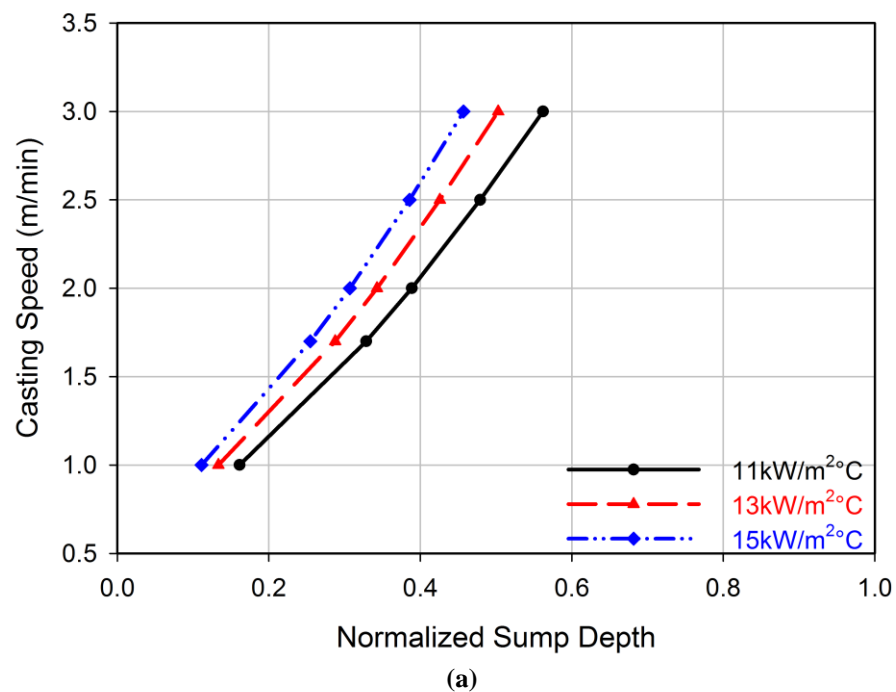


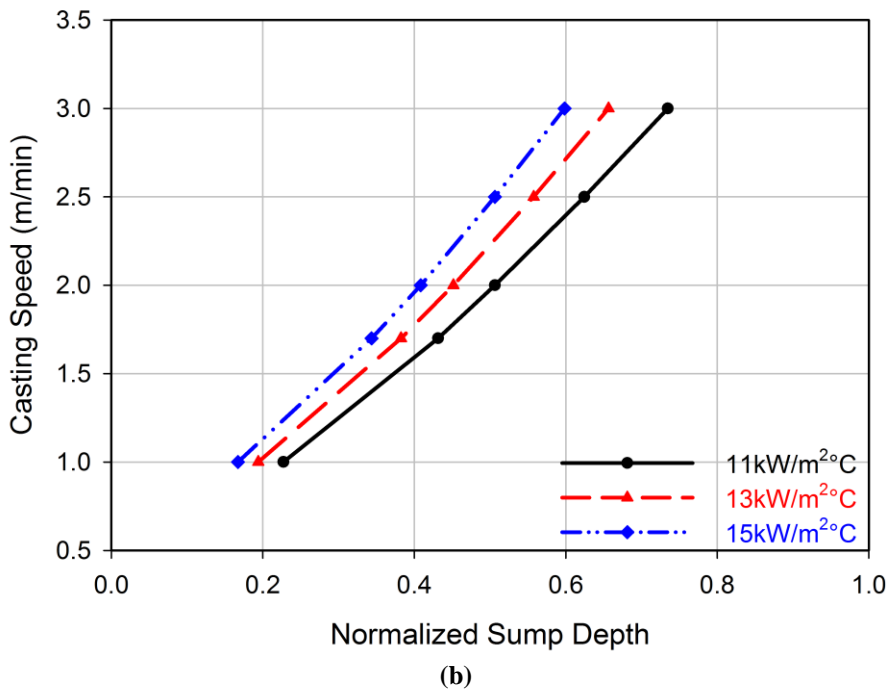
Figure 7-4- Model-predicted temperature difference between strip surface and center for different casting speeds, exit strip thicknesses and *HTCs*.

### 7.2.2 Sump Depth and Mushy Zone Thickness

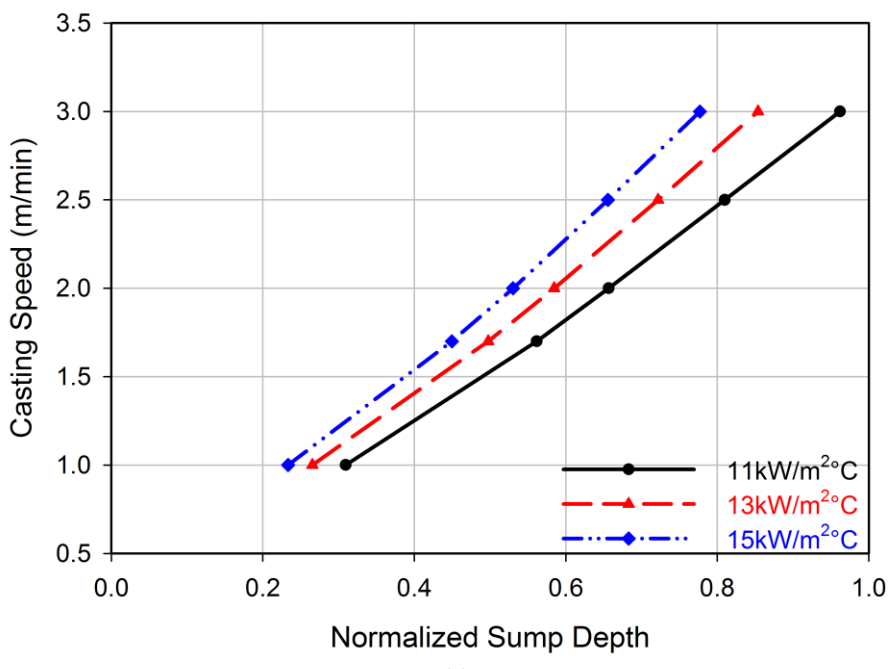
The effect of casting speed and *HTC* on the sump depth within the TRC process for different exit strip thicknesses is shown in Figure 7-5. As the position of the solidification front moves closer to the exit of the TRC at higher casting speeds the strip will undergo less plastic deformation as a consequence of the rolling process. As expected, increasing the *HTC* caused the solidification front to move further away from the exit point. Similar to the exit strip

temperature, as the casting speed increases, the process becomes more sensitive to the *HTC*. Moreover, increasing the final thickness causes the solidification front to move closer to the exit region, significantly at high casting speeds.





(b)



(c)

Figure 7-5- Model-predicted liquid sump depth for a final strip thickness of a) 4mm, b) 5mm and c) 6mm.

The mushy zone thickness at the center-line ( $\ell_3$  in Figure 5-1) also is affected by the casting parameters as shown in Figure 7-6. While increasing the casting speed causes a shift in the solidification front position, simultaneously the depth or width of the mushy zone increases. As expected, a deeper mushy zone is predicted when casting the thicker strips. The studies done by Yun *et al.* [28] and Gras *et al.* [33] suggest the center-line segregation formation for twin roll cast aluminum alloys is more frequent when a deeper sump ( $\ell_2$ ) occurs; more solute rich molten material is formed in deeper mushy zones which promotes the formation of this defect.

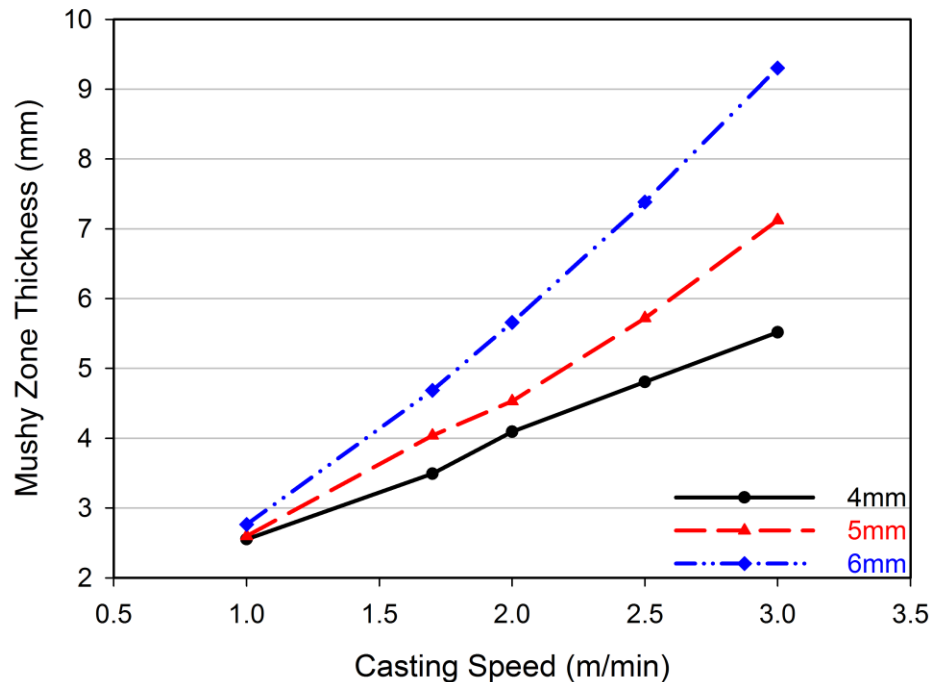
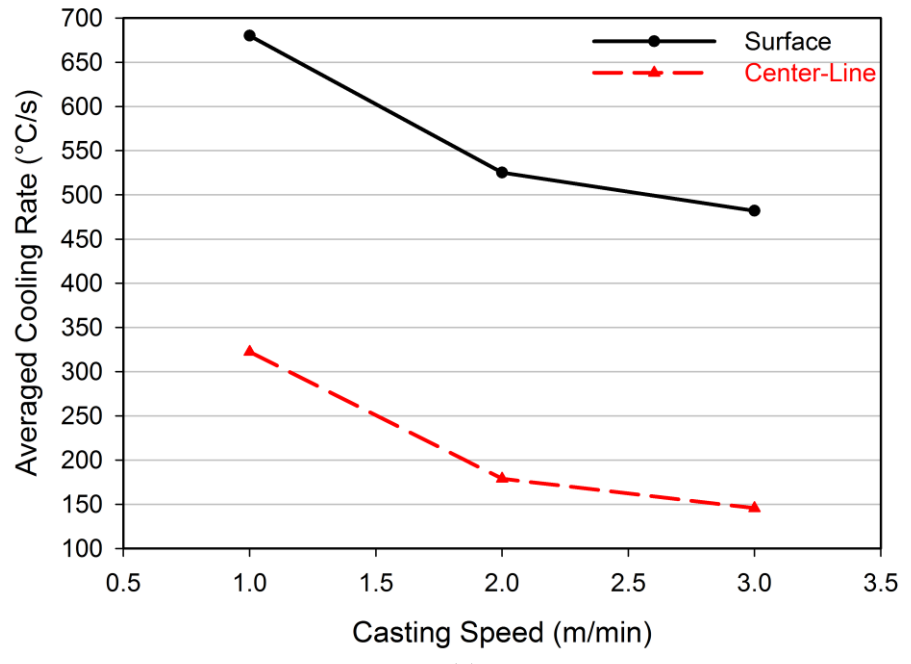


Figure 7-6- Model-predicted mushy zone thickness for  $HTC=11\text{kW/m}^2\text{C}$  and different exit strip thickness.

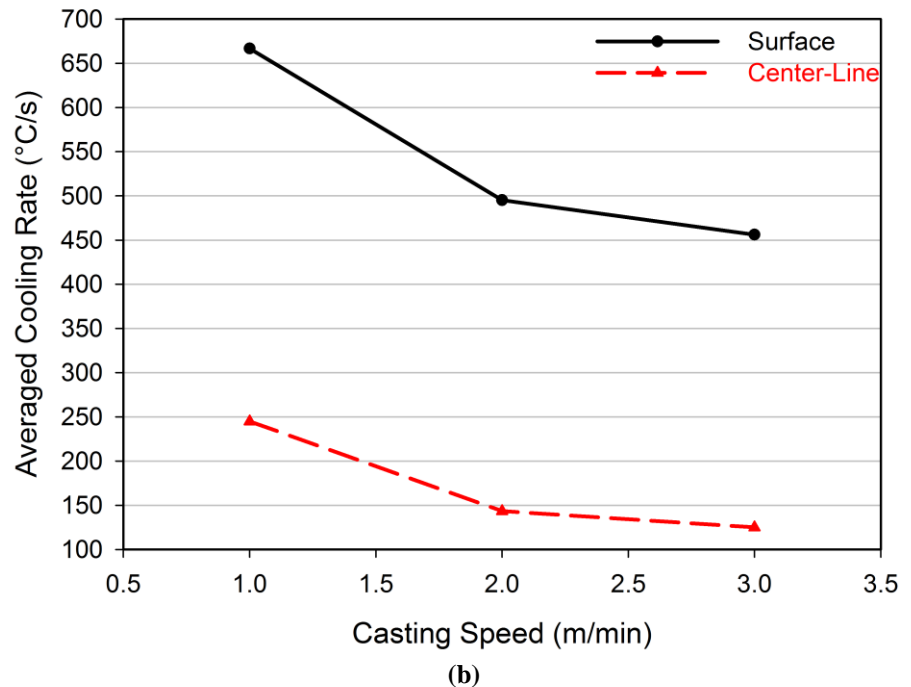
### 7.2.3 Microstructure Uniformity

The microstructure of a twin roll cast material is directly affected by the thermal history experienced during the solidification period from the liquid phase through to final solidification. A comprehensive understanding of the solidification cooling rate is helpful in predicting the final microstructure of the material including features such as the Secondary Dendrite Arm Spacing (SDAS). As described in Chapter 5, the averaged solidification cooling rate can be calculated using details of the flow field or the velocity profile at each position of the strip.

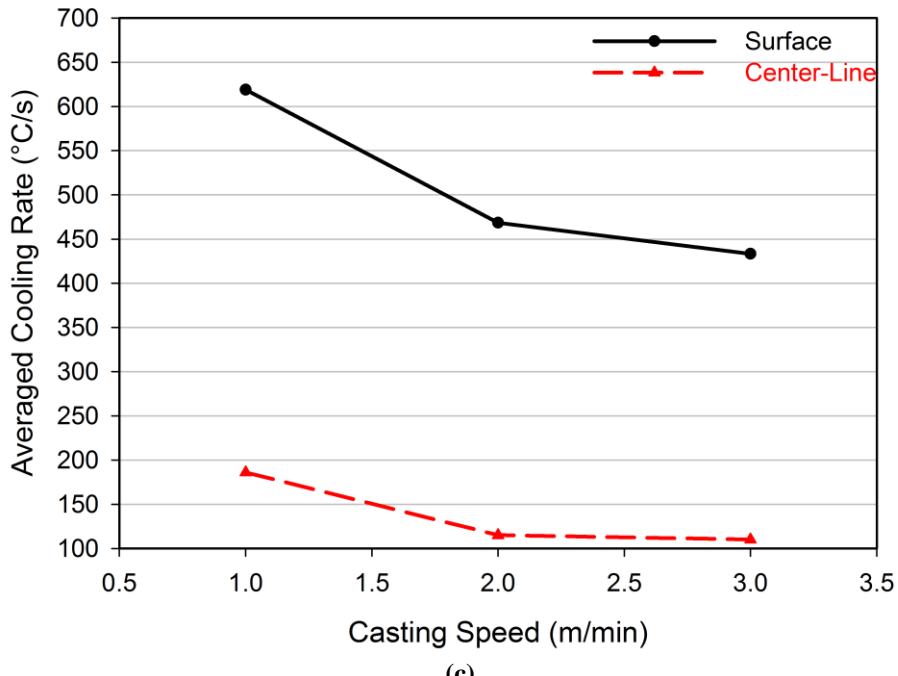
Figure 7-7 shows the predicted effect of casting speed on the average cooling rate during solidification for the AZ31 twin roll cast strip at the strip surface and center-line. As the casting speed increases the average cooling rate during solidification decreases. Increasing the casting speed will cause the distance over which the solidification occurs (mushy zone thickness) to increase; so, the solidification time increases and cooling rate decreases. Figure 7-8 illustrates the effect of *HTC* on the cooling rate at center-line and strip surface for final thickness of 6mm, as expected; higher cooling rates are obtained by raising the *HTC*.



(a)

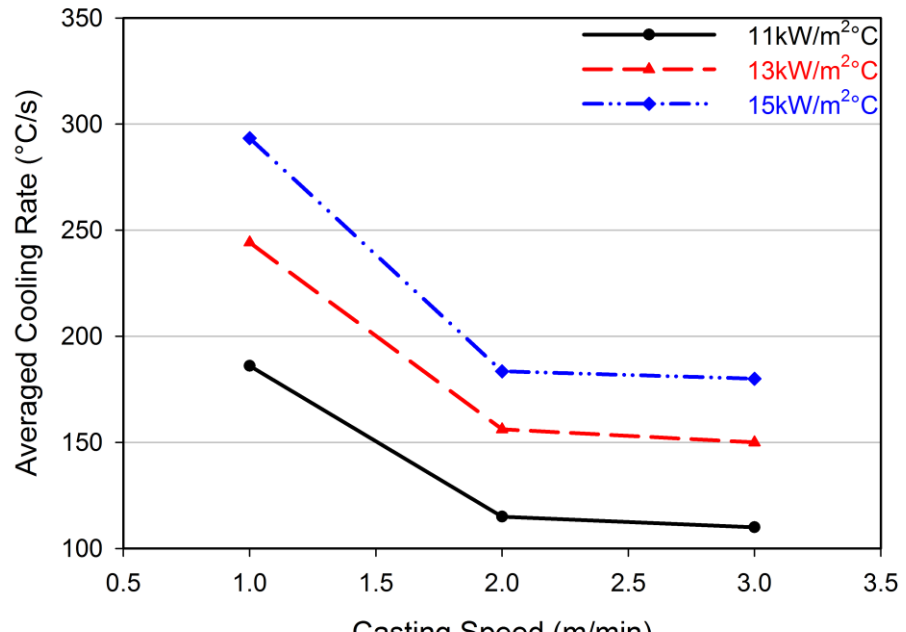


(b)

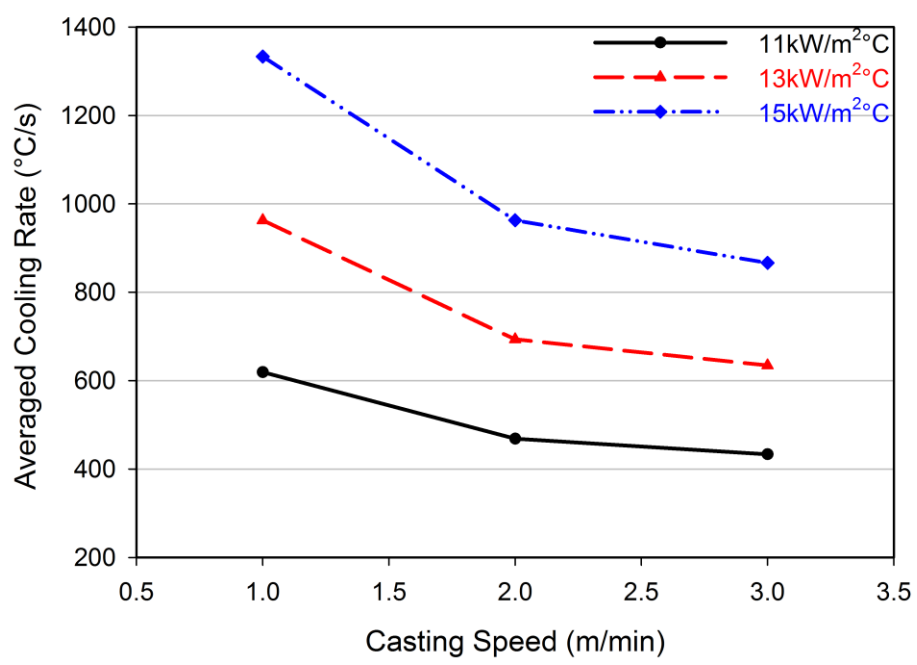


(c)

Figure 7-7- Effect of casting speed on the model-predicted cooling rate during solidification for the AZ31 twin roll cast strip at the surface and center-line for final thickness of a) 4mm, b) 5mm and c) 6mm ( $\text{HTC}=11\text{kW/m}^2\text{ }^{\circ}\text{C}$ ).



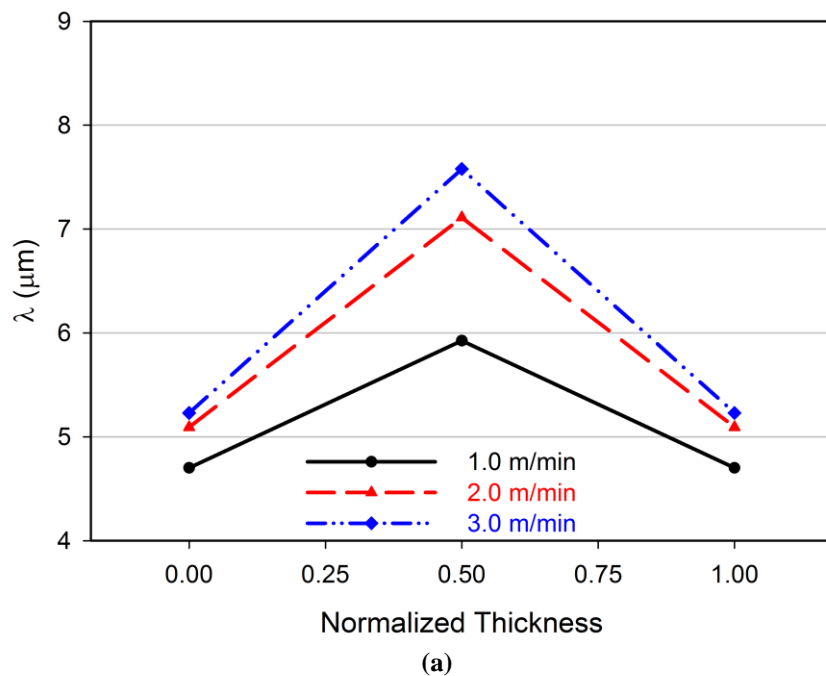
(a)



(b)

Figure 7-8- Model-predicted effect of *HTC* on the solidification cooling rate at a) center-line and b) strip surface for final thickness of 6mm.

Figure 7-9 represents the predicted SDAS through thickness affected by casting speed for  $HTC=11\text{kW/m}^2\text{°C}$ . It is observed that slower casting speeds should produce more uniform final microstructures. Similar effects are seen for higher final thicknesses. Moreover the  $HTC$  also influence the microstructure evolution; finer microstructure along thickness is obtained by increasing the  $HTC$  and the difference between strip surface and center-line in terms of  $SDAS$  values decreases, as shown in Figure 7-10 for the final thickness of 6m.



(a)

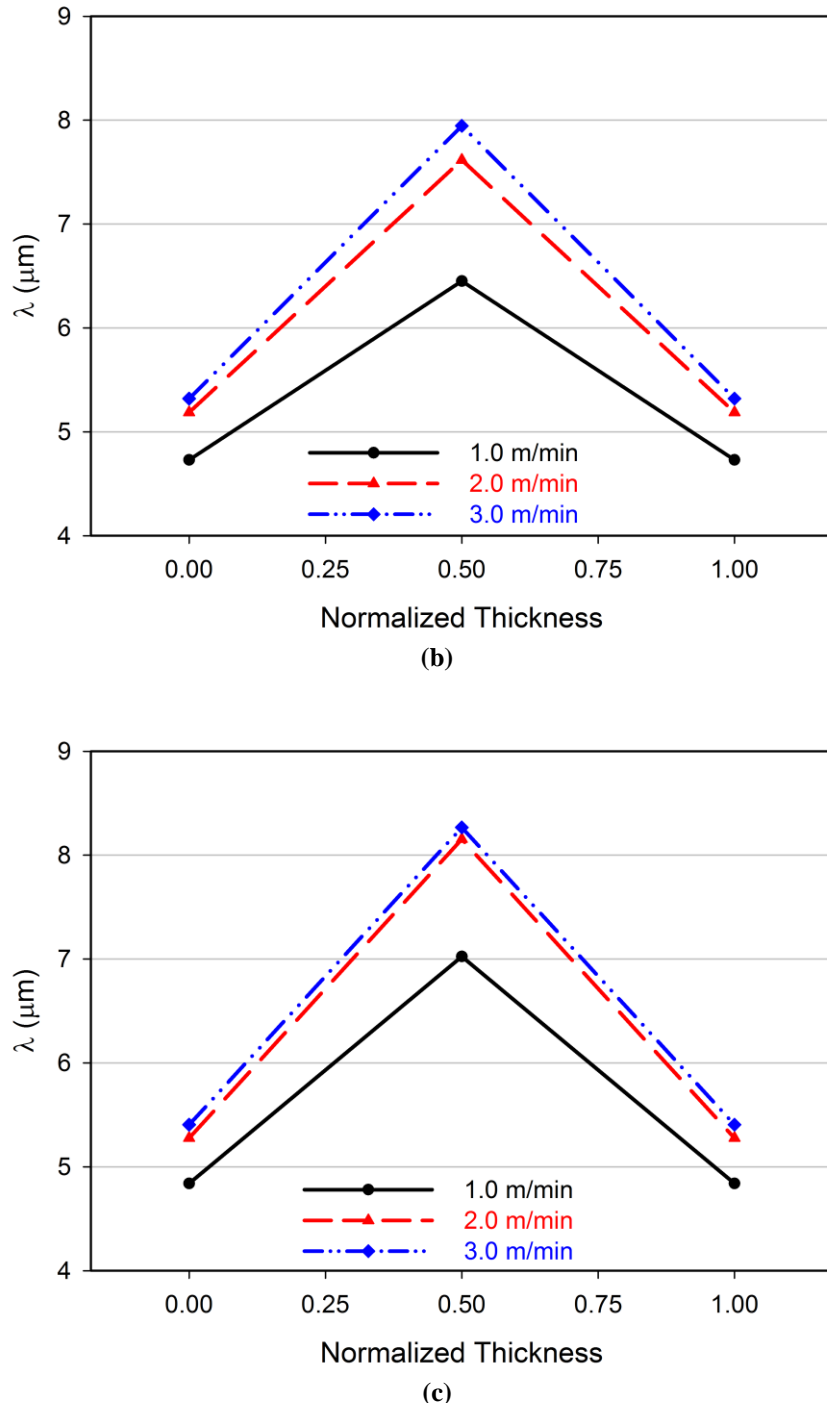
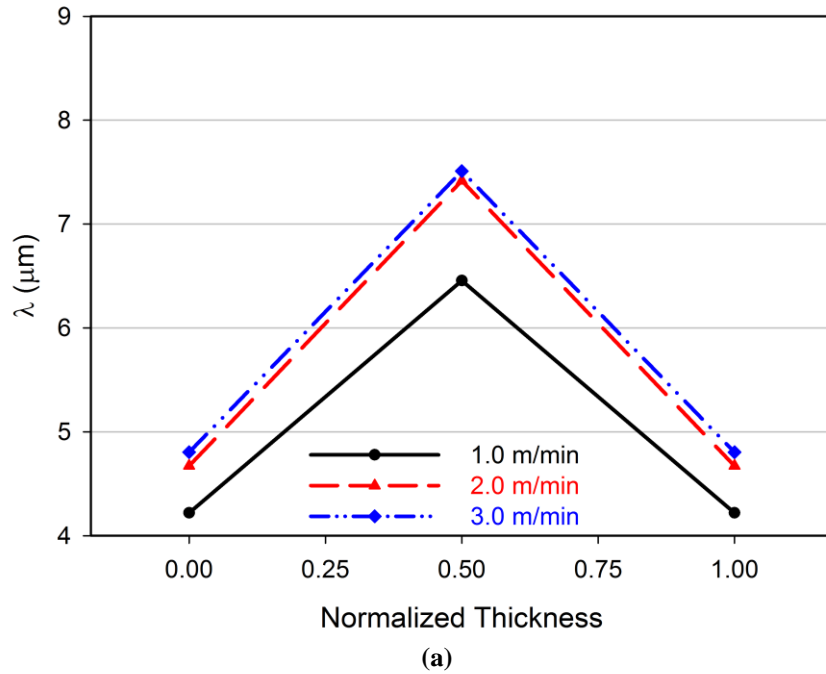
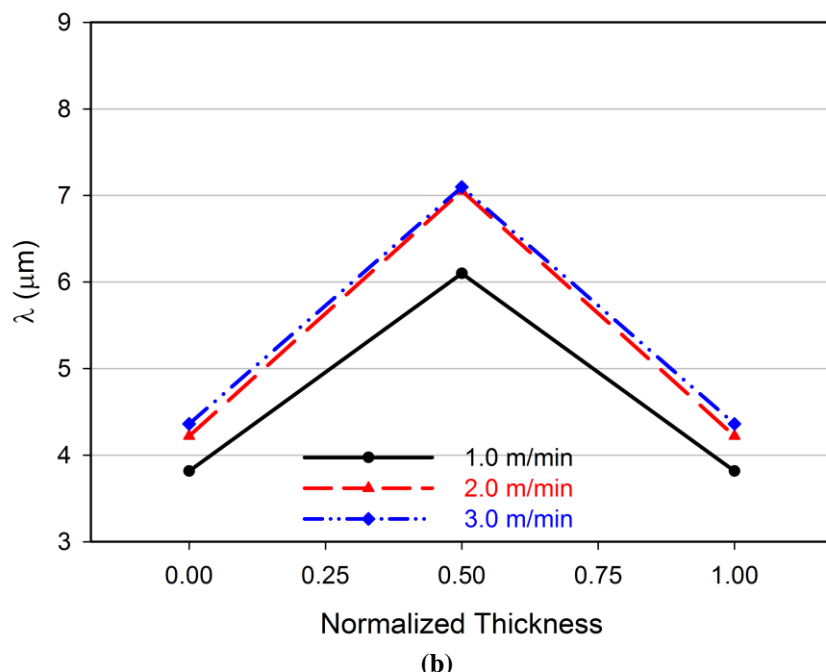


Figure 7-9- Model-predicted effect of casting speed on the secondary dendrite arm spacing through normalized thickness (0 = top and 1 = bottom) for an  $HTC=11\text{kW/m}^2\text{°C}$  and final thickness of a) 4mm, b) 5mm and c) 6mm.



(a)



(b)

Figure 7-10- Model-predicted SDAS through thickness for final thickness of 6mm and  $HTC$  of a)  $13\text{kW}/\text{m}^2\text{°C}$  and b)  $15\text{kW}/\text{m}^2\text{°C}$ .

If the uniformity of the microstructure is defined as the difference between the SDAS on the surface and center-line ( $\Delta\lambda = \lambda_{center\_line} - \lambda_{surface}$ ); a higher  $\Delta\lambda$  implies less uniformity and vice versa. Figure 7-11 shows the effect of casting speed and final thickness and Figure 7-12 shows the effect of casting speed and *HTC* on the AZ31 cast strip microstructure uniformity. As expected, increasing the casting speed leads to the evolution of a less uniform microstructure after casting. Moreover, more uniformity is obtained for thinner strips and more uniformity is achieved as the heat transfer coefficient is increased. Therefore, the most uniform microstructure is achieved by casting the AZ31 strip to a final thickness of 4mm, using a casting speed of 1.0m/min.

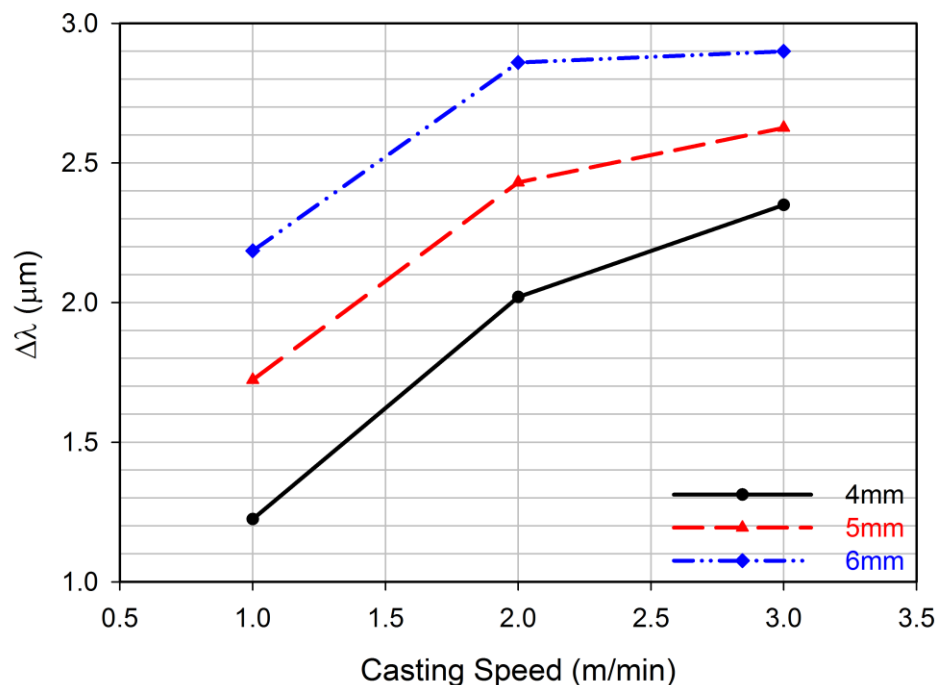


Figure 7-11- Model-predicted effect of casting speed and final thickness on the microstructure uniformity through thickness for AZ31 twin roll cast strip casting with  $HTC=11kW/m^2\circ C$ .

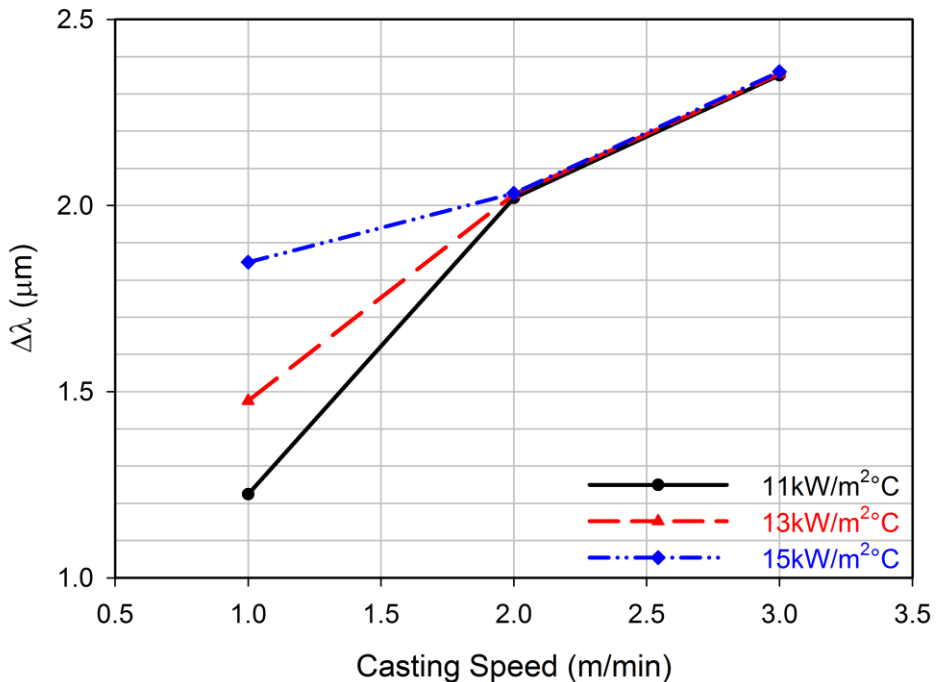


Figure 7-12- Model-predicted effect of casting speed and heat transfer coefficient on the microstructure uniformity through the thickness of 4mm AZ31 twin roll cast strip.

### 7.3 Summary

A two-dimensional Computational Fluid Dynamics (CFD) thermal-fluid model has been developed and validated for twin roll casting (TRC) of AZ31 magnesium alloy using the commercial package ANSYS® CFX®. The thermal history of the strip was studied in terms of the temperature gradient through the strip thickness at the exit of the caster, the sump depth and mushy zone thickness at the center-line and as-cast microstructure uniformity. The following conclusions can be drawn from this part of the work:

- 1) Higher casting speeds, thicker final exit gauges and lower HTC cause the strip to exit with higher temperatures as well as increase the depth of the sump and thickness of the mushy zone.
- 2) Lower temperature gradient through the strip thickness is achieved by casting at lower casting speed and reducing the final thickness. The effect of HTC on the temperature gradient is negligible.
- 3) The cooling rate which occurs during solidification at the strip surface and center-line decreases by increasing the casting speed.
- 4) More uniform microstructures are obtained by casting at lower speeds, casting the strip with lower final exit thickness and applying a lower *HTC*. The optimum condition in terms of microstructure uniformity is achieved by casting the AZ31 strip to a final thickness of 4mm using a casting speed of 1.0m/min and  $HTC=11\text{kW/m}^2\text{C}$ ; however, lower casting speeds can lead to lower productivity.
- 5) The process becomes more sensitive to *HTC* and strip thickness as the casting speed is increased.

## Chapter 8

### Thermal-Fluid-Stress Model Application

This chapter contains the results obtained by the application of the thermal-fluid-stress model developed using ALSIM. As mentioned previously, this is the first comprehensive mathematical model for magnesium TRC which has the ability of predicting the stress-strain development in the cast strip in addition to the thermal-fluid history.

#### **8.1 Effect of Casting Conditions on Thermal-Fluid-Stress History of the Strip**

Table 8-1 shows the casting conditions modeled in the present study. The purpose of the simulation study was to analyze the effect of casting speed ( $v$ ) and set-back distance ( $SB$ ,  $\ell_1$  in Figure 5-1 calculated by Equation (7-2)) on the evolution of the thermal and mechanical history experienced by the strip as it first solidifies and then is hot deformed during TRC. As seen in Equation (7-2), for a given roll radius (177.5mm for the current study), varying the amount of reduction changes the set-back distance. To change the reduction or amount of deformation, the entry height could be kept constant and the final thickness varied or vice versa. Both approaches have been used in the present work to analyze three set-back distances of 32.5, 37.5 and 41.8mm. First the entry height was set to 12mm and the final thickness varied between 2, 4 and 6mm. In another set of simulations, the final thickness was kept constant at 6mm and the entry height varied from 12 to 16mm. So for a given set-back distance the effect of both entry height and exit thickness was quantified.

Table 8-1- Casting conditions employed for thermal-fluid-stress model

Casting Temperature (°C)	Entry Height (mm)	Exit Thickness (mm)	Set-Back Distance (mm)	Strip Width (mm)	Heat Transfer Coefficient (kW/m <sup>2</sup> °C)	Friction Coefficient ( $\mu$ )	Casting Speed (m/min)
677	12	2	41.8	250	11	0.4	1.0-14
		4	37.5				
			32.5				
		6	37.5				
		16	41.8				
							1.0-2.5

### 8.1.1 Thermal History of the Cast Strip

The first criterion to assess the feasibility of the TRC process is the exit temperature of the strip at the center-line; it should be less than the coherency temperature. Otherwise, the non-fully coherent material exits the caster and a break out can occur.

As mentioned previously, once the molten material enters the space between the rolls and touches the roll surface, heat is extracted from the molten metal and solidification at the surface of the strip starts almost immediately as the material is pulled into the roll bite. The temperature continues to drop as the strip moves through the roll bite until the solidus temperature is reached and then the solid strip continues to cool and experience plastic deformation.

As expected, by increasing the casting speed, less time is provided for heat transfer to occur between the strip and the roll and consequently higher exit strip temperature are obtained. Figure 8-1 shows the model-predicted effect of casting speed on the temperature profile at the center-line position for  $SB=32.5\text{mm}$ .

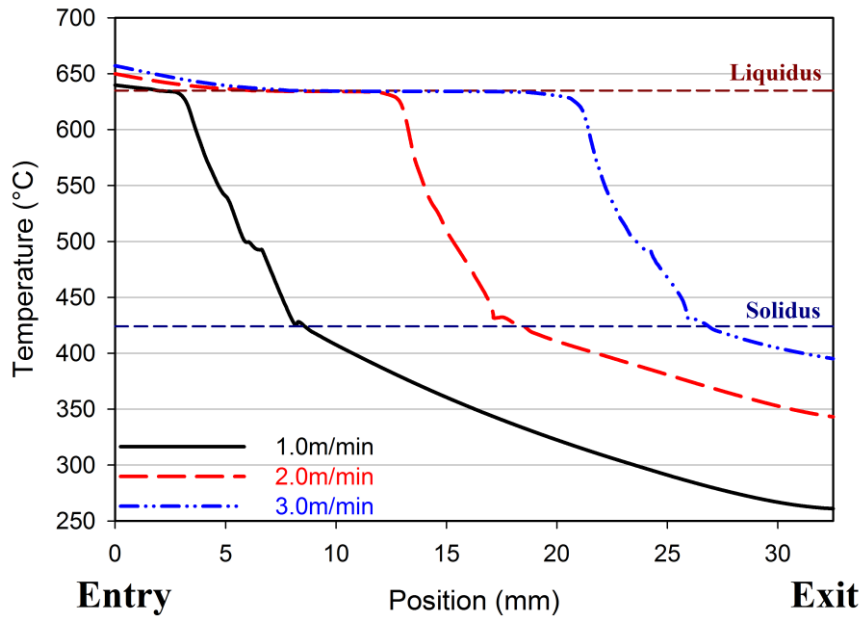


Figure 8-1- Model-predicted effect of casting speed on the temperature profile at the strip center-line for a  $SB=32.5\text{mm}$ .

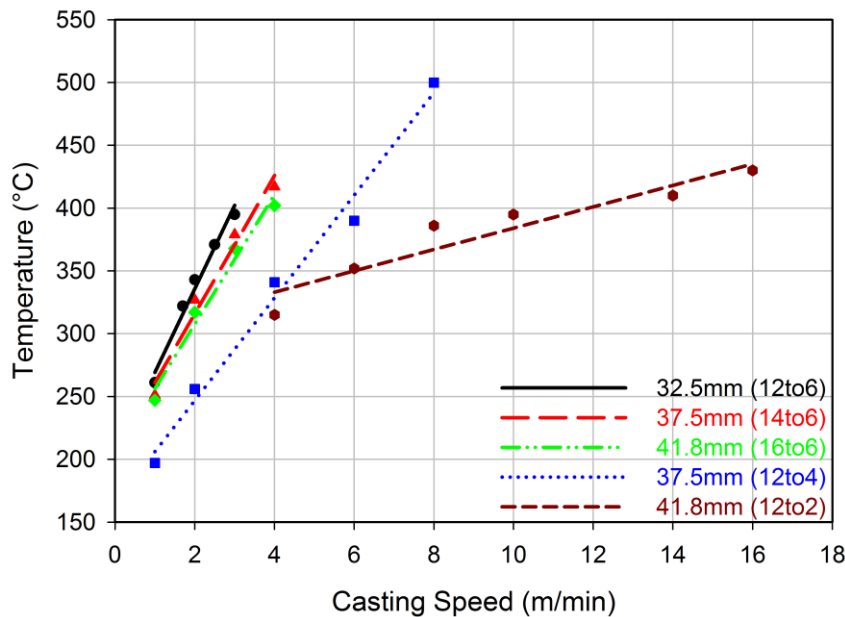


Figure 8-2- Model-predicted effect of casting speed and set-back distance on the exit temperature of the strip at the center-line position.

Referring to Figure 8-1, a plateau can be seen in the temperature history at the liquidus temperature and this is due to the release of the latent heat of fusion as solidification proceeds. Since the casting temperature for all cases is the same, 677°C, the temperature at the entry for the four cases is almost the same, but at the exit (kissing point) a significant variation in temperature is observed due to the different contact times between the strip and the roll. Moreover, by increasing the casting speed, the solidification front at the center-line is moved further into the roll gap towards the TRC exit and the thickness of the mushy zone increases as the casting speed increases. The occurrence of the solidification over a longer distance and variations in the strip temperature profile will also affect the stress field development in the solid strip. Figure 8-2 illustrates the model-predicted effect of casting speed on the exit temperature at the center-line for various set-back distances. As seen in Figure 8-2, as the set-back distance decreases for a given starting entry thickness, the exit temperature becomes more sensitive to the casting speed. The results are more complicated when examining the same set-back distance's that are achieved in a variety of ways since both the material energy entering the rolls as well as the arc of contact in the roll bite can be affected. Table 8-2 illustrates the linear correlation between casting speed and exit temperature. As observed in Figure 8-2 and Table 8-2, varying the final thickness affects the results more significantly than changing the entry height.

Table 8-2- The relation between casting speed ( $v$ ) and exit temperature at the CL ( $T_{CL}$ )

<b>Set-up #</b>	<b>Entry Height (mm)</b>	<b>Exit Thickness (mm)</b>	<b>Set-Back (mm)</b>	<b>Speed-Temperature Relationship</b>
1	12	6	32.5	$T_{CL} = 66.561v + 202.62$
2	14	6	37.5	$T_{CL} = 55v + 206$
3	16	6	41.8	$T_{CL} = 51.6v + 204.5$
4	12	4	37.5	$T_{CL} = 40.86v + 165.19$
5	12	2	41.8	$T_{CL} = 14.861v + 237.46$

### 8.1.2 Surface Stress Development

Similar to a cold or hot rolling process, normal stress occurs on the solidified strip surface during TRC. The normal stress (or roll pressure, yy-stress) gradually approaches a peak value and then decreases as the strip moves toward the exit region. Beside the normal stress, a shear stress is also developed on the strip surface due to the relative motion between the strip and work rolls. The cast material experiences a velocity profile which increases from the entry to the exit point; it moves slower than the rotating rolls prior to the neutral point, reaches the rolls' speed at the neutral point and then travels faster than the rolls beyond the neutral point [127]. This relative motion at the strip/roll interface leads to positive, zero and negative shear stress prior, at and beyond the neutral point, respectively, as shown in Figure 8-3. Figure 8-4 shows the normal (yy-stress) and shear stress development on the strip surface for  $SB=32.5\text{mm}$  at  $v=1.0\text{m/min}$  as well as the strip temperature profile in the roll bite. The liquid-solid profile in Figure 8-4 illustrates the liquid metal ( $f_s=0$ ), the non-coherent metal (mushy zone prior to the coherency point;  $f_s < 0.9$ ), coherent metal (mushy zone beyond the coherency point;  $f_s \geq 0.9$ ) and the fully solid metal ( $f_s=1$ ). As observed in Figure 8-4, the stress doesn't start to develop immediately at the point where the first fully coherent shell forms on the roll surface. The reason is that the pressure applied to the surface of the strip is transmitted to regions below the solid shell i.e. in the mushy zone and melt sump. Since the liquid and the non-coherent metal cannot sustain the stress, they don't support the solidified shell and hence no stress is experienced on the surface. Continuing the process, the solidified shell grows and thickens and also more coherent mushy material forms beneath the solid shell; once an adequate thick shell is reached and enough support is provided for the solid shell, the stress experienced at the surface rapidly increases. Analyzing the stress development for various casting speeds shows that by increasing the casting speed, the thickness of the solidified shell on the roll surface decreases and the stress development at the surface is delayed in the roll gap.

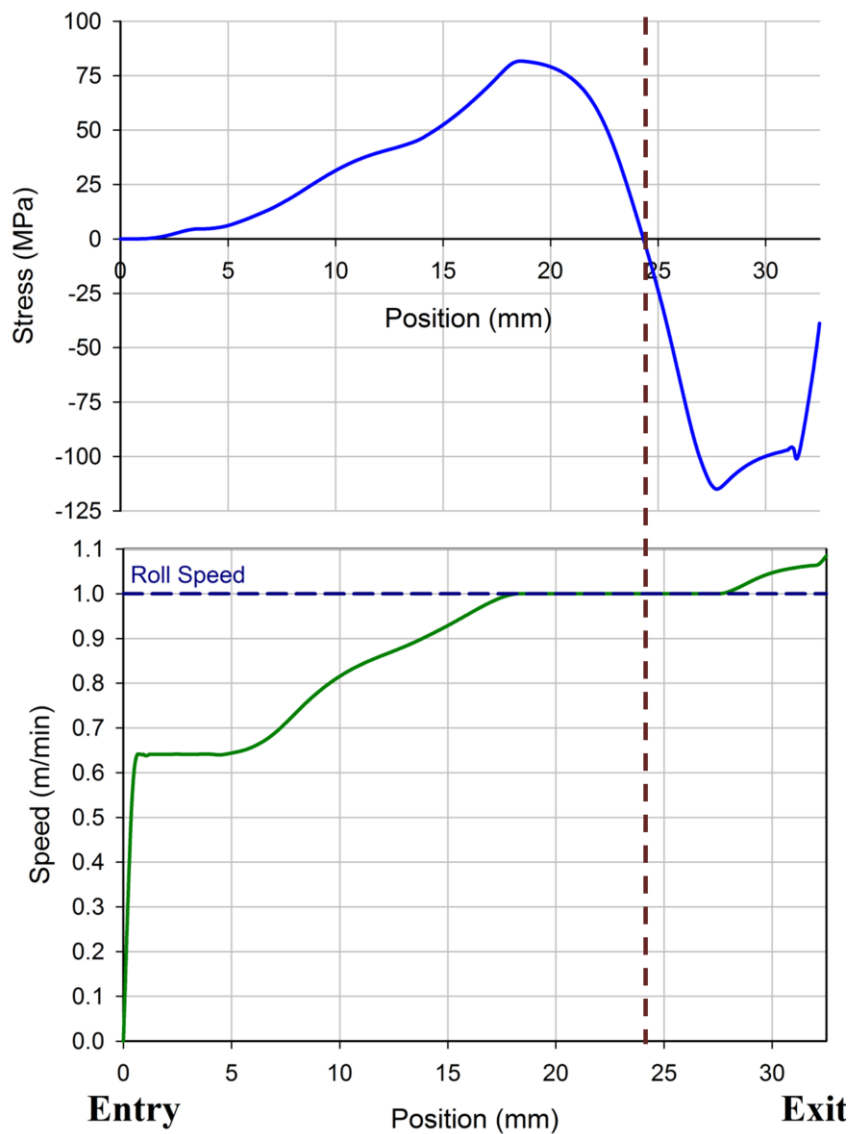


Figure 8-3- Model-predicted surface shear stress development for  $SB=32.5\text{mm}$  and  $v=1.0\text{m/min}$ .

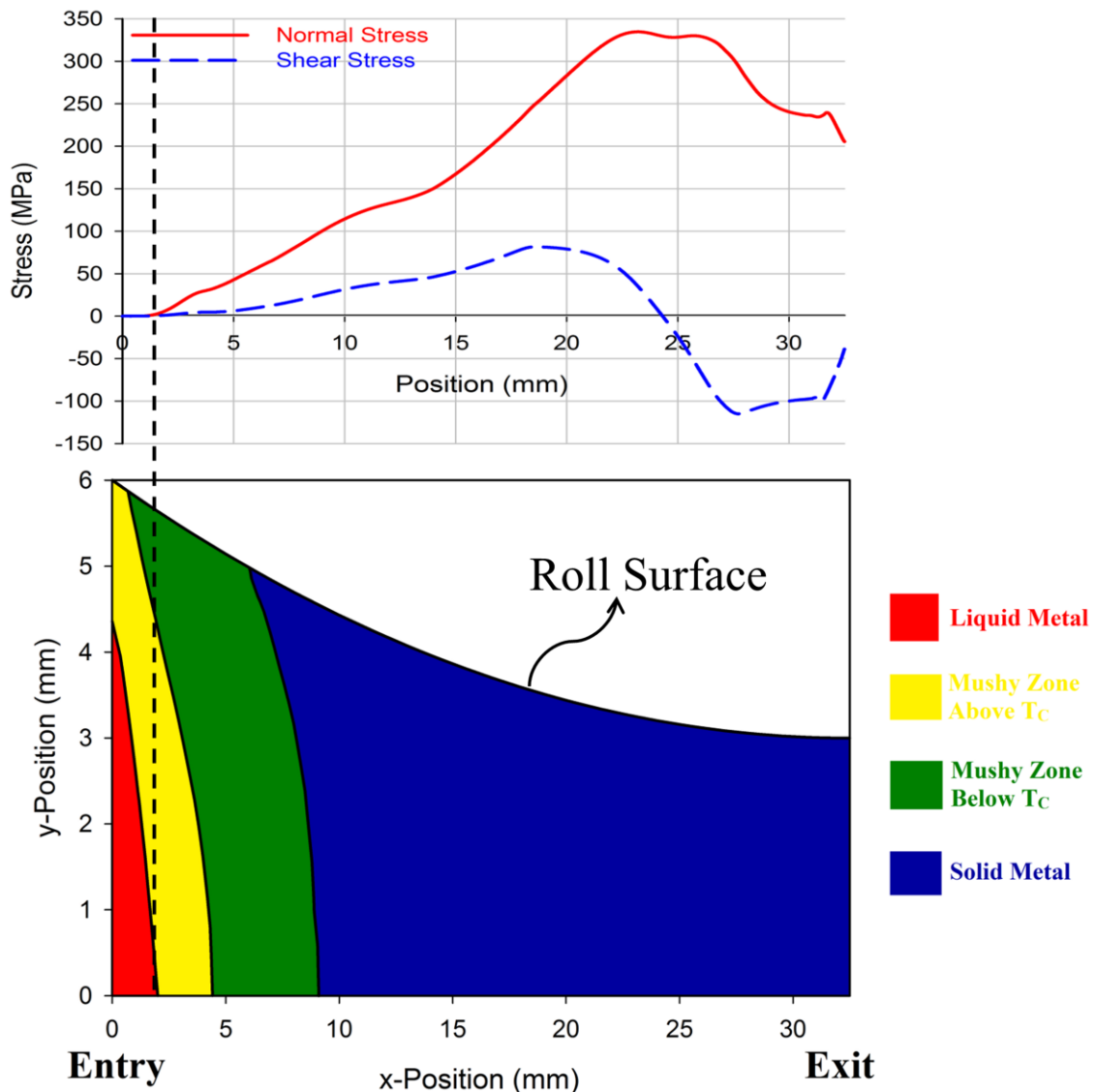


Figure 8-4- Model-predicted strip surface stress development (upper graph) and the corresponding liquid-solid profile (lower graph) for  $SB=32.5\text{mm}$  and  $v=1.0\text{m/min.}$

The effect of casting speed on the strip surface normal stress for all set-back distances is shown in Figure 8-5. Casting at higher speeds has two effects; spatial retardation of the stress development toward the exit region and a drop of the peak stress since solidification starts further into the roll bite. Moreover, as the casting speed increases, since less solidified material has undergone plastic deformation (as shown in Figure 8-6 for  $SB=32.5\text{mm}$ ) and this

deformation occurs at higher temperature (Figure 8-1), the stress level decreases but the point at which the peak occurs in the roll bite remains almost the same.

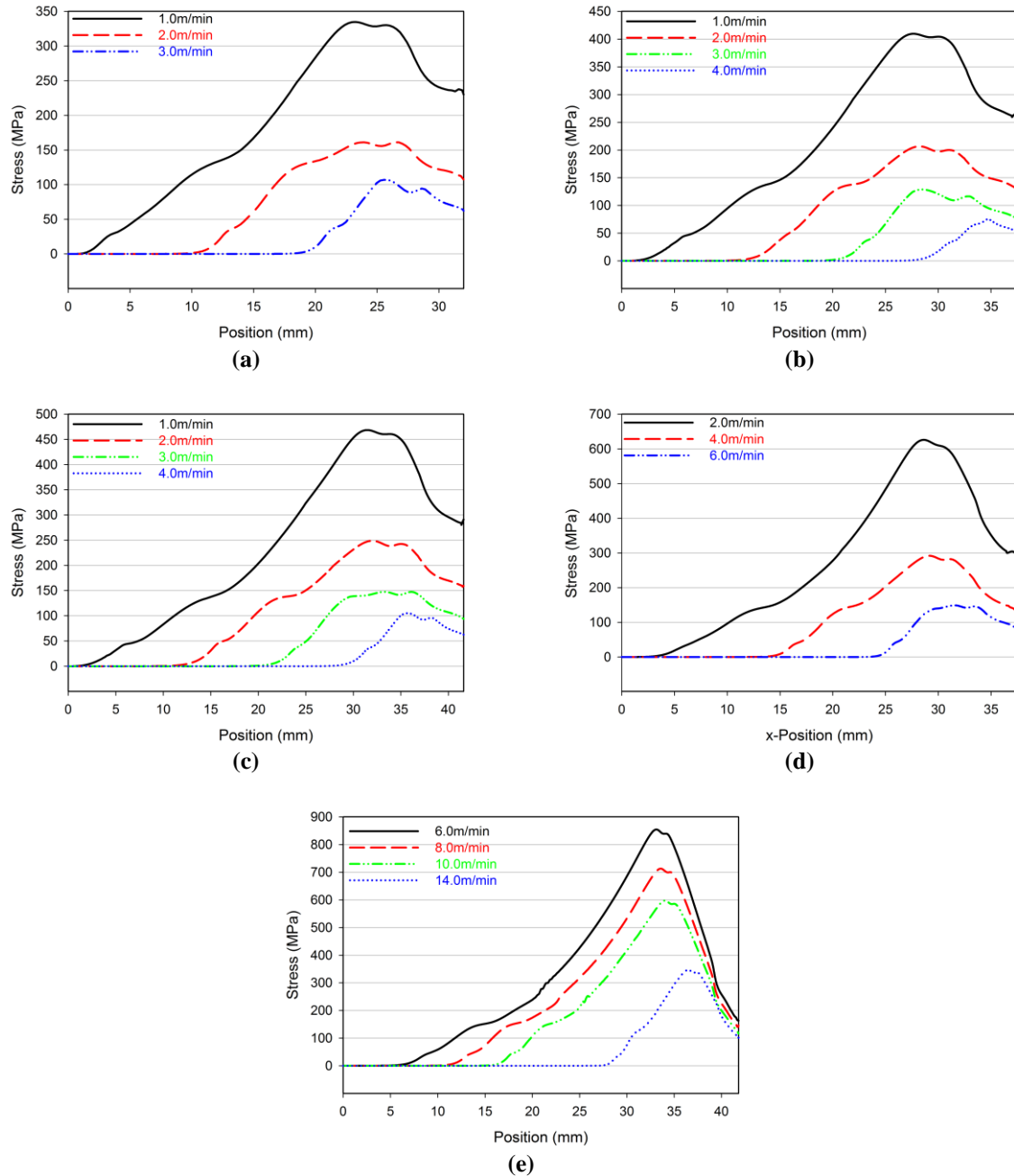


Figure 8-5- Model-predicted effect of casting speed on the surface normal stress for set-back distance of a) 32.5mm (12to6), b) 37.5mm (14to6), c) 41.8mm (16to6), d) 37.5mm (12to4) and e) 41.8mm (12to2).

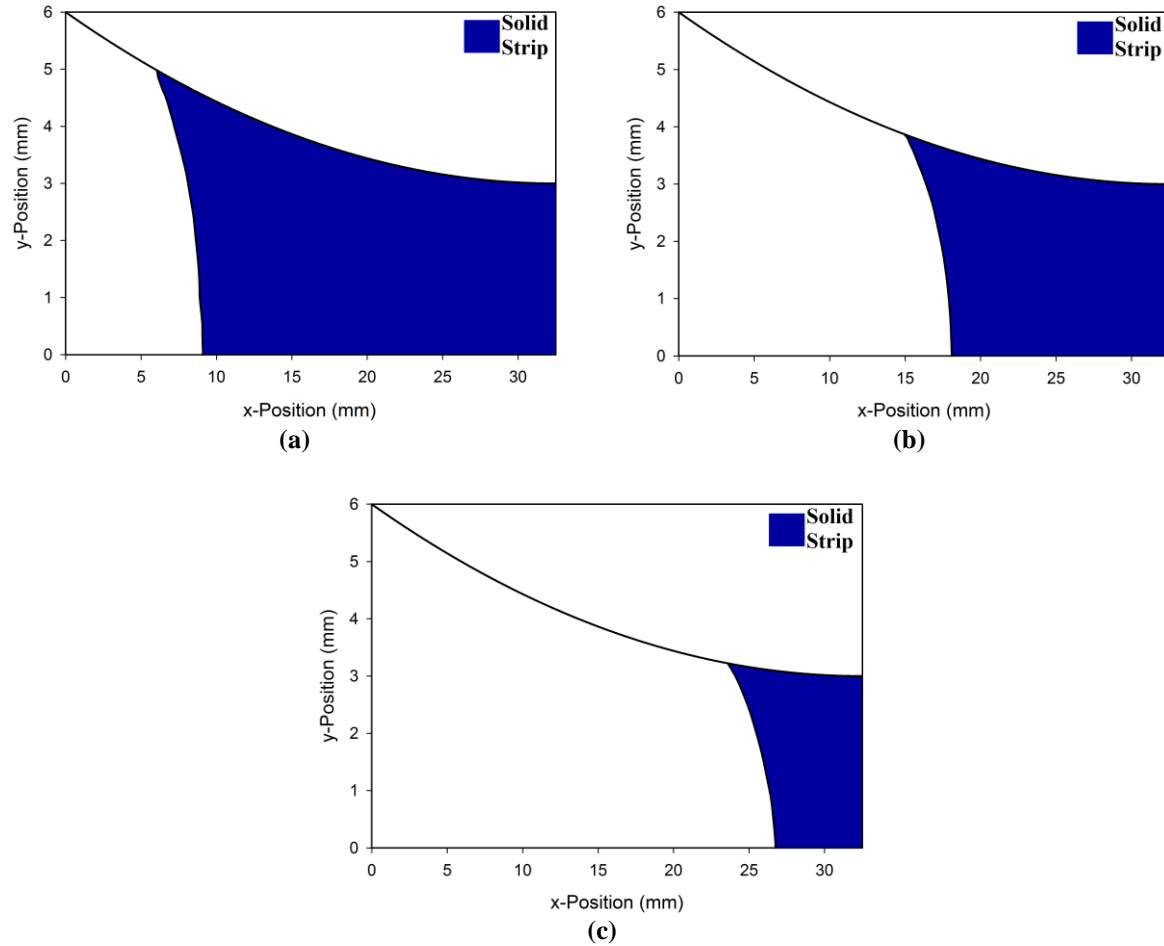
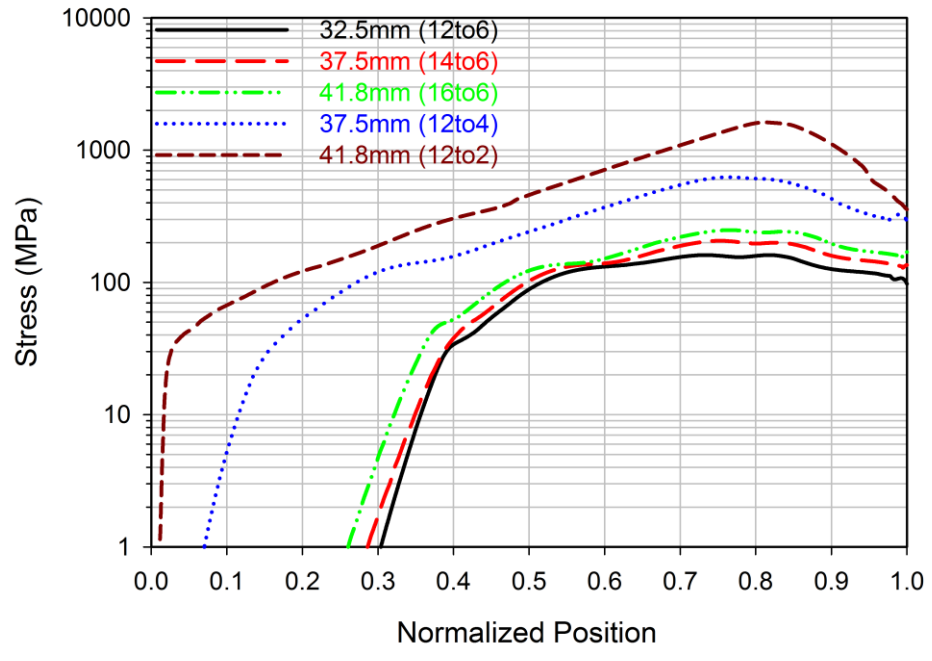
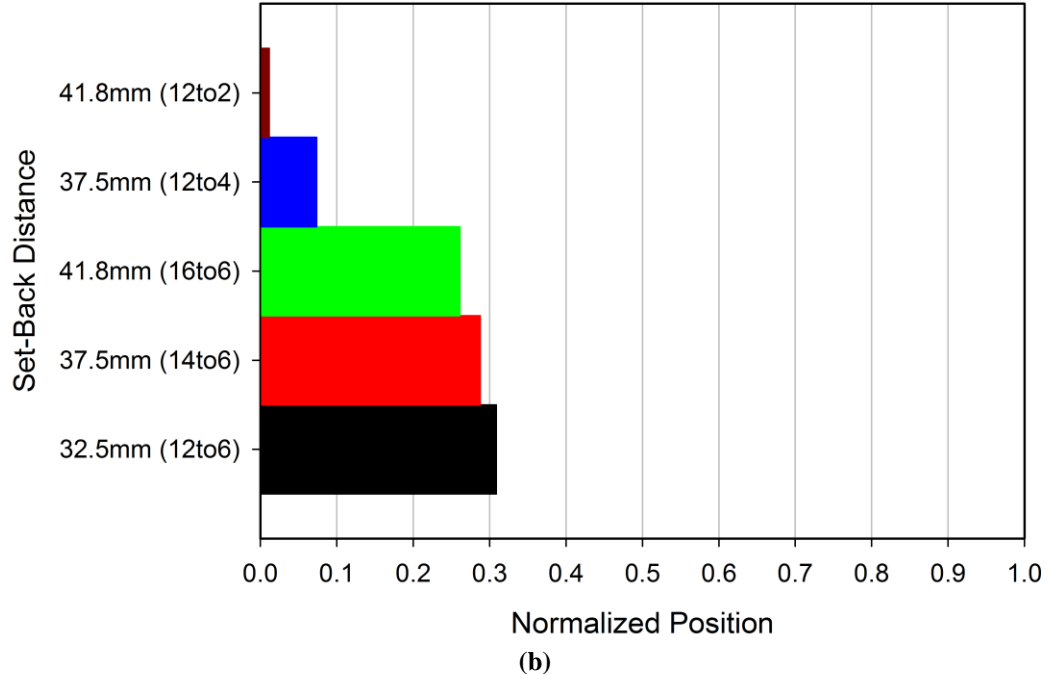


Figure 8-6- Model-predicted effect of casting speed on the amount of solidified material in the roll bite for  $SB=32.5\text{mm}$  and casting speed of a)  $1.0\text{m/min}$ , b)  $2.0\text{m/min}$  and c)  $3.0\text{m/min}$ .

Figure 8-7(a) shows the predicted normal stress on the surface for a range of set-back distances at  $v=2.0\text{m/min}$ . The x-axis is normalized relative to the roll bite entry (0) and exit (1) positions of the strip. The stress profiles depicted in Figure 8-7(a) shows that reducing the set-back distance leads to lower levels of stress and also a shift in the position in the roll bite where the stress starts to develop, as illustrated in Figure 8-7(b). Decreasing the set-back distance by increasing the strip thickness has a more significant effect on the stress level than reducing the entry height. The associated solid strip solidification profile in the roll bite region for three different cases with a final thickness of  $6\text{mm}$  is shown in Figure 8-8.



(a)



(b)

Figure 8-7- Model-predicted effect of set-back distance on (a) the surface normal stress and (b) position at which stress begins to develop at  $v=2.0\text{m/min}$ .

As seen in Figure 8-8, increasing the set-back distance decreases the sump depth and moves the solidification front position closer to the roll bite entry. As a consequence the stress experienced by the material starts to develop at a point closer to the entry and goes up to higher peak values since the thickness of the solid material which experience the plastic deformation increases. In other words, the amount of “reduction” during the “hot rolling” part of the TRC process increases by increasing the set-back.

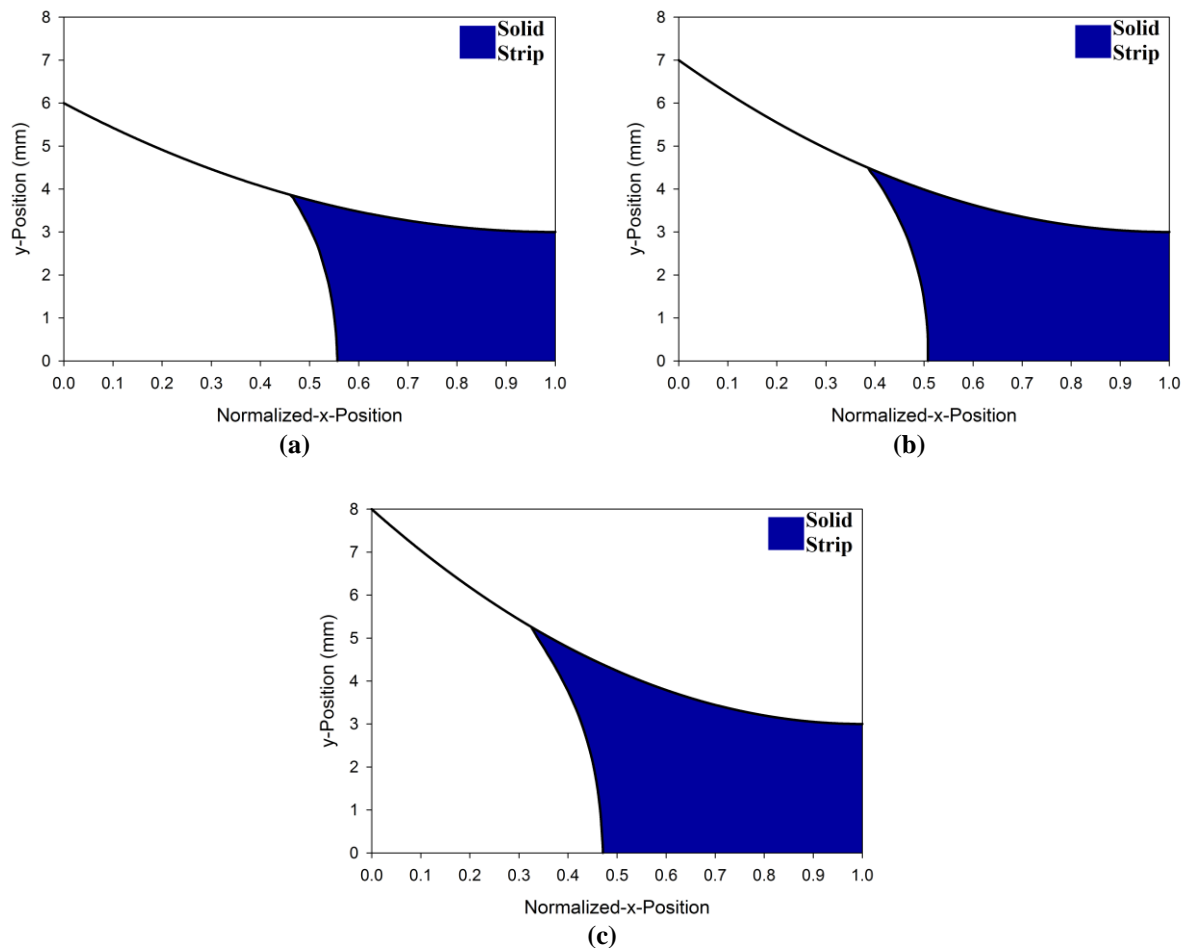


Figure 8-8- Model-predicted sump depth for a set-back distance of a) 32.5mm, b) 37.5mm and c) 41.8mm for final thickness of 6mm and  $v=2.0\text{m/min}$ .

Figure 8-9 depicts the effect of casting speed on the shear stress developed on the strip surface during TRC for all set-back distances. Similar to normal stress, increasing the casting speed leads to a drop in the stress level; both for the “positive” peak stress and “negative” peak stress. Besides, the neutral point moves toward the exit region. The reason for reduction of the stress level is the same as what mentioned for the normal stress.

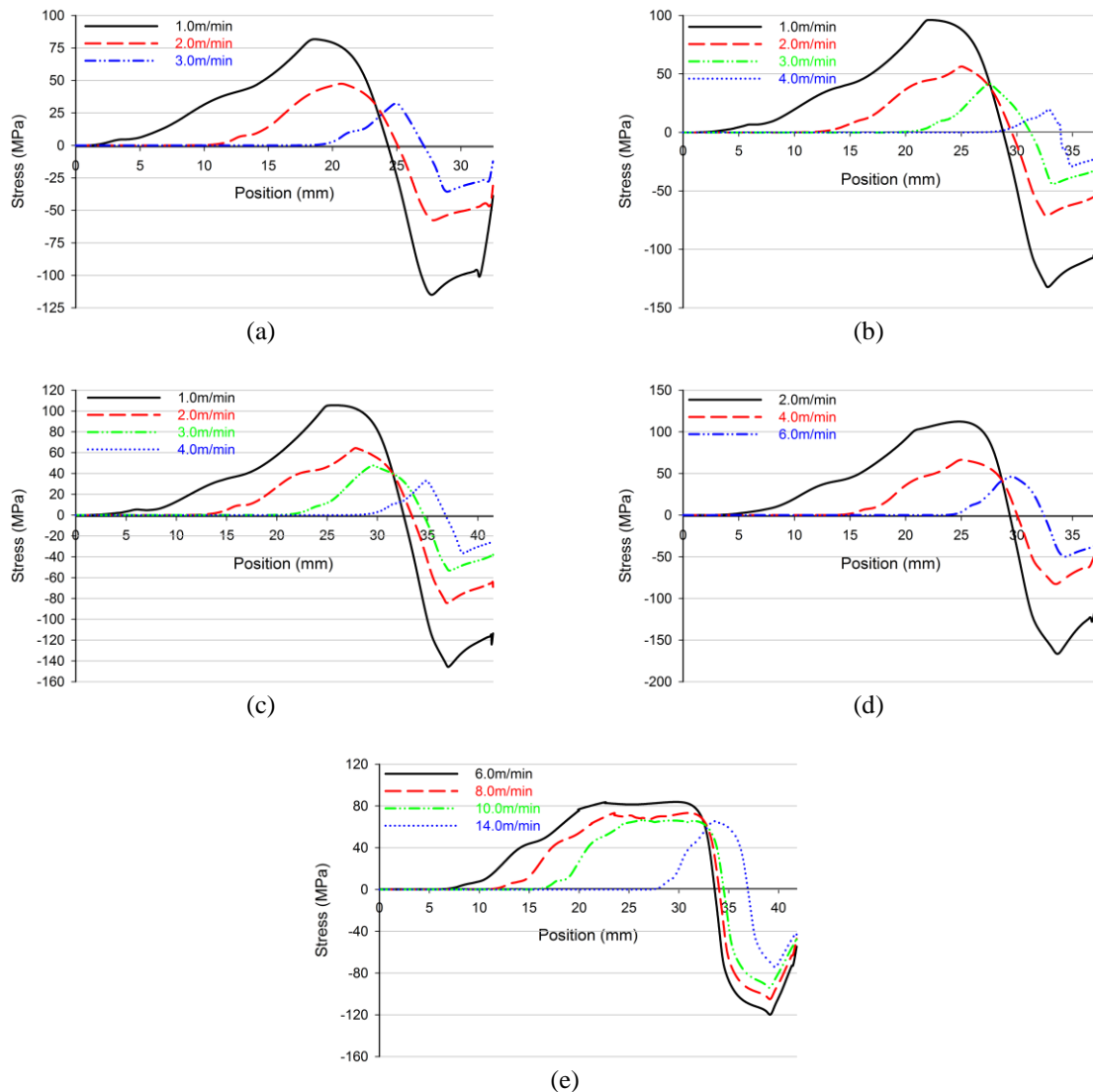


Figure 8-9- Model-predicted surface shear stress affected by casting speed for set-back distance of a) 32.5mm (12to6), b) 37.5mm (14to6), c) 41.8mm (16to6), d) 37.5mm (12to4) and e) 41.8mm (12to2).

### 8.1.3 Roll Separating Force

The roll separating force is the force applied to the work rolls in the vertical direction due to the deformation of the material and calculated using Equation (8-1) [128, 129].

$$SF = 1.15Q_P\sigma_{fm}lw \quad (8-1)$$

where  $SF$  is the roll separating force (in N),  $Q_P$  is stress state coefficient includes the effect of coefficient of friction,  $\sigma_{fm}$  is the mean flow strength of the metal (in Pa),  $l$  is the contact length (in mm) and  $w$  is the width of the cast strip (in mm).

Figure 8-10 shows the modeling results of casting speed's effect on the rolling force for different set-back distances. As expected from the trends observed for the surface normal stress, increasing the casting speed causes lower roll separating force since the amount of solid material which is imposed to the plastic deformation decreases. Moreover, casting with longer set-back distance leads to higher separating force; controlling the set-back distance by the final thickness causes higher separating forces than controlling the set-back distance by the entry height.

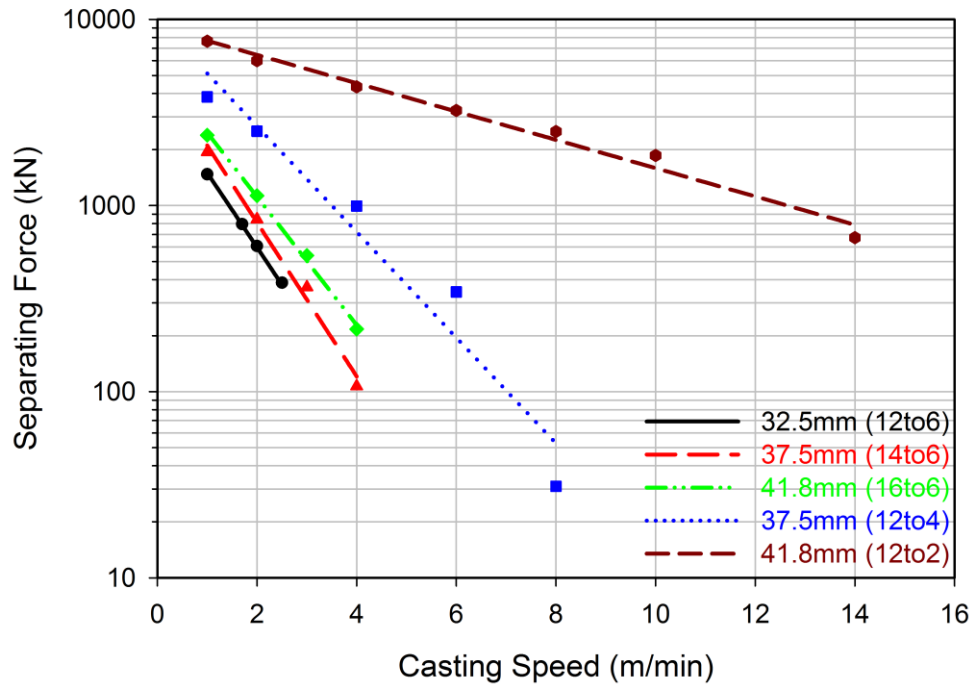


Figure 8-10- Model-predicted effect of casting speed on the roll separating force for different set-back distances.

The relationship between the roll separating force and the casting speed, as seen in Figure 8-10, follows an exponential trend in the form of Equation (8-2).

$$SF = \alpha \exp(-\beta v) \quad (8-2)$$

where  $SF$  is the separating force (in kN),  $\alpha$  and  $\beta$  constants and  $v$  casting speed (in m/min). Table 8-3 shows the constants for each set-back distance.

Table 8-3- Separating force ( $SF$ )-casting speed ( $v$ ) relationship

<b>Set-up</b>	<b>Entry Height</b>	<b>Exit Thickness</b>	<b>Set-Back</b>	<b>Force-Speed Relationship</b>
#	(mm)	(mm)	(mm)	
1	12	6	32.5	$SF = 3784.3exp(-0.924v)$
2	14	6	37.5	$SF = 5454.6exp(-0.953v)$
3	16	6	41.8	$SF = 5456.3exp(-0.794v)$
4	12	4	37.5	$SF = 9866.4exp(-0.654v)$
5	12	2	41.8	$SF = 9151.3exp(-0.175v)$

### 8.1.4 Effective Strain at the Center-line

The effective strain (von Mises) developed at the strip's center-line represents the amount of plastic deformation experienced by the cast material during the hot deformation stage of the TRC process. Figure 8-11 shows the effective strain at the center-line for  $SB=32.5\text{mm}$  at the casting speed of  $1.0\text{m/min}$  in conjunction with the strip's liquid-solid profile. The strain development begins immediately at the point where the mushy material at the center-line reaches the coherency temperature. A sharp jump to a plateau is observed prior to full solidification; this is due to a high strain rate experienced by the material in this region. The assessment of the velocity profile at the center-line showed that the material is being squeezed in the mushy zone since it is experiencing a reduction in thickness. Once the material reaches the coherency temperature, a high strain rate due to the squeezing is obtained and since the material is sensitive to strain rate at high temperature, a peak is observed in the stress at the center-line in the mushy zone. The high level of stress, consequently, causes a jump in the strain. Beyond the solidus temperature, the effective strain continues to increase gradually up to the maximum value and no more change is observed after the neutral point since the material is not deformed beyond this point (Figure 8-4). Figure 8-12 shows the effective strain at the center-line affected by the casting speed for all set-back distances. As expected, less plastic deformation is experienced by the cast metal by increasing the casting speed since solidification front shifts toward the exit region.

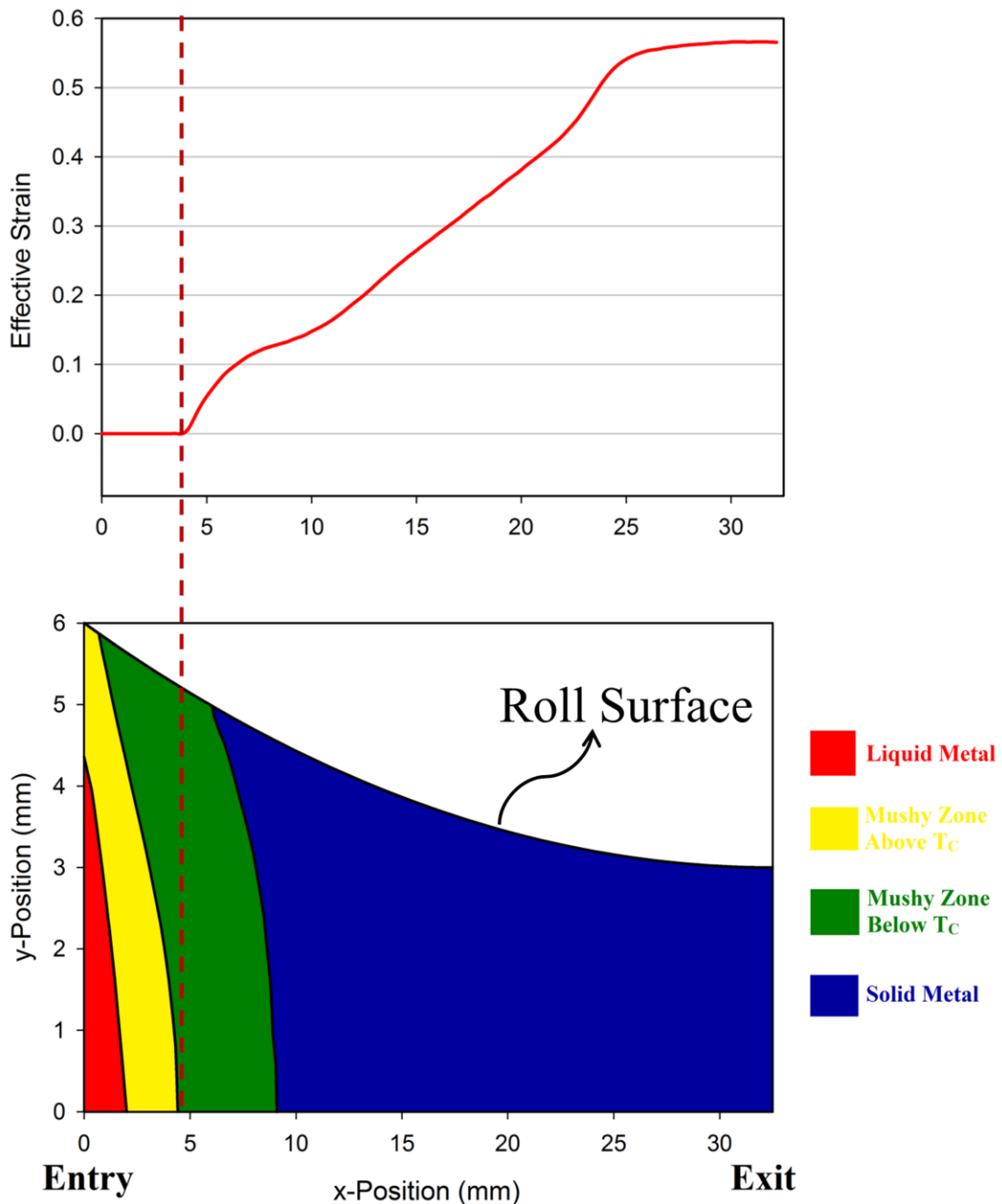


Figure 8-11- Model-predicted effective strain at the center-line (upper graph) in conjunction with the liquid-solid profile (lower graph) for  $SB=32.5\text{mm}$  and  $v=1.0\text{m/min}$ .

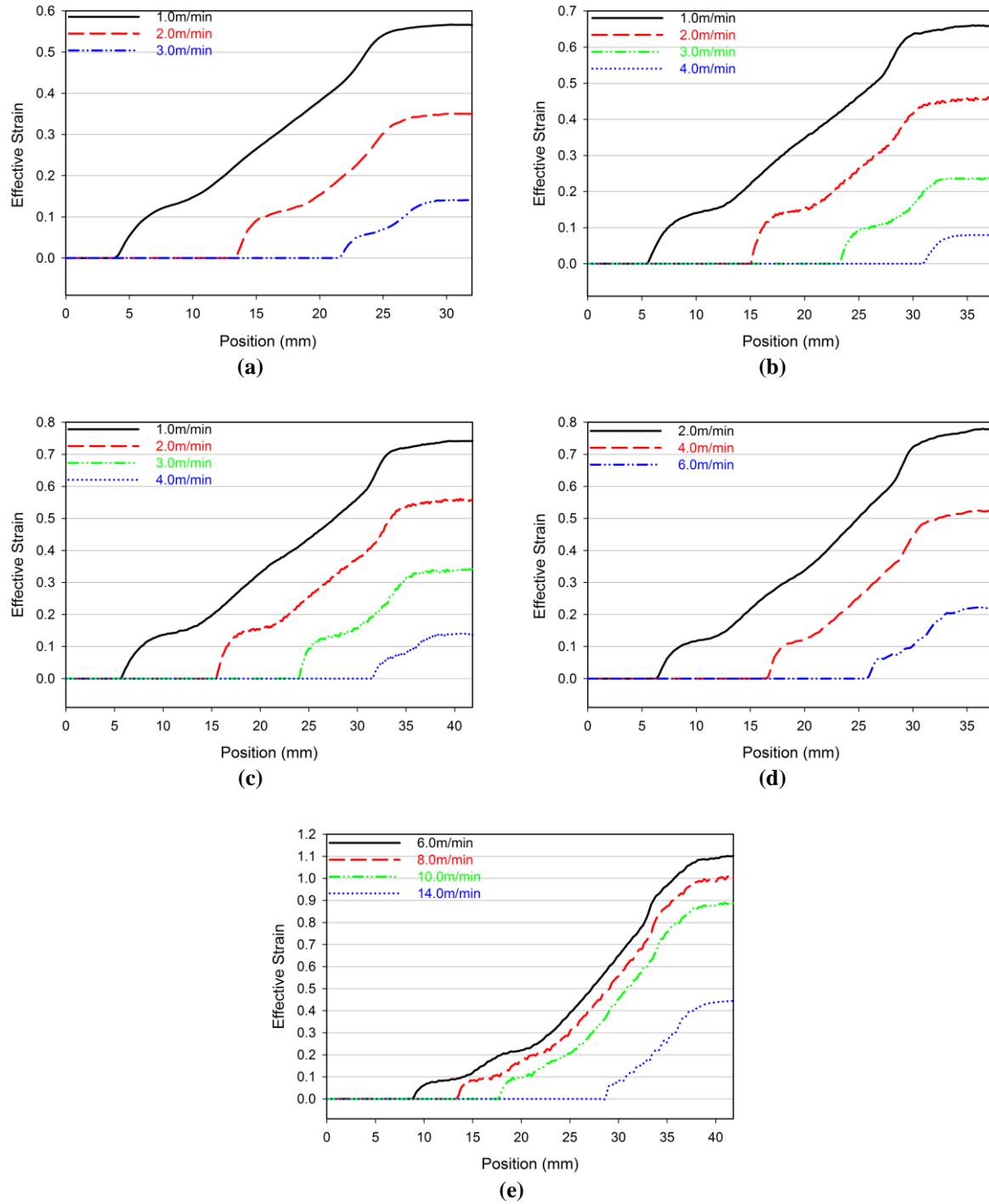


Figure 8-12- Model-predicted effect of casting speed on the effective strain at the center-line for set-back distance of a) 32.5mm (12to6), b) 37.5mm (14to6), c) 41.8mm (16to6), d) 37.5mm (12to4) and e) 41.8mm (12to2).

The effective strain at the center-line for different set-back distances at  $v=2.0\text{m/min}$  is shown in Figure 8-13. As the set-back distance increases for a final thickness of 6mm, a slight increase in the effective strain is observed; however, for an entry height of 12mm decreasing the final thickness leads to a dramatic increase of effective strain. Table 8-4 shows the reduction with respect to the thickness of the strip at which the strain starts to develop at the center-line for each case and the corresponding effective strain at the exiting point of the caster. Obviously, more reduction experienced by the solidified material causes higher effective strain at the exit point of the caster.

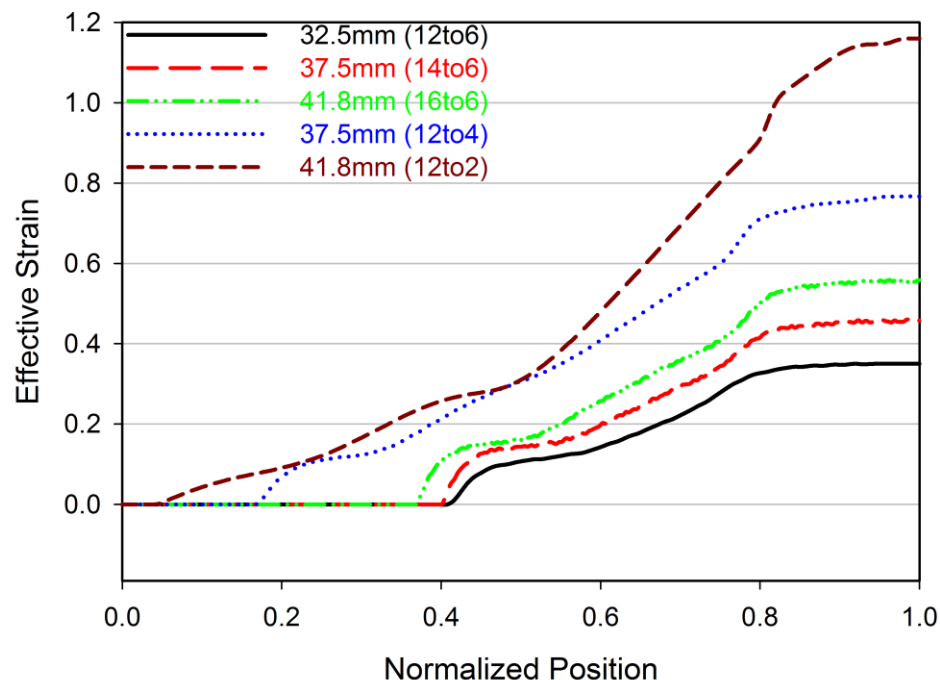


Figure 8-13- Effect of set-back distance on the effective strain development at the center-line for  $v=2.0\text{m/min}$ .

Table 8-4- The % reduction experienced by the solidified material for each set-up at  $v=2.0\text{m/min}$ 

Set-up #	Entry Height (mm)	Exit Thickness (mm)	Set-Back (mm)	Thickness Where Deformation Starts (mm)	Reduction (%)	Effective Strain at the Exit Point
1	12	6	32.5	7.97	32.83	0.35
2	14	6	37.5	8.80	46.7	0.46
3	16	6	41.8	9.89	64.83	0.56
4	12	4	37.5	9.39	134.75	0.77
5	12	2	41.8	5.29	164.5	1.16

## 8.2 Effect of Roll Diameter (Scale-Up Modeling)

Like the other manufacturing process development, advancement of the TRC process to produce sheet magnesium started with testing the viability using a laboratory-scale facility (roll diameter=355mm and strip width=250mm). After this was successful development shifted to a larger scale such as a pilot scale (roll diameter=600mm and strip width=600mm) and finally most recently POSCO has commissioned and is running an industrial-scale twin roll caster (roll diameter=1150mm and strip width=2000mm) for magnesium alloys. Insight into the effect of the scale-up process on the thermal-mechanical history developed in the sheet can be gained by using a mathematical model to examine trends. The thermal-fluid-stress model developed using ALSIM was employed to analyze the effect of roll diameter (355mm (laboratory scale), 600mm (pilot scale) and 1150mm (industrial scale)) on the thermo-mechanical history experience by the strip. The results were then used to generate a process map highlighting these effects.

For each roll diameter the entry height of the nozzle and the strip final thickness were kept constant, but since the set-back distance ( $SB$ ,  $\ell_1$  in Figure 5-1) is affected by both reduction and roll diameter (as shown in Equation (7-2)), three different set-back distances were obtained. Table 8-5 shows the casting conditions employed to examine the effect of roll diameter.

Table 8-5- Casting conditions used for effect of roll diameter study

<b>Set-Up Scale</b>	<b>Roll Diameter (mm)</b>	<b>Casting Temperature (°C)</b>	<b>Entry Height (mm)</b>	<b>Exit Thickness (mm)</b>	<b>Set-Back Distance (mm)</b>	<b>Strip Width (mm)</b>	<b>Casting Speed (m/min)</b>
Laboratory (Φ355)	355				32.5	250	
Pilot (Φ600)	600	677	12	6	42.3	600	1.0-6.0
Industrial (Φ1150)	1150				58.7	2000	

### 8.2.1 Strip Thermal History

Figure 8-14 shows the effect of casting speed on the strip exit temperature for different roll diameters. As the roll diameter increases, the set-back distance increases (Table 8-5) and consequently a longer arc of contact at the strip/roll interface is provided for heat transfer. As a result, more heat is extracted from the cast material and consequently higher casting speeds can be achieved with larger roll diameters as shown in Figure 8-14. Increasing the roll diameter from 355mm to 600mm and 1150mm increases the highest achievable casting speed from 3.0m/min to 5.0m/min and 6.0m/min, respectively.

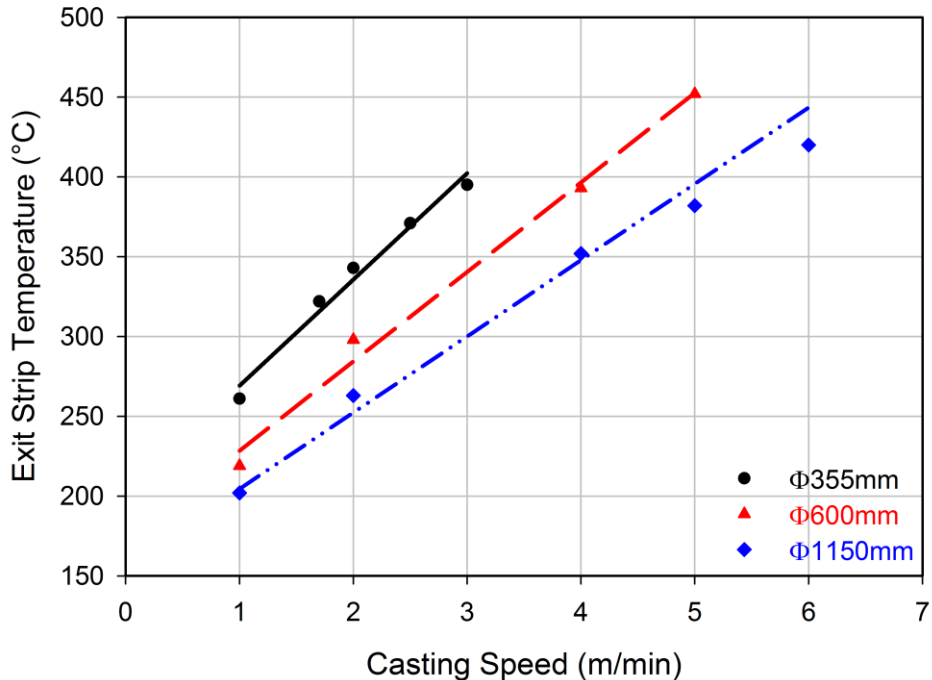


Figure 8-14- Effect of casting speed and roll diameter on the model-predicted temperature at the center-line, the symbols show the modeling results and the lines show the linear correlation.

The relationship between the exit temperature and casting speed appears fairly linear, as shown in Table 8-6 for each set-up. Integrating the effect of both casting speed and roll diameter together is helpful in terms of predicting the acceptable casting speed for roll diameters from 355mm to 1150mm. Equation (8-3) shows the corresponding correlation. By using this relationship a graph showing the effect of casting speed and roll diameter on the center-line exit temperature can be developed as shown in Figure 8-15.

$$T_{CL} = \frac{795.37v}{D^{0.419}} + \frac{707.68}{D^{0.216}} \quad (8-3)$$

where  $T_{CL}$  is the exit temperature at the center-line (in °C),  $v$  is the casting speed (in m/min) and  $D$  is the roll diameter (in mm).

Table 8-6- Exit temperature at the CL ( $T_{CL}$ )-casting speed ( $v$ ) relationship

Roll Diameter (mm)	Exit Temperature-Casting Speed
355	$T_{CL} = 66.561v + 202.62$
600	$T_{CL} = 56.1v + 172.2$
1150	$T_{CL} = 47.814v + 156.66$

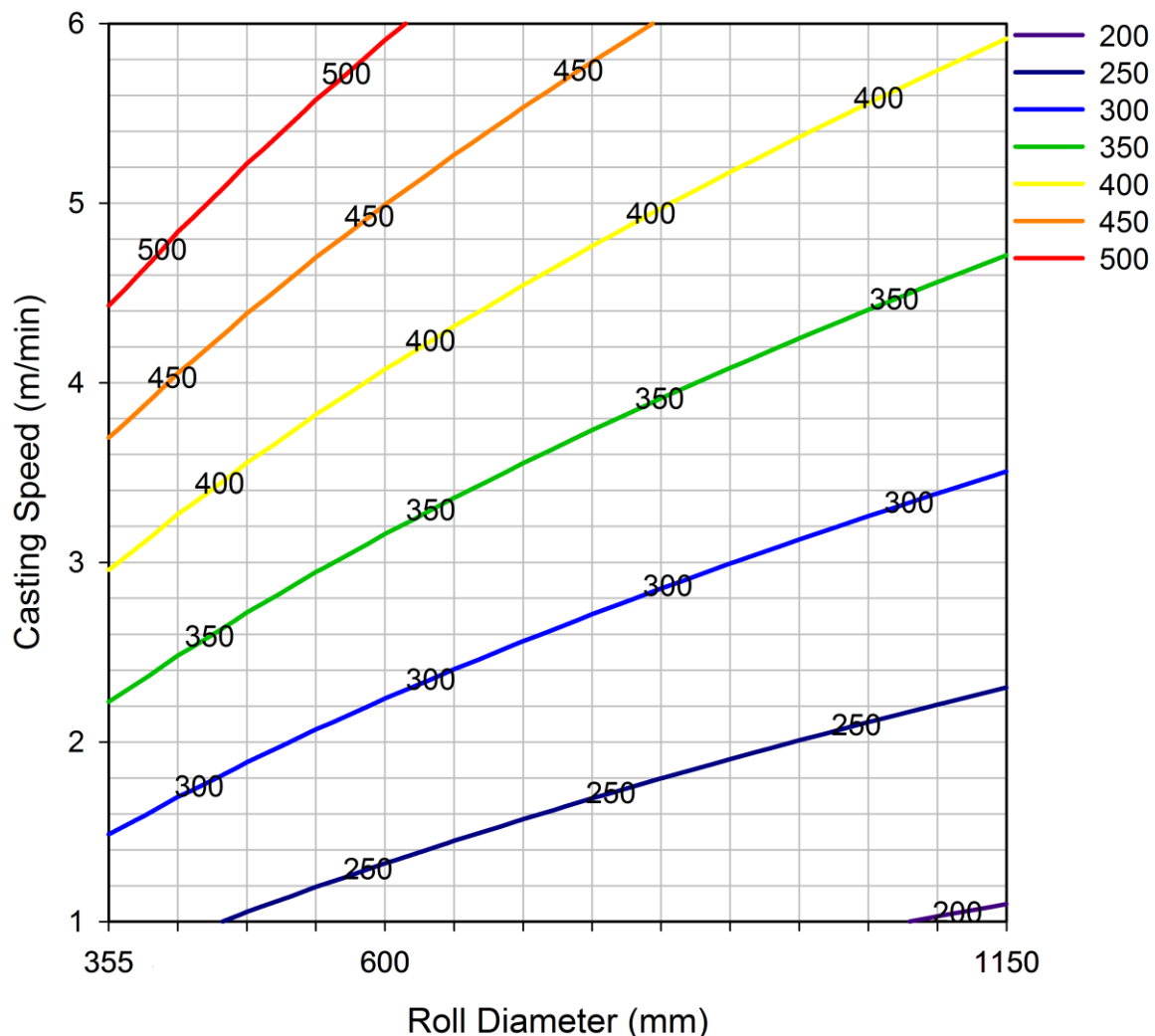


Figure 8-15- Contour map showing the effect of casting speed and roll diameter during TRC on strip center-line exit temperature.

In addition to the exit temperature, casting speed and roll diameter also affect other aspects of the solidification behavior of the strip during TRC. Figure 8-16, shows the effect of roll diameter and casting speed on the mushy zone thickness at the center-line ( $\ell_3$  in Figure 5-1). Referring to Figure 8-16, the width of the mushy zone is very sensitive to the casting speed but relatively insensitive to the roll diameter. This may have implications for the formation of center-line segregation which can form as the width of the mushy zone is increased [28, 33].

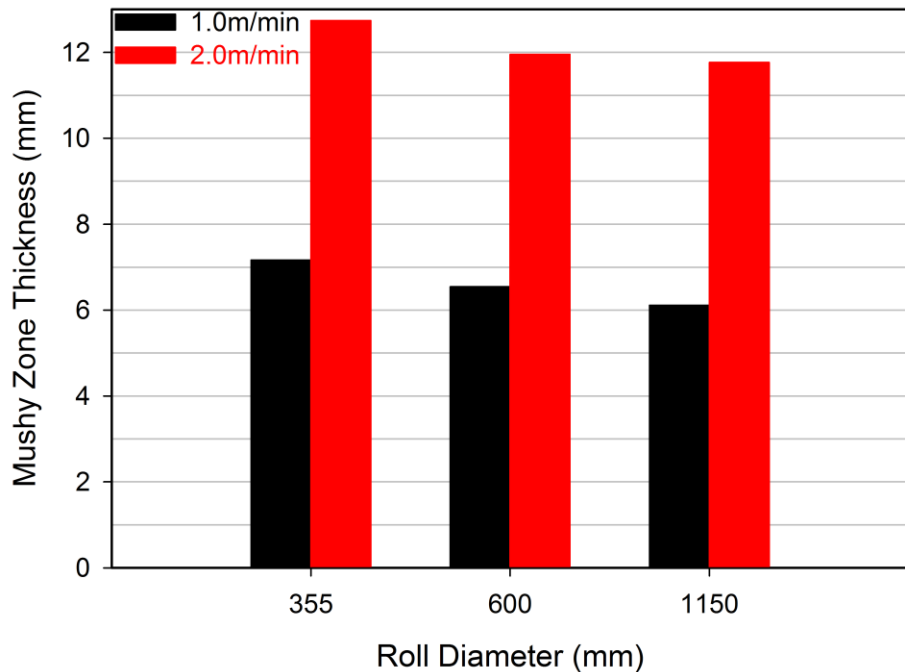


Figure 8-16- Model-predicted effect of casting speed and roll diameter on the mushy zone thickness at the center-line.

Figure 8-17 shows the effect of roll diameter on the average solidification cooling rate at the center-line and strip surface for  $v=2.0\text{m}/\text{min}$  for three caster set-ups. As seen in Figure 8-17, as the roll diameter increases, the SDAS microstructure will decrease slightly near the surface but doesn't affect the SDAS near the strip center-line.

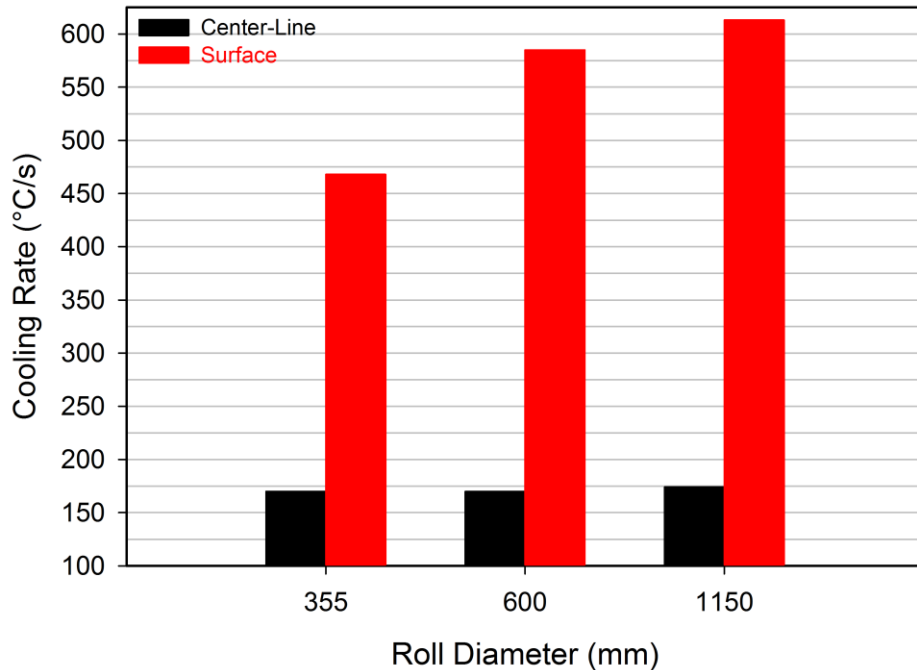


Figure 8-17- Model-predicted effect of roll diameter on the average solidification cooling rate.

The study done by Dunar *et al.* [130] on the TRC of aluminum 3003 by two different caster set-ups is in a very good agreement with the current study. In their study, two casters with roll diameters of 650 and 1100mm were employed to cast the aluminum strip. The results showed that by scaling up the caster no significant change in center-line segregation or in microstructure was observed.

### 8.2.2 Surface Normal Stress

Figure 8-18 illustrates the effect of roll diameter on the surface normal stress at a casting speed of  $v=2.0\text{m/min}$  on a normalized x-axis from entry (0) to exit (1) of the roll bite. In contrast to the thermal history of the cast strip, the mechanical behavior experienced by the strip is significantly influenced by the roll diameter. Enlarging the roll diameter, leads to

development of higher stress level at the strip surface. Part of the reason is due to the thermal behavior of the material; solidification is accomplished earlier on in the roll bite and consequently more solid material experiences plastic deformation as shown in Figure 8-19. Moreover, lower strip temperatures are obtained for larger roll diameters and there is a strong effect of temperature on the material flow stress.

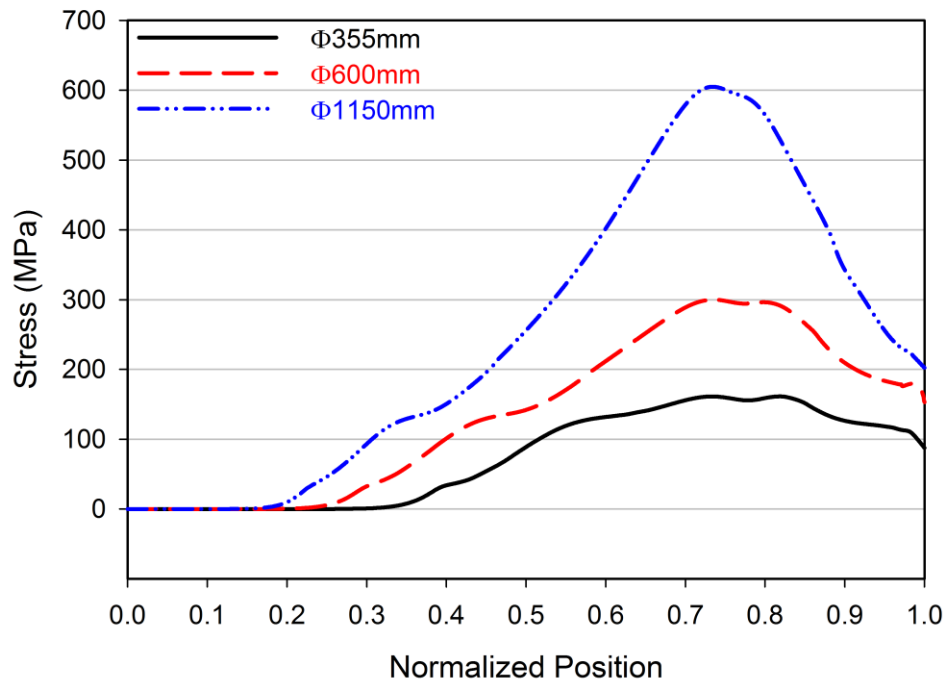


Figure 8-18- Model-predicted effect of roll diameter on the surface normal stress at  $v=2.0\text{m/min.}$

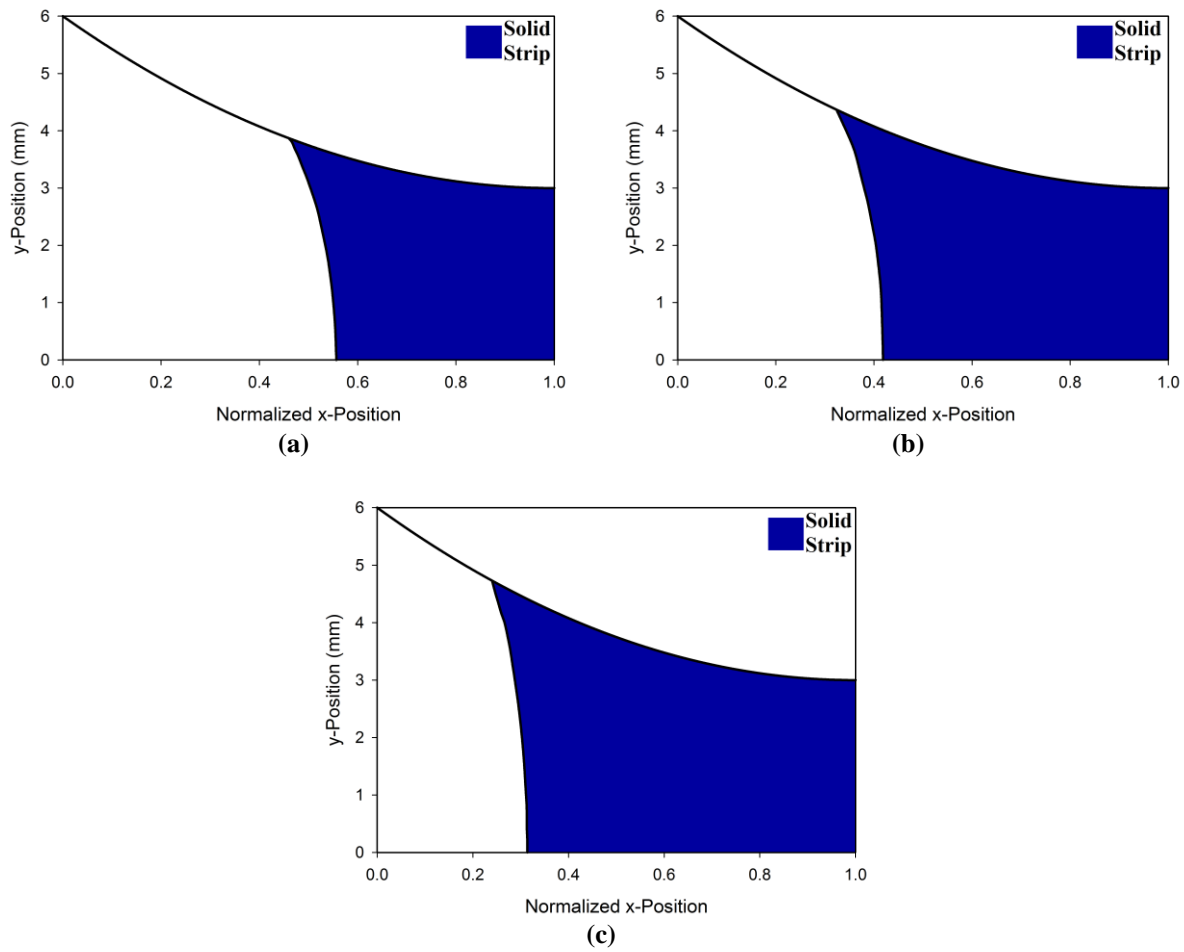


Figure 8-19- Model-predicted amount of solidified material in the roll bite for a roll diameter of a) 355mm, b) 600mm and c) 1150mm at  $v=2.0\text{m/min}$ .

### 8.2.3 Effective Strain at the Center-Line

In Figure 8-20 the effect of roll diameter on the effective strain at the center-line at  $v=2.0\text{m/min}$  is shown. Referring to Figure 8-20, by increasing the roll diameter the effective strain development starts at a point closer to the roll bite entry since solidification occurs earlier. The effect of roll diameter on the effective strain is not as great as the surface normal stress as the total nominal strain for all cases is limited to 50%. Dynamic recrystallization

during hot rolling can be affected by the hot deformed strain and the results suggest that roll diameter doesn't have a significant impact on it, which is in good agreement with the study done by Dunar *et al.* [130].

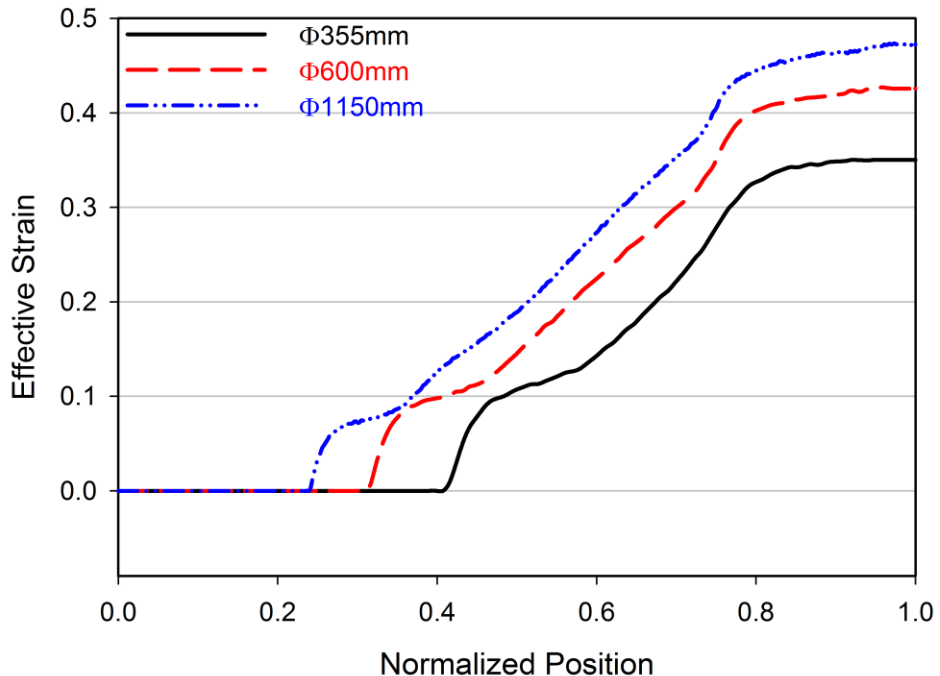


Figure 8-20- Model-predicted effect of roll diameter on the effective strain at the center-line for  $v=2.0\text{m/min}$ .

### 8.2.4 Roll Separating Force

Figure 8-21 illustrates the predicted roll separating force per unit width of the strip versus casting speed for different roll diameters. Roll separating force per unit width also follows the same trend as shown by Equation (8-2). Table 8-7 shows the corresponding relationship for each roll diameter.

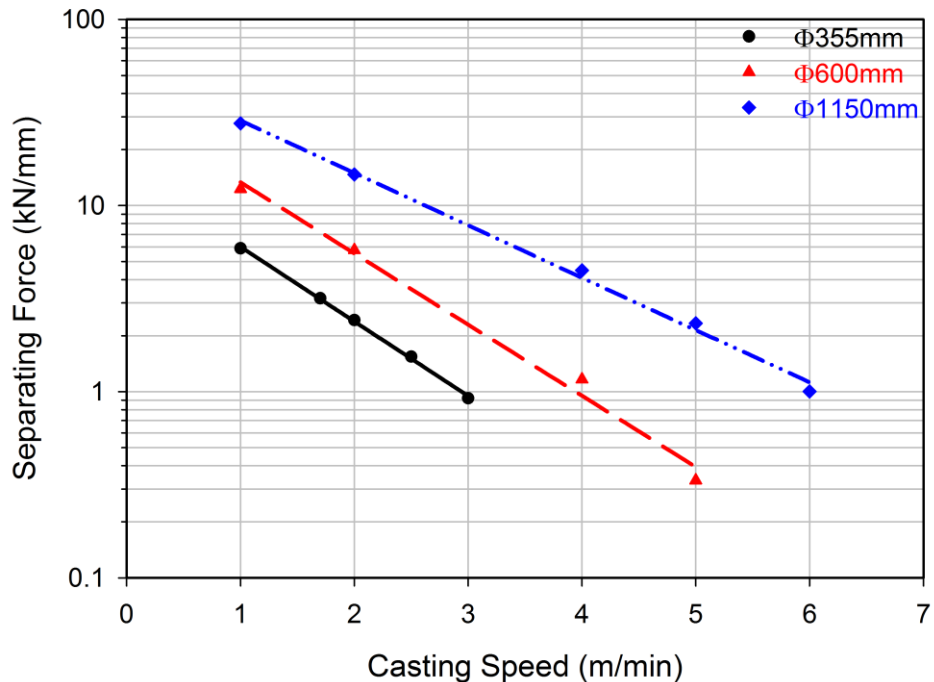


Figure 8-21- Model-predicted roll separating force per unit width of the strip for different casting speeds and roll diameters.

Table 8-7- Separating force (SF) per unit width of the strip -casting speed ( $v$ ) relationship

Roll Diameter (mm)	Force-Speed Relationship
355	$SF = 15.137 \exp(-0.924v)$
600	$SF = 32.206 \exp(-0.881v)$
1150	$SF = 54.744 \exp(-0.648v)$

The integrated effect of roll diameter and casting speed on the separating force is shown by Equation (8-4). Using this equation for roll diameters in the range of 355mm to 1150mm the separating force can be predicted.

$$SF = 0.028D^{1.0827} \exp\left(-\frac{5.8923v}{D^{0.309}}\right) \quad (8-4)$$

where  $SF$  is the roll separating force per unit width of the strip (in kN/mm),  $v$  is casting speed (in m/min) and  $D$  is roll diameter (in mm).

Roll separating force is a typical parameter measured during TRC casting. This parameter can be correlated to the amount of plastic deformation experienced by the cast strip during the process. A relationship between roll separating force and maximum effective strain at the center-line was determined. Figure 8-22 illustrates the maximum effective strain at the center-line versus roll separating force for each roll diameter. The correlation between two parameters for each set-up follows a logarithmic trend as shown by Equation (8-5). The corresponding constants are presented in Table 8-8.

$$\varepsilon_{eff-max} = \gamma \ln(SF) + \delta \quad (8-5)$$

where  $\varepsilon_{eff-max}$  is the maximum effective strain at the center-line and  $\gamma$  and  $\delta$  are constants.

Table 8-8- Maximum effective strain at the CL ( $\varepsilon_{eff-max}$ ) - separating force ( $SF$ ) relationship

<b>Roll Diameter (mm)</b>	<b>Effective Strain-Force Relationship</b>
355	$\varepsilon_{eff-max} = 0.2322 \ln(SF) + 0.1485$
600	$\varepsilon_{eff-max} = 0.1586 \ln(SF) + 0.1517$
1150	$\varepsilon_{eff-max} = 0.1646 \ln(SF) + 0.0213$

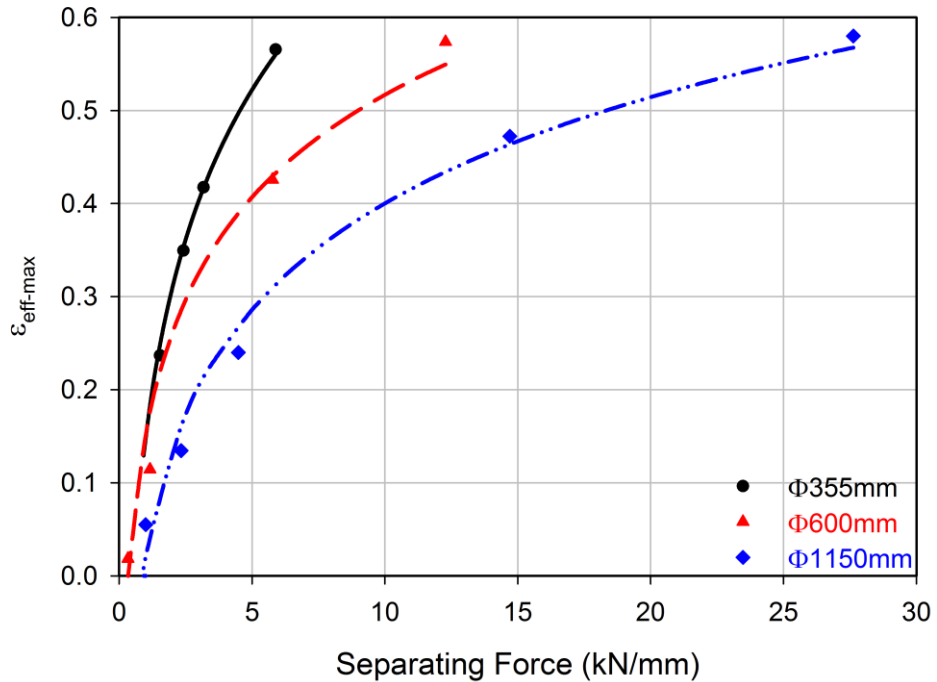


Figure 8-22- Model-predicted relationship between maximum effective strain at the center-line ( $\epsilon_{eff\text{-}max}$ ) and roll separating force for different roll diameters.

### 8.3 Defect Formation

As outlined earlier, two undesirable micro-defects formed during TRC of magnesium alloys include center-line and inverse segregation. Using the validated mathematical model, this section outlines some ideas around the effect of TRC parameters on the propensity to form these defects for AZ31.

#### 8.3.1 Center-Line Segregation

The validated mathematical model was used to try and more fully understand which process conditions will lead to defect formation based on some of the proposed mechanisms.

Figure 8-23 shows a typical contour map of the solidification profile through the strip thickness in the roll bite for  $SB=32.5\text{mm}$  ( $\Phi 355\text{mm}$ ) and  $v=3.0\text{m/min}$ . Once the liquid metal (red region) enters the roll bite and is in contact with the roll surface, heat extraction begins and the liquid temperature drops quickly to the liquidus. Moving along the arc of contact, heat extraction from the strip continues and the solid and liquid metal exists together in the mushy zone (yellow region). The solid shell grows in thickness as it moves toward the exit region until full solidification of the strip is achieved.

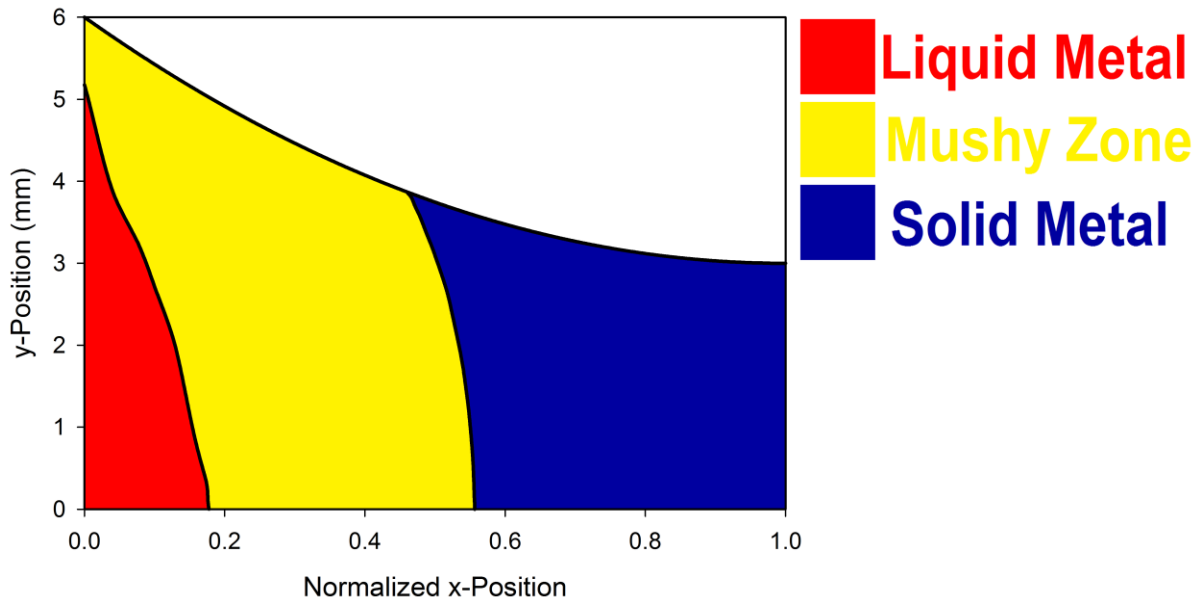


Figure 8-23- Model-predicted solidification profile contour map for  $SB=32.5\text{mm}$  and  $v=3.0\text{m/min}$ .

Referring to Figure 8-23, the widest part of the mushy zone occurs along the center-line. The fraction solid profile at the center-line is a key parameter to understand center-line segregation and its sensitivity to TRC process parameters. The “*Scheil Equation*” [131] is a well-known technique to describe solute redistribution during solidification of an alloy. This approach approximates non-equilibrium solidification by assuming a local equilibrium of the advancing solidification front at the solid-liquid interface. Unlike equilibrium solidification, the Scheil equation assumes solute does not diffuse back into the solid and is rejected completely into the liquid. Complete mixing of solute in the liquid is also assumed as a result of convection and/or stirring. A simplification has been applied to model solute distribution in magnesium alloy AZ31 and the binary phase diagram of Mg-Al is assumed to predict the aluminum concentration along the mushy zone instead of the ternary Mg-Al-Zn system, as shown by Equation (8-6) [131].

$$\frac{C_l}{C_0} = \frac{1}{1 - pf_s} \quad (8-6)$$

where  $C_l$  is the solute concentration in the liquid,  $C_0$  is the initial concentration of the solute (here 3wt.%),  $f_s$  is the solid fraction and  $p$  is complementary distribution coefficient and defined as  $p = 1 - K$  where  $K$  is the partition coefficient (=0.2 for AZ31 [123]). Referring to Equation (8-6), for temperatures above the liquidus, the solute concentration in the liquid is equal to the initial concentration. As the liquid temperature reaches the liquidus and solidification starts, the amount of solute in the liquid changes based on the change in the liquidus line; and, since the solubility of the alloying element in liquid material is higher than the solid material, the solute is rejected at the solidification front from the solid to the liquid phase. By continuing the solidification process and increasing the solid, the liquid metal becomes richer in solute. At the last stage of freezing the  $C_l$  approaches 15wt.%.

Figure 8-24 illustrates the solid fraction profile along the center-line for  $SB=32.5\text{mm}$  for different casting speeds. The “S” shape solid fraction profile gets wider as the casting speed increases. In other words, solidification takes place on a longer position at higher

casting speed. The corresponding aluminum concentration ( $C_l$ ) at the center-line is shown in Figure 8-25.

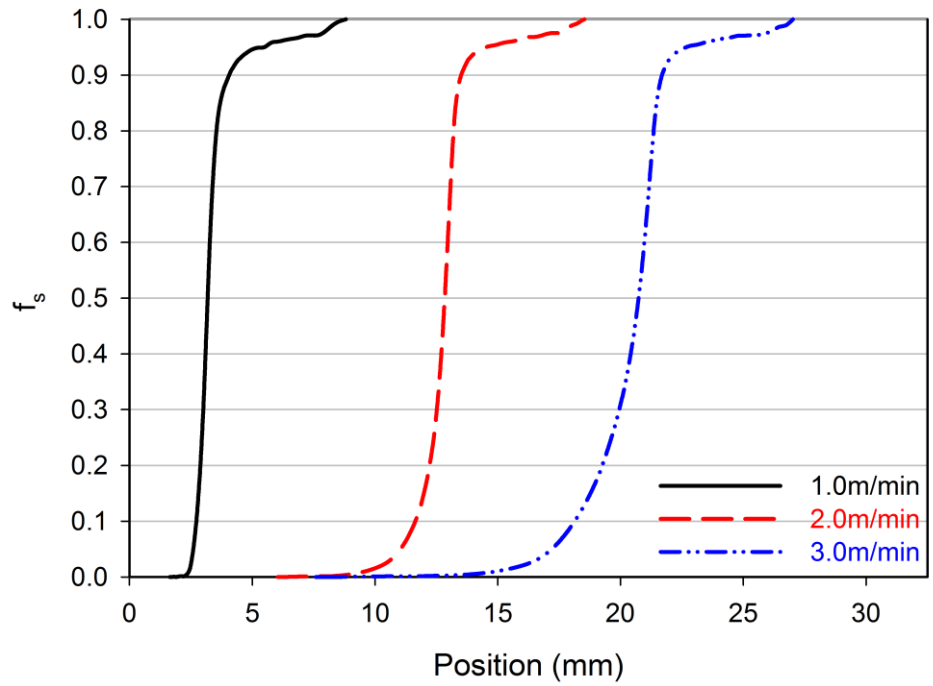


Figure 8-24- Model-predicted solid fraction at the center-line for  $SB=32.5\text{mm}$ .

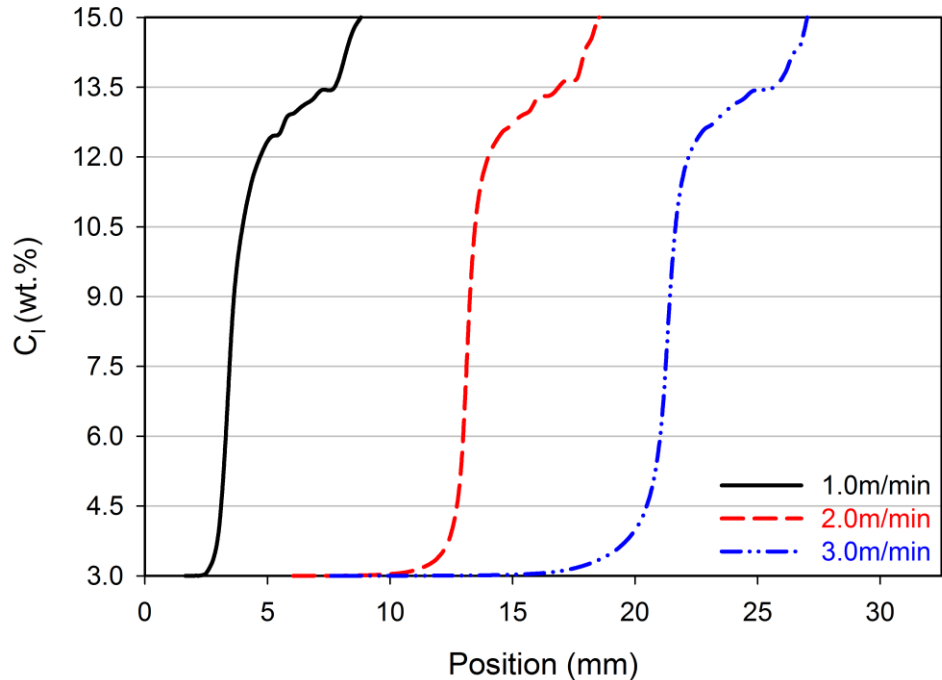


Figure 8-25- Model-predicted solute distribution at the center-line for  $SB=32.5\text{mm}$ .

The results through Figure 8-25 show that regardless of the casting speed, the solute concentration in the liquid metal varies in the range of 3.0-15.0wt.% in the mushy zone. By increasing the casting speed, the solute concentration variation occurs on a deeper mushy zone and solidification of such liquid metal leads to variation of composition on a longer distance. On the other hand, running the TRC process at higher speeds reduces the time for post-solidification diffusion of the solute in the solid state and the chance of redistribution of aluminum content at the center-line decreases. Consequently, the potential of center-line segregation formation increases. The results from Figure 8-24 and Figure 8-25 suggest that the key parameter in center-line segregation formation is the mushy zone thickness ( $\ell_3$  in Figure 5-1).

Figure 8-26 shows how the mushy zone thickness is affected by set-back distance and casting speed. As observed in Figure 8-26, by increasing the casting speed the mushy zone

thickness increases for all cases. The appearance of a deeper mushy zone represents a higher propensity of the strip to form center-line segregation, which is in agreement with the trend observed in the literature [33]. Moreover, increasing the set-back distance reduces the mushy zone thickness. The effect of final exit thickness on the mushy zone thickness is more pronounced than the entry thickness of the liquid into the roll bite. As seen in Figure 8-26, increasing the set-back distance from 32.5mm to 41.8mm by increasing entry thickness or nozzle opening has only a slight effect on the mushy zone thickness; while, decreasing the final exit thickness to create the same set back distance has a much more pronounced effect. This trend suggests that casting at higher set-back distances reduces the probability of center-line segregation.

Figure 8-27 represents the influence of roll diameter on the mushy zone thickness. In contrast to set-back distance, the roll diameter does not affect the mushy zone thickness significantly. Hence, strips cast using larger rolls will also contain some center-line segregation as those produced with small lab scale rolls. This is in good agreement with the study done by Dunar *et al.* [130]. Their study shows that increasing the roll diameter from 650mm to 1100mm for TRC of AA3003 aluminum alloy doesn't eliminate the center-line segregations.

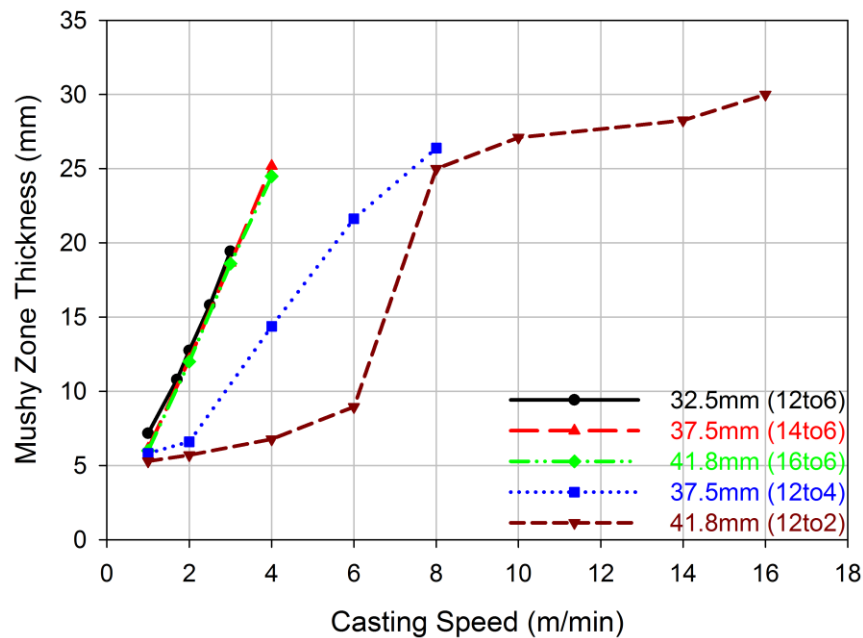


Figure 8-26- Model-predicted mushy zone thickness for different set-back distances and casting speeds.

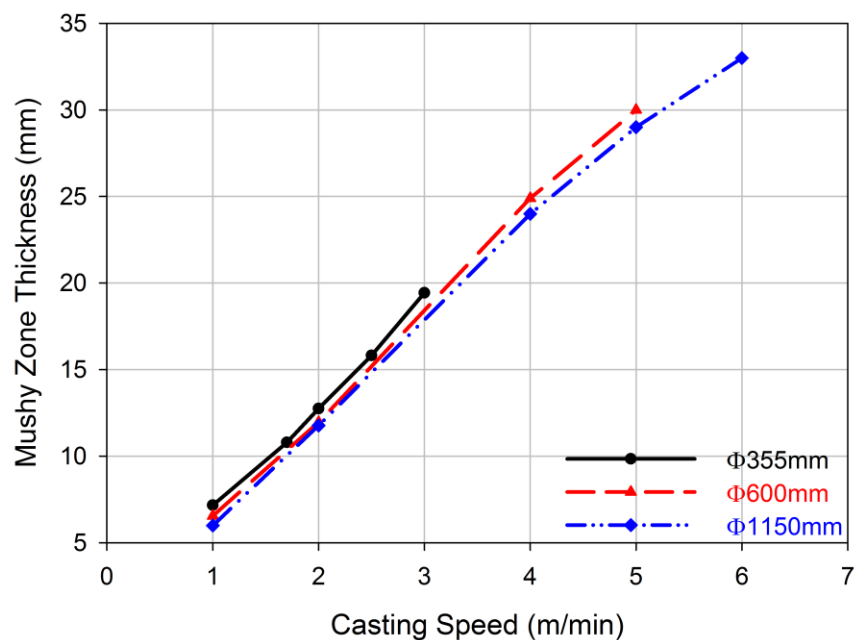
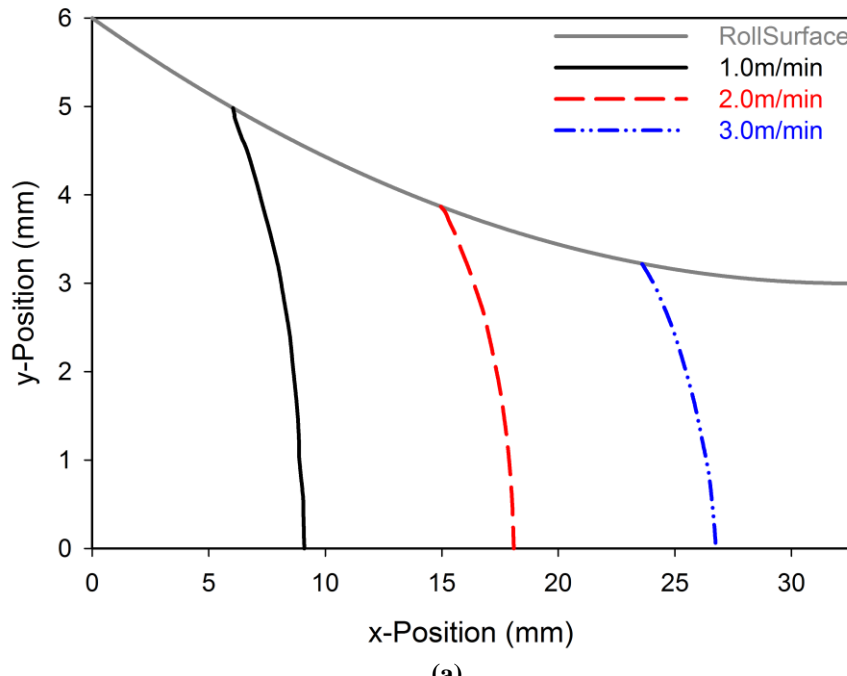


Figure 8-27- Model-predicted effect of scaling up on the mushy zone thickness.

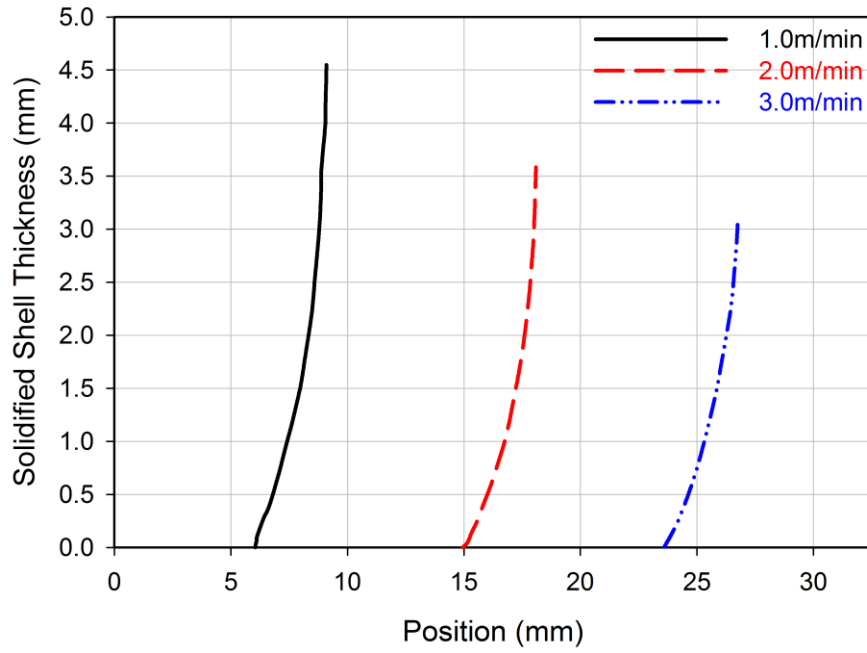
### **8.3.2 Inverse Segregation**

As mentioned before, by increasing the casting speed, the propensity of the twin roll cast strip to inverse segregation formation increases. The proposed mechanisms for inverse segregation formation consider two key parameters; the “path” for fluid flow from the center-line toward the surface and the “driving force” for such flow. The former is determined by the thickness of the solidified shell on the roll surface and the latter is caused by the rolling force (proposed mechanism by Prof Hunt Group) or the low pressure zone on the strip surface (proposed mechanism by the Norwegian Group).

Figure 8-28 shows the development of the solid shell profile on the roll surface during the process for  $SB=32.5\text{mm}$  under different casting speeds and the corresponding shell thickness along the roll. As expected, by increasing the casting speed, solidification occurs over a longer distance and the formation of the solid shell is delayed until closer to the exit point of the caster. The existence of a thinner shell can provide a shorter path for the liquid flow and hence may promote inverse segregation formation.



(a)



(b)

Figure 8-28- Model-predicted effect of casting speed on the a) solidified shell profile and b) corresponding shell thickness for  $SB=32.5\text{mm}$ .

Investigation of the roll separating force shows that by increasing the casting speed the roll separating force decreases since less solid material experienced plastic deformation (Figure 8-10 and Figure 8-21). Moreover, the level of the mean (hydrostatic) stress above the solid shell does not change significantly.

Figure 8-29 illustrates the yy-stress (compressive stress) profile at the center-line for  $SB=32.5\text{mm}$  and  $v=1.0\text{m/min}$ . The solidification contour map associated with this casting condition is also shown in the same Figure. As observed in Figure 8-29, prior to the liquidus point the stress is zero since the stress is not developed in the liquid metal. Once the temperature reaches the coherency temperature ( $T_C$ ), the solid network in the mushy zone is capable of sustaining stress and strain and stress starts to develop. The modeled stress profile at the center-line shows that the stress in the mushy zone beyond the coherency temperature reaches a peak value then decreases as the material cools down to the solidus and lower temperatures. The second peak of the stress occurs in the fully solid material due to relative motion between the roll surface and cast material. As mentioned previously, at the center-line the material is being squeezed in the mushy zone since it is experiencing a reduction in thickness. The high strain rate experienced by the material beyond the coherency temperature leads to a peak stress. This compressive peak stress interacts with the remaining liquid in the mushy zone and can squeeze this solute-rich liquid to the inter-dendritic regions in the solidified shell and push it out onto the roll surface.

Figure 8-30 depicts the yy-peak stress in the mushy zone along the set-back distance affected by casting speed for  $SB=32.5\text{mm}$ . The results show the fact that running the twin roll caster with higher speeds does not affect the yy-peak stress significantly; it ranges between 90-110MPa while casting speed varies between 1.0-3.0m/min. Referring to Figure 8-28, by increasing the casting speed, the yy-peak stress is applied to a thinner solidified shell to squeeze the liquid metal through it. In other words, although the yy-peak stress does not change much with casting speed, the solidified shell above it is thinner. Therefore, the interaction between the yy-peak stress and the solidified shell thickness at the peak stress

position can possibly be considered as an important parameter for inverse segregation formation. This interaction is defined as a new parameter; *Stress/Thickness* (in MPa/mm); calculated by dividing yy-peak stress by the thickness of the solid shell at the point where peak stress occurs. Higher values for *Stress/Thickness* imply a higher propensity to get inverse segregation. Figure 8-31 shows the effect of casting speed on the *Stress/Thickness* for  $SB=32.5\text{mm}$ ; as proposed by other researchers [28, 33, 68, 70-76] increasing the casting speed increases the propensity of the cast strip to inverse segregation formation.

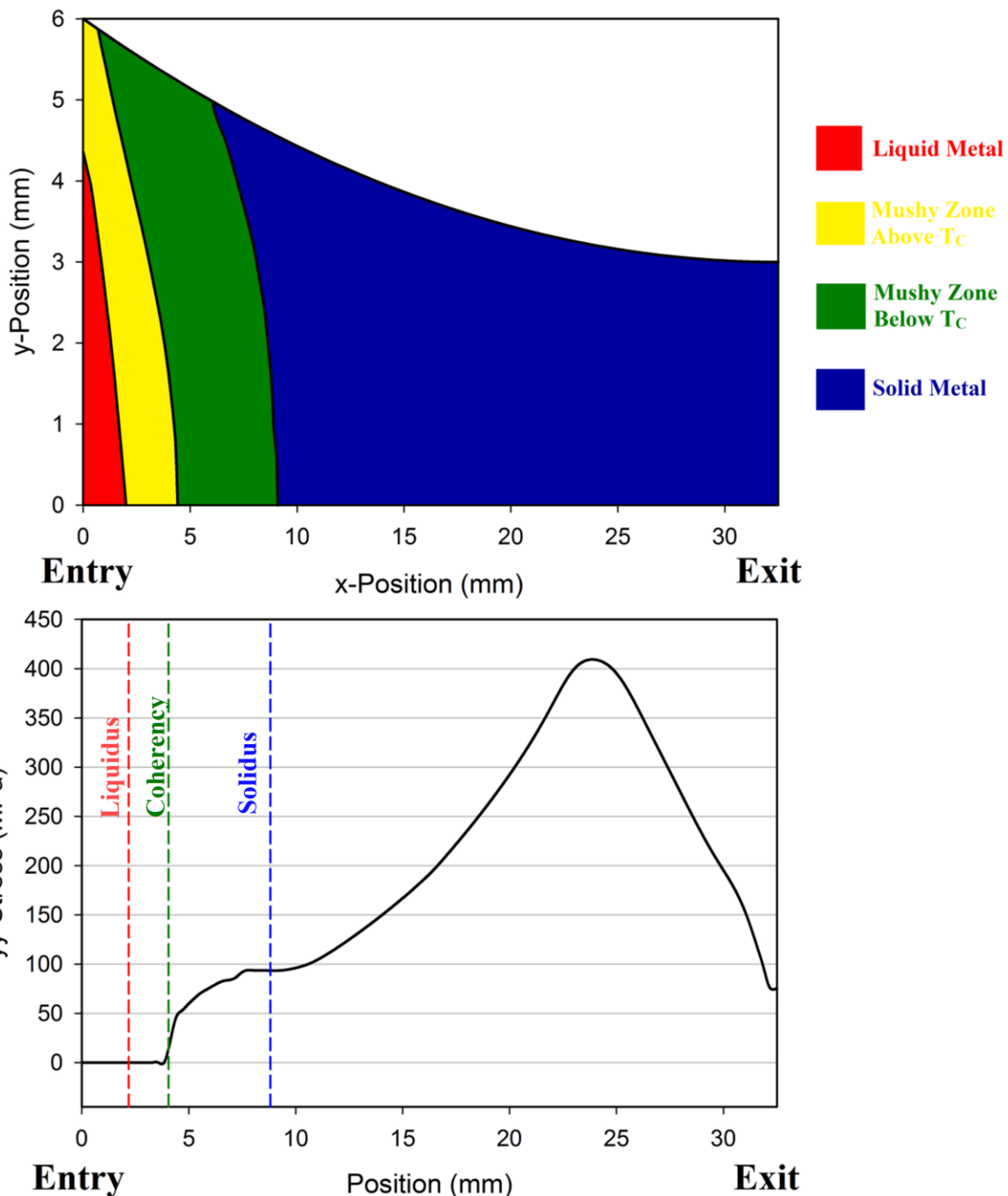


Figure 8-29- Model-predicted yy-stress (compressive stress) development at the center-line (lower graph) in conjunction with the corresponding solidification contour map (upper graph) for  $SB=32.5\text{mm}$  and  $v=1.0\text{m/min}$ .

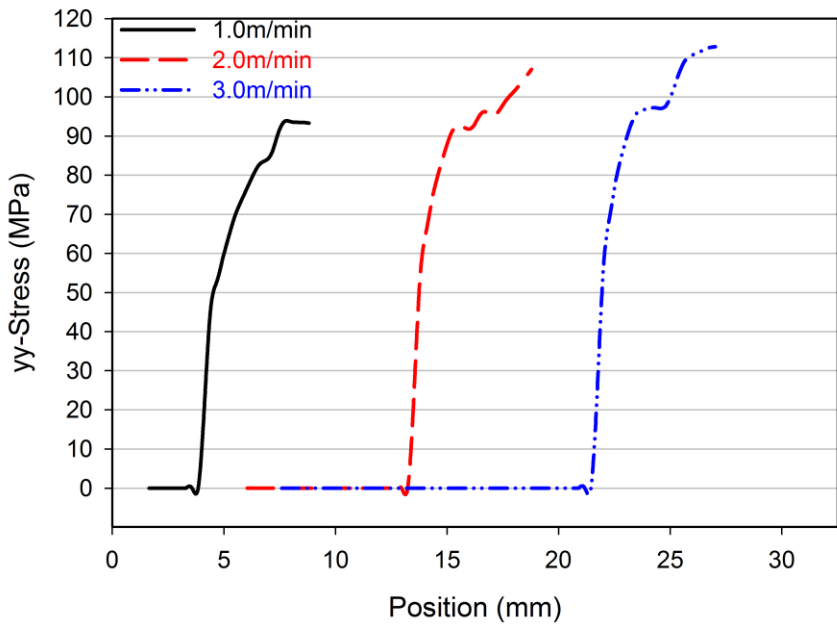


Figure 8-30- Model-predicted effect of casting speed on the yy-peak stress in the mushy zone for  $SB=32.5\text{mm}$ .

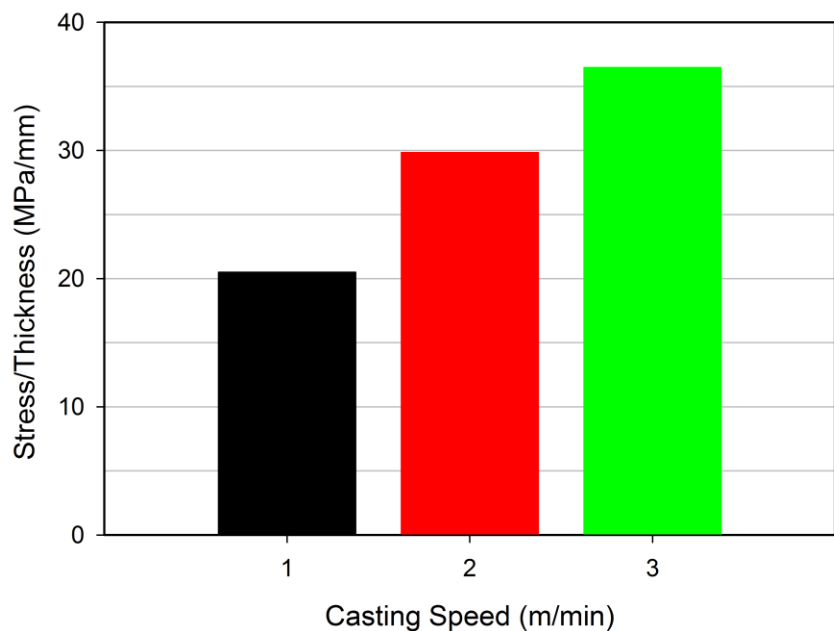


Figure 8-31- Model-predicted propensity of cast strip to inverse segregation affected by casting speed for  $SB=32.5\text{mm}$ .

In Figure 8-32 the influence of set-back distance on the inverse segregation propensity for  $v=2.0\text{m/min}$  is shown. Increasing the set-back distance reduces the *Stress/Thickness* values and consequently the conditions for defect-free strip production improve. Assessment of the thermal history of the strips cast with various set-back distances and identical casting speeds showed that by increasing the set-back distance, the solidification process occurs over a shorter distance. As a consequent, the thickness of the solid shell on the roll surface increases. This leads to lower values of *Stress/Thickness*. As observed in Figure 8-32, the effect of exit strip thickness on inverse segregation is more pronounced than the nozzle opening height. Hence, these results suggest that casting strips with lower final thicknesses improves the strip final quality in terms of inverse segregation.

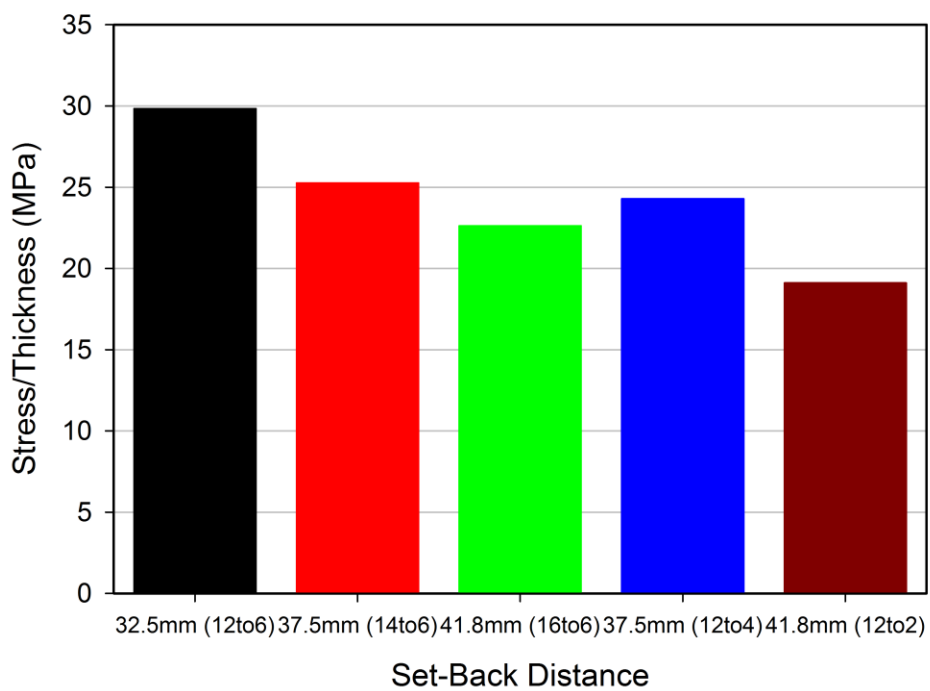


Figure 8-32- Model-predicted effect of set-back distance on the inverse segregation propensity for  $v=2.5\text{m/min}$ .

Figure 8-33 shows the effect of roll diameter on the inverse segregation propensity for  $v=2.0\text{m/min}$ . Since a longer arc of contact is provided for heat transfer by increasing the roll diameter, the thickness of the solidified shell on the roll surface increases for identical casting speeds. So, lower values for *Stress/Thickness* are obtained and it's predicted by scaling up the caster the quality of the cast strips can potentially be improved.

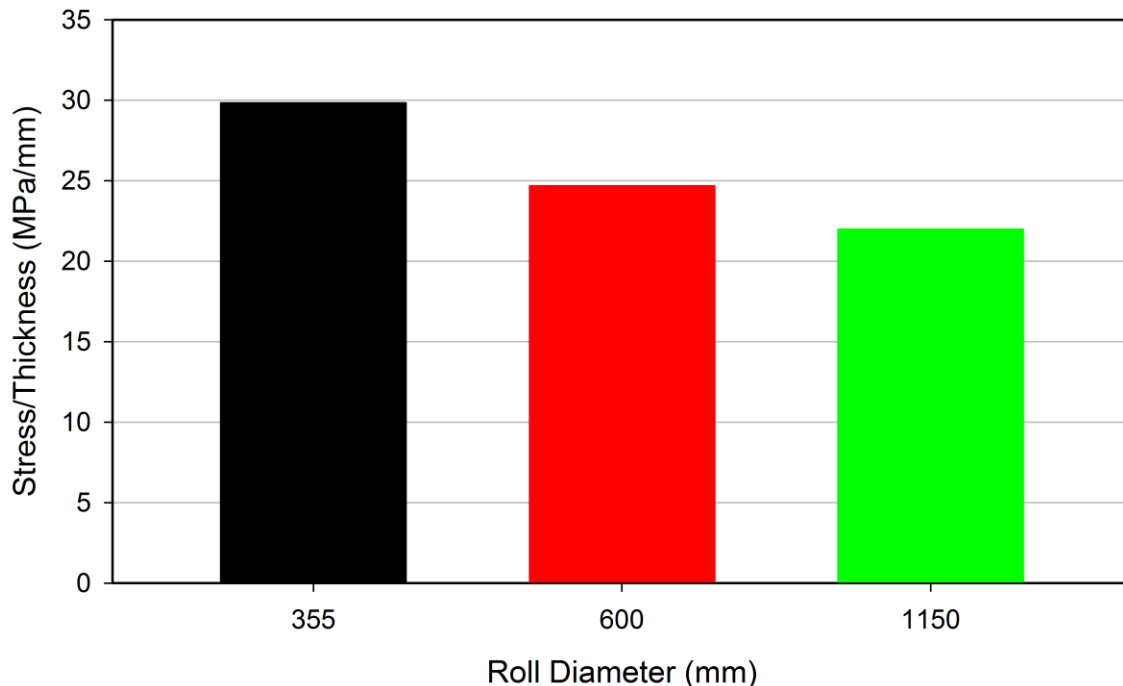


Figure 8-33- Model-predicted effect of caster scale up on the inverse segregation propensity.

### 8.3.3 A Comparison to Literature

Research in this area has resulted in the creation of various process maps [28, 33, 68, 70-76] to delineate the range of casting conditions that can lead to defect formation and those result in high quality strip production for aluminum alloys. Figure 8-34 illustrates an example of a process map generated for TRC of AA3105 aluminum alloy. As observed, the casting conditions are mentioned in terms of final gauge (strip final thickness) and specific load (separating force divided by strip width). This process map suggests that reducing the strip final thickness and increasing the casting speed which leads to lower specific loads increases inverse segregation formation probability.

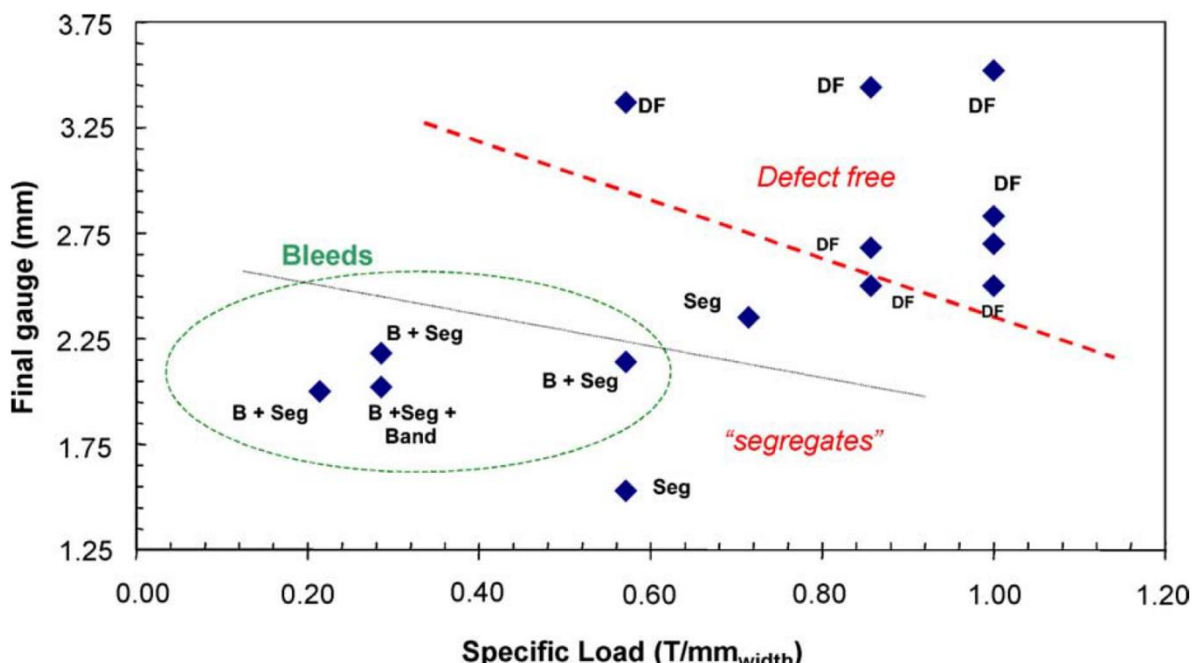


Figure 8-34- Defect map for AA3105 aluminum alloy TRC (B: inverse segregation, Seg: center-line segregation, DF: defect free) [33].

Figure 8-35 shows the data points modeled in this study for an entry height=12mm. A qualitative comparison between Figure 8-34 and Figure 8-35 shows that there is a higher propensity to inverse segregation formation on the lower left corner of the graph shown in Figure 8-35 which seems to be in contrast with the predication in the previous section; it was suggested that for a given casting speed reducing the final thickness decreases the defect formation propensity. It should be clarified that the important parameter introduced previously was *Stress/Thickness* while the studied parameter here is the specific load. So, to integrate these two parameters together, Figure 8-35 was reproduced as a contour map as shown in Figure 8-36.

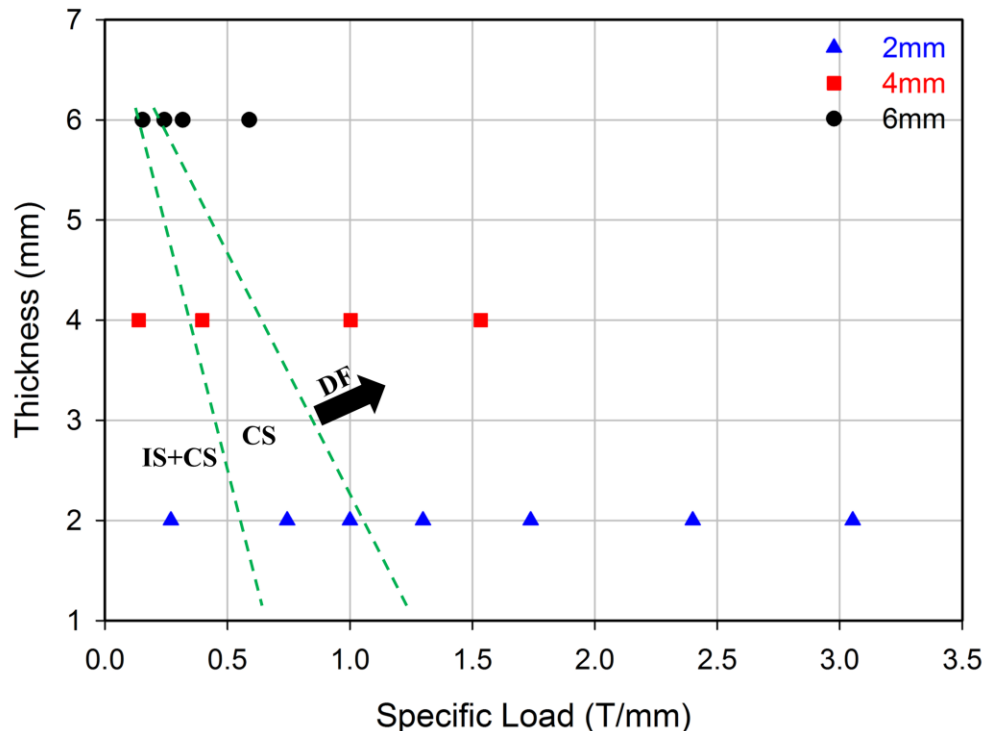


Figure 8-35- Propensity of modeled data points in the current study to defect formation for an entry height=12mm (IS: inverse segregation, CS: center-line segregation, DF: defect free).

As mentioned earlier, by reducing the final thickness for a given entry height, the process can be run with higher casting speeds without failure (in terms of the exit temperature). As seen in Figure 8-36, the highest casting speeds are achievable for a final thickness=2mm and consequently the lowest specific load are obtained for such conditions. Meanwhile, the highest *Stress/Thickness* values are predicted for the same conditions. Referring to Figure 8-36, the highest values of *Stress/Thickness* or inverse segregation propensity are located on the lower left corner of the graph which is in agreement with the trend presented in Figure 8-34. The modified mechanism proposed in the previous section should be considered for identical casting speeds. In other words, if the process is run with the same speed for lower final thickness the propensity to defect formation decreases. On the other hand, controlling the process for thin strips ran at low speeds is so complicated since the process could be failed due to solidification inside the nozzle. Therefore, the process for thinner strips is conducted with high speeds (this also increases the productivity) and as a consequent the probability of inverse segregation formation increases. This comparison confirms the reliability of the new parameter *Stress/Thickness*.

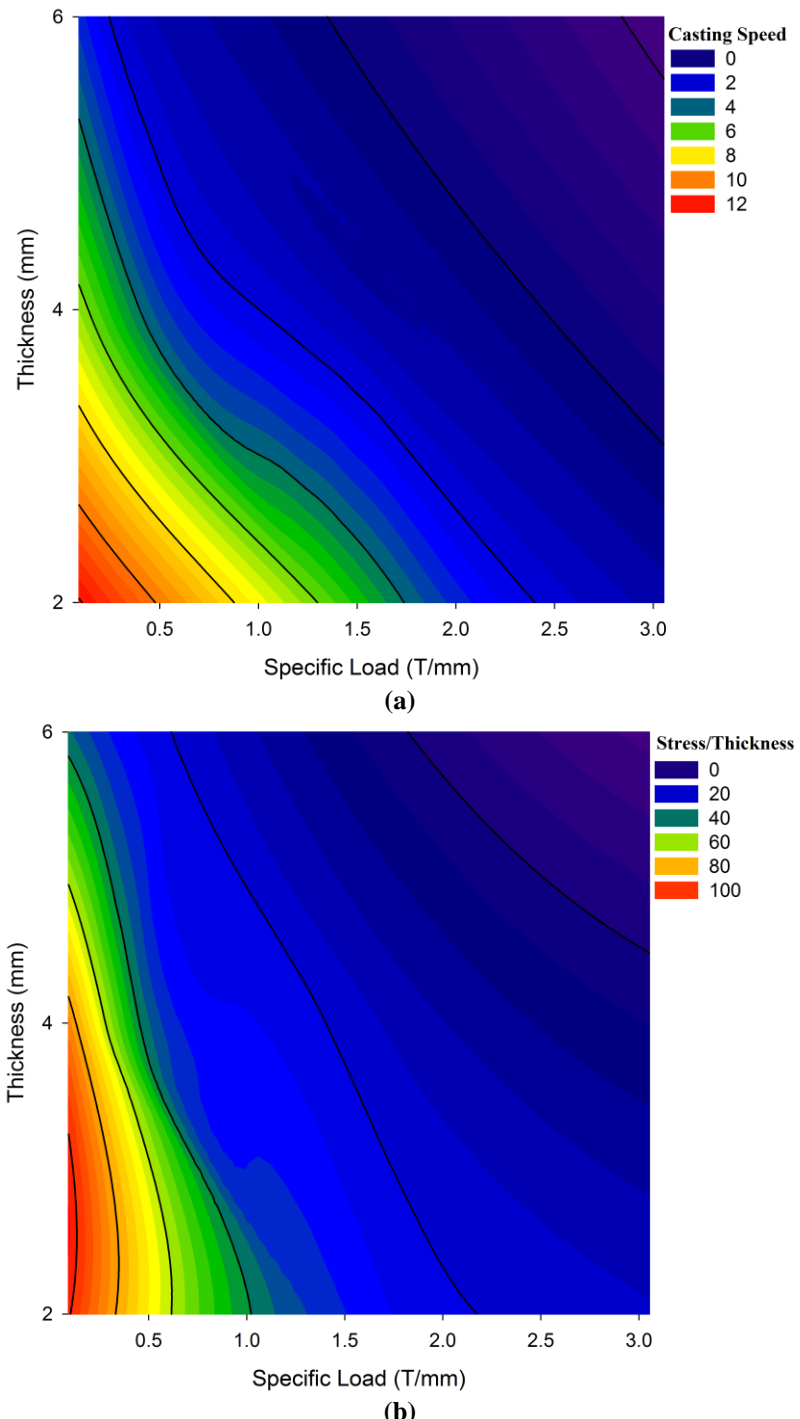


Figure 8-36- Model-predicted contour map of strip final thickness-specific load- a) casting speed and b)  
*Stress/Thickness* for an entry height=12mm.

## **8.4 Summary**

- 1- Increasing the casting speed and casting with shorter set-back distances causes higher temperature at the exit point of the caster. The relation between the casting speed and exit temperature seems to be linear and the exit temperature is more sensitive to set-back distance at higher casting speeds.
- 2- A lower level of normal stress on the strip surface is achieved when casting at higher speeds. Moreover, increasing the set-back distance leads to a higher peak stress and a shift in where the stress development starts towards the roll bite entry zone.
- 3- The roll separating force has a similar trend to strip surface normal stress; higher values are achieved at lower casting speeds and longer set-back distances. The relation between roll separating force and casting speed follows an exponential trend.
- 4- The cast strip experience higher effective strain at the center-line when it is cast with lower casting speed and longer set-back distance.
- 5- Changing the set-back distance by varying the final thickness has a more significant effect on the thermo-mechanical results than altering the nozzle entry height.
- 6- As the roll diameter used to perform TRC is increased, slightly higher casting speeds are achievable. Moreover, for a given casting speed, increasing the roll diameter should lead to a lower propensity of center-line segregation in the strip.
- 7- The surface normal stress level increases by increasing the roll diameter during TRC. Consequently, the amount of plastic deformation experienced by the cast strip goes up which could affect the amount of dynamic recrystallization that occurs in the strip during TRC.
- 8- Roll separating force follows the same trend as the surface normal stress; higher for bigger roll diameter. The roll separating force has a relationship to the total effective

strain at the center-line; using correlations developed, the roll separating force measured during the process can be used as a guide to help predict the amount of plastic deformation that occurs in the strip.

- 9- The key parameter for center-line segregation formation seems to be the size of the mushy zone at the center-line; deeper mushy zone increases the propensity to this defect. Increasing the set-back distance leads to the presence of a shorter mushy zone which reduces the risk of center-line segregation formation. Increasing the set-back distance by reducing the final thickness is more effective than increasing the nozzle opening height. The modeling results showed that scaling up has a minor effect on elimination of center-line segregation.
- 10- The determinant parameter for inverse segregation formation seems to be the interaction between the solidified shell on the roll surface and the yy-peaks stress at the center-line in the mushy zone which squeezes the liquid metal toward the surface. A new parameter was defined as *Stress/Thickness*; higher values indicate more propensity. Increasing the set-back distance leads to reduction of *Stress/Thickness*, more effectively by decreasing the final thickness. Moreover, scaling up also decreases *Stress/Thickness* values.

## Chapter 9

### Summary, Conclusions and Future Work

#### **9.1 Summary and Conclusions**

The objective of this research work was to develop and validate a mathematical model of the Twin Roll Casting Process (TRC) to produce AZ31 strip. The model was then used to provide insight into the process as well as the sensitivity of the product to process parameters and defect formation. The experimental facility studied in this work was the TRC at the Natural Resources Canada Government Materials Laboratory (CanmetMATERIALS) located in Hamilton, ON, Canada.

The model development was conducted in two stages, first a thermal-fluid model was developed by CFD method using the commercial package ANSYS® CFX®. Using this model, a comprehensive study was carried on the thermal history experienced by the strip during TRC for various casting speeds, final thicknesses and *HTCs*. The results showed that more uniform microstructure through thickness in terms of SDAS is obtained by increasing casting speed, increasing strip final thickness and decreasing the *HTC*. Moreover, the validation was performed by comparing the predicted exit strip surface temperature and SDAS through the strip thickness with those measured at CanmetMATERIALS. This validation suggested that the best value for *HTC* for the facility at CanmetMATERIALS is  $11\text{kW/m}^2\text{°C}$ .

In the second stage of the modeling work, a thermal-fluid-stress model developed using the FEM commercial package ALSIM. Employing this software, the thermo-mechanical behavior of the strip during the process were simulated and analyzed. Using this model the effects of casting speed and set-back distance were studied. The thermal-fluid-stress model was then used to study the effect of roll diameter on the TRC process.

The model was then used to correlate TRC casting conditions to the mechanisms proposed for center-line and inverse segregation formation. The results were also compared to the trends and process maps reported in the literature for aluminum TRC. The comparison showed that the proposed mechanisms are in agreement with current ideas for what in terms of defect formation during aluminum TRC.

The following conclusions can be drawn from the thermal-fluid model application:

- 1- The Biot number analysis showed that for *HTCs* higher than  $8\text{kW/m}^2\text{°C}$ , the process is initially dominated by internal heat transfer and as the thickness reduces in the roll bite region the process switches over to external heat transfer domination. For low *HTCs* the process is dominated externally along the whole roll bite region.
- 2- Higher casting speeds, thicker final exit gauges and lower *HTCs* cause the strip to exit with higher temperatures as well as increase the depth of the sump and width of the mushy zone.
- 3- A lower temperature gradient through the strip thickness is achieved by casting at lower casting speeds and reducing the final thickness. The effect of *HTC* on the temperature gradient is negligible.
- 4- The cooling rate which occurs during solidification at the strip surface and center-line decreases by increasing the casting speed.
- 5- More uniform microstructures are obtained by casting at lower speeds, casting the strip with lower final exit thickness and applying a higher *HTC*. The optimum condition in terms of microstructure uniformity is achieved by casting the AZ31 strip to a final thickness of 4mm using a casting speed of 1.0m/min and  $HTC=15\text{kW/m}^2\text{°C}$ , however lower casting speeds can lead to lower productivity.
- 6- The process becomes more sensitive to *HTC* and strip thickness as the casting speed is increased.

The important conclusions of the thermal-fluid-stress model application include:

- 11- Increasing the casting speed and casting with shorter set-back distances causes higher temperature at the exit point of the caster. The relation between the casting speed and exit temperature seems to be linear and the exit temperature is more sensitive to set-back distance at higher casting speeds.
- 12- A lower level of normal stress on the strip surface is achieved when casting at higher speeds. Moreover, increasing the set-back distance leads to a higher peak stress and a shift in where the stress development starts towards the roll bite entry zone.
- 13- The roll separating force has a similar trend to strip surface normal stress; higher values are achieved at lower casting speeds and longer set-back distances. The relation between roll separating force and casting speed follows an exponential trend.
- 14- The cast strip experience higher effective strain at the center-line when it is cast with lower casting speed and longer set-back distance.
- 15- Changing the set-back distance by varying the final thickness has a more significant effect on the thermo-mechanical results than altering the nozzle entry height.
- 16- As the roll diameter used to perform TRC is increased, slightly higher casting speeds are achievable. Moreover, for a given casting speed, increasing the roll diameter should lead to a lower propensity of center-line segregation in the strip.
- 17- The surface normal stress level increases by increasing the roll diameter during TRC. Consequently, the amount of plastic deformation experienced by the cast strip goes up which could affect the amount of dynamic recrystallization that occurs in the strip during TRC.
- 18- Roll separating force follows the same trend as the surface normal stress; higher for bigger roll diameter. The roll separating force has a relationship to the total effective

strain at the center-line; using correlations developed, the roll separating force measured during the process can be used as a guide to help predict the amount of plastic deformation that occurs in the strip.

- 19- The key parameter for center-line segregation formation seems to be the size of the mushy zone at the center-line; deeper mushy zone increases the propensity to this defect. Increasing the set-back distance leads to the presence of a shorter mushy zone which reduces the risk of center-line segregation formation. Increasing the set-back distance by reducing the final thickness is more effective than increasing the nozzle opening height. The modeling results showed that scaling up has a minor effect on elimination of center-line segregation.
- 20- The determinant parameter for inverse segregation formation seems to be the interaction between the solidified shell on the roll surface and the yy-peaks stress at the center-line in the mushy zone which squeezes the liquid metal toward the surface. A new parameter was defined as *Stress/Thickness*; higher values indicate more propensity. Increasing the set-back distance leads to reduction of *Stress/Thickness*, more effectively by decreasing the final thickness. Moreover, scaling up also decreases *Stress/Thickness* values.

## 9.2 Future Work

- 1- More trials are needed for more comprehensive validation; especially, it is a great idea to validate the stress part of the model by comparing the measured and predicted roll separating force. Moreover, some trials with different roll diameters should be performed to validate the model on the effect of roll diameter.

- 2- The effect of casting speed on the *HTC* should be quantified by conducting the TRC process with different casting speeds and comparing the modeled and measured results (the exit temperature and SDAS through thickness). In this study for all cases the *HTC* was assumed as a constant value equal to  $11\text{kW/m}^2\text{°C}$ . Although this value led to a good validation, more accurate knowledge will be obtained by correlating the *HTC* to casting speed.
- 3- The production of accurate process map on defect and defect-free AZ31 twin roll cast strip needs various trials under different conditions to reveal the boundary between defect and defect-free zones.
- 4- The modeling of TRC should be performed in conjunction with thermodynamic database such has FACTSage so that the castability of other magnesium alloy systems and their propensity for defect formation can be studied.

## References

- [1] "Environment Canada", 2012, <http://www.ec.gc.ca/>.
- [2] "NSERC Magnesium Network", 2012, <http://www.magnet.ubc.ca/>.
- [3] "National Highway Traffic Safety Administration (NHTSA)", 2012, <http://www.nhtsa.gov/fuel-economy/>.
- [4] K. U. Kainer, "*Magnesium Alloys and Technology*", WILEY-VCH Verlag GmbH & Co. KG aA, 2003.
- [5] H. E. Friedrich, B. L. Mordike, "*Magnesium Technology – Metallurgy, Design Data, Applications*", Springer, 2006.
- [6] D. Eliezer, E. Aghion, F. H. Froes, "*Magnesium Science, Technology and Applications*", Advanced Performance Materials, 5 (1998) 201-212.
- [7] B. L. Mordike, T. Ebert, "*Magnesium Properties-Applications-Potential*", Materials Science and Engineering A, 302 (2001) 37-45.
- [8] R. E. Brown, "*Magnesium in the 21st Century*", Advanced Materials and Processes, 167-1 (2009) 31-33.
- [9] M. K. Kulekci, "*Magnesium and Its Alloys Applications in Automotive Industry*", International Journal of Advanced Manufacturing Technology, 39 (2008) 851-865.
- [10] F. Czerwinski, "*Magnesium Injection Molding*", New York, Springer US, 2008.
- [11] S. Ehrenberger, H. E. Friedrich, "*Greenhouse Gas Balance of Magnesium Parts for Automotive Applications*", in the 9th International Conference on Magnesium Alloys and their Applications, W. J. Poole, K. U. Kainer (Eds.), Vancouver, BC, Canada, 2012.
- [12] "West High Yield (W.H.Y) Resources", 2012, <http://www.whyresources.com>.
- [13] L. A. Dobrzanski, T. Tanski, L. Cizek, Z. Brytan, "*Structure and Properties of Magnesium Cast Alloys*", Journal of Materials Processing Technology, 192-193 (2007) 567-574.
- [14] I. H. Jung, "*Mg Twin-Roll Casting*", Magnesium Processing Technology Workshop, McGill University, Montreal, 2008.

- [15] W. H. Hunt, “*Technical Cost Model for Magnesium Sheet Production*”, Technical Report, Aluminum Consultants Group Inc., 2005.
- [16] D. Liang, C. B. Cowley, “*The Twin-Roll Strip Casting of Magnesium*”, Journal of the Minerals, Metals and Materials Society, 56-5 (2004) 26-28.
- [17] E. E. M. Luiten, K. Blok, “*Stimulating R&D of Industrial Energy-Efficient Technology; The Effect of Government Intervention on the Development of Strip Casting Technology*”, Energy Policy, 31 (2003) 1339-1356.
- [18] H. S. Di, Y. L. Li, Z. L. Ning, Z. Li, X. Liu, G. D. Wang, “*New Processing Technology of Twin Roll Strip Casting of AZ31B Magnesium Strip*”, Materials Science Forum, 488-489 (2005) 615-618.
- [19] E. Essadiqi, I. H. Jung, M. A. Wells in “*Advances in Wrought Magnesium Alloys-Fundamentals of Processing, Properties and Applications*”, (Eds. C. Bettles, M. Barnett), Woodhead Publishing Limited, 2012.
- [20] R. Wechsler, “*The status of twin-roll casting technology*”, Scandinavian Journal of Metallurgy, 32 (2003) 58-63.
- [21] J. Wang, B. Jiang, P. Ding, F. Pan, Y. Dai, “*Study on Solidification Microstructure of AZ31 Alloy Strips by Vertical Twin Roll casting*”, Materials Science Forum, 546-549 (2007) 383-386.
- [22] C. Yang, P. Ding, D. Zhang, F. Pan, “*The Microstructure and Processing in Twin Roll Casting of Magnesium Alloy Strip*”, Materials Science Forum, 488-489 (2005) 427-430.
- [23] Y. Nakaura, K. Ohori, “*Properties of AZ31 Magnesium Alloy Sheet Produced by Twin Roll casting*”, Materials Science Forum, 488-489 (2005) 419-426.
- [24] T. Haga, K. Tkahashi, M. Ikawa, H. Watari, “*Twin Roll Casting of Aluminum Alloy Strips*”, Journal of Materials Processing Technology, 153-154 (2004) 42-47.
- [25] T. Haga, K. Tkahashi, M. Ikawa, H. Watari, “*A Vertical-Type Twin Roll Caster for Aluminum Alloy Strips*”, Journal of Materials Processing Technology, 140 (2003) 610-615.
- [26] O. Volkova, B. Sahebkar Moghaddam, S. Lachmann, P.-R. Scheller, “*Flow Conditions by Twin Roll Casting of Light Metals*”, Metall, 61-5 (2007) 314-318.

- [27] T. Haga, S. Suzuki, "Roll Casting of Aluminum Alloy Strip by Melt Drag Twin Roll Caster", Journal of Materials Processing Technology, 118 (2001) 165-168.
- [28] M. Yun, S. Lokyer, J. D. Hunt, "Twin Roll Casting of Aluminum Alloys", Materials Science and Engineering A, 280 (2000) 116-123.
- [29] T. Haga, H. Inui, H. Watari, S. Kumai, "Casting of Al-Si Hypereutectic Aluminum Alloy Strip Using an Unequal Diameter Twin Roll Caster", Journal of Materials Processing Technology, 191 (2007) 238-241.
- [30] T. Haga, S. Suzuki, "Study on High-Speed Twin-Roll Caster for Aluminum Alloys", Journal of Materials Processing Technology, 143-144 (2003) 895-900.
- [31] T. Haga, S. Suzuki, "A High Speed Twin Roll Caster for Aluminum Alloy Strip", Journal of Materials Processing Technology, 113 (2001) 291-295.
- [32] T. Haga, T. Nishiyama, S. Suzuki , "Strip Casting of A5182 Alloy Using a Melt Drag Twin-Roll Caster", Journal of Materials Processing Technology, 133 (2003) 103-107.
- [33] C. Gras, M. Meredith, J. D. Hunt,"Micro Defects Formation During the Twin-Roll Casting of Al-Mg-Mn Aluminum Alloys", Journal of Materials Processing Technology, 167 (2005) 62-72.
- [34] S. Das, N. S. Lim, J. B. Seol, H. W. Kim, C. G. Park, "Effect of the Rolling Speed on Microstructural and Mechanical Properties of Aluminum-Magnesium Alloys Prepared by Twin Roll Casting", Materials and Design, 31 (2010) 1633-1638.
- [35] T. Haga, H. Sakaguchi, H. Watari, S. Kumai, "High Speed Twin Roll Casting of 6061 Alloy Strips", Archives of Materials Science and Engineering, 31-1 (2008) 49-52.
- [36] T. Haga, "Semi-Solid Roll Casting of Aluminum Alloy Strip by Melt Drag Twin Roll Caster", Journal of Materials Processing Technology, 111 (2001) 64-68.
- [37] T. Haga, "Semisolid Strip Casting Using a Twin Roll Caster Equipped with a Cooling Slope", Journal of Materials Processing Technology, 130-131 (2002) 558-561.
- [38] S. Das, N. S. Lim, H. W. Kim, C. G. Park, "Effect of Rolling speed on Microstructure and Age-Hardening Behaviour of Al-Mg-Si Alloy Produced by Twin Roll Casting Process", Materials and Design, 32 (2011) 4603-4607.

- [39] T. Haga, H. Inui, H. Watari, S. Kumai, "*Semisolid Roll Casting of Aluminum Alloy Strip and Its Properties*", Solid State Phenomena, 379-382 (2006) 116-117.
- [40] T. Haga, M. Mtsuo, D. Kunigo, Y. Hatanaka, R. Nakamuta, H. Watari, S. Kumai, "*Roll Casting of 5182 Aluminium Alloy*", Journal of Achievements in Materials and Manufacturing Engineering, 34-2 (2009) 172-179.
- [41] R. I. L. Guthrie, M. Isac, J. S. Kim, R. P. Tavares, "*Measurements, Simulation, and Analyses of Instantaneous Heat Fluxes from Solidifying Steels to the Surfaces of Twin Roll Casters and of Aluminum to Plasma-Coated Metal Substrates*", Metallurgical and Materials Transactions B, 31 (2000) 1031-1047.
- [42] R. Guthrie, "*Recent High Temperature Adventures in the Casting of Metals and their Potential Implications for the Near Net Shape Production of Steel Sheets*", Canadian Metallurgical Quarterly, 48-3 (2009) 187-196.
- [43] S. S. Park, W. J. Park, C. H. Kim, B. S. You, N. J. Kim , "*The Twin-Roll Casting of Magnesium Alloys*", Jornal of the Minerals, Metals and Materials Society, 61-8 (2009) 14-18.
- [44] H. Watari, T. Haga, R. Paisern, N. Koga, K. Davey, "*Mechanical Properties and Metallurgical Qualities of Magnesium Alloy Sheets Manufactured by Twin-Roll Casting*", Key Engineering Materials, 345-346 (2007) 165-168.
- [45] H. Watari, N. Koga, K. Davey, T. Haga, M. T. Alonso Ragado, "*Warm Deep Drawing of Wrought Magnesium Alloy Sheets Produced by Semi-Solid Roll Strip-Casting Process*", International Journal of Machine Tools & Manufacture, 46 (2006) 1233-1237.
- [46] H. Watari, T. Haga, Y. Shibue, K. Davey, N. Koga , "*Twin Roll Casting of Magnesium Alloys with High Aluminum Contents*", Journal of Achievements in Materials and Manufacturing Engineering, 18 (2006) 419-422.
- [47] H. Watari, T. Haga, N. Koga, K. Davey, "*Feasibility Study of Twin Roll Casting Process for Magnesium Alloys*", Journal of Materials Processing Technology, 192-193 (2007) 300-305.
- [48] H. Watari, R. Paisarn, T. Haga, K. Noda, K. Davey, N. Koga, "*Development of Manufacturing Process of Wrought Magnesium Alloy Sheets by Twin Roll Casting*", Journal of Achievements in Materials and Manufacturing Engineering, 20 (2007) 515-518.

- [49] H. Watari, T. Haga, K. Davey, N. Koga, T. Yamazaki, "*Effects of Production Parameters on Characteristics of Magnesium Alloy Sheets Manufactured by Twin-Roll Casting*", Journal of Achievements in Materials and Manufacturing Engineering, 16 (2006) 171-176.
- [50] H. Watari, Y. Nishio, T. Haga, K. Davey, N. Koga, "*Microstructure and Mechanical Properties of High Aluminum Content Magnesium Alloys Fabricated by Twin Roll Casting Process*", Materials Science Forum, 638-642 (2010) 1608-1613.
- [51] H. Watari, K. Davey, M. T. Rasgado, T. Haga, S. Izawa, "*Semi-Solid Manufacturing Process of Magnesium Alloys by Twin-Roll Casting*", Journal of Materials Processing Technology, 155-156 (2004) 1662-1667.
- [52] T. Haga, H. Watari, S. Kumai, "*High Speed Roll Casting of Mg Alloy Strip by a Vertical Type Twin Roll Caster*", Journal of Achievements in Materials and Manufacturing Engineering, 15 (2006) 186-192.
- [53] H. Harada, S. Nishida, T. Nagumo, M. Endo, H. Watari, "*Fabrication of High Aluminum Content Mg Alloys Using a Horizontal Twin Roll Caster*", International Journal of Mechanical and Industrial Engineering, 6 (2012) 187-190.
- [54] D. Y. Ju, X. D. Hu, "*Effects of Casting Parameters and Deformation on Microstructure Evolution of Twin-Roll Casting Magnesium Alloy AZ31*", Transactions of Nonferrous Metals Society of China, 16 (2006) 874-877.
- [55] M. Numano, N. Mori, Y. Nakai, N. Kawabe, "*Properties of AZ31 and AZ91 Sheets Made by Twin Roll Casting*", Materials Science Forum, 539-543 (2007) 1650-1655.
- [56] N. Tang, M. P. Wang, H. F. Lou, Y. Y. Zhao, Z. Li, "*Microstructure and Texture of Twin-Roll Cast Mg-3Al-1Zn-0.Mn Magnesium Alloy*", Materials Chemistry and Physics, 116 (2009) 11-15.
- [57] G. S. Wang, H. S. Di, F. Huang, "*Preparation of AZ31 Magnesium Alloy Strips Using Vertical Twin-Roll Caster*", Transactions of Nonferrous Metals Society of China, 20 (2010) 973-979.
- [58] Y. Nakaura, A. Watanabe, K. Ohori, "*Microstructure and Mechanical Properties of AZ31 Magnesium Alloy Strip Produced by Twin Roll Casting*", Materials Transactions, 47-7 (2006) 1743-1749.

- [59] Y. Huang, I. Bayandorian, Z. Fan, "*Microstructure Control during Twin Roll Casting of an AZ31 Magnesium Alloy*", in the 3rd International Conference on Advances in Solidification Processes, Rolduc Abbey, Aachen, The Netherlands, 2011.
- [60] I. Bayandorian, I. Stone, Y. Huang, Z. Fan, "*Twin Roll Casting of Thin AZ31 Magnesium Alloy Strip with Uniform Microstructure and Chemistry*", in *Magnesium Technology 2012*, TMS (The Minerals, Metals & Materials Society), 2012, Orlando, FL, USA, 2012.
- [61] R. Kawalla, M. Oswald, C. Schmidt, M. Ullmann, H. P. Vogt, N. D. Cuong, "*New Technology for the Production of Magnesium Strips and Sheets*", *Metalurgija*, 47 (2008) 195-198.
- [62] H. Chen, S. B. Kang, H. Yu, H. W. Kim, G. Min, "*Microstructure and Mechanical Properties of Mg-4.5Al-1.0Zn Alloy Sheets Produced by Twin Roll Casting and Sequential Warm Rolling*", *Materials Science and Engineering A*, 492 (2008) 317-326.
- [63] X. Gong, H. Li, S. B. Kang, J. H. Cho, S. Li, "*Microstructure and Mechanical Properties of Twin-Roll Cast Mg-4.5Al-1.0Zn Sheets Processed by Differential Speed Rolling*", *Materials and Design*, 31 (2010) 1581-1587.
- [64] Z. Bian, I. Bayandorian, H. W. Zhang, G. Scamans, Z. Fan, "*Extremely Fine and Uniform Microstructure of Magnesium AZ91D Alloy Sheets Produced by Melt Conditioned Twin Roll Casting*", *Materials Science and Technology*, 25-5 (2009) 599-606.
- [65] Z. Bian, I. Bayandorian, H. W. Zhang, Z. Fan, "*Twin Roll Casting and Melt Conditioned Twin Roll Casting of Magnesium*", *Solid State Phenomena*, 141-143 (2008) 195-200.
- [66] S. B. Kanga, J. Choa, L. Chang, "*Influence of Twin Roll Casting and Differential Speed Rolling on Microstructure and Tensile Properties in Magnesium Alloy Sheets*", *Procedia Engineering*, 10 (2011) 1190-1195.
- [67] M. Aljarrah, E. Essadiqi, D. H. Kang, I. H. Jung, "*Solidification Microstructure and Mechanical Properties of Hot Rolled and Annealed Mg Sheet Produced Through Twin Roll Casting Route*", *Materials Science Forum*, 690 (2011) 331-334.
- [68] S. A. Lockyer, M. Yun, J. D. Hunt, D. V. Edmonds, "*Micro- and Macrodefects in Thin Sheet Twin-Roll Cast Aluminum Alloys*", *Materials Characterization*, 37 (1996) 301-310.

- [69] J.J. Kim, W. J. Park, D. Choo, "*Microstructural Analysis of Segregated Area in Twin Roll Cast Magnesium Alloy Sheet*", in Magnesium Technology 2011, TMS 140th Annual Meeting and Exhibition, San Diego, CA, USA, 2011.
- [70] P. J. Bradbury, J. D. Hunt, "*A Coupled Fluid Flow, Deformation and Heat Transfer Model*", in Proceedings of Modelling of Casting, Welding and Advanced Solidification Processes VII, The Minerals, Metals & Materials Society, Warrendale, PA, USA, 1995.
- [71] C. Gras, M. Meredith, K. Gatenby, J. D. Hunt, "*Defect Formation in Twin Roll-Cast AA 3xxx and 5xxx Series Aluminium Alloys*", Materials Science Forum , 396-402 (2002) 89-94.
- [72] M. Yun, S. A. Lockyer, J. D. Hunt, "*The Formation of Surface Bleeds in Twin Roll Cast Aluminium Sheet*", International Journal of Cast Metals Research, 13 (2001) 255-261.
- [73] S. A. Lockyer, M. Yun, J. D. Hunt, D. V. Edmonds, "*Microstructural Defects in Thin Sheet Twin Roll Cast Aluminium Alloys*", Materials Science Forum, 217-222 (1996) 367-372.
- [74] D. J. Monaghan, M. B. Henderson, J. D. Hunt, D. V. Edmonds, "*Microstructural Defects in High Productivity Twin-Roll Casting of Aluminium*", Materials Science and Engineering A, 173 (1993) 251-254.
- [75] I. Jin, L. R. Morris, J. D. Hunt, "*Centerline Segregation in Twin-Roll-Cast Aluminum Alloy Slab*", Journal of Metals, 6 (1982) 70-74.
- [76] B. Forbord, B. Andersson, F. Ingvaldsen, O. Austevik, J. A. Horst, I. Skauvik, "*The Formation of Surface Segregates during Twin Roll Casting of Aluminum Alloys*", Materials Science and Engineering A, 415 (2006) 12-20.
- [77] Material Property Data, 2012, <http://www.matweb.com/>.
- [78] S. Lee, "*Mathematical Modeling of a Twin-Roll Strip Casting Process with Turbulent Flow -On Molten Metal Flow Field-*", Korean Journal of Chemical Engineering, 9 (1992) 199-205.
- [79] T. Saitoh, H. Hojo, H. Yaguchi, C.G. Kang, "*Two-Dimensional Model for Twin-Roll Continuous Casting*", Metallurgical Transactions B, 20 (1989) 381-390.
- [80] S. M. Hwang, Y. H. Kang, "*Analysis of Flow and Heat Transfer in Twin-Roll Strip Casting by Finite Element Method*", Transactions of the ASME- Journal of Engineering for Industry, 117 (1995) 304-315.

- [81] R. J. O'Malley, M. E. Karabini, R. E. Smelser, "*The Roll Casting Process: Numerical and Experimental Results*", Journal of Materials Processing & Manufacturing Sciences, 3 (1994) 59-72.
- [82] P. Bradbury, "*A Mathematical Model for the Twin Roll Casting Process*", PhD Thesis, Oxford, UK, 1994.
- [83] J. G. Chang, C. I. Weng, "*Analysis of Flow and Heat Transfer in Twin-Roll Strip Casting Process*", International Journal of Heat and Mass Transfer, 41 (1998) 475-487.
- [84] J. G. Chang, C. I. Weng, "*Numerical Modeling of Twin-Roll Casting by the Coupled Fluid Flow and Heat Transfer Model*", International Journal for Numerical Methods in Engineering, 40 (1997) 493-509.
- [85] J. D. Hwang, H. J. Lin, W. S. Hwang, C. T. Hu, "*Numerical Simulation of Metal Flow and Heat Transfer during Twin Roll Strip Casting*", ISIJ International, 35-2 (1995) 170-177.
- [86] W. S. Kim, D. S. Kim, A. V. Kuznetsov, "*Simulation of Coupled Turbulent Flow and Heat Transfer in the Wedge-Shaped Pool of a Twin-Roll Strip Casting Process*", International Journal of Heat and Mass Transfer, 43 (2000) 3811-3822.
- [87] Y. Sahai, A. Saxena, "*Modeling of Twin-Roll Thin Strip Casting of Aluminum Alloys*", in TMS (The Minerals, Metals and Materials Society), Light Metals 2002, Seattle, WA, USA, 2002.
- [88] A. Saxena, Y. Sahai, "*Modeling of Fluid Flow and Heat Transfer in Twin-Roll Casting of Aluminum Alloys*", Materials Transactions, 43-2 (2002) 206-213.
- [89] M. A. Cruchaga, D. J. Celentano, R. W. Lewis, "*Modelling of Twin-Roll Strip Casting Process*", Communications in Numerical Methods in Engineering, 19 (2003) 623-635.
- [90] B. Wang, J. Zhang, J. Fan, S. Zhao, "*Water Modeling of Twin-Roll Strip Casting*", Journal of Iron and Steel Research International, 13-1 (2006) 14-17.
- [91] B. Wang, J. Zhang, Y. Zhang, Y. He, J. Fan, Y. Fang, S. An, "*Numerical and Physical Simulation of a Twin-Roll Strip Caster*", Journal of University of Science and Technology Beijing, 13-5 (2006) 393-400.
- [92] B. Wang, J. Y. Zhang, Y. Zhang, J. F. Fan, Y. Fang, S. L. An, "*Numerical Analysis of Fluid Flow and Heat Transfer in Pool of Twin Roll Strip Caster*", Ironmaking and Steelmaking, 35-1 (2008) 75-80.

- [93] B. Wang, J. Y. Zhang, J. F. Fan, S. L. Zhao, S. B. Ren, K. C. Chou, "*Modelling of Melt Flow and Solidification in the Twin-Roll Strip Casting*", Steel Research International, 80-3 (2009) 218-222.
- [94] J. Zhang, B. Wang, J. Fan, Y. Fang, S. Zhao, S. Ren, "*Numerical Simulation of Twin-Roll Strip Casting*", in Materials Characterization, Computation and Modeling, TMS , New Orleans, LA, USA, 2008.
- [95] Y. Fang, Z. M. Wang, Q. X. Yang, Y. K. Zhang, L. G. Liu, H. Y. Hu, Y. Zhang, "*Numerical Simulation of the Temperature Fields of Stainless Steel with Different Roller Parameters during Twin-Roll Strip Casting*", International Journal of Minerals, Metallurgy and Materials, 16-3 (2009) 304-308.
- [96] P. Zhang , Y. Zhang, L. Liu, X. Ren, Y. Zhang, Y. Fang, Q. Yang , "*Numerical Simulation on the Stress Field of Austenite Stainless Steel during Twin-Roll Strip Casting Process*", Computational Materials Science, 52 (2012) 61-67.
- [97] X. Zhang, Z. Jiang, X. Liu, G. Wang, "*Simulation of Fluid Flow, Heat Transfer and Micro-Segregation in Twin Roll Strip Casting of Stainless Steel*", Journal of Materials Science Technology, 22-3 (2006) 295-300.
- [98] X. M. Zhang, Z. Y. Jiang, L. M. Yang, X. H. Liu, G. D. Wang, A. K. Tieu, "*Modeling of Coupling Flow and Temperature Fields in Molten Pool during Twin-Roll Strip Casting Process*", Journal of Materials Processing Technology, 187 (2007) 339-343.
- [99] X. M. Zhang, Z. Y. Jiang, X. H. Liu, G. D. Wang, L. M. Yang, A. K. Tieu, "*Influence of Casting Speed on Temperature and Flow Fields in Molten Pool during Twin-Roll Strip Casting Process*", Materials Science Forum, 505-507 (2006) 1315-1320.
- [100] X. M. Zhang, Z. Y. Jiang, L. M. Yang, X. H. Liu, G. D. Wang, "*Flow and Temperature Analysis of Molten Pool in Twin-Roll Strip Casting Process*", Key Engineering Materials, 340-341 (2007) 695-700.
- [101] Y. C. Miao, X. M. Zhang, H. S. Di, G. D. Wang, "*Numerical Simulation of the Fluid Flow, Heat Transfer, and Solidification of Twin Roll Strip Casting*", Journal of Materials Processing Technology, 174 (2006) 7-13.
- [102] Y. C. Miao, X. M. Zhang, G. D. Wang, H. S. Di, X. H. Liu, "*Coupled simulation of Flow and Thermal Field of Twin-Roll Strip Casting Process*", Journal of Iron and Steel Research International, 8-2 (2001) 16-19.

- [103] Y. C. Miao, X. M. Zhang, G. D. Wang, H. S. Di, X. H. Liu, "*Simulation of the Twin Roll Stainless Strip Casting Process*", Acta Metallurgica Sinica (English Letters), 14-3 (2001) 199-204.
- [104] R. I. L. Guthrie, R. P. Tavares, "*Mathematical and Physical Modeling of Steel Flow and Solidification in Twin-Roll/Horizontal Belt Thin-Strip Casting*", Applied Mathematical Modeling, 22 (1998) 851-872.
- [105] R. P. Tavares, M. Isac, R. I. L. Guthrie, "*Roll-Strip Interfacial Heat Fluxes in Twin-Roll Casting of Low-Carbon Steels and Their Effects on Strip Microstructure*", ISIJ International, 38-12 (1998) 1353-1361.
- [106] D. Lixin, Y. Shan, H. Hai, W. Tongmin, Z. Xianshu, J. Junze, "*The Influence of Interfacial Heat Transfer on Solidification Process during the Twin Roll Strip Casting*", in Proceedings of Modeling of Casting, Welding and Advanced Solidification Processes-XI, Opio, France, 2006.
- [107] C. Ohler, H. J. Odenthal, H. Pfeifer, "*Physical and Numerical Simulation of Fluid Flow and Solidification at the Twin-Roll Strip Casting Process*", Steel Research International, 74 (2003) 739-747.
- [108] X. B. Liu, D. H. Mao, J. Zhong, "*Development and Application of Coupling Model of Aluminum Thin-Gauge High-Speed Casting*", Transactions of Nonferrous Metals Society of China, 15-3 (2005) 485-490.
- [109] D. Y. Ju, H.Y. Zhao, X. D. Hu, K. Ohori, M. Tougo, "*Thermal Flow Simulation on Twin Roll Casting Process for Thin Strip Production of Magnesium Alloy*", Materials Science Forum, 488-489 (2005) 439-444.
- [110] X. D. Hu, D. Y. Ju, H. Y. Zhao, "*Thermal Flow Simulation and Concave Type Slot Nozzle Design for Twin Roll Casting of Magnesium Alloy AZ31*", Materials Science Forum, 539-543 (2007) 5037-5043.
- [111] J. W. Bae, C. G. Kang, S. B. Kang, "*Mathematical Model for the Twin Roll Type Strip Continuous Casting of Magnesium Alloy Considering Thermal Flow Phenomena*", Journal of Materials Processing Technology, 191 (2007) 251-255.
- [112] J. Zeng, R. Koitzsch, H. Pfeifer, B. Friedrich, "*Numerical Simulation of the Twin-Roll Casting Process of Magnesium Alloy Strip*", Journal of Materials Processing Technology, 209 (2009) 2321-2328.

- [113] H. Zhao, P. Li, L. He, "*Coupled Analysis of Temperature and Flow during Twin-Roll Casting of Magnesium Alloy Strip*", Journal of Materials Processing Technology, 211 (2011) 1197-1202.
- [114] R. N. Grugel, "*Secondary and Tertiary Dendrite Arm Spacing Relationships in Directionally Solidified Al-Si Alloys*", Journal of Material Science, 28 (1993) 677-683.
- [115] M. S. Turhal, T. Savaskan, "*Relationships between Secondary Dendrite Arm Spacing and Mechanical Properties of Zn-40Al-Cu Alloys*", Journal of Material Science, 38 (2003) 2639 – 2646.
- [116] V. Jayakrishnan, "*Feasibility of Producing Clad Twin Roll Cast (TRC) AZ31*", MSc Thesis, University of Waterloo, Waterloo, ON, Canada, 2011.
- [117] H. G. Fjær, A. Mo, "*ALSPEN - A Mathematical Model for Thermal Stresses in Direct Chill Casting of Aluminium Billets*", Metallurgical Transactions B, 21 (1990) 1049-1061.
- [118] D. Mortensen, M. Rudshaug, H.G. Fjær, "*Coupled Stress, Thermal and Fluid Flow Modelling in Materials Processing*", in MekIT'05 Third national conference on Computational Mechanics, Trondheim, Norway, 2005.
- [119] M. M'Hamdi, A. Mo, H.G. Fjær , "*TearSim: A Two-Phase Model Addressing Hot Tearing Formation During Aluminium Direct Chill Casting*", Metallurgical and Materials Transactions A, 37 (2006) 3069-3083.
- [120] D. Mortensen, "*ALSIM Reference Manual Version 6.1*", Norway, 2011.
- [121] B. J. Howes, M. A. Wells, R. Bathla, D. M. Maijer, "*Constitutive Behaviour of As-Cast Magnesium Alloy AZ31 Under Deformation Conditions Relevant to DC Casting*", in Proceedings of the 2nd International Light Metals Technology Conference, St. Wolfgang, Austria, 2005.
- [122] H. Hao, D. M. Maijer, M. A. Wells, S. L. Cockcroft, D. Sediako, S. Hibbins, "*Development and Validation of a Thermal Model of Direct Chill Casting of AZ31 Magnesium Billets*", Metallurgical and Materials Transactions A, 35 (2004) 3843-3854.
- [123] Y. He, A. Javaid, E. Essadiqi, M. Shehata, "*Numerical Simulation and Experimental Study of the Solidification of a Wedge-Shaped AZ31 Mg Alloy Casting*", Canadian Metallurgical Quarterly, 48-2 (2009) 145-156.

- [124] H. Hao, D. M. Maijer, M. A. Wells, A. Phillion, S. L. Cockcroft, "*Modeling the Stress-Strain Behavior and Hot Tearing during Direct Chill Casting of an AZ31 Magnesium Billet*", Metallurgical and Materials Transactions A, 41 (2010) 2067-2077.
- [125] R. V. Allen, D. R. East, T. J. Johnson, W. E. Borbridge, D. Liang, "*Magnesium Alloy Sheet Produced by Twin Roll Casting*", in Magnesium Technology 2001, 130th Annual Meeting & Exhibition of The Minerals, Metals & Materials Society, TMS 2001, New Orleans, LA, USA, 2001.
- [126] F. P. Incropera, D. P. DeWitt, T. L. Bergman, A. S. Lavine, "Fundamentals of Heat and Mass Transfer", 6th Edition, Wiley, 2007.
- [127] S. Kalpakjian, S. R. Schmid, "*Manufacturing Processes for Engineering Materials*", Fifth Edition, Jurong, Singapore: Pearson Education South Asia Pte Ltd., 2008.
- [128] C. Huang, H. Deng, J. Chen, X. Hu, S. Yang, "*Research on Rolling Force Model in Hot-Rolling Process of Aluminum Alloys*", Procedia Engineering, 16 (2011) 745-754.
- [129] J. G. Lenard, M. Pietrzyk, L. Cser, "*Mathematical and Physical Simulation of the Properties of Hot Rolled Products*", Oxford, UK: Elsevier, 1999.
- [130] M. Dunar, A. S. Akkurt, K. Sarioglu, C. Romanowski, "*The Influence of Caster Roll Diameter on the Microstructure of Twin Roll Cast Aluminum Strip*", in Light Metal 2003, TMS Annual Meeting & Exhibition, San Diego, CA, USA, 2003.
- [131] W. Kurz, D. J. Fisher, "*Fundamentals of Solidification*", Third Revised Edition, Brookfield, VT, USA: Trans Tech Publications, 1989.

## Appendix A

### Equivalent Specific Heat Calculation

In this appendix the procedure of calculating the equivalent specific heat which includes the effect of latent heat of fusion is presented in details. Figure A-1 illustrates a typical enthalpy of an alloy as a function of temperature.

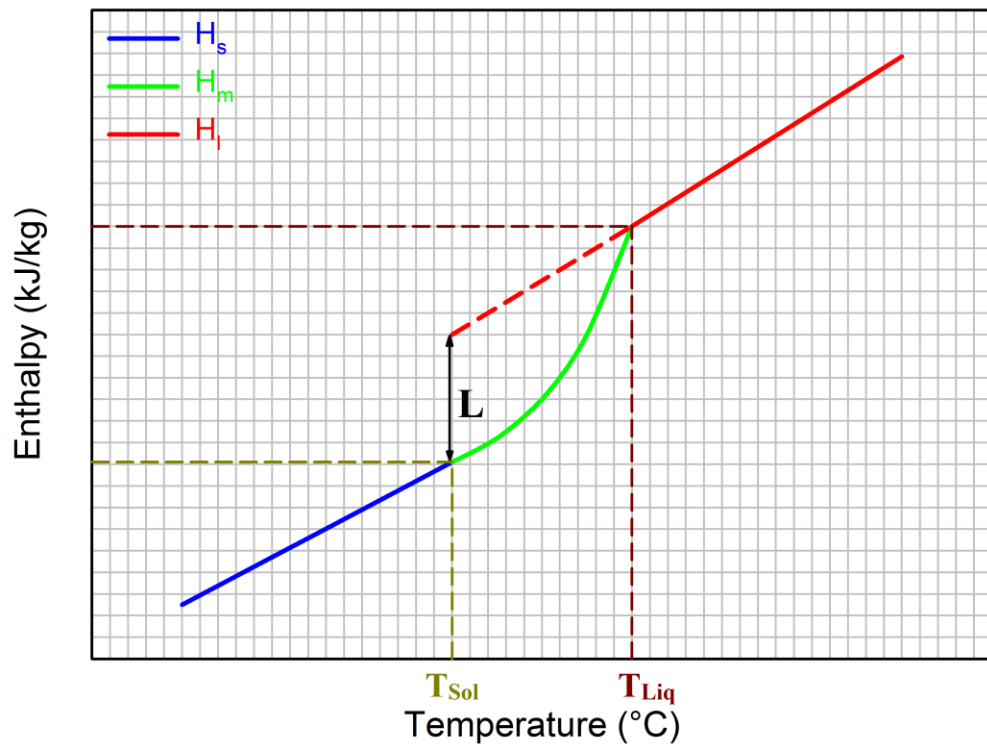


Figure A-1- Typical enthalpy-temperature relationship of an alloy.

Referring to Figure A-1, the latent heat of fusion is the difference between the solid and liquid phase enthalpy at the solidus as shown by Equation (A-1).

$$L = (H_l - H_s)|_{T_{Sol}} \quad (A-1)$$

where  $L$  is the latent heat of fusion (in kJ/kg),  $H_l$  and  $H_s$  are liquid and solid phase enthalpy at solidus, respectively (in kJ/kg) and  $T_{sol}$  is the solidus temperature (in °C).

Enthalpy of the mushy material is calculated using Equation (A-2). Since the relationship between the specific heat and enthalpy follows the Equation (A-3), the specific heat of the mushy material is calculated using Equation (A-4).

$$H_m = f_s H_s + f_l H_l \quad (\text{A-2})$$

$$C_p = \frac{dH}{dT} \quad (\text{A-3})$$

$$C_{P_m} = \frac{dH_m}{dT} = \frac{df_s}{dT} H_s + f_s \frac{dH_s}{dT} + \frac{df_l}{dT} H_l + f_l \frac{dH_l}{dT} \quad (\text{A-4})$$

where  $H_m$  is the enthalpy of the mushy material (in kJ/kg),  $f_s$  and  $f_l$  are solid and liquid fraction, respectively,  $C_p$  is the specific heat (in kJ/kg°C),  $T$  is temperature (in °C) and  $C_{P_m}$  is the specific heat of the mushy material (in kJ/kg°C).

In the mushy zone the relationship between the solid and liquid fraction follows Equation (A-5) and the derivative of Equation (A-5) with respect to temperature is shown by Equation (A-6). So, the derivative of solid fraction and liquid fraction in the mushy zone follows Equation (A-7).

$$f_s + f_l = 1 \quad (\text{A-5})$$

$$\frac{df_s}{dT} + \frac{df_l}{dT} = 0 \quad (\text{A-6})$$

$$\frac{df_l}{dT} = -\frac{df_s}{dT} \quad (\text{A-7})$$

So, the specific heat in the mushy zone is calculated using Equation (A-8).

$$C_{P_m} = (H_s - H_l) \frac{df_s}{dT} + f_s C_{P_s} + f_l C_{P_l} \quad (\text{A-8})$$

where  $C_{P_s}$  and  $C_{P_l}$  are the specific heat of solid and liquid metal, respectively (in  $\text{kJ/kg}^{\circ}\text{C}$ ).

In the solid phase:

$$\begin{cases} f_s = 1 \\ f_l = 0 \\ \frac{df_s}{dT} = 0 \end{cases} \quad (\text{A-9})$$

$$C_{P_m} = C_{P_s} \quad (\text{A-10})$$

In the liquid phase:

$$\begin{cases} f_s = 0 \\ f_l = 1 \\ \frac{df_s}{dT} = 0 \end{cases} \quad (\text{A-11})$$

$$C_{P_m} = C_{P_l} \quad (\text{A-12})$$

Temperature dependent enthalpy of the solid metal is calculated using Equation (A-13) and for the liquid metal Equation (A-14) is used (recalling Equation (A-1)).

$$H_s(T) = H_{Sol} + \int_{T_{Sol}}^T C_{P_s}(T') dT' \quad (\text{A-13})$$

$$H_l(T) = H_{Sol} + L + \int_{T_{Sol}}^T C_{P_l}(T') dT' \quad (\text{A-14})$$

So, the difference between the solid and liquid enthalpy is calculated using Equation (A-15).

$$H_s - H_l = -L + \int_{T_{Sol}}^T [C_{P_s}(T') - C_{P_l}(T')]dT' \quad (\text{A-15})$$

Recalling Scheil equation for solid fraction calculation (Equation (A-16)), the derivative of solid fraction with respect to temperature will follow Equation (A-17).

$$f_s = 1 - \left(\frac{T_f - T}{T_f - T_l}\right)^{1/(k-1)} \quad (\text{A-16})$$

$$\Delta T_{fl} = T_f - T_l \quad (\text{A-16a})$$

$$\alpha = 1/(k - 1) \quad (\text{A-16b})$$

$$\frac{df_s}{dT} = \frac{\alpha}{\Delta T_{fl}} \left(\frac{T_f - T}{\Delta T_{fl}}\right)^{\alpha-1} \quad (\text{A-17})$$

where  $k$  is the partition coefficient,  $T_f$  the melting point of pure Mg (in °C) and  $T_l$  liquidus temperature (in °C).

By replacing Equations (A-15) and (A-17) in Equation (A-8), the new form of specific heat in the mushy material will follow Equation (A-18).

$$\begin{aligned} C_{P_m} = & \left[ \frac{\alpha}{\Delta T_{fl}} \left(\frac{T_f - T}{\Delta T_{fl}}\right)^{\alpha-1} \right] \left[ -L + \int_{T_{Sol}}^T [C_{P_s}(T') - C_{P_l}(T')]dT' \right] + [1 \\ & - \left(\frac{T_f - T}{\Delta T_{fl}}\right)^\alpha] [C_{P_s}] + \left(\frac{T_f - T}{\Delta T_{fl}}\right)^\alpha C_{P_l} \end{aligned} \quad (\text{A-18})$$

By using Equation (A-19) the equivalent specific heat includes the effect of latent heat of fusion is calculated which is shown in Figure A-2.

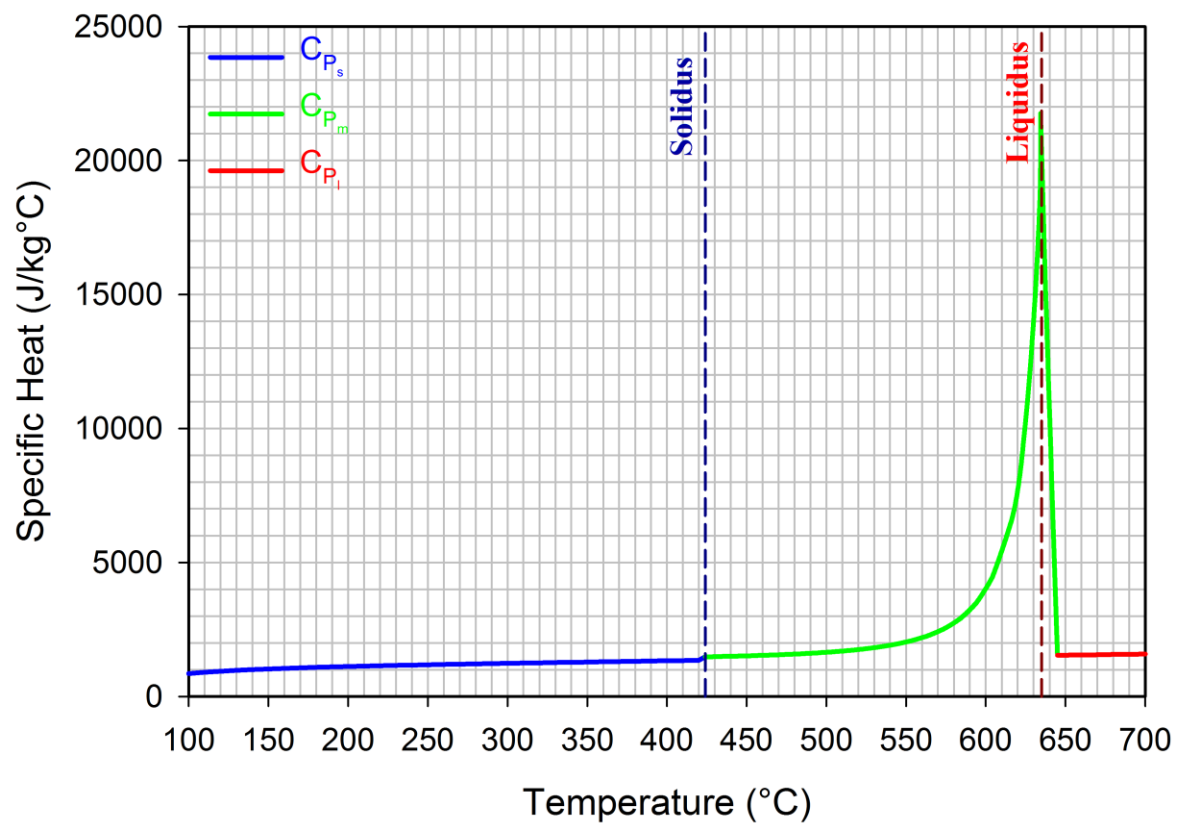


Figure A-2- Equivalent specific heat of AZ31 magnesium alloy includes the effect of latent heat of fusion.